

# **Design of a Smart Tire Sensor System**

by

Jennifer Bastiaan

A thesis  
presented to the University of Waterloo  
in fulfilment of the  
thesis requirement for the degree of  
Doctor of Philosophy  
in  
Mechanical Engineering

Waterloo, Ontario, Canada, 2015

© Jennifer Bastiaan 2015

## **AUTHOR'S DECLARATION**

I hereby declare that I am the sole author of this thesis. This is a true copy of the thesis, including any required final revisions, as accepted by my examiners.

I understand that my thesis may be made electronically available to the public.

## ABSTRACT

A research project is conducted that involves the design of a smart tire sensor system that can determine six tire outputs, including tire longitudinal force, tire lateral force, tire vertical force, tire aligning moment, tire / road friction coefficient and tire air inflation pressure. All of these quantities are estimated using in-tire deformation sensors. The rationale for conducting the smart tire research project is that its results have the potential to improve ground vehicle safety. The objectives of the research project are to identify the quantity and types of sensors required, determine the sensor locations and orientations in the tire, develop post-processing methods for the raw sensor output and confirm correct operation of the sensor system, which involves prototyping and physical testing.

Strain is predicted in the tire inner liner as part of a tire finite element analysis study. The tire finite element model is used to calculate strain (inputs) and tire forces (outputs) for use in artificial neural networks. Results from the radial basis function networks studied are excellent, with calculated tire forces within 1% and tire aligning moment within 1%. The conclusion is that radial basis function networks can likely be used effectively for analysis of strain sensor measurements in the smart tire sensor system. Further studies using virtual strain show that the system should have two in-tire strain sensors located near one another at the outside sidewall, with one oriented longitudinally and the other oriented radially, along with an angular position sensor.

Commercially available piezoelectric deformation sensors are installed in this layout, along with a rotary encoder, in a smart tire physical prototype. On-road data collected during physical testing are used with radial basis function neural networks to estimate the three orthogonal tire forces and the tire aligning moment. The networks are found capable of predicting the correct trends in the tire force data over several testing events. While the smart tire sensor system in its current state of development is not production-ready, the research project has resulted in new scientific knowledge that will be the foundation of future smart tire work. Contributions include the identification of in-tire sensor quantity, locations and orientations, confirmation that an angular position measurement is necessary and the determination of the artificial neural network architecture.

The most significant remaining smart tire technical hurdle is the identification of a sufficiently durable strain sensor for in-tire use. If this strain sensor can be found, the next steps will include validation of the non-force tire estimates and studies of temperature effects, wireless data transmission and energy harvesting for a battery free design. Despite these outstanding concerns, the results of the smart tire research project show that the concept is feasible and further work is justified.

## **ACKNOWLEDGEMENTS**

I would like to thank Professor Amir Khajepour of University of Waterloo for supervising the smart tire research project and for reviewing the thesis. I would also like to thank the internal examiners at University of Waterloo, Professors Nasser Lashgarian Azad, Kaan Inal and Sriram Narasimhan for reading the research proposal and thesis, attending the examination meetings and helping to improve the results.

Additionally, I would like to thank the external examiner, Professor Ridha Ben-Mrad of University of Toronto, for providing a formal assessment of the thesis and participating in the final exam. Finally, I would like to thank my family for their support, and I would also like to acknowledge the financial support of the Automotive Partnership Canada, Ontario Research Fund and the financial and technical support of General Motors.

# Table of Contents

<b>Author's Declaration</b> . . . . .	<b>ii</b>
<b>Abstract</b> . . . . .	<b>iii</b>
<b>Acknowledgements</b> . . . . .	<b>iv</b>
<b>List of Figures</b> . . . . .	<b>viii</b>
<b>List of Tables</b> . . . . .	<b>xvi</b>
<b>List of Abbreviations</b> . . . . .	<b>xix</b>
<b>1 Introduction</b> . . . . .	<b>1</b>
1.1 Rationale and Purpose . . . . .	2
1.2 Objectives and Methods . . . . .	5
1.3 Thesis Organization . . . . .	6
<b>2 Literature Review</b> . . . . .	<b>7</b>
2.1 Tire Forces and Models . . . . .	7
2.2 Physical Testing of Tire Forces . . . . .	13
2.3 Finite Element Analysis of Tire Forces . . . . .	15

---

## TABLE OF CONTENTS

---

2.4	Existing Tire Force Measurement Methodologies . . . . .	21
2.5	Engineering Specifications . . . . .	32
2.6	Summary . . . . .	35
<b>3</b>	<b>Tire Finite Element Modeling and Analysis . . . . .</b>	<b>37</b>
3.1	Overview . . . . .	37
3.2	Material Properties . . . . .	38
3.3	Model Validation . . . . .	59
3.4	Analysis Studies . . . . .	61
3.5	Summary . . . . .	62
<b>4</b>	<b>Virtual Strain Processing . . . . .</b>	<b>64</b>
4.1	Motivation . . . . .	64
4.2	Reduced System . . . . .	65
4.3	Strain Calculation . . . . .	66
4.4	Neural Network Categories . . . . .	79
4.5	Neural Network Selection . . . . .	82
4.6	Neural Network Studies . . . . .	91
4.7	Summary . . . . .	96
<b>5</b>	<b>Smart Tire Prototyping and Testing . . . . .</b>	<b>98</b>
5.1	In-Tire Piezoelectric Sensor . . . . .	98
5.2	Smart Tire Revision 1 . . . . .	98

---

**TABLE OF CONTENTS**

---

5.3	Smart Tire Revision 2 . . . . .	130
5.4	Summary . . . . .	138
<b>6</b>	<b>Smart Tire Outputs Estimation . . . . .</b>	<b>140</b>
6.1	Estimation of Tire Forces . . . . .	140
6.2	Estimation of Other Outputs . . . . .	159
6.3	Summary . . . . .	166
<b>7</b>	<b>Conclusion . . . . .</b>	<b>169</b>
7.1	System Description . . . . .	169
7.2	Future Work . . . . .	172
	<b>References . . . . .</b>	<b>175</b>
	<b>APPENDICES . . . . .</b>	<b>182</b>
<b>A</b>	<b>Tire FEM Procedures and Geometry . . . . .</b>	<b>183</b>
<b>B</b>	<b>Computer Specifications . . . . .</b>	<b>207</b>
<b>C</b>	<b>Tire FEA Studies . . . . .</b>	<b>209</b>
<b>D</b>	<b>Virtual Strain in Pure Slip . . . . .</b>	<b>231</b>
<b>E</b>	<b>Virtual Strain Studies . . . . .</b>	<b>244</b>
<b>F</b>	<b>Sensor Durability Bench Test . . . . .</b>	<b>255</b>
<b>G</b>	<b>Physical Sensor Measurements . . . . .</b>	<b>278</b>

# List of Figures

1.1	STSS Data Flow Block Diagram . . . . .	4
2.1	Aligning Moment versus Slip Angle for a Truck Tire . . . . .	10
3.1	Finite Element Model of Michelin Tire . . . . .	38
3.2	Experimental Rubber Stress-Strain Curves from Treloar . . . . .	40
3.3	Tread Longitudinal (Top) and Lateral (Bottom) Tire Samples . . . . .	45
3.4	Tread Lugs Longitudinal Tire Samples . . . . .	45
3.5	Sidewall Longitudinal Tire Sample . . . . .	45
3.6	Instron Machine with Tire Sample . . . . .	46
3.7	Tread Longitudinal Tire Sample During Testing . . . . .	46
3.8	Tire Tread Rubber Sample No. 301 . . . . .	47
3.9	Uniaxial Compression and Tension Arruda-Boyce . . . . .	48
3.10	Biaxial and Planar Tension Arruda-Boyce . . . . .	49
3.11	Uniaxial Compression and Tension Yeoh . . . . .	49
3.12	Biaxial and Planar Tension Yeoh . . . . .	50
3.13	Slope of Uniaxial Compression and Tension Arruda-Boyce . . . . .	50
3.14	Slope of Uniaxial Compression and Tension Yeoh . . . . .	51
3.15	Slope of Uniaxial Compression and Tension All Models . . . . .	51
3.16	FRF Tire Testing Setup with Tread Accelerometer . . . . .	54
3.17	Frequency Response Functions for the Michelin Tire . . . . .	54
3.18	Frequency Response Functions for the Hercules Tire . . . . .	55
3.19	Damping Ratio versus Frequency for Tire Rubber . . . . .	57



---

## LIST OF FIGURES

---

3.20	Loads and Boundary Conditions in Uniaxial Tension . . . . .	58
3.21	Uniaxial Tension Displacement Contours in Tire Tread . . . . .	58
3.22	Force versus Extension for Tire Tread Longitudinal Samples . . . . .	59
3.23	Force versus Extension for Tire Tread Lateral Samples . . . . .	59
3.24	Displacement in Tire Inflation Finite Element Analysis . . . . .	60
3.25	Displacement in Tire Vertical Load Finite Element Analysis . . . . .	61
4.1	Longitudinal Force versus Slip Ratio in Pure Braking . . . . .	68
4.2	Tread Centerline Longitudinal Strain in Braking . . . . .	69
4.3	Tread Centerline Lateral Strain in Braking . . . . .	69
4.4	Sidewall Left Longitudinal Strain in Braking . . . . .	70
4.5	Sidewall Left Radial Strain in Braking . . . . .	70
4.6	Sidewall Right Longitudinal Strain in Braking . . . . .	71
4.7	Sidewall Right Radial Strain in Braking . . . . .	71
4.8	Lateral Force versus Slip Ratio in Pure Cornering . . . . .	72
4.9	Aligning Moment versus Slip Ratio in Pure Cornering . . . . .	72
4.10	Tread Centerline Longitudinal Strain in Cornering . . . . .	73
4.11	Tread Centerline Lateral Strain in Cornering . . . . .	73
4.12	Sidewall Left Longitudinal Strain in Cornering . . . . .	74
4.13	Sidewall Left Radial Strain in Cornering . . . . .	74
4.14	Sidewall Right Longitudinal Strain in Cornering . . . . .	75
4.15	Sidewall Right Radial Strain in Cornering . . . . .	75
4.16	Tread Centerline Longitudinal Strain in Combined Slip . . . . .	76
4.17	Tread Centerline Lateral Strain in Combined Slip . . . . .	76
4.18	Sidewall Left Longitudinal Strain in Combined Slip . . . . .	77
4.19	Sidewall Left Radial Strain in Combined Slip . . . . .	77
4.20	Sidewall Right Longitudinal Strain in Combined Slip . . . . .	78
4.21	Sidewall Right Radial Strain in Combined Slip . . . . .	78
4.22	MLP Network with Two Hidden layers . . . . .	80
4.23	RBF Network . . . . .	82

---

## LIST OF FIGURES

---

4.24	Training Error for MLP Networks . . . . .	85
4.25	Training Error for RBF Networks . . . . .	90
4.26	Location and Orientation of Two Sensors . . . . .	92
4.27	Strain Data for Six Strain Sensors in Pure Braking . . . . .	95
4.28	Strain Data for Six Strain Sensors in Pure Cornering . . . . .	95
4.29	Tread Centerline Longitudinal Signal in Pure Slip . . . . .	96
5.1	Instrumented Tire for Smart Tire Revision 1 . . . . .	99
5.2	Alloy Rim with Four Tire Valve Holes . . . . .	100
5.3	Modified Tire Valve Electrical Cables . . . . .	100
5.4	Back of Adapter Plate . . . . .	101
5.5	Instrumented Rim with Modified Valves and Plate . . . . .	101
5.6	Smart Tire Prototype Revision 1 . . . . .	102
5.7	Voltage versus Time for Revision 1 in Hammer Strike . . . . .	102
5.8	Test Setup for EMF Interference Test . . . . .	103
5.9	Voltage in EMF Interference Test . . . . .	104
5.10	On-Road Test of Smart Tire Revision 1 . . . . .	105
5.11	Research Vehicle Front Corners . . . . .	106
5.12	Smart Tire Data Acquisition Box . . . . .	106
5.13	Piezoelectric Output in Hard Straight Line Acceleration . . . . .	111
5.14	Sensor Output in Hard Straight Line Braking . . . . .	112
5.15	Vehicle ABS Sensor Output in Hard Straight Line Braking . . . . .	113
5.16	Piezoelectric Sensor Output in Hard Straight Line Braking . . . . .	114
5.17	Piezoelectric Sensor Output in Steady Speed Driving . . . . .	115
5.18	Filtered Sidewall Left Longitudinal Piezoelectric Output . . . . .	115
5.19	Filtered Sidewall Right Radial Piezoelectric Sensor Output . . . . .	116
5.20	Sidewall Strain in Hard Straight Line Braking . . . . .	117
5.21	Elliptic Filter Frequency Response . . . . .	117
5.22	Piezoelectric Output in Hard Straight Line Acceleration . . . . .	118
5.23	Piezoelectric Sensor Data Surfaces in Step Steer Left . . . . .	119

---

## LIST OF FIGURES

---

5.24	Wheel Load Transducer Data Surfaces in Step Steer Left . . . . .	121
5.25	Vehicle ABS Sensor Output in Smart Tire Revision 1 . . . . .	122
5.26	Wheel Load Transducer Averages in Step Steer Left . . . . .	123
5.27	Piezoelectric Sensor Data Surfaces in Braking in a Turn Left . . . . .	124
5.28	Wheel Load Transducer Data in Braking in a Turn Left . . . . .	126
5.29	Wheel Load Transducer Averages in Braking in a Turn Left . . . . .	127
5.30	Piezoelectric Sensor Data Surfaces in Step Steer Right . . . . .	129
5.31	Instrumented Tire for Smart Tire Revision 2 . . . . .	130
5.32	Detail of Sidewall Sensor Pair in Smart Tire Revision 2 . . . . .	131
5.33	Sensor Groups in Smart Tire Revision 2 . . . . .	132
5.34	Voltage versus Time for Revision 2 in Hammer Strike . . . . .	133
5.35	Smart Tire Prototype Revision 2 . . . . .	133
5.36	Encoder Position Index Measurements versus Time . . . . .	134
5.37	Inside Data Acquisition Systems for Smart Tire Revision 2 . . . . .	134
5.38	On-Road Test of Smart Tire Revision 2 . . . . .	135
5.39	Research Vehicle Views . . . . .	135
6.1	Piezoelectric Sensor Data in Test No. 31 . . . . .	141
6.2	Wheel Load Transducer Data Surfaces in Test No. 31 . . . . .	143
6.3	Wheel Load Transducer Averages in Test No. 31 . . . . .	144
6.4	Training Error for Networks in Points Study . . . . .	145
6.5	Estimated Longitudinal Tire Force in Test No. 22 . . . . .	145
6.6	Estimated Lateral Tire Force in Test No. 22 . . . . .	146
6.7	Estimated Vertical Force in Test No. 22 . . . . .	146
6.8	Estimated Aligning Tire Moment in Test No. 22 . . . . .	147
6.9	Piezoelectric Sensor Data Surfaces in Test No. 11 . . . . .	148
6.10	Estimated Tire Forces in Test No. 22 – Sector Study . . . . .	149
6.11	Estimated Tire Forces in Straight Line Braking . . . . .	150
6.12	Estimated Tire Forces in Step Steer Left . . . . .	152
6.13	Estimated Tire Forces in Braking in a Turn . . . . .	153

---

## LIST OF FIGURES

---

6.14	Time Domain Data in Light Straight Line Braking . . . . .	155
6.15	Piezoelectric Sensor Data Surfaces in Round 3 . . . . .	156
6.16	Estimated Tire Forces in Round 3 . . . . .	158
6.17	Longitudinal Strain for Free Rolling From the Tire FEM . . . . .	159
6.18	Lateral Strain for Free Rolling From the Tire FEM . . . . .	160
6.19	Free Rolling Strain Offset versus Inflation Pressure . . . . .	161
6.20	Sidewall Left Radial Strain in Combined Slip . . . . .	162
6.21	Magnitude of Displacement Contours, Bottom View . . . . .	163
6.22	Magnitude of Displacement Contours, Top View . . . . .	164
6.23	Tread Centerline Longitudinal Strain in Pure Slip . . . . .	166
7.1	STSS Sensors in Tire Cross-Section . . . . .	171
7.2	Flow Chart for STSS in Vehicle . . . . .	172
A.1	Analysis Steps . . . . .	185
A.2	Michelin Used Tires . . . . .	189
A.3	Scan of Michelin Tire Tread . . . . .	190
A.4	Annotated Scan of Michelin Tire Cross-Section . . . . .	191
A.5	Half of Tire Cross-Section Feature Lines . . . . .	191
A.6	Full Tire Cross-Section Feature Lines . . . . .	192
A.7	Simplified Tire FEM with Element Size = 5-mm . . . . .	194
A.8	Incorrect Inflation Stress Contours in 5-mm FEM . . . . .	194
A.9	Simplified Tire FEM with Element Size = 8-mm . . . . .	195
A.10	3D Tire FEM Sector Size . . . . .	196
A.11	2D Tire Inflation Analysis for 1-mm FEM . . . . .	199
A.12	2D Tire Inflation Analysis for 2.5-mm FEM . . . . .	200
A.13	2D Tire Inflation Analysis for 8-mm FEM . . . . .	201
A.14	Lateral Displacement Contours in Inflation Analysis . . . . .	203
A.15	Coarse FEM Strain Free Rolling . . . . .	204
A.16	Coarse FEM Strain Pure Braking . . . . .	205
A.17	Coarse FEM Strain Pure Cornering Oblique View . . . . .	206

---

**LIST OF FIGURES**

---

A.18 Speedup Factor versus Number of CPUs . . . . .	206
C.1 Tire Size Study FEM Cross-Sections . . . . .	210
C.2 Displacement in Tire Size Study Inflation Analysis . . . . .	213
C.3 Displacement in Tire Size Study Vertical Load Analysis . . . . .	214
C.4 Displacement versus Rim Diameter in the Tire Size Study . . . . .	215
C.5 Tread Geometry Effect Study Models . . . . .	216
C.6 Treaded Tire Finite Element Sector . . . . .	217
C.7 Magnitude of Displacement Contours in Inflation Analysis . . . . .	219
C.8 Contact Pressure Contours in Vertical Load Analysis . . . . .	220
C.9 Tire Inner Liner Strain Gage Locations . . . . .	221
C.10 Longitudinal Free Rolling Strain in Tread Geometry Study . . . . .	222
C.11 Lateral Free Rolling Strain in the Tread Geometry Study . . . . .	223
C.12 Braking Force in the Tread Geometry Study . . . . .	224
C.13 Longitudinal Braking Strain in the Tread Geometry Study . . . . .	224
C.14 Lateral Force in the Tread Geometry Study . . . . .	225
C.15 Aligning Moment in the Tread Geometry Study . . . . .	226
C.16 Lateral Cornering Strain in the Tread Geometry Study . . . . .	226
C.17 First, Second and Third Mode of Tire Finite Element Model . . . . .	229
C.18 Fourth, Fifth and Sixth Mode of Tire Finite Element Model . . . . .	230
D.1 Tread Centerline Longitudinal Strain in Pure Braking . . . . .	232
D.2 Tread Centerline Long. Strain in Pure Braking – Detail . . . . .	232
D.3 Tread Centerline Lateral Strain in Pure Braking . . . . .	233
D.4 Tread Centerline Lateral Strain in Pure Braking – Detail . . . . .	233
D.5 Sidewall Left Longitudinal Strain in Pure Braking . . . . .	234
D.6 Sidewall Left Longitudinal Strain in Pure Braking – Detail . . . . .	234
D.7 Sidewall Left Radial Strain in Pure Braking . . . . .	235
D.8 Sidewall Left Radial Strain in Pure Braking – Detail . . . . .	235
D.9 Sidewall Right Longitudinal Strain in Pure Braking . . . . .	236
D.10 Sidewall Right Longitudinal Strain in Pure Braking – Detail . . . . .	236

---

## LIST OF FIGURES

---

D.11 Sidewall Right Radial Strain in Pure Braking . . . . .	237
D.12 Sidewall Right Radial Strain in Pure Braking – Detail . . . . .	237
D.13 Tread Centerline Longitudinal Strain in Pure Cornering . . . . .	238
D.14 Tread Centerline Long. Strain in Pure Cornering – Detail . . . . .	238
D.15 Tread Centerline Lateral Strain in Pure Cornering . . . . .	239
D.16 Tread Centerline Lateral Strain in Pure Cornering – Detail . . . . .	239
D.17 Sidewall Left Longitudinal Strain in Pure Cornering . . . . .	240
D.18 Sidewall Left Longitudinal Strain in Pure Cornering – Detail . . . . .	240
D.19 Sidewall Left Radial Strain in Pure Cornering . . . . .	241
D.20 Sidewall Left Radial Strain in Pure Cornering – Detail . . . . .	241
D.21 Sidewall Right Longitudinal Strain in Pure Cornering . . . . .	242
D.22 Sidewall Right Long. Strain in Pure Cornering – Detail . . . . .	242
D.23 Sidewall Right Radial Strain in Pure Cornering . . . . .	243
D.24 Sidewall Right Radial Strain in Pure Cornering – Detail . . . . .	243
E.1 Footprint Data Section Highlighted . . . . .	244
E.2 Peaks Indicated With Triangle Marker . . . . .	246
E.3 Valleys Indicated With Square Marker . . . . .	246
E.4 Radial Pure Braking – Sampling Frequency = 1000 Hz . . . . .	248
E.5 Radial Pure Braking – Sampling Frequency = 200 Hz . . . . .	248
E.6 Longitudinal Pure Braking – Brake Torque = 240 N-m . . . . .	250
E.7 Radial Pure Braking – Brake Torque = 240 N-m . . . . .	250
E.8 Long. Pure Braking – Two Velocities and Brake Torques . . . . .	251
E.9 Radial Pure Braking – Two Velocities and Brake Torques . . . . .	252
E.10 Longitudinal Strain – Random Angular Shift . . . . .	253
E.11 Longitudinal Strain – Fixed Retarded Angular Shift . . . . .	253
F.1 Piezoelectric Deformation Sensor . . . . .	258
F.2 Piezoelectric Sensor Electric Circuit . . . . .	258
F.3 Sketches for Bench Test Parameters Calculations . . . . .	260
F.4 Tire Braking Strain with Sidewall Radial Sensor . . . . .	261

---

## LIST OF FIGURES

---

F.5	Tire Braking Displacement of Sidewall Radial Sensor . . . . .	262
F.6	Durability Bench Testing Machine with Tire Sample . . . . .	262
F.7	Electric Motor in Durability Bench Testing Machine . . . . .	263
F.8	Deformation of Tire Sample in Bench Test . . . . .	263
F.9	Modified Tire Sidewall Sample No. 5 . . . . .	266
F.10	Sample No. 1 Time Domain Signals – Day 1 . . . . .	267
F.11	Sample No. 1 Time Domain Signals – Day 2 . . . . .	268
F.12	Maximum Voltage for Sample No. 1 . . . . .	268
F.13	Sample No. 2 Time Domain Signals – Day 1 . . . . .	269
F.14	Maximum Voltage for Sample No. 1 and Sample No. 2 . . . . .	269
F.15	Sample No. 3 Time Domain Signals – Day 1 . . . . .	270
F.16	Sample No. 3 Time Domain Signals – Day 2 . . . . .	271
F.17	Maximum Voltage for Sample No. 3 . . . . .	271
F.18	Sample No. 4 Time Domain Signals . . . . .	272
F.19	Maximum Voltage for Sample No. 4 . . . . .	273
F.20	Piezoelectric Sensor From Sample No. 4 . . . . .	273
F.21	Sample No. 5 Time Domain Signals . . . . .	274
F.22	Maximum Voltage for Sample No. 5 . . . . .	275
F.23	Sample No. 5M Time Domain Signals . . . . .	276
F.24	Maximum Voltage for Sample No. 5M – Day 6 . . . . .	277
G.1	Sensor Data in Straight Line Driving Test No. 4 . . . . .	279
G.2	Sensor Data in Straight Line Creeping Test No. 5 . . . . .	280
G.3	Sensor Data in Light Straight Line Acceleration Test No. 7 . . . . .	281
G.4	Sensor Data in Moderate Straight Line Braking Test No. 14 . . . . .	282
G.5	Sensor Data in Braking in a Turn Right Test No. 26 . . . . .	283
G.6	Sensor Data in Step Steer Right Test No. 28 . . . . .	284

# List of Tables

1.1	STSS Outputs . . . . .	2
1.2	In-Tire / Wheel Raw Sensor Measurements . . . . .	3
2.1	Tire Forces and Moments . . . . .	8
2.2	Pacejka Tire Model Parameters . . . . .	9
2.3	STSS Engineering Specifications: Output Estimates . . . . .	33
2.4	STSS Engineering Specifications: Operating Speeds . . . . .	34
3.1	Isotropic Hyperelastic Models . . . . .	41
3.2	Anisotropic Hyperelastic Models . . . . .	43
3.3	Tire Samples for Uniaxial Tension Testing . . . . .	44
3.4	Arruda-Boyce Material Coefficients for Tire Rubber . . . . .	52
3.5	Information From Hercules New Tire Sidewall . . . . .	54
3.6	Modal Damping in Michelin Tire . . . . .	55
3.7	Modal Damping in Hercules Tire . . . . .	56
3.8	Linear Elastic Material Properties . . . . .	58
3.9	Tire Static Load Cases . . . . .	60
3.10	Tire Static Loaded Radius [mm] . . . . .	62
4.1	Complete System and Reduced System Outputs . . . . .	66
4.2	Combined Slip Testing Cases for Neural Networks . . . . .	79
4.3	Actual Values for Combined Slip Testing Cases . . . . .	79
4.4	MLP Networks Overview . . . . .	83
4.5	MLP Networks Training Performance . . . . .	84



---

**LIST OF TABLES**

---

4.6	MLP Networks Solve Time . . . . .	84
4.7	Testing Output from fitnet1 . . . . .	86
4.8	Change from Actual Values for fitnet1 . . . . .	86
4.9	RBF Networks Overview . . . . .	87
4.10	RBF Networks Training Performance . . . . .	87
4.11	RBF Networks Solve Time . . . . .	88
4.12	Testing Output from newrb4 . . . . .	89
4.13	Change from Actual Values for newrb4 . . . . .	89
4.14	Generalization: Worst Case Test Error . . . . .	91
4.15	Extrapolation: Worst Case Test Error . . . . .	91
4.16	Test Error for Number of Sensors Study . . . . .	94
5.1	Complete System and Physical Prototype System Outputs . . . . .	108
5.2	UW Parking Lot Tests for Smart Tire Revision 1 . . . . .	109
5.3	Frequencies in Piezoelectric Output in Steady Driving . . . . .	114
5.4	Test Cases From Step Steer Left Test No. 6 . . . . .	125
5.5	Actual Values for Event 6 Testing Cases . . . . .	128
5.6	Change from Actual Values for 6 Sensors (Within 549%) . . . . .	128
5.7	Change from Actual Values for 2 Sensors (Within 152%) . . . . .	128
5.8	Rotary Encoder Information . . . . .	134
5.9	UW Parking Lot Tests for Smart Tire Revision 2 in Round 1 . . . . .	137
6.1	Statistics for Testing Rounds 1 and 3 . . . . .	141
6.2	Average Error in Tire Force Estimates – Points Study . . . . .	147
6.3	Average Error in Tire Force Estimates – Sector Study . . . . .	148
6.4	Round 1 Training and Testing Data . . . . .	151
6.5	Average Error in Tire Force Estimates – Training Size Study . . . . .	151
6.6	Average Error in Tire Force Estimates . . . . .	154
6.7	Average Error in Tire Force Test Estimates . . . . .	157
6.8	Friction Scenarios in Preliminary Tire FEA . . . . .	162
7.1	STSS Sensors . . . . .	170

---

## LIST OF TABLES

---

A.1	Tire Finite Element Model Static Load Cases . . . . .	186
A.2	Tire Finite Element Model Steady-State Dynamic Load Cases . . . . .	187
A.3	Information From Michelin Used Tire Sidewalls . . . . .	190
A.4	Location and Orientation of Fiber Reinforcements . . . . .	192
A.5	Diameter and Spacing of Fiber Reinforcements . . . . .	193
A.6	Computer Resources Required for 8-mm Linear FEM . . . . .	197
A.7	Displacement in 2D Inflation Analysis, $P = 220$ kPa . . . . .	198
A.8	Maximum Lateral Displacement in Sidewall for 3D Models . . . . .	202
B.1	Specifications of Computer A: Lenovo Laptop . . . . .	207
B.2	Specifications of Computer B: Hewlett-Packard Laptop . . . . .	207
B.3	Specifications of Computer C: Lenovo Desktop . . . . .	208
C.1	Tire Size Study Overview . . . . .	211
C.2	Radial Expansion of Tire FEM With $P = 220$ kPa . . . . .	218
C.3	Maximum Contact Stress in Tire FEM With $F_z = 4000$ N . . . . .	218
C.4	Strain Measurement Locations and Directions . . . . .	221
C.5	Tire Natural Frequencies and Mode Shapes From FEA . . . . .	228
E.1	Training Vectors in Footprint Study . . . . .	245
E.2	Test Error for Footprint Data . . . . .	245
E.3	Test Error for Peaks Data . . . . .	247
E.4	Test Error for Valleys Data . . . . .	247
E.5	Test Error for Differing Sampling Frequencies Study . . . . .	249
E.6	Test Error for Differing Velocities Study . . . . .	251
E.7	Test Error for Differing Velocities and Torques Study . . . . .	252
E.8	Test Error for Random Shift Study . . . . .	254
E.9	Test Error for Fixed Shift Study . . . . .	254
F.1	Piezoelectric Strain Sensor Information . . . . .	257
F.2	Number of Cycles in Proposed Ring Road Test . . . . .	261
F.3	Tire Sidewall Sample Attachment Durability Trials . . . . .	265
F.4	Maximum Voltage Change After One Hour . . . . .	270

# List of Abbreviations

The following abbreviations are used in the thesis.

ABS	Anti-Lock Braking System
AC	Alternating Current
AWG	American Wire Gage
CG	Center of Gravity
CL-LAT	Tread Centerline Lateral
CL-LON	Tread Centerline Longitudinal
CPU	Central Processing Unit
DC	Direct Current
DMP	Distributed Memory Parallel
EMF	Electromagnetic Field
FEA	Finite Element Analysis
FEM	Finite Element Model
FRF	Frequency Response Function
M	Modified
MLP	Multilayer Perceptron
MLPN	Multilayer Perceptron Network
MSE	Mean Squared Error
PVDF	Polyvinylidene Fluoride
RBF	Radial Basis Function
RBFN	Radial Basis Function Network
SA	Slip Angle
SMP	Shared Memory Parallel
SR	Slip Ratio
STSS	Smart Tire Sensor System
SWA	Steering Wheel Angle

## LIST OF ABBREVIATIONS

---

SWL-LON	Sidewall Left Longitudinal
SWL-RAD	Sidewall Left Radial
SWR-LON	Sidewall Right Longitudinal
SWR-RAD	Sidewall Right Radial
TPMS	Tire Pressure Monitoring System
UW	University of Waterloo
VDC	Volts Direct Current

# Chapter 1

## Introduction

Ground vehicle motion is primarily determined by tire forces. Aerodynamic forces are also a factor in ground vehicle motion, but they are less important than tire forces, especially at low speeds. Therefore, knowledge of tire forces is required in order to understand and predict the behavior and safety of a vehicle. Ground vehicle safety is also significantly related to road conditions, which can be quantified from the perspective of the vehicle as the tire / road friction coefficient.

The longitudinal and lateral forces that a tire can produce are a function of the vertical force and the friction coefficient between the tire and the road. Since the vertical force and friction coefficient are both limited, there is a limit to how much longitudinal and lateral force a tire can develop. Real-time sensing of tire forces is highly desirable in a vehicle, since knowledge of these forces can be used to determine the fraction of tire force capacity already expended.

Measured tire forces can be employed by a vehicle safety control system to mitigate the effects of unreasonable and unachievable demands for tire force on the part of the driver, especially in rapidly changing road conditions. For example, it is possible that a tire force sensing system can detect reduced tire force capacity in “glare ice” winter driving conditions before a change in the road surface is recognized by the driver.

Tire force estimates used by current vehicle safety control systems are usually obtained through state observers, where vehicle states are acquired from existing vehicle sensors such as steering wheel torque and angle measures, wheel speed sensors, accelerometers and others [1]. The main problem with observer-based tire force evaluation systems is that they require a change in either a longitudinal or a lateral force to make an estimate [2]. In effect, these systems prefer highly dynamic, short time duration, high amplitude inputs to vehicle controls on the part of the driver in order to make good estimates. In addition to this disadvantage, the accuracy of the tire forces estimated using an observer-based system may be insufficient.

To improve on existing tire force estimation systems, the challenge is to find a tire force sensor that can measure tire forces in real-time during all modes of vehicle operation. To meet this goal, a research project was conducted in order to identify a smart tire sensor system (“STSS”) that can measure tire forces whenever a vehicle is in motion, along with other useful tire characteristics.

## 1.1 Rationale and Purpose

The main reason for conducting the STSS research project is that its results can be used in the development of more effective vehicle controllers as well as provide information about road conditions to the driver. This could significantly improve ground vehicle safety. Based on data collected in the United States from 1995 to 2005, each year about 7,400 people are killed and over 673,000 people are injured in weather related vehicle accidents on U.S. roads [3]. A weather related crash is defined as occurring “in the presence of rain, sleet, snow, fog, wet pavement, snowy / slushy pavement, and / or icy pavement”.

While not all weather related vehicle accidents can be prevented by a STSS, it is conceivable that some vehicle accidents associated with changing weather conditions can be avoided with better tire force data. Vehicle safety is a field that still has opportunities, especially considering the human and property costs associated with weather related crashes.

A “smart tire”, or “intelligent tire”, is a tire that can monitor itself using in-tire sensors and provide information regarding its own conditions, which may include temperature, air inflation pressure, tire / road friction, tire forces and moments and other characteristics. The purpose of the research project is to study and develop a STSS that can measure tire forces in real-time. In order to be useful to a vehicle safety control system, the tire sensor system must measure characteristics in addition to the three tire forces. Table 1.1 lists the targeted outputs for inclusion in the STSS.

**Table 1.1 – STSS Outputs**

Symbol	Description	Priority
$F_x$	Tire Longitudinal Force	First
$F_y$	Tire Lateral Force	First
$F_z$	Tire Vertical Force	First
$\mu$	Tire / Road Friction Coefficient	First
p	Tire Air Inflation Pressure	First
$M_z$	Tire Aligning Moment	Second

From Table 1.1 it can be seen that all of the six STSS outputs are related to ground vehicle safety concerns, including the three tire forces, the tire aligning moment, the

tire / road friction coefficient and the tire air inflation pressure. The air inflation pressure is included as an output mainly because this added feature would make the STSS more desirable to ground vehicle manufacturers. Tire pressure monitoring systems are already mandatory in passenger cars and light trucks in many countries as a homologation requirement; if this feature can be included in the STSS it may negate the need for a dedicated inflation pressure sensor.

The tire aligning moment has been included in the list of desired outputs for the STSS as a secondary priority. The tire aligning moment is expected to have some effect on the total yaw moment applied to a ground vehicle from its tires, but it is insignificant compared to the yaw moment effect from lateral tire forces. Therefore, the tire aligning moment can often be ignored from the perspective of vehicle dynamics. However, it is usually calculated by tire handling mathematical models, and its absence may alarm potential users of the STSS. Thus, the tire aligning moment was listed as a secondary output in the STSS if possible, perhaps as a calculated quantity based on other estimated outputs.

The STSS outputs of Table 1.1 cannot be measured directly in current production ground vehicles without the use of measurement systems that are bulky, fragile and difficult to package and implement, with the exception of inflation pressure. Implementation of a production STSS requires the use of common in-tire sensors and measurements. The practical in-tire / wheel raw sensor measurements that are available for use in the STSS are listed in Table 1.2.

**Table 1.2 – In-Tire / Wheel Raw Sensor Measurements**

Symbol	Description
$u$	Tire Displacement
$\ddot{u}$	Tire Acceleration
$\epsilon$	Tire Strain
$\theta$	Wheel Angular Position
$\omega$	Wheel Angular Velocity

Tire radial displacement can be measured between the wheel and the tire inner liner, and displacement of the tire sidewall can also be measured. Radial displacement measurement devices reported in the literature range from a very simple string potentiometer device [4] all the way to a sophisticated optical system using a light source and a lens [1]. One patent suggests using radially placed wires to measure sidewall displacement; the capacitance variation that depends on the distance between the wires is used to measure sidewall extension and contraction [5]. Most of these tire displacement sensors are reasonably efficient, but durability may be a concern.

Tire acceleration is a desirable raw sensor measurement since the accelerometers used to measure it are widely available, small and they can be physically strong. However,

in-tire accelerometers measure impacts, and thus they are suitable for establishing the tire angular position, especially with respect to identification of the tire / road contact patch. While it may be possible to relate contact patch location and length to tire forces, it is likely that tire strain measurements can be more directly associated with the forces generated by a tire.

Tire strain is also a desirable raw output since traditional foil-type strain gages are small and easy to obtain. However, the stiffness of these sensors (and their adhesive) is much higher than tire rubber. To address this incompatibility, specially designed tire strain sensors with elastomer substrates have been suggested [6, 7]. As in the case of tire displacement and tire acceleration measurements, tire strain measurements should be feasible in the real circumstances of the in-tire environment. It is assumed that wheel angular velocity is available from a rotary wheel encoder that already exists in the vehicle as part of an anti-lock braking system (ABS). It should also be possible to obtain wheel angular position from the ABS, although the position measurement is not normally available.

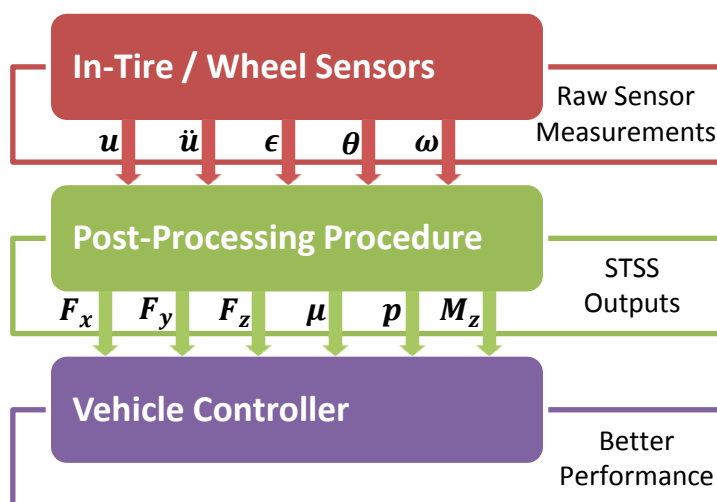


Figure 1.1 – Data Flow Block Diagram for STSS

Figure 1.1 is a block diagram depicting data flow in the STSS. The in-tire / wheel sensors are used to obtain the raw sensor measurements, which are then input to the post-processing procedure. The issue from this procedure is the STSS outputs that are used by a vehicle controller to improve vehicle safety and performance. Identification of the post-processing scheme is a major portion of the STSS research project. In general, the raw sensor measurements can be processed by a “look-up” table, or they can be used as inputs to a tire handling mathematical model in order to calculate the processed outputs, or some other multiple input, multiple output post-processing procedure can be used.



## 1.2 Objectives and Methods

Implementation of the STSS in a production environment will require a long-life power source and a method of wireless data transmission to the vehicle. There are significant constraints on these requirements in practice, considering the hostile tire environment with its high acceleration and temperature levels and its limited package space. Another important practical concern is the need for energy efficient devices. Furthermore, the way in which STSS outputs will be used by vehicle controllers is a considerable area of study all by itself. None of these matters were the focus of the STSS research project. Instead, the study concentrated on the following primary objectives.

1. Identify the type of sensors required.
2. Determine the sensor quantity, locations and orientations inside the tire.
3. Process raw measurements in order to obtain the desired outputs.
4. Confirm correct STSS operation through prototyping and evaluation.

The sensors and their locations and orientations were selected with the goal of identifying measurements that have the maximum sensitivity to the desired outputs of the STSS, especially the tire forces. The tire quantity that has the maximum sensitivity to tire forces is the most desirable for measurement; however, an additional criterion is the identification of measurements that are decoupled from other quantities. Deformation and strain gradients in the tire were calculated and examined in order to determine sensor types and placement.

Research methods employed during the STSS research project included mathematical modeling and physical experimentation. Mathematical modeling involved using finite element analysis (FEA) in the early phases of the research project in order to help determine the types and positions of the in-tire sensors. In solid mechanics applications, FEA can be used to calculate all of the variables of interest in the tire as listed in Table 1.2. Therefore, it is a numerical method that is well suited to the design phase of the STSS research project. During the physical testing phase the research project involved on-road vehicle testing of STSS prototypes. Reasonable efforts were made to collect physical test data from a statistically significant sample size, subject to time restrictions and equipment limitations.

Temperature and aging effects were not studied; these effects and their influence on the effectiveness of the STSS is the subject of future research. The STSS research project was focused on one particular tire make and model, which was considered representative of modern radial passenger car tires. The generalization of the STSS as designed to tire makes and models other than the particular tire studied was not within the scope of the research project, and is included in the work that is still to come.

### 1.3 Thesis Organization

The STSS research project is presented in seven chapters. Chapter 1 is an introduction that summarizes the purpose and objectives of the STSS research project. Chapter 2 is a literature review that concentrates on existing methods for measurement of tire characteristics. Chapter 3 outlines the tire finite element modeling and analysis performed as part of the project, including physical testing conducted to obtain material properties and validate the model. Chapter 4 summarizes the analysis of virtual strain from the model and describes the neural network configuration selected for use in post-processing.

Chapter 5 reports on the fabrication of STSS physical prototypes. Chapter 6 details the estimation of smart tire outputs, including tire forces estimated from on-road physical test data and the remaining outputs estimated using tire FEA data. Chapter 7 is the conclusion that describes the STSS technology and outlines future work.

Appendices A through C provide supplemental information regarding the tire finite element analysis, including a detailed explanation of model creation and an overview of studies performed using the validated tire model. Appendices D and E contain plots of virtual strain as calculated by the tire model and summarize the results of neural network studies performed using virtual strain. Appendix F reports on a durability bench test study of the piezoelectric deformation sensors used in the STSS prototypes. Appendix G includes examples of physical piezoelectric sensor measurements collected during on-road testing.

## Chapter 2

# Literature Review

**Chapter Brief**—An overview of existing methods for the measurement of tire forces and other tire characteristics is provided in the literature review in order to identify opportunities for improvement to in-tire sensor systems and their output. Literature reviews focus on the tire forces that must be estimated by a STSS and how these forces are mathematically modeled and physically tested. Tire force finite element analysis studies are summarized since the FEA modeling approach is used to help develop the STSS. Existing methods to estimate tire forces are outlined, including those described in published articles and disclosed in patents. Results from the literature review show that scientific and commercial opportunities exist for the design and development of a STSS, especially if the system can be shown to accurately estimate tire forces during all modes of vehicle operation.

---

### 2.1 Tire Forces and Models

A sensor that can provide tire forces and moments to a downstream vehicle safety or control system must calculate the most important tire forces and moments and resolve them to the wheel center. The calculation of tire forces and moments is the purpose of a tire mathematical model, and therefore some of these models are examined in order to help identify the minimum output required from a STSS.

Gillespie [8] provides an overview of tire construction, forces and moments. The SAE tire axis coordinate system is defined and described in detail. In this right-hand coordinate system the positive X-direction is in the wheel travel direction and the positive Z-direction points downward. The Y-direction is the lateral direction. The three tire forces (longitudinal, lateral and normal) and three tire moments (overturning, rolling resistance and aligning) at the tire / road interface are described. These six tire force quantities are summarized in Table 2.1.

Rajamani [9] explains tire forces and moments and provides an easy to follow explanation of the Pacejka (also known as “Magic Formula”) empirical tire model. Calculation

**Table 2.1 – Tire Forces and Moments**

Force / Moment	Description
$F_x$	Longitudinal Force
$F_y$	Lateral Force
$F_z$	Vertical Force
$M_x$	Overturning Moment
$M_y$	Rolling Resistance Moment
$M_z$	Aligning Moment

of lateral and longitudinal tire forces is included in this model, along with calculation of the tire aligning moment. Rajamani summarizes how the Pacejka empirical model calculates tire forces. An explanation of how an analytical “elastic foundation”, or brush-type, tire model calculates tire forces is also included.

In a brush tire model, the tire contact patch consists of independent elements that relate to the ground through springs; this modeling approach was invented by Fiala [10]. Brush tire models do not calculate tire forces accurately at large slip and in combined slip conditions, due to simplifying assumptions including symmetrical contact pressure distribution, among others. Improved accuracy in tire force prediction involves the use of an empirical model such as the Magic Formula tire model.

A tire force friction circle diagram for several combined slip scenarios is included in Rajamani’s discussion. The friction circle concept is related to the fact that the vector sum of the lateral and longitudinal tire forces is limited to the coefficient of friction times the vertical load. Put another way, the friction coefficient is equal to the maximum normalized traction force, defined with the following expression:

$$\mu = \frac{\sqrt{F_x^2 + F_y^2}}{F_z} \quad (2.1)$$

where  $\mu$  is the friction coefficient and  $F_x$ ,  $F_y$  and  $F_z$  are the longitudinal, lateral and vertical tire forces, respectively. If  $\mu = 1$  then the maximum possible lateral force is equal to the normal force, assuming the longitudinal force is zero, and vice versa.

Pacejka and Bakker explain the Pacejka / Magic Formula tire model and its coefficients [11]. This model calculates longitudinal and lateral forces as well as aligning moment for pure and combined slip conditions. The expected shape of the tire force curves including the linear (first), peak (second) and asymptotic (third) regions is illustrated graphically. The Pacejka tire force equations for fitting physical tire test data are as follows:

---

**CHAPTER 2. LITERATURE REVIEW**

---

$$\alpha = X + S_h, \tag{2.2}$$

$$Y(X) = y(\alpha) + S_v \quad \text{and} \tag{2.3}$$

$$y(\alpha) = D \sin \left[ C \cdot \arctan(B\alpha - E(B\alpha - \arctan B\alpha)) \right] \tag{2.4}$$

where the parameters in the Pacejka tire force Equations (2.2) through (2.4) are defined in Table 2.2. Note that the parameters listed are some – but not all – of the Pacejka tire coefficients. Some of the parameters listed are dependent on other parameters that are not included in the list. The total number of Pacejka tire coefficients depends on the version of the Magic Formula being used. The horizontal and vertical shift parameters are employed to represent offsets in the force and moment curves due to physical characteristics of the tire including conicity, ply steer and rolling resistance effects.

**Table 2.2 – Pacejka Tire Model Parameters**

Input	Description
$X$	Input Variable – <i>Slip Angle or Slip Ratio</i>
$Y$	Output Variable – <i>Longitudinal Force, Lateral Force or Aligning Moment</i>
$S_h$	Horizontal Shift
$S_v$	Vertical Shift
$B$	Stiffness Factor
$C$	Shape Factor
$D$	Peak Value
$E$	Curvature Factor

Figure 2.1 is a graph of aligning moment versus slip angle for a truck tire for four different vertical loads and a 4 degree camber angle. This tire was physically tested as part of a vehicle design program and Pacejka tire coefficients were fitted to the test data. The aligning moment graph was created by the author using the Pacejka tire coefficients along with the Pacejka mathematical formulae in a Microsoft Excel 2010 spreadsheet. The aligning moment versus slip angle relationships for this tire illustrate the general trend of the Pacejka force and moment curves. Linear behavior is observed up to 3 degrees of slip angle, a peak occurs at 4 degrees of slip angle and the curve tends to an asymptotic value at higher slip angles in this particular case.

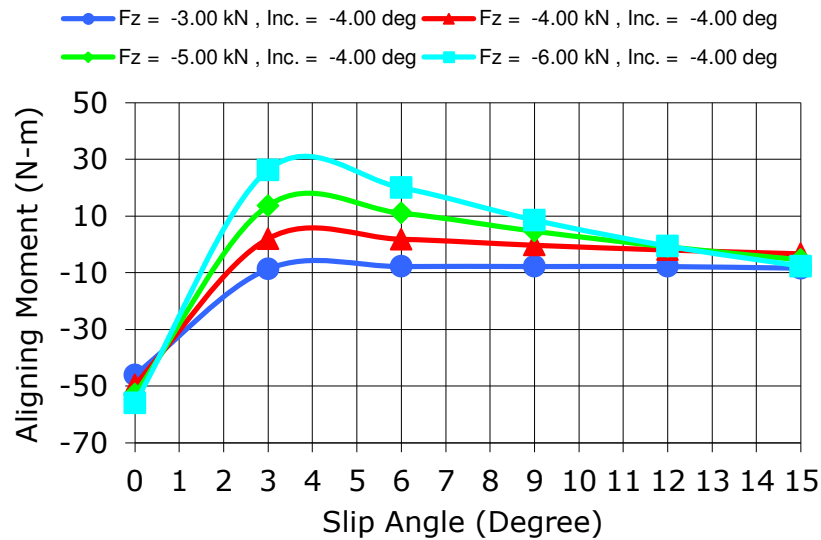


Figure 2.1 – Aligning Moment versus Slip Angle for a Truck Tire

Blundell and Harty [12] provide an overview of tire forces and moments and how these are calculated in multi-body dynamic models for vehicle handling analysis. Both the SAE and ISO tire axis coordinate systems are described. The ISO system differs from the SAE system primarily in that the positive Z direction points upward. Interpolation, Fiala and Pacejka tire models are described in detail, and a sample tire input file for ADAMS in each format is provided. A suggested procedure for obtaining Pacejka tire coefficients from physical test data is described.

An overview of the Fiala tire model is included along with a list of its coefficients and a description of the practical limitations of the model, including the lack of lateral forces due to camber and the inability to model combined slip conditions. The Fiala tire model is used to calculate longitudinal and lateral forces as well as aligning moment for pure slip conditions. Despite its drawbacks, the Fiala tire model is advantageous in that it is defined using only eight physically intuitive parameters, which consist mainly of tire stiffness and friction coefficients.

Blundell and Harty provide a definition for longitudinal slip ratio in the pure braking case, when a brake torque is applied to the wheel center. In this braking scenario the tire starts initially with a free rolling angular velocity; the event ends with the wheel fully locked and a tire angular velocity of zero. The longitudinal slip ratio  $S$  is defined for braking using the following relationship:

$$S = \frac{\omega_0 - \omega_B}{\omega_0} \quad (2.5)$$

where  $\omega_0$  is the angular velocity of the free rolling tire and  $\omega_B$  is the angular velocity with brake torque applied. Equation (2.5) implies that when the slip ratio is 0 the tire is free rolling, and when it is 1 the tire is fully locked and skidding. This is the definition for slip ratio that is used in the STSS research project. Note that this definition for longitudinal slip is not universally accepted. For example, the SAE J670e standard [13] modifies the signs of the tire angular velocities such that the slip ratio is -1 for a fully locked wheel.

The ADAMS/Tire software user documentation [14] provides detailed information about the tire handling models available for use in ADAMS. The ISO tire axis coordinate system is used in ADAMS/Tire. A table is provided that helps the user decide on a tire model based on the vehicle event to be simulated in ADAMS. ADAMS/Tire handling models include the Fiala model, several Pacejka models, the University of Arizona model and the 5.2.1 model. Sample tire input files for use with ADAMS/Tire are provided in every case. Example Pacejka tire input files show that many parameters (approximately 50) are required in order to represent physical tire test data. Fiala, University of Arizona and 5.2.1 are simpler tire models with fewer parameters (approximately 10) having intuitive physical meaning.

The latest Pacejka tire model, called PAC2002 (Pacejka version 2002), is recommended as the best choice for vehicle handling simulations in ADAMS. PAC2002 is capable of accurately calculating tire forces in common handling maneuvers such as lane changes, as well as limit handling maneuvers such as J-turns. Accuracy in tire forces, especially at high slip angles, comes at the cost of complexity, as PAC2002 has more tire coefficients than any other tire model intended for vehicle handling analysis in ADAMS.

In ADAMS/Tire handling models the tire vertical force is usually calculated using a simple relationship based on linear vertical tire stiffness. Rolling resistance moment and overturning moment may also be estimated; they are generally defined to be a function of the vertical force. Ordinarily the rolling resistance moment, which effectively produces a longitudinal resistance force on the vehicle, is relatively unimportant when modeling vehicle handling maneuvers. The overturning moment can be neglected in passenger car tires, although this is not true in the case of motorcycle and aircraft tires [12].

Kiebre et al. [15] perform a sensitivity study of two tire models, Fiala and Pacejka, at University of Haute-Alsace. Lateral force during steady-state cornering is calculated with a fixed vertical load. Equations for lateral force in pure cornering as calculated by both tire models are presented. The tire lateral force is calculated by Fiala using the following relationship:

$$F_y = -\mu|F_z| \left( 1 - \left( 1 - \frac{C_\alpha |\tan(\alpha)|}{3\mu|F_z|} \right)^3 \right) \text{sgn}(\alpha) \quad (2.6)$$

where  $F_y$  is the lateral force,  $\mu$  is the friction coefficient,  $F_z$  is the vertical force,  $C_\alpha$  is the cornering stiffness,  $\alpha$  is the slip angle and  $\text{sgn}(\alpha)$  represents the sign of the slip angle. Therefore, in the Fiala model the tire lateral force is a function of vertical load, cornering stiffness, slip angle and friction coefficient. The tire lateral force is calculated by Pacejka using the following relationship:

$$F_y = \mu F_z \sin \left[ C \cdot \arctan \left( \frac{C_\alpha}{\mu F_z C} (\alpha + S_h) - E \left( \frac{C_\alpha}{\mu F_z C} (\alpha + S_h) - \arctan \left( \frac{C_\alpha}{\mu F_z C} (\alpha + S_h) \right) \right) \right) \right] + S_v \quad (2.7)$$

where  $F_y$ ,  $\mu$ ,  $F_z$ ,  $C_\alpha$  and  $\alpha$  have the same meanings as in Equation (2.6) and  $C$ ,  $E$ ,  $S_h$  and  $S_v$  are defined in Table 2.2. The Pacejka lateral force is a function of vertical load, cornering stiffness, slip angle and friction coefficient, plus the empirical parameters  $C$ ,  $E$ ,  $S_h$  and  $S_v$ . Results show that slip angle is the most influential lateral force parameter in the case of Fiala, but the slip angle, friction coefficient and cornering stiffness all have significant influences on lateral force calculated in the case of Pacejka. The authors also mention that civil aircraft tires are expected to have a maximum lateral force at 14 degrees or more slip angle, although the study in general does not focus on aircraft applications.

Wei [16] develops a “ring elastic foundation” analytical tire model at Tsinghua University for the purpose of predicting tire vertical forces when traveling over cleats. A two degree of freedom, damped, linear gyroscopic system is used to calculate tire vertical dynamic response. Vertical tire force is calculated in the time domain, with graphs presented for different tire translational velocities. Results are said to be “quite good qualitatively”, but no physical test data are provided for comparison. This study illustrates the additional mathematical complexity required of an analytical tire model if accurate vertical responses are required for vehicle durability and / or vibration studies, especially when the tire is subjected to base excitation from road inputs at a frequency of 8 Hz or more, where most tire handling models are invalid [14].

Velenis et al. [17] of Georgia Institute of Technology present a capabilities extension of the LuGre transient tire model from longitudinal tire force to combined longitudinal and lateral tire forces, including calculation of the tire aligning moment. This is a lumped parameter transient dynamic model that is based on a physical representation of Coulomb friction. Tire forces as calculated by the model are shown in graphical form; these plots indicate that the model is capable of predicting similar static tire force behavior compared to empirical models such as Pacejka. Additionally, the model can predict dynamic effects such as a difference in longitudinal force level when slip is rapidly increasing versus when it is rapidly decreasing. The tire dynamic model as presented is also free from the low speed singularities of static tire models, which do not function at 0 KPH. Current commercially available vehicle dynamics software programs do not include transient dynamic tire models like the extended LuGre, mainly due to computational complexity, but the added proficiencies described are certainly attractive.



A review of the tire forces and models literature shows that the STSS must calculate longitudinal, lateral and vertical tire forces, and possibly the tire aligning moment. Evidently, rolling resistance and overturning moments are of secondary importance when analyzing passenger car vehicle dynamics. Therefore, the STSS should ideally identify all six tire forces and moments, but priority should be placed on measuring the three forces and the aligning moment. The tire aligning moment is less important than the tire forces.

## 2.2 Physical Testing of Tire Forces

Literature describing the physical testing of tire forces and moments is summarized. Physical tire tests are required in order to develop and confirm the performance of the STSS. Some of these physical tire tests should be simulated using finite element analysis to assist in the early design of the STSS. Therefore, physical tire tests performed to determine tire forces and moments must be understood as part of the STSS research project.

Van Oosten [18] of MSC Software outlines the physical testing requirements to obtain passenger car tire coefficients for the PAC2002 tire model in ADAMS. The ISO tire axis coordinate system is used during testing. A full tire test program is described along with a reduced test program that includes estimates for some tire parameters. The physical tire tests in both programs primarily involve lateral slip and longitudinal slip sweeps; both pure and combined slip conditions are tested. The reduced testing program includes 27 dynamic tests and 2 static tests. The entire prescribed physical testing program would likely be challenging to simulate using finite element analysis, considering that the number of tests required is high and the majority are dynamic rather than static tests. The recommended translational tire velocity during physical testing is 80 KPH, or some other “realistic driving speed”.

Van Oosten and Bakker [19] describe the physical testing that is performed at TNO, a research organization, in order to obtain Pacejka tire coefficients. A specially designed trailer is used for on-road physical testing of a tire, rather than a laboratory tire test rig. Vertical loads and camber angles are varied, and two different sweep tests are performed. The first test, called an “alpha-sweep”, is used to test pure cornering; the free rolling tire is subjected to slip angles varying from -20 to 20 degrees. The second test is called a “kappa-sweep” and is used to test braking; the slip angle is maintained at a constant value and the brake torque is varied, such that the tire transitions from free rolling to full lockup. All of the tests are performed at a constant speed of 110 KPH and the vertical load on the tire is maintained at a constant value during each test. Pure and combined slip conditions are tested.

Lidner [20] describes the methods used to fit Pacejka tire coefficients to measured tire test data at Volvo; a custom Fortran routine is utilized. The physical tire test program used to obtain Pacejka tire coefficients is outlined. A constant speed of 60 KPH is used in all of the tests. The “alfa sweep” test is performed from -14 to 14 degrees of slip angle.

## CHAPTER 2. LITERATURE REVIEW

---

The “kappa sweep” test is performed from 0 to  $-100\%$  longitudinal slip (i.e. braking only). Each sweep test has different vertical loads and camber angles; the kappa sweep test also has various prescribed slip angles. A total of 57 sweep tests are performed in order to obtain Pacejka tire coefficients.

Salaani et al. [21] perform a physical tire testing program involving shaved tires on a wet surface. The study is a joint project of the Transportation Research Center, Ohio State University and NHTSA. A Goodyear passenger car tire is tested on a tire test rig in both wet and dry conditions. Tire physical tests are described in detail, including all of the different loading and event conditions. Pure cornering and braking tests are performed, along with combined cornering and braking tests. Wet tests are performed at four different tire translational velocities, 30, 45, 60 and 75 MPH, whereas dry tests are performed at a single speed of 30 MPH. The goal in testing different wet velocities is to create partial hydroplaning conditions at the tire / road interface. The tire force and moment results are synthesized in an empirical tire model that is further used in a driving simulator. The tire model is able to produce estimates for tire forces in wet conditions.

Dora et al. [22] describe the design and implementation of physical tire test rigs for motorcycle tires at TVS Motor Company, an Indian motorcycle manufacturer. Each motorcycle tire is tested on its own vehicle wheel; no special wheel is required. Three relatively simple physical laboratory test setups are described along with their test procedures. Tire tests are aimed primarily at obtaining lateral forces with respect to slip and camber angles, although a procedure to obtain vertical stiffness and damping is also described. The authors fit their measured tire data to a Pacejka tire model. The calculation of Pacejka tire coefficients involves a least squares curve fitting process in Microsoft Excel.

A motorcycle vehicle dynamics model is built and exercised in ADAMS along with a Pacejka tire model produced during the study. A few calculated outputs from the motorcycle model are shown, including time-domain vertical acceleration measured on the frame that is presented with little comment. The main value in this study from the perspective of the STSS research project is in the detailed description of the physical tire test setups and procedures. The physical tire test procedures outlined can likely be simulated using finite element analysis methods.

Cossalter et al. [23] perform a motorcycle tire force and moment physical testing program at the University of Padova. A “rotating disk” tire test rig that is designed especially for testing motorcycle tires at high camber angles is employed during the study. The tire test rig appears to be relatively simple, with load cells used to measure forces. Published measurements consist primarily of lateral tire forces due to slip and camber angles, which are presented in the form of graphs for several sets of tires, including super-sport tires and scooter tires.

Interesting results are presented for “yaw torque” about the vertical axis, which includes the traditional aligning torque as well as a “twisting torque” due to the vertical component of the velocity of the spinning wheel when a camber angle is present. The

twisting torque does not tend to align. The aligning torque is determined from a pure slip angle test with no camber angle; the twisting torque is determined from a pure camber angle test with no slip angle. Results show that yaw torque can be positive (not aligning) during typical handling maneuvers, which can have a significant effect on motorcycle handling.

Physical tire tests for the purpose of measuring tire forces and moments generally consist of dynamic sweep tests at a fixed tire translational velocity, vertical load and camber angle. Translational velocities vary from 50 to 110 KPH. Pure longitudinal slip sweeps usually have brake torques applied with the tire transitioning from free rolling to full lockup. Pure lateral slip sweeps are performed with a free rolling tire and slip angles varied (approximately) within the +/- 15 degree range. Combined lateral and longitudinal slip tests are also performed. Considering that the tire force and moment physical tests are dynamic rather than static, the use of finite element analysis to simulate these tests may be computationally expensive. In practice, most physical tests of passenger car tires are performed using dedicated tire test rigs either in laboratories or in specially designed trailers for on-highway use.

### 2.3 Finite Element Analysis of Tire Forces

The use of finite element analysis to calculate tire forces and moments in published literature is summarized, and the finite element analysis software and compute hardware used is noted. Special emphasis is placed on the time and cost associated with finite element analysis procedures. In order to use finite element analysis as a STSS development tool, reasonable compute solve times and compute hardware requirements are required. Thus, the impetus is not simply to validate the use of finite element analysis methods for the calculation of tire forces and moments, but to ascertain the usefulness of finite element analysis as a STSS design aid.

The ABAQUS finite element analysis software example manual [24] provides several examples of tire simulation. Detailed examples are provided for the analysis of an axisymmetric two-dimensional tire finite element model (FEM) as well as for the analysis of full three-dimensional tire finite element models. Examples of static tire simulations including inflation and vehicle corner weight loading using implicit finite element methods are provided. Examples of dynamic tire analysis are provided that illustrate the analysis of braking and cornering events using the steady-state transport and explicit dynamic finite element methods. One dynamic finite element analysis example is for a tire curb climbing simulation using the explicit dynamic method. The steady-state transport method is recommended for analysis of a spinning tire in contact with a flat road or drum. This approach is represented as less computationally expensive compared to the explicit dynamic method when simulating tire motion for the purpose of calculating tire forces and moments.

## CHAPTER 2. LITERATURE REVIEW

---

Steady-state transport analysis in ABAQUS is used for analysis of rolling and sliding contact between a tire and a flat, convex or concave road. In this approach the reference frame is attached to the axle. An observer in this reference frame perceives points on the tire to be stationary; the tire material moves through the points. Thus, the tire finite element model does not undergo large rigid body rotation. Deformation is calculated relative to rotation using steady-state transport analysis that is a mixed Lagrangian / Eulerian finite element method. Rigid body motion is analyzed using a spatial (Eulerian) approach and deformation is analyzed using a material (Lagrangian) approach. It is an inexpensive method, especially considering that its costs are independent of tire rolling speed.

Explicit dynamic analysis in ABAQUS is used for analysis of rolling and sliding contact between a tire and an arbitrary road. In this approach the reference frame is associated with the material. Explicit dynamic analysis is a pure Lagrangian finite element method in which steady-state rolling of a tire is a time dependent process. It is an expensive method, considering that a small time increment may be necessary in the analysis. Costs increase with tire rolling speed.

Chargin and Bella [25] develop a tire model for use in vehicle dynamics analysis. This is a joint effort of CDH, a consulting engineering firm, and MSC Software. The tire model is a finite element model in a reduced form, with a lower number of degrees of freedom. The finite element software used in the study is not mentioned, but based on the “punch file” reference and the MSC Software affiliation of the second author, it is probably NASTRAN. A superelement approach is used to reduce of the number of degrees of freedom in the tire finite element model. Neither details of the finite element model nor extent of degree of freedom size reduction is presented. Shaded images of the tire finite element model are shown; these images provide little insight into the level of fidelity with respect to tire construction, geometry and materials contained in the finite element model.

The reduced tire finite element model is intended to be used directly in a vehicle dynamics analysis, although an example of its use is not provided. While it should be possible to use such a tire finite element model in a co-simulation with a vehicle dynamics analysis for the purpose of calculating tire forces, this is a potentially time consuming and complicated process. Since the authors do not provide an example of the use of their reduced tire finite element model in a vehicle dynamics simulation, it is unclear as to the time and cost associated with such an approach to calculating tire forces.

Ardeh et al. [26] develop a “surrogate” tire model based on the results from an ABAQUS tire finite element analysis study at the University of Wisconsin–Madison. The surrogate tire model considers only vertical forces and is intended for use in ADAMS full vehicle durability studies, especially for simulation of off-road driving over obstacles. The surrogate tire model is said to be a “fast running” approximation of the full tire finite element model. The tire forces as calculated by the surrogate tire model compare very well with the tire forces as predicted by the ABAQUS full tire finite element model.

## CHAPTER 2. LITERATURE REVIEW

---

A shaker test is simulated in ABAQUS with the wheel center fixed. A shaker table represents the road (in contact with the tire) and provides vertical excitation to the tire. Reaction forces at the wheel center are calculated using ABAQUS. There is a claimed time reduction of  $1100\times$  when using the surrogate tire model compared to the ABAQUS full tire finite element model for tire force calculations; however, the ABAQUS runs require up to 10 hours of compute time for 0.2 seconds of simulated shaker time.

The ABAQUS compute jobs were performed using an Intel Pentium processor desktop workstation with a 32-bit Windows XP operating system. Based on the reported compute solve times, the simulation time in ABAQUS is 50 hours per second of real time; a  $1000\times$  reduction is still 0.05 hours or 3 minutes per second of real time. This may be a reasonable compute solve time for tire force calculation in a simulation of a vehicle on a durability road course, although the authors make no comment on the subject, and they do not compare their tire force calculation times with those from existing tire models for durability analysis.

The surrogate tire model is used in an ADAMS full vehicle durability analysis of an HMMWV military medium duty truck along with “arbitrary” road profiles. Tire forces are calculated via a Simulink co-simulation. Chassis vertical acceleration results for the truck as calculated by ADAMS are presented without comment. The results seem reasonable but no physically measured data are provided for comparison. The surrogate tire model study shows that significant time savings can be realized by using a finite element solver to calculate parameters for a tire model that can approximate the vertical behavior of a tire, compared to using the full finite element model of the tire in a co-simulation with a vehicle dynamics model.

Duni et al. [27] present an approach for performing full vehicle durability analysis using finite element methods in ABAQUS as developed at Fiat. An entire passenger car including tires is modeled in finite elements and both implicit and explicit finite element methods are used to solve the vehicle model. A physical cobblestone durability road course is measured and represented as a 3D rigid road in the finite element analysis. Analytically predicted body accelerations are presented and these compare well with physical measurements; however, the weakness with the full finite element analysis approach appears to be long compute solve times; the authors report that 20 compute hours are required to simulate one second of road course time.

The authors of the study were able to simulate one second of a full vehicle durability analysis in 20 hours using ABAQUS versus the 50 hours required for one second for the tire alone in the University of Wisconsin–Madison study [26]. The authors of the Fiat study [27] do not comment on the computer they used to perform ABAQUS jobs; it is clear, however, that more compute resources were in effect at Fiat, which is to be expected since Fiat is a major automaker. The authors of the Fiat study also report that normally 60 to 120 seconds of data are recorded during physical durability testing. Thus, in order to simulate a full 120 seconds of road course real time, 2400 hours, or 100 days, of compute time is required. Therefore, solution times appear to be unreasonably long,

although the authors do not state this directly. This study shows that a full finite element analysis approach to vehicle durability analysis produces accurate results, but compute requirements may make the approach too time consuming to be practical.

Berzeri et al. [28] from Ford and MSC Software present a Ford in-house tire model for use in full vehicle multi-body dynamic analysis for the purpose of calculating road loads input to a vehicle chassis. In this methodology, a tire finite element model is built and exercised in ABAQUS in order to calculate tire parameters for the Ford proprietary “Analytical Road Loads” tire model. This tire model calculates longitudinal and vertical tire forces accurately, and it is valid in the 0 to 80 Hz frequency range. Lateral tire forces do not correlate well with physical experiments. Almost no information is provided about the ABAQUS tire finite element model used for calculation of tire parameters, except that it is “nonlinear” and “detailed”. This study indicates Ford’s desire to replace physical tire tests with virtual tire tests, but at the time of writing (2004) not all of the calculated tire forces from their Analytical Road Loads tire model correlated sufficiently well with physical test results. Interestingly, tire forces directly calculated by ABAQUS are not presented; rather, the finite element model is referred to as “validated”.

Rao et al. [29] investigate finite element analysis methods in ABAQUS for the purpose of calculating Pacejka tire model coefficients at the Indian Institute of Technology. The authors describe their approach to calculating Pacejka coefficients as a “cost effective and efficient tool” that can eliminate physical testing of tires. Lateral force and aligning torque versus slip angle curves are calculated using ABAQUS and compared with experimentally obtained measurements. Trends in the lateral tire forces from the finite element analysis results compare well with experiments, although the analysis results correlate better at low slip angles, up to 4 degrees. Analytically predicted lateral tire forces deviate from experimental results as much as 20% at higher slip angles.

The authors report that a mixed Lagrangian / Eulerian finite element analysis technique is less expensive than both the implicit and explicit finite element analysis approaches, but they do not provide compute solves times for their analysis jobs. Thus it is not possible to verify their claim that the finite element analysis procedure used is more cost effective than physical tire tests, since the authors do not report on the time and cost associated with the analysis procedure.

Rao et al. [30] conduct a study at the Indian Institute of Technology in which the coefficients of a Pacejka tire model are calculated using finite element analysis. This study is similar to [29] performed at the same academic institution, although [30] was published two years later. The mixed Lagrangian / Eulerian finite element analysis technique is used with an ABAQUS tire finite element model, and the Pacejka tire parameters are fitted using a least squares procedure in MATLAB. Lateral force and aligning moment versus slip angle are predicted and compared graphically with similar data obtained physically using a tire test rig. Lateral force compares well up to 10 degrees slip angle, but aligning moment correlates well up to 2 degrees only.

## CHAPTER 2. LITERATURE REVIEW

---

The bulk of the study involves investigating the effect of modifying features of the tire finite element model (such as friction coefficient and tread geometry) and predicting their effect on lateral force. The cost associated with creating and running the tire finite element analysis and Pacejka tire coefficient fitting procedure is not mentioned, despite the claimed development of a “highly economical and viable tool”. The authors report 240 analysis runs each taking up to 8 Central Processing Unit (CPU) hours; this means that the analysis jobs alone required at least 1,920 hours, or 80 days of compute solve time. Presumably this was the total compute solve time for the entire study; regardless, the finite element analysis approach presented appears to be a costly process that would not necessarily reduce the costs associated with tire physical tire testing.

Balaramakrishna and Kumar [31] conduct a finite element analysis study at the Indian Institute of Technology in order to calculate SWIFT tire model parameters. The SWIFT tire model is an extension of the Pacejka tire models for use in vehicle durability analysis. It is capable of accurately predicting tire forces over cleats and other road obstacles. The finite element analyses used in ABAQUS to predict the SWIFT parameters employ a mix of implicit and mixed Lagrangian / Eulerian methods. Raw data from the ABAQUS solutions are post-processed using commercial MF-Tool software in order to obtain the SWIFT tire model parameters. The authors state that the longitudinal and vertical tire forces as calculated in ABAQUS simulations of a tire rolling over a cleat are similar to published results, but these results are not provided for comparison. Furthermore, no indication of the time and cost associated with the analysis study is provided, despite claims that the method will significantly reduce tire development time.

Ju et al. [32] at Clemson University investigate an aluminum honeycomb structure designed to replace rubber in a “shear band” that is used in a lunar rover vehicle tire. Geometry of the honeycomb structure is optimized to minimize tire / road contact pressure, which is calculated using ABAQUS. Contact pressure versus contact patch length is shown for the shear bands studied, including a solid elastomer case. No elastomer pneumatic tire is studied, however.

Veeramurthy et al. [33] at Clemson University optimize a non-pneumatic rubber tire (similar to Michelin Tweel) using an ABAQUS two-dimensional finite element model and design of experiments methods in ISIGHT software. The tire is optimized for rolling resistance and vertical stiffness; in the final design the shear band is thicker and the elastic spokes thinner compared to the initial design. Ogden hyperelastic and viscoelastic material properties for polyurethane and synthetic rubber used in ABAQUS are reported. Also included is a graph showing contact pressure versus contact patch length.

Narasimhan et al. [34] at Clemson University build and exercise a three-dimensional solid finite element model of the Michelin Tweel, which is a non-pneumatic rubber tire. ABAQUS software is employed and details about elements types and material constants used are provided. The polyurethane material of the Tweel is modeled using the Marlow, Mooney-Rivlin and Neo-Hookean hyperelastic material models. The Marlow material model is considered the baseline, with the other two material models having parameters

## CHAPTER 2. LITERATURE REVIEW

---

fitted to match the baseline model. Shear moduli in the Mooney-Rivlin and Neo-Hookean material models are modified in order to determine their effect on load / displacement curves.

ABAQUS/Standard is used to calculate vertical load / displacement curves. Results show that Tweel vertical stiffness is directly proportional to the polyurethane shear modulus. The load / displacement curves are more sensitive to shear modulus changes in the softer Neo-Hookean material compared to the Mooney-Rivlin material. In general, the Mooney-Rivlin material model matches the baseline stress-strain data well in tension, and the Neo-Hookean material model matches well in compression. An analysis of spoke vibration is performed with the Tweel travelling at 100 KPH in ABAQUS/Explicit. Both the Mooney-Rivlin and Neo-Hookean material models result in higher spoke vibration amplitudes compared to baseline, with the Neo-Hookean material predicting the highest levels. No compute solve times are reported for the ABAQUS/Explicit analysis jobs.

Ryu et al. [35] design a separable non-pneumatic polyurethane bicycle tire at Korea Aerospace University. Its hollow cross-section is optimized such that vertical stiffness and contact pressure are similar compared to a conventional pneumatic bicycle tire. ABAQUS finite element analysis software is used to calculate vertical load / displacement curves, and the Ogden hyperelastic material constants used to model polyurethane are included. Contact pressure distributions as calculated by ABAQUS are presented.

Mohsenimanesh et al. [36] develop a tractor tire finite element model in ANSYS at University College Dublin. Tire materials are physically tested for properties to be input to the model; Mooney-Rivlin hyperelastic material constants for rubber are reported. Tire contact patch length and stress distribution are calculated using ANSYS and compared with physical experimental results, with the model correlating well. This study is a good reference for tractor tire contact stress patterns, since they have been physically validated, but the exaggerated shape of the tractor tire tread lugs may render the results inappropriate for comparison with passenger car tire contact pressure contours.

Yang et al. [37] at University of Birmingham use simple physical tests to obtain tire rubber material properties for use in ABAQUS. A tension test and stress relaxation test are used to obtain Yeoh hyperelastic and viscoelastic material property constants, which are reported. Output from the tire finite element model is compared with a physical test in which the tire is inflated and loaded vertically, with good results calculated by the finite element model. Rubber material properties as reported in this study can be used directly in ABAQUS tire models as early estimates in the absence of real material data.

Behroozi et al. [38] perform a finite element analysis study of aircraft tires at the University of Birmingham. Three levels of structural complexity are modeled in two different tires. ABAQUS is used, with rebar elements included and Yeoh hyperelastic material properties applied to rubber components. Regular and burst inflation pressures are applied as load conditions. Displacement analytical results compare well with experimental results regardless of the mesh used, but relatively small elements are required



for good stress results. The study shows that the construction of an aircraft tire can be simplified in its finite element representation without significant degradation in predicted displacement.

Kim et al. [39] at Korea Aerospace University investigate tire and pavement contact interactions using ABAQUS finite element analysis. Different material models are applied and investigated. Results show that the hyperelastic material model is better than the elastic material model for modeling rubber when predicting contact pressure at the tire / road interface is the primary concern. Synthetic rubber Ogden hyperelastic material properties are reported. The important conclusion is that a rigid road model is acceptable if the only concern is stress in the tire, since tire contact pressure does not change much whether the pavement is represented as rigid or flexible.

In general, the tire finite element analysis literature shows that the large majority of finite element studies employ ABAQUS software. Since most studies are focused on simulation of dynamic sweep tests with a tire in contact with a flat road or drum, the inexpensive mixed Lagrangian / Eulerian method is ubiquitous. The more costly explicit method is reserved for simulation of dynamic tire events that require travel over rough roads, as required in vehicle durability studies. While the literature shows that finite element analysis can be used to calculate tire forces accurately, reported compute solve times are either long or entirely absent, leaving open the question of usefulness of the method with respect to wait times.

Rubber is universally modeled as a hyperelastic material in the tire finite element analysis studies reviewed. Many papers contain details of the particular form of hyperelastic material used and the hyperelastic material constants assigned to the tire finite element model. Therefore, there are many existing sources of hyperelastic material properties that can be used as early estimates for rubber material setup in a tire finite element modeling project.

## **2.4 Existing Tire Force Measurement Methodologies**

### **2.4.1 Literature Search**

Published studies of smart tire sensor systems are reviewed for the purpose of understanding existing tire force measurement methodologies. The goal of this review is to identify the tire characteristics that are being estimated and the sensors systems employed in order to estimate these characteristics. Deficiencies in existing sensor systems and opportunities for further work are identified.

#### 2.4.1.1 Pressure Measurement Methods

A major impetus for the development of passenger car tire pressure measurement methods is the United States Federal Motor Vehicle Safety Standard (FMVSS) No. 138 [40]. This rule requires that a Tire Pressure Monitoring System (TPMS) be installed in all light vehicles for sale in the United States up to a Gross Vehicle Weight Rating (GVWR) of 10,000 pounds, excepting vehicles with dual-wheel axles. Full compliance on the part of vehicle manufacturers came into effect on September 1, 2008. The required TPMS must detect under-inflation of 25% or more below the recommended tire inflation pressure for one or more tires, up to and including all four tires. The system is supposed to identify dangerously low air pressure conditions, and not necessarily small decreases in air pressure.

Zhang et al. [41] at Chinese Academy of Sciences use a surface acoustic wave sensor to measure tire pressure and temperature. The basic operating concept of the sensor is described as follows. A surface acoustic wave travels along the elastic substrate of the in-tire sensor. When tire pressure and temperature changes occur, the sensor substrate is altered, with resulting changes to the length of the substrate and velocity of the surface acoustic wave. Since the time that the surface acoustic wave takes to travel along the substrate changes, the phase output from two reflectors installed at either end of the sensor changes. The phase information is used to determine the tire pressure and temperature. No images of the sensor system are provided, and no description of the design is provided other than a generic one.

Two detailed flowcharts are included showing how the output from the surface acoustic wave sensor is used to calculate pressure and temperature and how a decision is made about whether the pressure is too low or the temperature is too high. The authors state that a measurement was made using the sensor, but no details of the physical testing performed are provided. Post-processed phase versus pressure and temperature graphs are included, with a comment indicating that the plots “prove our theory”. No explanation is provided as to how any conclusions can be drawn from the graphs since no comparison is made between pressure and temperature estimated by the sensor and the expected values. Furthermore, the authors state that the sensor is “not practical”, but the reasons for this are difficult to ascertain since no details of the actual sensing system are provided.

Flatscher et al. [42] describe the design and implementation of a tire pressure monitoring system. A bulk acoustic wave sensor is used in a wireless system with a complete in-tire sensor package of one cubic centimetre volume. Very little information is provided about the operation of the pressure sensor itself or about the pressure estimates output from it. Great detail is provided regarding data transmission to and from the sensor and power consumption of the sensor. The sensor is powered using coin-style batteries, but a future design will employ vibrational energy scavenging. This is a good study for anyone wanting to learn about the practical realities of communicating with an in-tire wireless sensor system.

The tire pressure studies reviewed show that in-tire sensor systems are being used to estimate air pressure. Therefore, it is not necessary to rely on traditional tire pressure monitoring technology such as direct measurement systems incorporated into valve stems. Regulatory requirements for TPMS imposed on vehicle manufacturers make the inclusion of an air pressure monitoring feature desirable in a STSS, even if the primary purpose of the system is to estimate tire characteristics other than air pressure. A multi-function STSS may be more acceptable to vehicle manufacturers if it includes air pressure monitoring, since this feature is already required for United States homologation.

### 2.4.1.2 Displacement Measurement and Processing

Holscher et al. [43] conduct a finite element modeling study of a passenger car tire at the Center of Advanced European Studies and Research. MARC is used to solve the tire finite element model, which is set up in a similar way compared to ABAQUS tire finite element models in the ABAQUS user documentation, including the use of rebar elements to model steel cords and the use of the Mooney-Rivlin hyperelastic material formulation for tire rubber. A sensor is modeled in finite elements and physically tested that employs magneto-elastic and magneto-impedance effects. Practically no information is provided about this “ $\pi$ -sensor” other than the claim that it is capable of measuring deformation and strain.

Tire vertical deformation is analytically predicted and physically tested in free rolling and pure longitudinal slip tire tests with no lateral forces present. Physically measured displacement output from the  $\pi$ -sensor shows the same general trends compared to those predicted by the tire finite element model, which the authors consider to be “reasonable agreement”. The sensor is also said to be able to measure tire pressure to within 0.1 bar.

Sergio et al. [44] at University of Bologna investigate the possibility of using the tire itself as a capacitive-resistive sensor for measuring tire forces, according to the following theory. Steel belts in a passenger car tire are made of rubber coated steel cords, with an electrical impedance associated with any adjacent pair of cords (the electrodes) due to their coupling capacitance. The rubber between the steel cords acts as a resistor. Thus each steel belt is conceived of as a “distributed array of impedances”. Tire deformation results in a change in length and spacing of the steel wires, which produces modifications to capacitance and resistance. Therefore, measurements of impedance changes can be associated with tire deformation and ultimately tire forces.

In the study two small samples are cut from a passenger car tire and physically tested in tension. A sinusoidal excitation voltage is input to the tire’s built-in sensor circuit and a tension load is applied to the tire samples. Capacitance measurements are shown versus time, with measured capacitance changing instantly when the coupons are loaded in tension; then a static value is achieved and maintained. This study shows that the built-in steel belts in a tire can possibly be used to measure tire deformation, but further study, especially of a complete tire, is required. The stated conclusion that the “sensor can

## CHAPTER 2. LITERATURE REVIEW

---

measure all needed phenomena in tire-road contact and operate in real road conditions” is unjustified, since the authors do not publish any output other than unprocessed electrical quantities, and they study only samples cut from tires, not real tires. Additionally, the equipment that would be required to measure electrical impedance changes in a real tire is not discussed.

Yi [45] of San Diego State University designs a polyvinylidene sensor system for measurement of tire / road friction characteristics. A polyvinylidene sensor generates an electric charge in response to tire deformation, while providing similar flexibility compared to tire rubber. An analytical model of the electric charge output from the polyvinylidene sensor is developed; a graph showing expected charge versus time is presented for the period of time when the tire is in contact with the road. In a physical test with a “skid-steered” four-wheel robot, two polyvinylidene sensors are attached with glue inside one tire and a wireless data transmission system is used in differential wheel velocity tests. Left hand side wheel speeds are about twice that of right hand side wheel speeds. Results from physical measurements suggest that longitudinal slip and coefficient of friction can be predicted by the sensor and data analysis system. The author indicates that future work will involve optimization of sensor size and location.

Koskinen and Peussa [1], members of the EU FRICTION consortium, design and physically test a system of vehicle sensors with the goal of measuring and estimating friction and friction potential at the tire / road interface, for improved traffic safety especially in wet and snowy driving conditions. The system of sensors includes cameras for identifying environmental conditions, tire force sensors and generic vehicle sensors for measuring global parameters such as acceleration and ambient air temperature. The tire force sensor is carried over from their previous APOLLO project. APOLLO is an in-tire optical displacement sensor that measures deformation of the tire. An LED light source is attached to the inside of the tire; the lens and the remainder of the sensor is attached to the wheel. Data from the displacement sensor are transmitted wirelessly.

Tire displacement, as measured by the optical sensor, is used to estimate both longitudinal and vertical tire forces. The output from the sensing system in a tire test rig physical test shows that the sensor estimates both the longitudinal and vertical forces versus time very well. A different physical test is used to measure lateral displacement from the sensor and estimate lateral force versus time, which also produces good results. Details are lacking regarding the lateral tire physical test but it is implied that it is a pure cornering test. The authors are working on estimating slip angle from the sensor output and also the tire aligning moment. The tire force estimates from the APOLLO sensor look promising, but the prototype hardware is expensive, fragile and bulky.

Erdogan et al. [2] study lateral passenger car tire displacement at University of Minnesota. A pure lateral tire deflection sensor system is designed to measure sidewall deflections uncoupled from radial and tangential deformation. The sensor is a complex assembly that incorporates a polyvinylidene piezoelectric film to measure lateral deflection. An oblique shaded design drawing is provided that illustrates the sensor assembly;

other than this, very few details such as materials used in its construction are provided. Physical tests are performed with a free rolling tire and fixed vertical load, with varying fixed slip angles. The piezoelectric in-tire sensor is used in combination with an optocoupler outside the tire that is fixed to the test rig and is stationary. The optocoupler determines the location of the piezoelectric sensor inside the tire and is used to identify the start and finish locations of the contact patch.

By post-processing the outputs from the piezoelectric sensor and the optocoupler the tire slip angle can be accurately estimated up to 2 degrees. The slip angle accuracy can be good up to 5 degrees if the output is modified with the assumption that the tire sidewall behaves laterally like a hardening spring. A simple brush tire model is used to calculate lateral tire force and friction coefficient. The vertical tire force is required as an input to the brush model; the authors simply assume that this force is known.

Friction coefficients and lateral forces at 1, 1.5 and 2 degrees of slip angle as output from the sensor system are presented in a table. No comment is made about the estimated lateral forces. The friction coefficients are merely compared with one another at different slip angles, with reported levels said to indicate that the system is “quite promising”. Even if the results have potential, the sensor used appears to be large, complex and delicate, meaning that the system may not be useful outside of the laboratory.

In general, investigations of tire displacement sensor systems tend to publish raw quantities output from the sensor with little further processing. Usually some comments are provided indicating that the authors believe the sensor output can be manipulated further to identify tire characteristics such as tire forces. The EU FRICTION consortium is an exception, since they publish all three tire forces versus time as estimated using their APOLLO optical displacement sensor [1]. Some lateral force estimates output from the University of Minnesota displacement sensor [2] are also published. While these studies are noteworthy in that they include estimated tire forces, the sensors involved are impractical due to size, complexity and lack of durability. Small size and high durability are requirements for a STSS if it is to gain acceptance.

### 2.4.1.3 Strain Measurement and Processing

Dennehy et al. [46] conduct a physical test study of tire forces at University of Warwick. In the test setup a passenger car tire is loaded vertically and put in contact with a plate that translates. Slip angles representing normal driving, up to +/- 4 degrees, are tested. A strain gauge transducer is applied to the plate that can measure lateral, longitudinal and vertical tire / plate contact stresses. Lateral and longitudinal stress versus contact patch distance plots are presented. The authors suggest that contact patch deformation and the resulting stress distribution can be related to tire forces, although they do not attempt to process their stress data in order to determine these forces.

Ohori et al. [47] perform a smart tire investigation at University of Tokyo. Their stated goal is to measure all six components of tire force and torque at the tire / road interface.

A passenger car tire mounted on a five-spoke aluminum wheel is physically tested using a drum-style tire test rig as well as on an economy car. Each spoke of the wheel has three strain gages applied, for a total of fifteen strain gages. Therefore, wheel strain is measured instead of tire strain. The authors state that the vertical tire force, slip angles, camber angles and brake torques are all varied during the physical bench test. A pure braking event is performed in the vehicle physical test. A graph of tire forces versus time is presented for both physical tests.

In the tire test rig case, the longitudinal, lateral and vertical tire forces are graphed, both directly measured and estimated from the strain measurements. The tire forces from the strain gages seem to compare well with directly measured forces, but the estimated forces from the strain gage sensor system are noisy and there is no indication of the particular test conditions used on the test rig in the graphs. Longitudinal and vertical tire forces are shown for the vehicle test, but in this case the results are estimated from the strain gages only, and there are no comments about how the estimated tire forces compare with the expected values.

Matsuzaki and Todoroki [48] at Tokyo Institute of Technology provide a review of smart tire sensing and data transmission technology. A summary of sensors is presented, including direct and indirect sensing methods. A review of sensor powering issues and data transmission problems is included. Their review states that direct methods of measuring tire deformation are more accurate than indirect methods, but direct sensing systems at the time of writing (2008) are not sufficiently compatible with tire rubber, especially with respect to its low material stiffness. The authors intend to pursue future work that involves the identification of a tire sensor that is more compatible stiffness-wise with tire rubber.

Matsuzaki et al. [6] at Tokyo Institute of Technology and Imperial College London investigate a rubber-based capacitance sensor for measuring strain in tire rubber. The sensor includes an electrical conductor made from gold that is deposited in a particular pattern onto a rubber base using a photo-lithography technique. Samples of tire rubber with the sensor applied are subjected to physical tensile tests. Rubber at the base of the sensor has similar stiffness to tire rubber, so the use of the sensor along with a flexible adhesive does not significantly alter the local stiffness of a tire where it is attached. Results show that there is an almost linear relationship between the capacitance output of the sensor and the strain in the tire rubber where the sensor is attached.

Significant time is dedicated to testing and reporting on the durability of the capacitance sensor; the authors indicate that it is not yet sufficiently durable for passenger car tire use, since it is expected to give accurate capacitance output up to 1 million tensile cycles, but tires typically have an 8 million cycle design life. The results of the study show that the capacitance sensor as designed may be a way of accurately measuring strain in a tire without altering its stiffness, but they do not post-process the capacitance and strain results further to obtain tire forces.

Matsuzaki and Todoroki [49] at Tokyo Institute of Technology investigate passenger car tire forces using an ANSYS finite element model. Mooney-Rivlin hyperelastic material constants used in the tire rubber material are provided. Strain is calculated using the ANSYS tire finite element model at the contact patch location on the inside of the tire. The finite element model is used in static analyses only, with static vertical loads and static brake torques applied. The authors show that the strain calculated by ANSYS at the bottom of the tire can be used to determine contact patch length and vertical tire force. No experimental strains are shown for comparison, so no judgement can be made about the accuracy of the tire finite element model. The main trouble with the study is that static tire tests are simulated rather than dynamic tests. Since tire forces must be estimated during real, dynamic vehicle operations, the simulations used to investigate tire forces must be dynamic.

Studies reviewed involving in-tire strain measurements generally include the estimation of simple tire parameters such as tire loaded radius and contact patch length due to varying tire vertical loads. The researchers usually indicate their belief that strain measured by an in-tire sensor can be post-processed further in order to determine tire forces, but this subsequent operation was not performed in the studies reviewed. The combined Tokyo Institute of Technology and Imperial College London study [6] shows that a strain sensor can be designed that has similar stiffness compared to tire rubber, but the sensor developed is probably very expensive.

### 2.4.1.4 Acceleration Measurement and Processing

Nepote et al. [50] at the EU APOLLO intelligent tire project present information related to a tire force and friction measuring system, especially related to wireless data transmission between the sensor and the vehicle. The in-tire sensor system includes an accelerometer, a battery and a radio transceiver. Much detail is provided related to processing of the raw tire data from the sensor once it is available inside the vehicle. This investigation is interesting for the description of data transmission protocols and data transfer rates, but little information is provided on the function of the sensor itself.

Savaresi et al. [51] study longitudinal and vertical tire forces in a research study undertaken jointly by the Politecnico di Milano and Johannes Kepler University. An existing ABS wheel speed encoder is used along with an in-tire accelerometer to determine phase shifts between encoder output and accelerometer impulses recorded at the beginning and end of the tire / road contact patch. The sensor system is physically tested in a passenger car; straight-line acceleration and deceleration tests are performed. The accelerometer is glued to the inside of the tire and the data from it are exported wirelessly using a wheel-mounted transmitter unit that is battery powered. The authors state that phase differences between accelerometer and encoder output are strongly correlated with longitudinal and vertical tire forces, although tire forces are not estimated as part of the study.

## CHAPTER 2. LITERATURE REVIEW

---

Ergen et al. [52] describe an intelligent tire sensing system produced in a joint project between University of California, Berkely and Pirelli Tyres. A single accelerometer is used in the system, which is said to estimate longitudinal, lateral and vertical tire forces along with kinetic friction. The system is also said to estimate friction potential and tire slip. No images are provided of the sensor setup. The only sample output from the sensor system published is a graph of load transfer versus time in a longitudinal vehicle dynamics physical test. These same data are shown as estimated using indirect methods based on existing vehicle sensors. Direct measurements of load transfer in the event are not shown for comparison.

The authors state that error in the “important parameters” is about 5%, but estimates from the sensing system are neither shown nor receive any further comment. The study includes a very good overview of the practical constraints on a STSS, such as the harsh, high centrifugal acceleration tire environment, the need for wireless communication to and from the sensor, the likely requirement of energy scavenging and the need for low power devices. The bulk of the investigation is dedicated to a detailed description of the communication methods used with the sensor. The contrast between full disclosure of data transmission methods and near silence regarding the performance of the sensor with respect to tire forces and friction at the tire / road interface is curious. Desire to create and disseminate knowledge may be a low priority compared to creating a profitable product in this case.

Erdogan et al. [53] at University of California, Berkely investigate the use of an accelerometer embedded in a passenger car tire to measure slip angle and tire / road friction coefficient. A tire finite element model in ABAQUS is presented along with the hyperelastic and viscoelastic tire rubber material properties used. A single tri-axial accelerometer is represented in the tire finite element model. A dynamic tire test with a translational velocity of 40 KPH and a slip angle of 2 degrees is simulated in ABAQUS and also physically tested on a drum-style tire test rig at the Pirelli Research Laboratory. Acceleration versus tire angular displacement is plotted for the three acceleration directions in both the analysis and the physical test.

Qualitatively the analytically predicted accelerations compare well with the experimental measured accelerations, with trends in the analysis generally correct, although some peak acceleration amplitudes are incorrect. Physically measured acceleration is used along with a brush tire model to estimate slip angle and friction coefficient. Estimated slip angles are very good up to 2 degrees and estimated friction coefficients are good from 0.5 to 0.8. According to a graph shown for estimated versus actual friction coefficients, the estimated friction coefficients are incorrect by up to 30% in the 0.2 to 0.5 range, but the authors do not mention this, instead referring to the estimated friction coefficients as “comparable”. A minor part of the study is dedicated to showing how the output from the in-tire accelerometer could be used in a vehicle adaptive control system to enhance vehicle safety.



In general, studies of in-tire sensing systems using accelerometers suffer from similar problems compared to studies measuring displacement and strain, namely that unmodified sensor outputs are usually published without further manipulation. However, post-processing is required in every case since the goal is to estimate tire forces and possibly tire / road friction coefficient, tire slip angles, air pressure and other quantities. Accelerometers are attractive since they can be small, durable and relatively inexpensive. The in-tire accelerometer used by University of California, Berkely and Pirelli Tyres [52] is said to be an effective sensor, but outputs estimated from it are not published, raising questions rather than answering them.

### 2.4.2 Patent Search

A search of United States patents for smart tire sensor systems and intelligent tire systems was conducted. Search results show that thousands of patents exist for tire pressure measurement methods, but only a few patents exist for tire force measurement systems and smart tire systems. Tire companies have been primarily involved in patenting tire force measurement inventions, including Michelin and Pirelli. The research group with the most significant smart tire patent success is Pirelli Tyre / Politecnico di Milano. Three new United States patents were issued for this group in 2014 alone, with all three inventions processing data from a single, in-tire, radially oriented accelerometer.

#### 2.4.2.1 Patent Claims Summary

The short list of smart tire patents already granted and their associated claims are summarized here, in the order of oldest to most recent date of patent.

1. US 7,203,603 [5]

**METHOD OF DETERMINING COMPONENTS OF FORCES EXERTED ON A TIRE AND DETERMINING THE SELF-ALIGNMENT TORQUE**

Date: **April 10, 2007**

Inventor: **Bertrand**

Owner: **Michelin, Switzerland**

Claims to make a rudimentary estimate of at least one tire characteristic selected from the three tire forces and the tire self-aligning torque. Tire sidewall deformation measured by two longitudinally oriented dielectric deformation sensors mounted across from one another on opposite tire sidewalls is used along with a rotary encoder. Tire forces are estimated based on linear combinations of raw measurements. Neural networks are suggested as a way of post-processing the measurements in order to refine the force estimates.

2. US 7,546,764 [54]

**ESTIMATION METHOD AND APPARATUS OF TIRE DYNAMIC STATE AMOUNT AND TIRE WITH SENSORS**

Date: **June 16, 2009**

Inventor: **Morinaga et al.**

Owner: **Bridgestone, Japan**

Claims to estimate three tire forces using tire tread longitudinal deformation. Raw measurements are made using two laterally adjacent strain sensors located in-tire at the tread location, along with a rotary encoder. Post-processing of strain measurements involves calculating the time derivatives of the strain waveforms.

3. US 7,707,876 [7]

**METHOD FOR ESTIMATING TIRE FORCE ACTING ON ROLLING TIRE**

Date: **May 4, 2010**

Inventor: **Miyoshi**

Owner: **Sumitomo, Japan**

Claims to estimate all tire forces and moments along with tire air inflation pressure using an array of eight strain sensors on the outside of the tire sidewall, along with a rotary encoder. A linear relationship between raw strain measurements and tire force components is used.

4. US 8,165,827 [55]

**METHOD FOR CALCULATING FORCES ACTING ON THE FOOTPRINT AREA OF A TYRE AND APPARATUS FOR CALCULATING SAID FORCE**

Date: **April 24, 2012**

Inventors: **Savaresi et al.**

Owner: **Pirelli Tyre, Italy**

Claims to estimate longitudinal and vertical tire forces using the measured angular displacement difference between the tire footprint and the wheel hub. Raw measurements are performed using a single in-tire accelerometer at the center of the tread and a rotary encoder. Force estimates are improved using experimentally obtained values.

5. US 8,626,454 [56]

**METHOD AND SYSTEM FOR DETERMINING THE POTENTIAL FRICTION BETWEEN A TYRE FOR VEHICLES AND A ROLLING SURFACE**

Date: **January 7, 2014**

Inventors: **Tebano et al.**

Owner: **Pirelli Tyre, Italy**

Claims to estimate potential friction using radial acceleration measurements, where potential friction is defined as the maximum point in a friction versus slip curve. Raw measurement is performed using a single in-tire accelerometer at the center of the tread. Measured waveforms are fitted with parametric exponential functions. Calculated parameters are compared with a database of experimentally determined parameters to estimate potential friction.

6. **US 8,833,151 [57]**

**METHOD AND SYSTEM FOR ESTIMATING THE INFLATION PRESSURE OF A TIRE**

Date: **September 16, 2014**

Inventors: **Tebano et al.**

Owner: **Pirelli Tyre, Italy**

Claims to estimate tire air inflation pressure using radial acceleration measurements. Raw measurement is performed using a single in-tire accelerometer at the center of the tread. Two different quantities obtained from the acceleration measurement are used in quadratic combination to estimate inflation pressure.

7. **US 8,847,386 [58]**

**METHOD AND SYSTEM FOR DETERMINING A TYRE LOAD DURING THE RUNNING OF A MOTOR VEHICLE**

Date: **October 28, 2014**

Inventors: **Brusarosco et al.**

Owner: **Pirelli Tyre, Italy**

Claims to estimate tire vertical force by using radial acceleration, rotational speed and inflation pressure measurements. Raw measurements are performed using a single in-tire accelerometer at the center of the tread along with a wheel rotational speed sensor and a tire air inflation pressure sensor. Polynomial curve fits of mathematical relationships between tire vertical force and raw measurements are made in advance for a particular tire and stored in-tire.

#### **2.4.2.2 Patented Technology Disadvantages**

Disadvantages of the existing patented technology include the following.

**Limited Outputs.** Patented systems have one or several tire characteristics as outputs, but none of the systems has a complete package of tire force, inflation pressure and friction condition outputs that is required in order for the system to be attractive to vehicle manufacturers.

**Unknown Update Frequency.** No claims are made with respect to the frequency of tire force estimates in patented systems, leaving a potential user to wonder how long they will have to wait for the system to update. Furthermore, no claims are made regarding the vehicle speeds at which the systems will function properly, and whether high vehicle (and wheel angular) speeds will affect update frequencies.

**Inaccurate Assumptions.** Basic mathematical methods are used in patented systems, including peak-picking and algebra, sometimes in combination with a simplifying assumption such as a linear (or other small degree polynomial) relationship between tire deformation and tire force. This scenario is relatively easy to execute computationally but may be highly inaccurate depending on the level of slip. Such simplifying assumptions and methods do not have the accuracy required in a real vehicle application.

**Results Not Validated.** Validation claims in existing patents regarding accuracy of outputs are either non-existent or unimpressive. For example, US 8,626,454 [56] claims to have physical on-road vehicle test data in support of its friction determination system, but reported results show that the system is actually capable of identifying a few broad friction classes (dry asphalt, wet asphalt, dry granite, wet granite) rather than friction coefficients. At least this patent claims a certain level of accuracy; none of the patented tire force systems makes any claim with respect to the accuracy of the tire forces estimated by the system.

## 2.5 Engineering Specifications

The performance targets for the STSS are listed in Tables 2.3 and 2.4, which list engineering specifications for the output estimates and operating speeds of the system, respectively. In comparison, existing smart tire systems described in published literature and patents have fewer outputs. Operating speeds for these systems, both at the vehicle and data acquisition levels, are not disclosed.

**Table 2.3 – STSS Engineering Specifications: Output Estimates**

Item No.	Specification Description	Specification Definition / Notes	System Activity Type	Objective	Threshold	Unit of Measure
1	Tire Longitudinal Force Estimate	Objective is an accuracy goal; estimated force is compared with actual value.	Output Estimates	+/- 5%	+/- 10%	Percent Change
2	Tire Lateral Force Estimate	Objective is an accuracy goal; estimated force is compared with actual value.	Output Estimates	+/- 5%	+/- 10%	Percent Change
3	Tire Vertical Force Estimate	Objective is an accuracy goal; estimated force is compared with actual value.	Output Estimates	+/- 5%	+/- 10%	Percent Change
4	Tire / Road Friction Coefficient Estimate	Objective is an accuracy goal; estimated friction coefficient is compared with actual value. Threshold is an easier friction conditions classification problem.	Output Estimates	+/- 5%	Classification of friction condition into one of four categories: 1) dry, 2) wet, 3) snowy and 4) icy.	Percent Change / Category Classification
5	Tire Air Inflation Pressure Estimate	Objective is an accuracy goal; estimated inflation pressure is compared with actual value. Threshold is relatively low since a dedicated TPMS may already exist in the vehicle, in which case the STSS may augment it rather than replace it.	Output Estimates	+/- 5%	+/- 20%	Percent Change
6	Tire Aligning Moment Estimate	Objective is an accuracy goal; estimated moment is compared with actual value. Threshold is lower than for forces since aligning moment is a secondary priority.	Output Estimates	+/- 10%	+/- 15%	Percent Change

**Table 2.4 – STSS Engineering Specifications: Operating Speeds**

Item No.	Specification Description	Specification Definition / Notes	System Activity Type	Objective	Threshold	Unit of Measure
7	Vehicle Longitudinal Speed	Top vehicle driving speed at which STSS outputs will be required with their targeted accuracies. Threshold is based on typical highway speeds.	Operating Speeds	150	120	KPH
8	Wheel Angular Speed	Top wheel angular speed at which STSS outputs will be required with their targeted accuracies; based on vehicle longitudinal speed specifications and an assumed tire radius of 0.35 m.	Operating Speeds	19	15	Hz
9	Outputs Update Rate	Assumed number of estimated outputs required, issued evenly over each wheel revolution.	Operating Speeds	6	1	Quantity per Wheel Revolution
10	Sensor Sample Rate	Assumed number of in-tire sensor samples required, acquired evenly over each wheel revolution.	Operating Speeds	120	120	Quantity per Wheel Revolution
11	Sensor Sample Frequency	Maximum sensor sampling frequency.	Operating Speeds	2250	1800	Hz
12	Data Acquisition Frequency	Required practical data acquisition frequency in order to avoid aliasing.	Operating Speeds	8192	4096	Hz

## 2.6 Summary

The following conclusions can be made based on the STSS literature reviews, including the primary and supplemental reviews.

- A STSS for ground vehicles (excluding motorcycles) must calculate longitudinal, lateral and vertical tire forces, and possibly the tire aligning moment; rolling resistance and overturning moments are of secondary importance and are not required as outputs.
- Physical tire tests for the purpose of measuring tire forces and moments generally consist of dynamic sweep tests at a fixed tire translational velocity, vertical load and camber angle; pure longitudinal slip sweeps and pure lateral slip sweeps are performed along with combined slip tests.
- Physical tire tests are usually performed using dedicated tire test rigs either in laboratories or in specially designed vehicle trailers.
- Most tire finite element analysis studies employ ABAQUS software, taking advantage of the relatively inexpensive mixed Lagrangian / Eulerian method for simulation of dynamic sweep tests of a tire in contact with a flat road or drum.
- Finite element analysis can be used to calculate tire forces accurately, but reported compute solve times are either long or entirely absent; thus the efficiency of using the finite element method for the purpose of STSS development is uncertain.
- In-tire sensor systems can be used to estimate air pressure; regulatory requirements for tire pressure monitoring systems make the addition of an air pressure monitoring feature desirable in a STSS, even though the main purpose of the system is to estimate tire forces.
- Many in-tire sensing systems described in the literature are impractical due to large size, high cost, complexity and low durability.
- Regardless of whether in-tire sensing systems measure displacement, strain or acceleration, researchers tend to publish raw measured sensor data that are unmodified; very few studies publish tire forces as estimated and post-processed by the sensor system.
- The most significant recent smart tire patents are owned by Pirelli; all of these inventions process data from a single, in-tire, radially oriented accelerometer.
- Existing patented smart tire systems suffer from limited outputs, unknown update frequencies, inaccurate assumptions and results that are not validated.

## CHAPTER 2. LITERATURE REVIEW

---

- Opportunities exist for the design and development of a STSS that is small, light, durable and inexpensive, especially if the system can be shown to accurately estimate tire forces; acceptance may be enhanced if other tire characteristics such as tire / road friction coefficient and air pressure are also estimated.
- The STSS must be able to estimate tire forces accurately in pure and combined slip conditions and at low and high values of slip; if a STSS can correctly estimate tire forces for these conditions, and the methodology publicly disclosed, it will be a new scientific contribution.



## Chapter 3

# Tire Finite Element Modeling and Analysis

**Chapter Brief**—Physical testing is performed in support of finite element model creation for a 50-series passenger car tire. Uniaxial tension testing of tire samples cut from the tread composite, tread rubber and sidewall composite is performed in order to obtain material properties. Hyperelastic material coefficients for tread rubber are fit using uniaxial tension test data. Results show that the Arruda-Boyce hyperelastic material model fits the test data well and it predicts reasonable overall behavior in uniaxial tension and uniaxial compression. Most other hyperelastic material models are found to predict unrealistic behavior in uniaxial compression for the tire samples, especially in the 0 to 20% compressive strain range. The tire FEM with updated material properties is simulated for nine combinations of air inflation pressure and vertical load in order to calculate static loaded radius. The analysis results are compared with physical test results and the analysis results are found to deviate at most by 3% compared to the tests. The validated tire FEM is a phenomenological model that is capable of predicting the generally expected tire behavior, including tire forces and moments generated at the wheel center and displacements and strains developed in the tire itself, and therefore it is suitable for use as a STSS design tool.

---

### 3.1 Overview

The tire FEM built and exercised during the STSS research project appears in Figure 3.1. The model was used to calculate strain at the tire inside surface, where virtual strain sensors were located, along with tire forces generated at the (rigid) wheel center. All of the procedures and assumptions associated with the tire FEM are summarized in Appendix A. Also detailed in Appendix A is the reverse engineering process used to obtain physical geometry and mesh geometry for the tire cross-section and reinforcements.

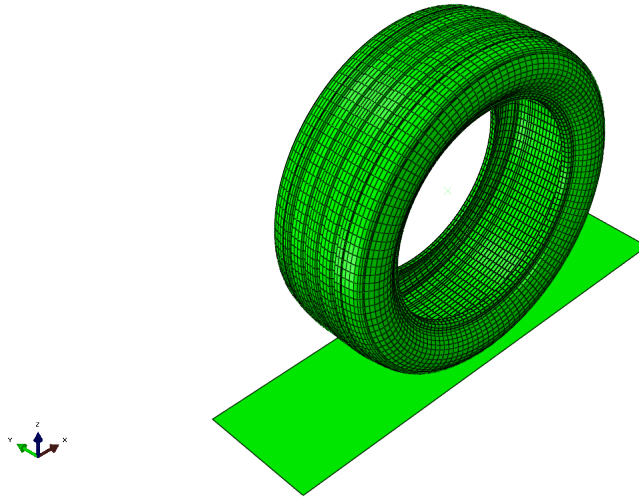


**Figure 3.1 – Finite Element Model of Michelin 235 / 50 R 18 Passenger Car Tire – Rigid Wheel Masked**

## 3.2 Material Properties

The material properties investigation was conducted to determine material properties for use in the tire FEM. Tire construction materials consist of several different rubbers and reinforcement materials including polyamide, polyester and steel. Physical tests using commonly available test equipment were conducted as part of the STSS research project in order to obtain tire material properties. Tire rubber was a special focus of the material properties investigation, since rubber is known to exhibit highly non-linear hyperelastic behavior. Suitable material models and coefficients can be difficult to obtain from published literature. A review of hyperelastic material models typically available in finite element analysis software was undertaken before any testing took place, to identify and select models especially suited to modeling tire rubber.

Material coefficients for several hyperelastic material models were fit to experimental uniaxial tension stress-strain data obtained from samples cut from the tire under study. Finite element models of rubber samples were used along with fitted material coefficients to identify the best hyperelastic material models for tire rubber applications and to gain confidence in the performance of these models. While fitting hyperelastic material models to uniaxial tension test data only is not ideal, it is a realistic scenario as uniaxial tension data are often available, even if data from other deformation modes are not. Therefore, the goal was to identify a hyperelastic material model that performs well under these circumstances.

### 3.2.1 Hyperelastic Material Behavior

Hyperelastic constitutive material models are reviewed and their advantages and disadvantages are compared. Particular attention is paid to the hyperelastic material models available in ABAQUS version 6.12-3, since this finite element analysis software was used to model and analyze the rubber samples. Hyperelasticity is often used to model the mechanical behavior of incompressible (or almost incompressible) rubbery materials when performing finite element analysis; the Neo-Hooke [35] and Mooney-Rivlin [36] are especially common isotropic hyperelastic forms found in published literature.

Hyperelasticity is by definition time independent, and therefore it is suitable for use in static finite analysis. Viscoelastic material models can be used in ABAQUS in conjunction with hyperelastic material models to incorporate material effects that have a time dependence. For example, viscoelasticity can be added to hyperelasticity in a dynamic analysis to include material damping in the rubber. The focus of this study is primarily hyperelasticity and static finite element analysis; viscoelastic effects and dynamic analysis are considered secondarily in the form of physical tire frequency response tests used to calculate modal damping ratios.

#### 3.2.1.1 Rubber Stress-Strain Curves

Rubber materials typically exhibit fully reversible elastic deformation, in some cases even when subject to strain levels in the hundreds of percent. Figure 3.2 shows experimental stress-strain curves from Treloar [59] for vulcanized rubber with 8% sulfur by weight, which was chosen by Treloar for testing because of its highly reversible behavior. Three different tension deformation modes are plotted; uniaxial, biaxial and planar. The Treloar data exhibit the expected trends; the stiffness of the rubber increases from the uniaxial to the planar to the biaxial deformation modes, and all three stress-strain curves have a similar S-shape.

Uniaxial tension refers to extension of a test sample in one direction while allowing unrestricted deformation in the other two directions. Biaxial tension refers to simultaneous extensions in two perpendicular directions, with free deformation in the third direction. Treloar achieved this scenario in the laboratory by clamping a circular sheet at its periphery and inflating it like a balloon; the strain developed near the “pole” of the inflated sheet was close to uniform. Planar tension refers to pure shear deformation.

Fitting of hyperelastic material models to experimental stress-strain data usually requires physical testing of multiple deformation modes. Physical results from uniaxial tension, biaxial tension and planar tension tests can be used for fitting of material coefficients, along with output from uniaxial compression, simple shear and volumetric experiments. Data from multiple experiments will result in significantly better results from the material models [60]. However, often stress-strain data are only available from

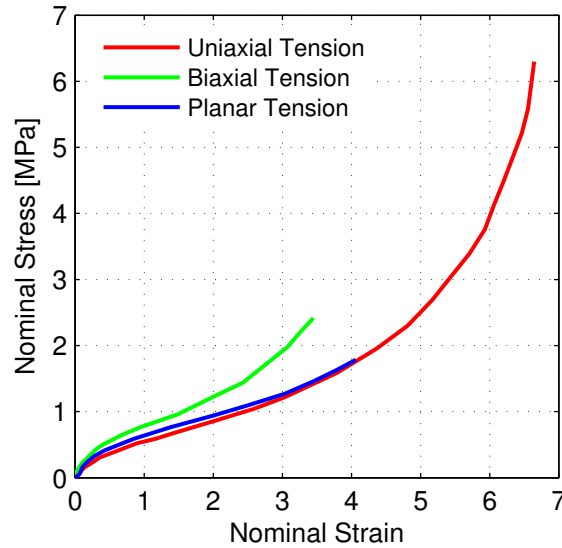


Figure 3.2 – Experimental Rubber Stress-Strain Curves from Treloar [59]

a uniaxial tension test, as was the case during the STSS research project. This study is designed to investigate the hyperelastic material models most suited to this scenario.

### 3.2.1.2 Mechanical Constitutive Law

The material constitutive law for hyperelasticity is shown below [61]; this relationship is used for three-dimensional finite element analysis. Fully recoverable elastic deformation behavior is modeled using this constitutive law. The hyperelastic law is presented in Equation (3.1):

$$\boldsymbol{\sigma} = \frac{\partial U}{\partial \boldsymbol{\epsilon}} \quad (3.1)$$

where  $\boldsymbol{\sigma}$  and  $\boldsymbol{\epsilon}$  are stress and strain work conjugates and  $U$  is a strain energy function that relates deformation to the strain energy stored in the material. The stress-strain relationship is obtained by differentiating the strain energy function. Elasticity is non-linear, and elastic strains can be large. Work done in the deformation of a hyperelastic material is path independent, and therefore it depends only on the initial and final configurations of the continuum.

The strain energy function, or elastic potential, is used to characterize a hyperelastic material in terms of its deformation. For isotropic hyperelastic materials the strain energy (per unit of original volume) is a function of strain as shown in Equation (3.2):

$$U = U(\boldsymbol{\epsilon}) = U(\bar{I}_1, \bar{I}_2, J) \quad (3.2)$$

where strain energy is a function of the first and second deviatoric strain invariants ( $\bar{I}_1, \bar{I}_2$ ) and the volume ratio,  $J$ , assuming compressibility.

Isotropy is assumed in most of the hyperelastic material models in ABAQUS. Built-in strain energy functions for isotropic hyperelasticity are written by adding two separate functions, which represent the deviatoric and volumetric components of the strain energy, respectively, as shown in Equation (3.3):

$$U = U_{\text{deviatoric}}(\bar{I}_1, \bar{I}_2) + U_{\text{volumetric}}(J_{el}) \quad (3.3)$$

where the elastic volume ratio,  $J_{el}$ , incorporates the strain due to thermal expansion.

### 3.2.1.3 Isotropic Models

Information regarding the hyperelastic material models available in ABAQUS is summarized based on the software documentation [62]. The isotropic models available are listed in Table 3.1.

**Table 3.1 – Isotropic Hyperelastic Models**

Form	Cases
Arruda-Boyce	N/A
Ogden	N/A
Polynomial	Mooney-Rivlin
Reduced Polynomial	Yeoh Neo-Hooke
Van der Waals	N/A

### Synopsis

An overview of the isotropic hyperelastic material models is provided for rubber and elastomer modeling applications. This study found the Arruda-Boyce model to be the most suitable when only uniaxial tension stress-strain data are available for fitting. Therefore, the Arruda-Boyce model is described in detail.

1. **Best Fit:** Ogden, Van der Waals and Polynomial

- Complex models with approximately four material parameters that depend on the first and second strain invariants.
- Requires physical stress-strain test data in uniaxial, biaxial and planar tension deformation modes for good results.

**2. Better Fit:** Arruda-Boyce, Yeoh and Reduced Polynomial

- Medium complexity models with approximately three material parameters that depend on the first strain invariant only.
- With uniaxial tension physical stress-strain test data only the predicted behavior in other deformation modes should be reasonable.
- Can be used to create estimated stress-strain curves in the absence of physical stress-strain test data.

**3. Good Fit:** Neo-Hooke and Mooney-Rivlin

- Simple models with approximately two material parameters that are linear functions of the strain invariant(s).
- Rubber stress-strain curve S-shape cannot be represented.
- Used in early modeling phases to predict rubber behavior in the absence of physical stress-strain test data.

**Arruda-Boyce**

The Arruda-Boyce relationship is based on an “eight chain” model, where eight springs emanate from the center of a cube to its corners, which is a representative volume in the continuum. The eight springs are stretched equally; the first strain invariant represents this deformation. The second strain invariant does not appear in the Arruda-Boyce form. This is a statistical mechanics approach where the strain energy function is derived from a distribution of polymer molecule chain lengths [63].

The Arruda-Boyce strain energy function is shown in Equation (3.4):

$$\begin{aligned}
 U = \mu \left\{ \frac{1}{2} (\bar{I}_1 - 3) + \frac{1}{20\lambda_m^2} (\bar{I}_1^2 - 9) \right. \\
 + \frac{11}{1050\lambda_m^4} (\bar{I}_1^3 - 27) + \frac{19}{7000\lambda_m^6} (\bar{I}_1^4 - 81) \\
 \left. + \frac{519}{673750\lambda_m^8} (\bar{I}_1^5 - 243) \right\} \\
 + \frac{1}{D} \left( \frac{J_{el}^2 - 1}{2} - \ln J_{el} \right) \tag{3.4}
 \end{aligned}$$

where  $\mu$ ,  $D$  and  $\lambda_m$  are temperature dependent material coefficients. The “locking stretch” is represented by  $\lambda_m$ ; beyond this value the stress-strain curve rises sharply. The initial bulk modulus is  $K_0 = \frac{2}{D}$ . The initial shear modulus,  $\mu_0$ , is defined in Equation (3.5):

$$\mu_0 = \mu \left( 1 + \frac{3}{5\lambda_m^2} + \frac{99}{175\lambda_m^4} + \frac{513}{875\lambda_m^6} + \frac{42039}{67375\lambda_m^8} \right). \quad (3.5)$$

The Arruda-Boyce strain energy function can be used if limited material data are available, since it has only a few parameters that can be estimated if necessary. In the case that only uniaxial tension physical test data are available for fitting, the Arruda-Boyce hyperelastic model should predict reasonable behavior in other deformation modes.

### 3.2.1.4 Anisotropic Models

In practice, the assumption of isotropy is restrictive in the case of some polymer materials that may consist of an elastomer substrate and a reinforcement with a particular orientation. In this anisotropic type of material, the material properties change depending on the direction. Two anisotropic hyperelastic material models are included in ABAQUS; these are listed in Table 3.2. Anisotropic hyperelastic materials employ either a strain-based or an invariant-based formulation.

**Table 3.2 – Anisotropic Hyperelastic Models**

Form	Formulation
Generalized Fung	Strain-Based
Holzapfel-Gasser-Ogden	Invariant-Based

One application for the Generalized Fung anisotropic form is in the modeling of reinforced rubber. Often the reinforcement fibers have an initial alignment due to the manufacturing process. This scenario fits well with the Generalized Fung form, and strain-based anisotropic hyperelastic formulations in general, since the fibers must be aligned with an orthogonal coordinate system at the start of the analysis.

The Holzapfel-Gasser-Ogden anisotropic form is the most general hyperelastic material model that is shipped with ABAQUS. One important application for the Holzapfel-Gasser-Ogden form is in the modeling of soft biological tissues. Unlike the strain-based formulation, initial alignment of fibers is not required at the beginning of the analysis. The fibers can be aligned due to deformation during the analysis, at which time a strain-stiffening effect can be analyzed.

An interesting finite element analysis study of human artery tissue using the Holzapfel-Gasser-Ogden material model is reported in [64]. Strips are cut from an artery and analyzed in tension simulations. This particular artery is reinforced with two collagen fiber systems, each oriented about 50° from the circumferential direction and crossed over one another, similar to the construction of a bias-ply tire.

Arterial strips are modeled such that the tensile force is not aligned with the collagen reinforcements at the beginning of the analysis. Load-displacement curves show that the material is initially very compliant; however, once the fibers are aligned with the loading direction the material stiffens significantly. These results show that the built in Holzapfel-Gasser-Ogden function performs well, with the anisotropic artery behaving as expected. While the relative complexity and improved fidelity of this model is not suited to the finite element analyses performed on the STSS research project, it may be appropriate in other more advanced tire modeling applications.

### **3.2.2 Tire Sample Uniaxial Tension Testing**

#### **3.2.2.1 Laboratory Setup**

**Table 3.3 – Tire Samples for Uniaxial Tension Testing**

Tire Sample Type	Description
Tread Longitudinal Samples	<ul style="list-style-type: none"> <li>• No Tread Lugs</li> <li>• Dumbbell Shape</li> <li>• 19 cm × 7.5 cm</li> </ul>
Tread Lateral Samples	<ul style="list-style-type: none"> <li>• No Tread Lugs</li> <li>• Dumbbell Shape</li> <li>• 19 cm × 7.5 cm</li> </ul>
Tread Lugs Longitudinal Samples	<ul style="list-style-type: none"> <li>• Tread Rubber Only</li> <li>• Rectangular Shape</li> <li>• 19 cm × 2.5 cm</li> </ul>
Sidewall Longitudinal Samples	<ul style="list-style-type: none"> <li>• Rectangular Shape</li> <li>• 15 cm × 5.5 cm</li> </ul>

Tire samples were cut from the used tires with a bandsaw. The samples created are described in Table 3.3. One sample type was cut from the sidewall and the three other samples types were cut from the tread. Tread samples were cut in a dumbbell shape according to a predefined template. The tread samples were taken from both the longitudinal and lateral directions and consisted of the entire composite thickness of the tire except for the outermost tread lugs. In the case of the lateral tread samples, the tread



---

## CHAPTER 3. TIRE FINITE ELEMENT MODELING AND ANALYSIS

---

lugs were removed and discarded. In the case of the longitudinal tread samples the strips of tread lugs were retained and tested separately. These samples contained pure tread rubber without any reinforcement. Photographs of typical tire samples are shown in Figures 3.3 through 3.5. Eight samples of each type were created and tested.

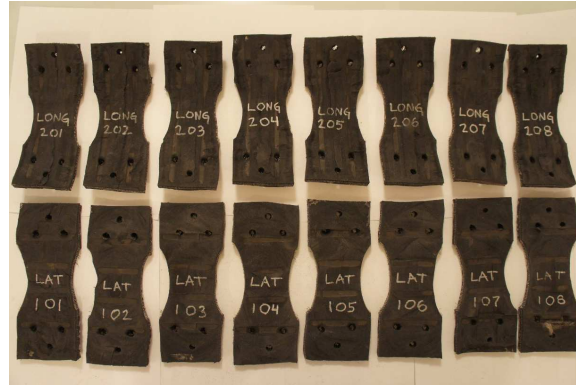


**Figure 3.3 – Tread Longitudinal (Top) and Lateral (Bottom) Tire Samples**



**Figure 3.4 – Tread Lugs Longitudinal Tire Samples**



**Figure 3.5 – Sidewall Longitudinal Tire Sample**

The tire samples were tested using an Instron uniaxial testing machine to obtain force versus deflection curves. Figure 3.6 shows the Instron machine with one of the samples

---

## CHAPTER 3. TIRE FINITE ELEMENT MODELING AND ANALYSIS

---

cut from the tread in the longitudinal direction. This sample is shown in detail in Figure 3.7, which also shows the custom fixtures that were fabricated to attach some of the tire samples to the Instron machine. This is because the jaws of the machine were not wide enough to fit all of the tire samples.



**Figure 3.6 – Instron Machine with Tire Sample**

In the uniaxial tension testing of the tire samples the Instron machine was used to measure force and overall extension of the sample during the test, but the actual extension of the sample was measured at a marked center segment using a photographic method. The marked center segment section is shown with white lines in Figure 3.7. A digital camera that was mounted on a tripod was used to take high resolution pictures of the sample throughout each test.

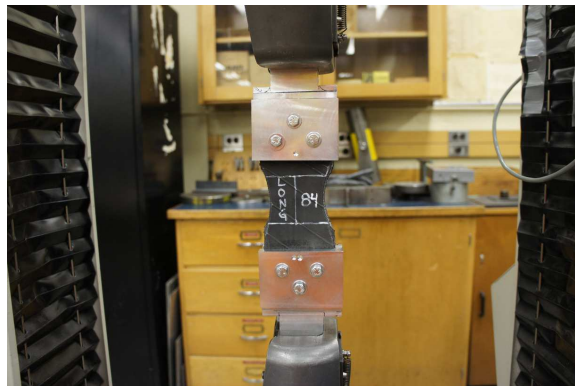


**Figure 3.7 – Tread Longitudinal Tire Sample During Testing**

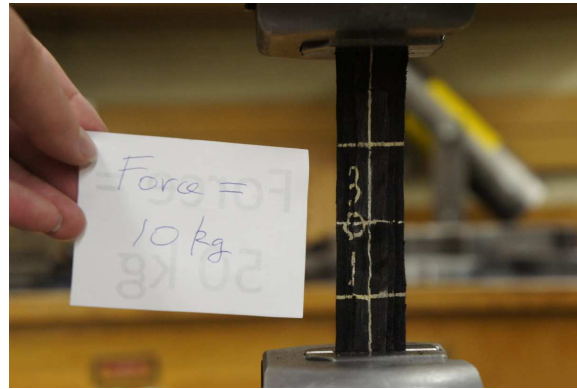
The MATLAB Image Processing Toolbox was used to determine the distance between the lines defining the center segment; this information was used to calculate the actual extension of the sample. The unloaded length of the center segment was 5 cm for all of the samples. A series of three photographs showing the extension of a tread rubber sample due to three different uniaxial loads is shown in Figure 3.8. The uniaxial tension

---

### CHAPTER 3. TIRE FINITE ELEMENT MODELING AND ANALYSIS

---

test of tire tread rubber sample no. 301 is depicted; this sample consists of tread rubber only (without reinforcement). The tread rubber sample is adapted to the Instron machine using its own jaws.



(a)



(b)



(c)

Figure 3.8 – Uniaxial Tension Test of Tire Tread Rubber Sample No. 301: (a) Load = 10 kg (b) Load = 15 kg (c) Load = 20 kg

3.2.2.2 Hyperelastic Curve Fitting for Tread Rubber

Four isotropic hyperelastic material models are fitted to the set of experimental uniaxial tension test data obtained from the tread lugs tire samples; these samples contained tread rubber only and thus one single hyperelastic material. The four isotropic hyperelastic material models are Yeoh, Neo-Hooke, Arruda-Boyce and Van der Waals; these models are defined by strain energy functions that depend on the first deviatoric strain invariant only (or can be forced to depend on it only in the case of Van der Waals). Such forms are expected to fit the uniaxial tension stress-strain data well and predict reasonable behavior in biaxial and planar tension when stress-strain curves from these other deformation modes are not available (as in this case).

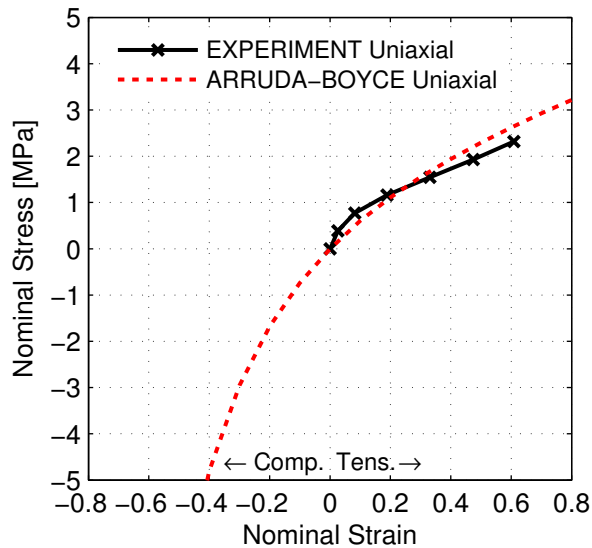


Figure 3.9 – Uniaxial Compression and Tension Arruda-Boyce

In general, the Arruda-Boyce and Neo-Hooke models exhibit similar behavior, and the Yeoh and Vand der Waals models behave similarly. The Neo-Hooke model was rejected in favor of the Arruda-Boyce model since the Neo-Hooke cannot represent the rubber stress-strain curve S-shape. This is not an issue when fitting the tire tread rubber stress-strain data obtained during this study, since the maximum tested tensile strain tested was around 60%. The stiffening effect at higher tensile strains was not measured; however, if further tensile testing at higher strains is performed then the Arruda-Boyce model has the flexibility to model the stiffening phenomenon. The Yeoh model was selected instead of the similarly behaving Van der Waals model since the Van der Waals has additional complexity and is more suited to fitting stress-strain data from multiple deformation modes. Therefore, the choice was between the Arruda-Boyce and Yeoh isotropic hyperelastic material models.

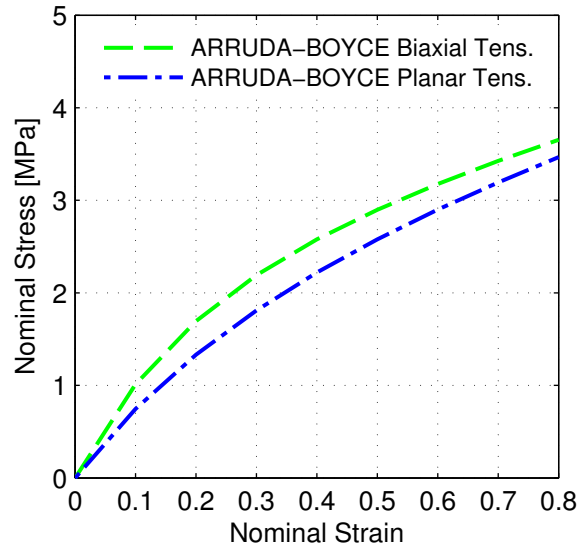


Figure 3.10 – Biaxial and Planar Tension Arruda-Boyce

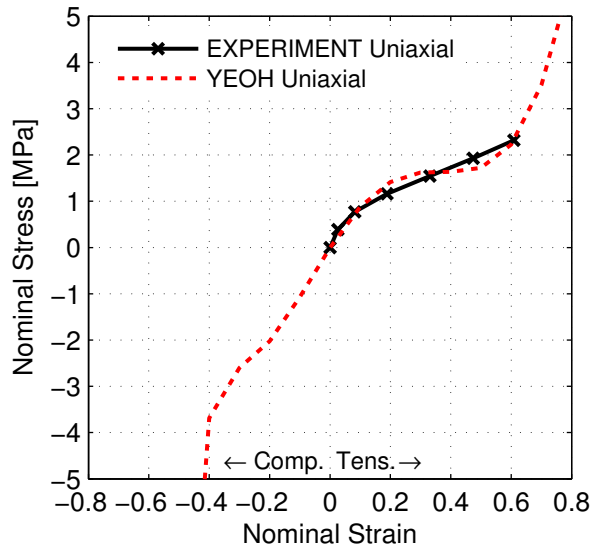


Figure 3.11 – Uniaxial Compression and Tension Yeoh

Stress-strain curves for the Arruda-Boyce model appear in Figs. 3.9 and 3.10; stress-strain curves for the Yeoh model appear in Figs. 3.11 and 3.12. In every case the experimentally obtained uniaxial tension curve is shown as a black line. Fitted curves for uniaxial, biaxial and planar tension appear as red, green and blue lines, respectively. Scales

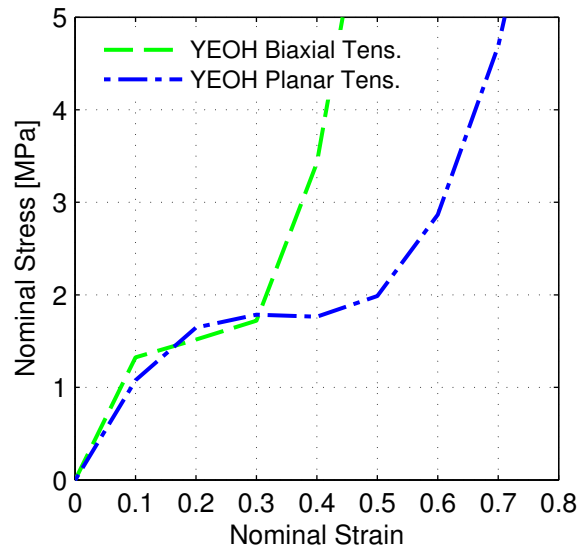


Figure 3.12 – Biaxial and Planar Tension Yeoh

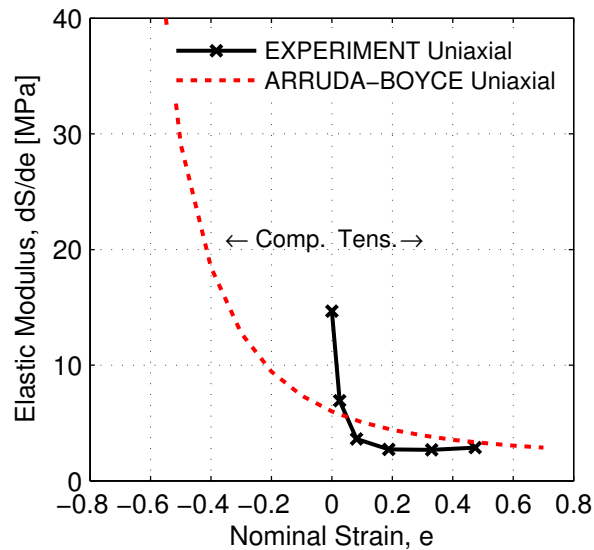


Figure 3.13 – Slope of Uniaxial Compression and Tension Arruda-Boyce

are the same in all of the stress-strain plots so they can be compared directly. “Comp.” labels in the plots refer to compression; “Tens.” labels refer to tension.

A review of Figs. 3.9 and 3.11 shows that both the Yeoh and Arruda-Boyce models predict reasonable behavior in the uniaxial tension deformation mode. The Yeoh model

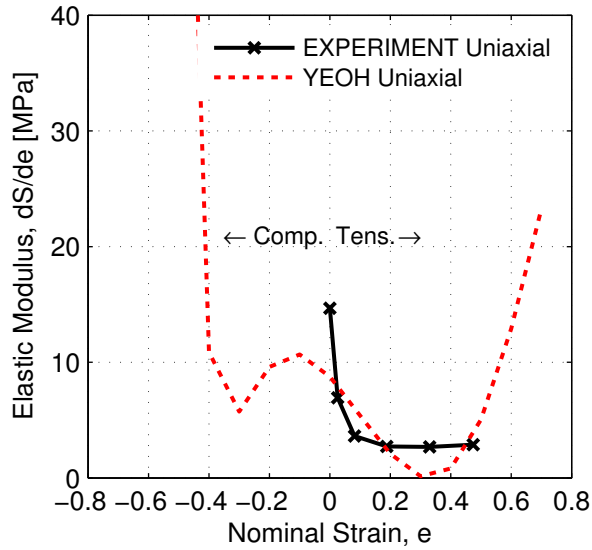


Figure 3.14 – Slope of Uniaxial Compression and Tension Yeoh

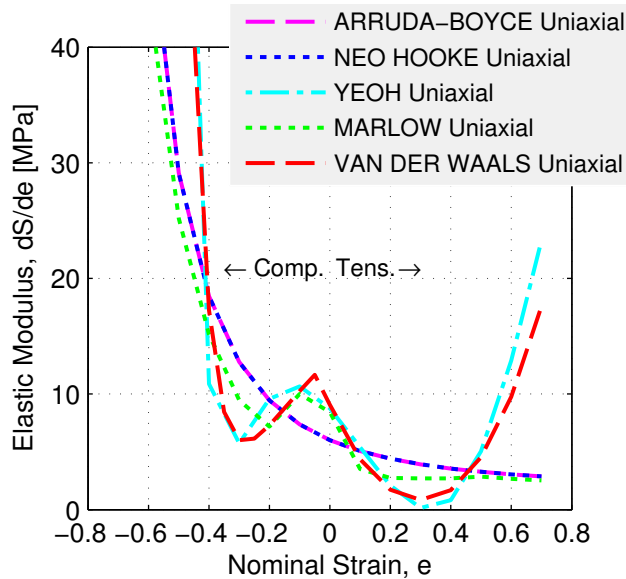


Figure 3.15 – Slope of Uniaxial Compression and Tension All Models

is better at reproducing the experimental curve at low tensile strains. However, the fitted uniaxial tension stress-strain curve for Yeoh has an odd decreasing then increasing stiffness character with an inflection point at around 30% tensile strain. This same trend can be seen in the Yeoh biaxial and planar tension stress-strain curves in Figure 3.12. In contrast, the Arruda-Boyce biaxial and planar tension curves of Figure 3.10 seem reasonable,

with biaxial stiffness higher than planar stiffness and without a sharp increase in stiffness at or below 50% strain as seen in Yeoh. It is impossible to know exactly how well the models fit the biaxial and planar tension cases since experimental data are unavailable. Still, it is possible to eliminate the Yeoh model based on presumed unrealistic behavior.

Figures 3.13 and 3.14 show the slope of the uniaxial compression and tension stress-strain curves versus strain. These “Considère” plots show that the Arruda-Boyce model has the expected general behavior, with the elastic modulus decreasing smoothly over the -60 to +60% strain range under consideration, even if the predicted curve does not exactly match the experimental curve. The Considère plot for the Yeoh model identifies a problem. It can be seen that there is unrealistic behavior predicted in the 0 to 20% compressive strain range, which is a very important region with respect to tire modeling and behavior. There is a peak at around 10% compressive strain in the Yeoh model, where at greater compressive strains and at lesser compressive strains the elastic modulus is decreasing. Furthermore, there is a discontinuity in the curve at 30% compressive strain. Based on the behavior in uniaxial compression alone, the Yeoh model as fitted can be removed from consideration, even without having physical test data for comparison.

Figure 3.15 shows the Considère plots for the four isotropic hyperelastic material models fitted to the tire tread rubber stress-strain data, along with a fifth curve representing the Marlow model, which is a hyperelastic model special to ABAQUS that, like the others investigated here, does not depend on the second deviatoric strain invariant. From Figure 3.15 it can be seen that the Arruda-Boyce and Neo-Hooke models predict the expected rubber behavior; the rest predict unrealistic behavior in the compressive strain range. Figure 3.15 highlights the value of the Considère plots, which make plain the material behavior that is already present in the uniaxial stress-strain curves, but which may be difficult to visualize.

**Table 3.4 – Arruda-Boyce Material Coefficients for Tire Rubber**

$\lambda_m$	3285.9
$\mu$ [Pa]	2235963.9
D [1/Pa]	4.548E-08
$\mu_0$ [Pa]	2235964.1
$\mu_0$ [MPa]	2.24
$\mu_0$ [psi]	324.3
$K_0$ [Pa]	4.397E+07
Stability	Stable All Strains

Table 3.4 lists the material coefficients fitted to the Arruda-Boyce isotropic hyperelastic material model for the tire tread rubber stress-strain test data. These material coefficients were used in all the rubber components of the tire finite element model. The initial bulk modulus associated with the Arruda-Boyce model ( $K_0 \approx 44$  MPa) is the result of assigning a Poisson’s ratio of 0.475. An ideal incompressible rubber has a Poisson’s ratio of 0.5. The



lower value was chosen for generality such that the rubber material could be used with both implicit and explicit finite element methods.

In future work, the tire finite element model may be analyzed in ABAQUS/Explicit, which employs an explicit time integration approach to solve the equilibrium equations of the continuum, as opposed to the implicit method of ABAQUS/Standard. A Poisson's ratio of 0.475 is a "default" value in ABAQUS/Explicit [62] that is expected to provide good performance from the solver but assigns more compressibility than expected of typical elastomers, which is in the 0.49 to 0.49995 range.

In the explicit finite element method, a stable time increment is used that can be very small. The stable time increment is inversely related to the dilatational wave speed, as shown in Equation (3.6):

$$\Delta t \approx \frac{L_{\min}}{c_d} \quad (3.6)$$

where  $\Delta t$  is an estimate of the stable time increment,  $L_{\min}$  is the smallest element length and  $c_d$  is the dilatational, or elastic, wave speed, which is itself related to the mass density, shear modulus and Poisson's ratio of the material. The stable time increment is, therefore, effectively the elastic wave transit time across the smallest element in the mesh. ABAQUS/Explicit cannot analyze perfect incompressibility. Even materials with Poisson's ratio values close to 0.5 cause trouble for explicit finite element analysis solvers since the elastic wave speed is very high, and the stable time increment approaches zero.

The initial shear modulus associated with the Arruda-Boyce model ( $\mu_0 \approx 2.2$  MPa) is lower than expected, as the initial shear modulus of the rubber material being fitted is  $\mu_0 = 14.7$  MPa. This discrepancy is clear from Figure 3.9 where the Arruda-Boyce curve can be seen to have a lower slope at low uniaxial tensile strains compared to the experimental result. The hyperelastic material under study is relatively stiff for a passenger car tire rubber. According to the United States Department of Transportation, the shear modulus for the rubber used in a steel belted radial passenger car tire is in the 0.4 to 1.7 MPa range, whereas the expected range is 0.9 to 1.7 MPa in a truck tire [65]. Therefore, the experimental stress-strain data used for curve fitting are realistic, although they represent the high end of the stiffness range for a passenger car tire rubber.

### **3.2.3 Tire Frequency Response Testing**

Tire driving point frequency response function (FRF) measurements were made using one of the Michelin used tires and one Hercules new tire of 215 / 55 R 17 size (see Table 3.5 for more information). Both tires were inflated to 220 kPa (32 psi) for the measurements made and reported here. Figure 3.16 is a photograph of the laboratory setup for physical frequency response testing, including impact hammer, accelerometer in the tread measurement position, accelerometer power supply and dynamic signal analyzer. Two

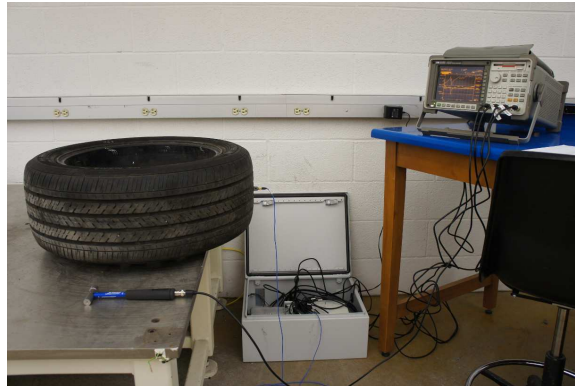


Figure 3.16 – FRF Tire Testing Setup with Tread Accelerometer

driving point measurement locations were used; one at the center of the tread and one at the center of the sidewall. Both tires were attached at the wheel center to a massive table using a bolt. Spacers were used to raise the tire vertically and prevent it from contacting the surface of the table during testing.

Table 3.5 – Information From Hercules New Tire Sidewall

Make	Hercules
Model	Raptis WR1 M+S
Size	P 215 / 55 ZR 17 98W
Tread Plies	2 Polyester, 2 Steel, 2 Nylon
Sidewall Plies	2 Polyester

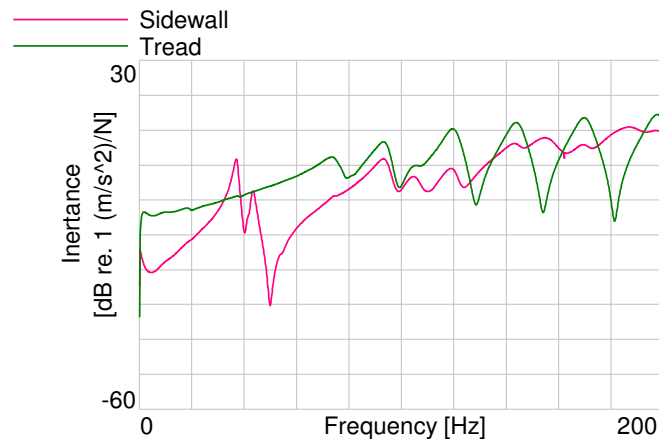


Figure 3.17 – Driving Point Frequency Response Functions From Physical Testing for the Michelin Tire

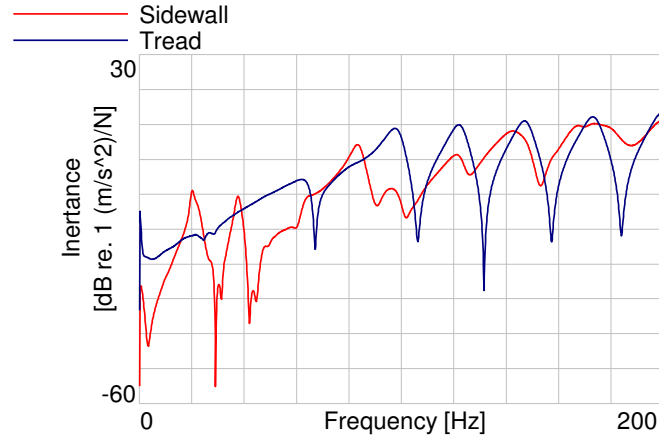


Figure 3.18 – Driving Point Frequency Response Functions From Physical Testing for the Hercules Tire

Figures 3.17 and 3.18 show the driving point frequency response function curves for both tires at both measurement locations. The response curves, modal density and modal damping are all remarkably similar considering that the tires tested are of different sizes, materials, manufacturers and age. Tables 3.6 and 3.7 present the modal damping ratio for select modal frequencies in the 0 to 200 Hz frequency range for both tires. In general, tire modal damping was in the 2 to 4% range, with the average close to 3%. Therefore, an assumption of 3% modal damping for the modal frequencies of a tire, short of any other information, is likely a good starting estimate when setting up the material damping in a tire finite element analysis model, whether using the viscoelastic material model or some other means of including damping depending on the analysis type.

Table 3.6 – Modal Damping in Michelin Tire

Frequency [Hz]	Damping Ratio [%]
37	2.5
43	2.3
93	3.9
120	2.8
144	2.3

The Rayleigh damping method was used to add material damping to rubber in the tire finite element model. In the Rayleigh method, the damping ratio for the  $i$ th normal mode,  $\zeta_i$ , is written as follows [66]:

$$\zeta_i = \frac{\alpha}{2\omega_i} + \frac{\beta\omega_i}{2} \quad (3.7)$$

**Table 3.7 – Modal Damping in Hercules Tire**

Frequency [Hz]	Damping Ratio [%]
38	3.2
83	3.1
98	3.6
122	2.6
147	2.2

where  $\omega_i$  is the circular frequency of the mode,  $\alpha$  is the mass proportional damping and  $\beta$  is the stiffness proportional damping. Rayleigh damping is called proportional because the damping matrix is expressed as a linear combination of the mass and stiffness matrices,  $\mathbf{M}$  and  $\mathbf{K}$ , as follows:

$$\mathbf{C} = \alpha \mathbf{M} + \beta \mathbf{K} \tag{3.8}$$

where  $\alpha$  and  $\beta$  are the proportionality constants.

In order to obtain reasonable damping ratios of around 2 or 3%, and considering the frequency range of 0 to 200 Hz that will certainly include the global tire modes, the values of  $\alpha = 8.0$  and  $\beta = 6.0 \times 10^{-5}$  were selected for use in the tire finite element model. Figure 3.19 is a graph of the fraction of critical damping versus frequency for these Rayleigh damping constants and also for a tabular definition of damping using the viscoelastic material model. The viscoelastic material model can be used to create a consistent damping ratio by defining complex shear and bulk moduli, along with frequency, in tabular form. This particular type of viscoelastic definition can be used in frequency-domain analysis in ABAQUS/Standard; however, it is not available in ABAQUS/Explicit. The Rayleigh damping method is available for time-domain analysis in ABAQUS/Explicit. It should be noted, though, that it has the disadvantage of reducing the stable time increment.

In the STSS research project, the tire finite element model was primarily used in static simulations, and therefore the rubber material damping included in the model was not an issue. If the tire finite element model is used in ABAQUS/Explicit in future work, however, the damping setup will have to be reviewed and improved in order to ensure reasonable results and solve times. The current Rayleigh damping setup is a placeholder that should allow testing and debugging of the model in ABAQUS/Explicit, but it is neither the best nor the final method for incorporating tire rubber material damping.

### 3.2.4 Tire Sample Uniaxial Tension Simulation

Tire sample finite element models were analyzed in uniaxial tension simulations that were similar to the physical testing performed on the Instron machine, for the purpose of improving both the material properties and the geometry of the fiber reinforcements. The

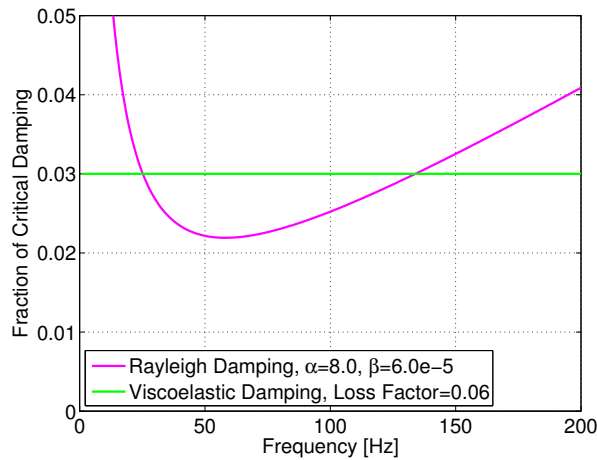


Figure 3.19 – Damping Ratio versus Frequency for Tire Rubber

first tire sample modeled and analyzed was the sidewall longitudinal sample, as it was used to determine the material properties for polyester. This is because the sidewall contains only rubber and polyester cords; since the rubber material properties were known, the polyester material properties could be determined by simulating a uniaxial tension test and modifying the polyester properties until the extension of the model was the same as the extension measured in the physical test. Polyester was modeled as a linear elastic material. The first revision of the model had textbook material properties applied; the textbook elastic modulus was modified by about 20% in order to achieve good correlation with experiment. The final elastic modulus was still within the realistic range.

Tread longitudinal and lateral samples were modeled next, along with the fixtures used to adapt them to the Instron machine. This is a two-step analysis procedure. In the first step the fixtures are put into contact with the sample by the application of fastener preloads that represent bolt assembly torques. The second step is shown in Figure 3.20. A tensile force is applied at the fixture end faces. The end faces are restricted to zero displacement in the lateral and thickness directions. The maximum tensile force applied is 5000 N in the case of the lateral sample and 10000 N in the case of the longitudinal sample. Displacement contours in the tire tread lateral sample in the uniaxial tension simulation are shown in Figure 3.21. Polyamide and steel, like polyester, were modeled as linear elastic materials. Table 3.8 lists the linear elastic material properties used in the tire sample and tire finite element models.

Figures 3.22 and 3.23 show the force versus extension curves for the tread longitudinal and lateral tire samples. Physical test results are shown along with finite element analysis results. The analysis results, shown as magenta color dotted lines, compare well with the test average results, shown as thick blue color lines. In order to achieve this level of correlation between analysis and test, the steel fiber orientation angle was altered by a few

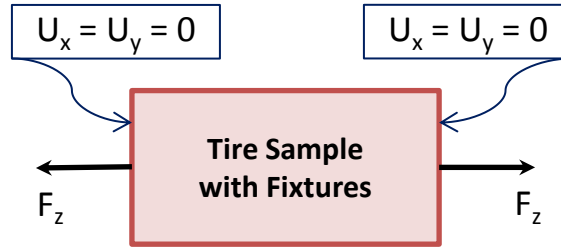


Figure 3.20 – Loads and Boundary Conditions in the Uniaxial Tension Finite Element Analysis of Tire Samples

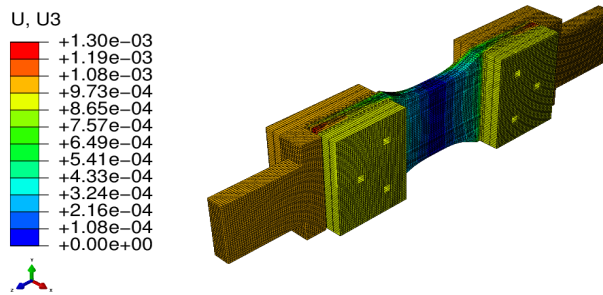


Figure 3.21 – Uniaxial Tension Displacement [meter] Contours in Tire Tread Lateral Sample Finite Element Analysis at Force = 2000 N

degrees, from 30° to 28°. The material properties were not altered. The maximum extensions expected in the longitudinal and lateral directions of the tire tread occur at a force of 2500 and 2200 N, respectively. These force levels are associated with maximum tire inner liner centerline strain levels of approximately 1% in the longitudinal direction and 2% in the lateral direction. The performance of the models is good up to and including these strain levels.

Table 3.8 – Linear Elastic Material Properties

Material Name	Elastic Modulus [Pa]	Poisson's Ratio
Polyamide	$1.000 \times 10^{10}$	0.4
Polyester	$2.236 \times 10^{10}$	0.3
Steel	$2.068 \times 10^{11}$	0.29

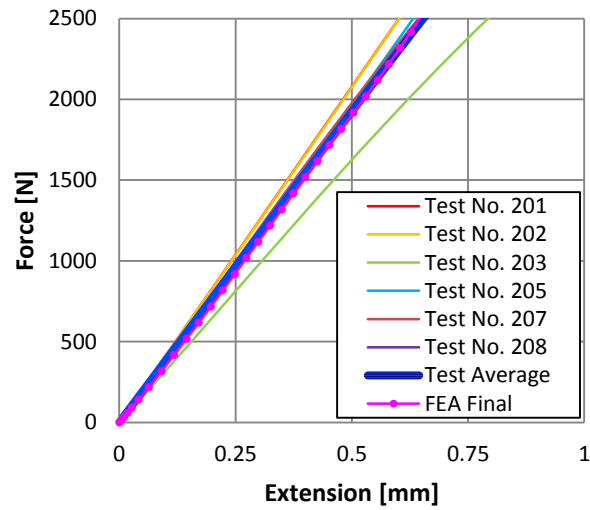


Figure 3.22 – Force versus Extension for Tire Tread Longitudinal Samples in Uniaxial Tension

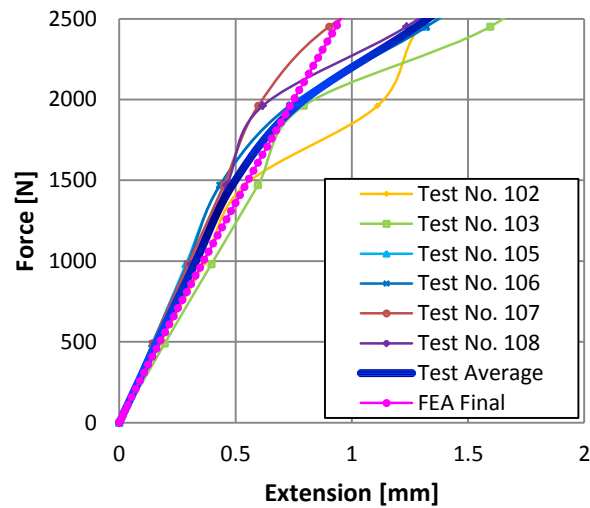


Figure 3.23 – Force versus Extension for Tire Tread Lateral Samples in Uniaxial Tension

### 3.3 Model Validation

Inflation and vertical load analysis of the full tire was conducted for validation of the material properties and geometry representations developed. Physical test results of static

---

### CHAPTER 3. TIRE FINITE ELEMENT MODELING AND ANALYSIS

---

loaded radius for the tire (of the same make, model and size) were obtained from an independent outside laboratory for nine different combinations of inflation pressure and vertical load. The inflation pressures ranged from 120 to 280 kPa (17.4 to 40.6 psi). The vertical loads ranged from 515 to 775 kg (c. 1135 to 1710 lb). A list of all the static load cases appears in Table 3.9.

**Table 3.9 – Tire Static Load Cases**

Load Case No.	Pressure [kPa]	Vertical Load [kg]
1	120	515
2	140	555
3	160	590
4	180	630
5	200	660
6	220	695
7	240	730
8	260	755
9	280	775

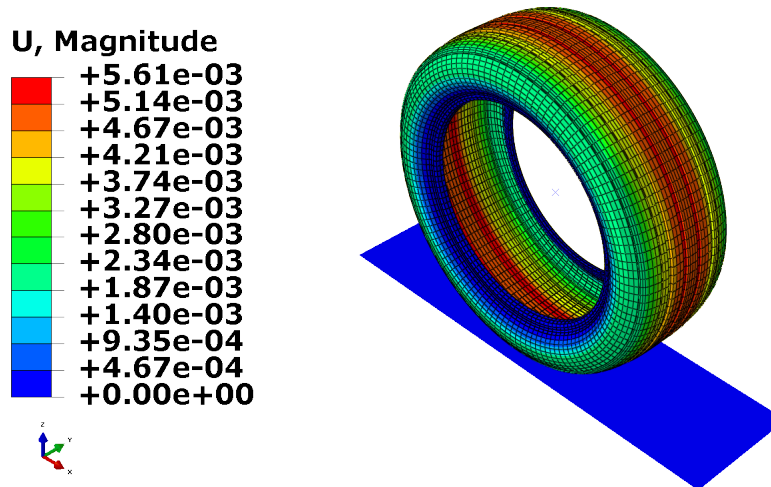


**Figure 3.24 – Magnitude of Displacement [meter] Contours in Tire Inflation Finite Element Analysis for Load Case 9**

The nine load cases were simulated in ABAQUS using a two step procedure. First, air inflation pressure is applied to the tire inside surface. Second, a vertical load is applied to the wheel center. The vertical position of the wheel center with respect to the road surface at the end of the analysis is used to determine static loaded radius. Note that the rigid wheel is masked in the analysis contour plots. Figures 3.24 and 3.25 show displacement



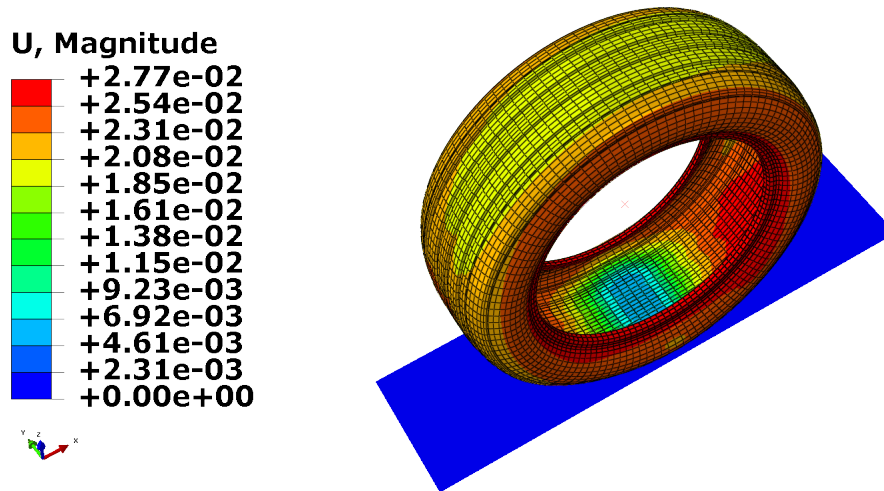


Figure 3.25 – Magnitude of Displacement [meter] Contours in Tire Vertical Load Finite Element Analysis for Load Case 9

contours from the two analysis steps for load case no. 9, which has an inflation pressure of 280 kPa (41 psi) applied as well as a vertical load of 775 kg (1710 lb) applied.

Table 3.10 lists the tire static loaded radius results for both test and analysis. The results show that the static loaded radii as calculated using the tire finite element model deviate from the test results by between 1 and 3%, depending on the load case. Therefore, it can be concluded that results calculated by the tire finite element model correlate well with physical experiments, at least from a global static point of view.

### 3.4 Analysis Studies

Several investigations were performed using the validated tire finite element model, including a tire size effect study, a tread geometry effect study and a simulated modal analysis. These tire FEA studies are described in detail in Appendix C.

**Table 3.10 – Tire Static Loaded Radius [mm]**

Load Case No.	Test	FEA	Change
1	311.0	319.0	3%
2	313.0	319.9	2%
3	315.0	320.8	2%
4	316.0	321.5	2%
5	317.0	322.4	2%
6	318.0	322.9	2%
7	319.0	323.5	1%
8	319.0	324.3	2%
9	320.0	325.2	2%

---

### **3.5 Summary**

The following conclusions can be made based on the results of the tire finite element modeling and analysis study.

1. Static and steady-state dynamic finite element analysis procedures were selected for use with the tire finite element model, since these are computationally inexpensive methods that can simulate events relevant to the early STSS design process.
2. Simulated events using the tire finite element model include air inflation, vertical loading, free rolling and pure braking and pure cornering sweeps.
3. A reverse engineering process was employed to model a used Michelin 235 / 50 R 18 passenger car tire in finite elements, from both a geometry and material properties perspective.
4. A coarse density tire finite element model was built with solid elements representing tire rubber and surface elements representing reinforcement layers; the final model had an element size of  $18 \times 8 \times 4$ -mm.
5. The tire finite element model created is suited to the analysis of tire dynamics phenomena that are meaningful to the STSS research project, even if the model is not converged in terms of element size.
6. Isotropic hyperelastic material models for tire rubber, with strain energy functions that depend on the first deviatoric strain invariant only, are suitable for use when only physical stress-strain data from uniaxial tension testing are available.
7. Fitting of experimental uniaxial tension test stress-strain data from the tire tread with four isotropic hyperelastic material models shows that two models (Arruda-Boyce and Neo-Hooke) produce reasonable results in uniaxial, biaxial and planar

tensile deformation modes, whereas two models (Yeoh and Van der Waals) produce unreasonable results.

8. The slope of the uniaxial stress-strain curves as predicted by the fitted hyperelastic material models should be plotted versus strain; a review of these plots was used to disqualify most of the material models considering their unrealistic behavior in the 0 to 20% compressive strain range.
9. Tire rubber material behavior can be modeled well using the Arruda-Boyce and Neo-Hooke isotropic hyperelastic material models, especially when only uniaxial tension test data are available for fitting; the Arruda-Boyce model should be preferred over the Neo-Hooke due to its ability to represent the S-shape of the rubber stress-strain curve.
10. The Arruda-Boyce isotropic hyperelastic form fit the uniaxial tension stress-strain data well along with producing qualitatively expected results in the biaxial and planar tensile deformation modes; this form was selected for use in the tire finite element model.
11. Physical frequency response measurements of two inflated passenger car tires show that tire modal damping is generally between 2 and 4%; the average value of 3% is a good estimate.
12. The tire finite element model was validated overall statically by comparison with physical vertical loading test results; static loaded radii as calculated using the tire finite element model deviated from the test results by 3% or less, depending on the test case.
13. Simulated modal analysis using the tire finite element model found the six global modes of vibration below 80 Hz; the first mode was a lateral translation mode with a frequency of 44 Hz at an inflation pressure of 220 kPa.
14. A tire size effect study found that tire displacement patterns due to inflation pressure and vertical load do not differ significantly with tire size; therefore, the STSS can likely be used with different tire sizes without major modifications.
15. A tread geometry effect study found that for a slick tire versus a grooved tire, braking and cornering forces are about 5% higher at low slip, and in-tire strain measurements show a corresponding increase in peak strain levels from 5 to 8%, although the waveforms are similar outside of the peaks.

## Chapter 4

# Virtual Strain Processing

**Chapter Brief**—Virtual strain measurements are analyzed using two neural network types. A tire finite element model is used to calculate strain (inputs) and tire forces (outputs) for use in the neural networks. Neural networks are trained on pure slip conditions and tested on combined slip conditions with the goal of accurately predicting tire longitudinal and lateral forces and tire aligning moment in combined slip events. The large mapping function is fitted using multilayer perceptron networks and radial basis function networks. Results from the radial basis function networks are excellent, with calculated tire forces within 1% and tire aligning moment within 1% for the best design; training times are less than one minute and testing times are around 0.004 second. The conclusion is that radial basis function networks can likely be used effectively for real time analysis of strain sensor measurements in a STSS. Further studies using the radial basis function networks show that the STSS should have two in-tire strain sensors located near one another at the outside sidewall, with one oriented longitudinally and the other oriented radially, along with an angular position sensor.

---

### 4.1 Motivation

This study involves the design of an artificial neural network to be used in the STSS. The neural network will be used to process the raw in-tire strain sensor measurements and transform them into the tire forces and other desirable tire characteristics that are the planned outputs of the STSS. Thus, the neural network will be used as the post-processing block shown in the STSS data flow diagram of Figure 1.1. Identification of the post-processing procedure is clearly a major part of the smart tire project.

The post-processing procedure could possibly utilize a mathematical model based on the mechanics of tire behavior such as the Fiala tire force model. Fiala is an analytical brush-type tire model that calculates tire forces. Brush tire models do not calculate tire forces accurately at large tire slips and in combined slip conditions. In general, analytical tire models are known to over-simplify the highly complicated and very non-linear behavior of a tire. Empirical tire models such as Pacejka have higher accuracy in tire force

predictions compared to brush tire models. However, empirical tire models are complex, often having many coefficients.

While it may be possible to create and store a set of Pacejka coefficients for a particular tire, it would still be necessary to somehow relate raw in-tire sensor measurements to the inputs to the model, which include slip angle and slip ratio. There is no straightforward, direct way to measure tire slips, so there is no obvious way to use an empirical tire model in a STSS. Ultimately, tire models do not have outputs for vertical force, friction coefficient and inflation pressure, all of which are required outputs in the STSS.

Due to deficiencies in existing analytical and empirical tools, the post-processing scheme of the STSS seems well suited to the methods of artificial intelligence, specifically neural networks. Furthermore, while some limited smart tire systems have been proposed in the literature, none of them employ neural networks. Therefore, the successful use of a neural network in this application will be a new and unique scientific contribution. A soft computing approach to STSS data processing will be inexpensive, real time, based on training and capable of incorporating the complexities of the tire dynamics problem.

The main goal of this study is to identify a suitable neural network structure for the STSS post-processing procedure and determine how to train it. All of the in-tire strain data used with the neural networks were calculated using the tire finite element model. Therefore, the conclusions made are based on virtual strain as calculated by FEA. This study is the start of the work in artificial intelligence. Further work will involve physically measured strain measured in a real tire.

## 4.2 Reduced System

Per Negnevitsky [67], the first stage in the design of an intelligent system is the development of a prototype. A prototype is a small version of the proposed complete system that is validated with a number of test cases. It is possible that the wrong problem solving approach may be selected during the prototype phase. In that case the reduced system can be investigated using other tools of artificial intelligence at low cost. The idea is to find the right tool using the prototype system and ultimately impress the downstream users, some of whom may be encouraged to fund / become personally involved in the development of the final system due to the convincing results of the prototype.

Table 4.1 lists the reduced outputs for the prototype system used during this study. In the prototype system, here called the “reduced system” to avoid confusion with physical prototypes, the outputs are reduced to three, from the complete system outputs of six. The number of outputs is reduced to three by fixing the remaining three. The vertical force, friction coefficient and air inflation pressure are all fixed to constant values. The remaining output variables are the longitudinal force, lateral force and aligning moment. These are the outputs to be calculated by the reduced intelligent system. In order to

further restrict the size of the reduced problem, the translational wheel speed is fixed to a steady 60 KPH.

**Table 4.1 – Complete System and Reduced System Outputs**

Complete System Output	Reduced System Output?
$F_x$	Yes
$F_y$	Yes
$F_z$	No (Fixed to 4000 N)
$\mu$	No (Fixed to 1.0)
$p$	No (Fixed to 220 kPa)
$M_z$	Yes

### 4.3 Strain Calculation

Strain was selected as the raw sensor output to be used for training and testing the neural networks. Strain measurements were obtained from the inside surface of the tire. Six virtual strain measurements were made using the tire finite element model, from three locations with two orthogonal measurements at each location, as listed in Table C.4 and illustrated in Figure C.9. The locations are at the tread centerline and the left and right sidewalls; the measurements are made in the longitudinal and lateral directions at each location. Sidewall strain is expected to be the same on both sides when braking, but it is expected to differ depending on the side during cornering, which is why strain measurements from both sidewalls are included.

Given that there are three outputs in the reduced system and six virtual strain measurements, it is tempting to label the system as a six-to-three mapping function. That would be an over-simplification, however, since the strain gages measure a curve for each revolution of the wheel. Therefore, the size of the problem depends on the sampling rate of the strain measurements, and whether all of the data from the strain gages are used or a subset of the data are used.

#### 4.3.1 Finite Element Analysis

ABAQUS software was used to solve the tire finite element model. The model represents a radial passenger car tire of size P 235 / 50 R 18. The model was used to calculate both the in-tire strain measurements and the tire forces developed at the wheel center. In the case of the training input vectors for the neural networks, the forces were assigned as the target values. In the case of the testing input vectors, the forces were recorded but not

provided to the network. The forces in the testing cases were retained as the actual values and used to determine the accuracy of the testing outputs of the networks.

The finite element model was analyzed as follows. The model was exercised in two separate pure slip scenarios in order to create training data: 1) pure braking and 2) pure cornering. The model was also exercised in combined slip scenarios for testing data creation. Combined slip occurs when both braking and cornering happen simultaneously, as when steering and decelerating at the same time in order to avoid an accident. Therefore, the neural networks were trained on pure slip scenarios and tested on combined slip scenarios, to see if they could successfully generalize from pure to combined slip conditions.

All of the strain data used during the study were specially created using the tire finite element model in ABAQUS. Previous and preliminary results from the finite element model were not re-used. New finite element analysis jobs were run in order to ensure that the tire models were identical except for the events they were simulating. Therefore, comparisons between the predicted strain measurements can be made directly in order to determine which, if any, of the forces can be determined using neural networks.

### 4.3.2 Pure Slip Training Data

Training data, including strain inputs and force targets, are presented in the form of plots. Three dimensional plots for pure slip scenarios showing strain as a function of both slip ratio / slip angle and wheel angular position are included. Each pure slip scenario was solved for one hundred different slip ratios (pure braking) or slip angles (pure cornering). The neural networks were trained on both pure slip scenarios; thus there were a total of 200 training input vectors.

The three dimensional plots are presented for the purpose of visualizing the strain data. The slip information was not available to the neural networks, though, since this information cannot be directly measured (using inexpensive sensors). Furthermore, the angular position of the wheel was not explicitly provided to the neural networks, since adding this information would double the length of the training input vectors. Only the output from the strain gages was supplied to the neural networks.

Strain training vectors were evenly spaced with respect to slip ratio or slip angle, and no slips were removed from the training data base. In the case of pure braking, the fixed change in slip ratio was 0.25% and the maximum slip ratio was 25%. For pure cornering, the fixed change in slip angle was  $0.15^\circ$  and the maximum slip angle was  $15^\circ$ .

It is assumed that there will be a sensor in the smart tire system, such as a rotary encoder, that can measure the wheel angular position and trigger the acquisition of one revolution of strain data. Each revolution of data is the “static” data set that is input to the neural network. In this way the dynamic strain measurement becomes a series of static data sets strung together, each representing one full wheel revolution.

Ideally the neural network will be fast enough to predict the forces once for each wheel revolution. If not, the network will skip some revolutions, then calculate again on the latest incoming data set associated with the latest wheel cycle. At a speed of 60 KPH, the time for one complete revolution of the tire in the free rolling case is  $t = 0.128$  second, or approximately one-eighth of one second. Therefore, the neural network should calculate its output in less than one-eighth of one second.

#### 4.3.2.1 Pure Braking

Longitudinal force versus slip ratio in pure braking is shown in Figure 4.1. In pure braking the lateral force and aligning moment are zero, so these curves are not shown. The maximum longitudinal force is 4000 N, which is reasonable since the vertical force is 4000 N, the friction coefficient is 1.0 and there is no lateral force present to reduce the longitudinal force capacity of the tire.

Three dimensional plots showing the pure braking strain data appear in Figures 4.2 through 4.7. Strain measurements taken from the left and right sidewalls are almost identical in the pure braking case, as expected. These same pure braking strain plots are presented differently in Appendix D.1, where the two dimensional strain versus angular position views are shown in order to better visualize what the neural networks “see” of the strain data. Note that strain scales vary in the strain plots.

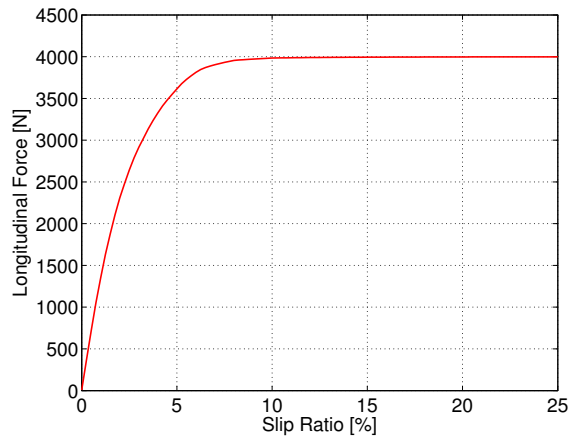
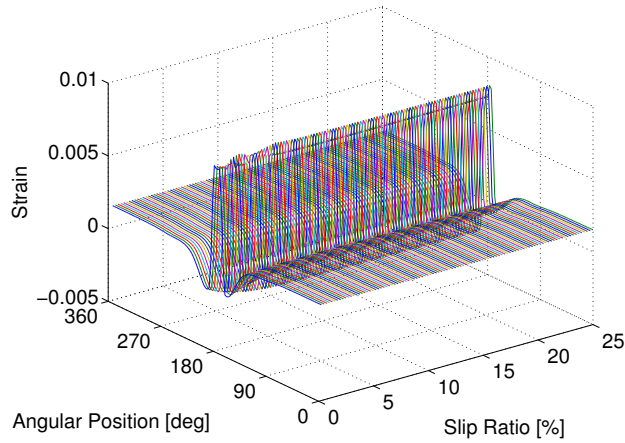


Figure 4.1 – Longitudinal Force versus Slip Ratio in Pure Braking

#### 4.3.2.2 Pure Cornering

Lateral force and aligning moment versus slip angle in pure cornering are shown in Figures 4.8 and 4.9. Three dimensional plots showing the pure cornering strain data





**Figure 4.2 – Training Data: Tread Centerline Longitudinal Strain in Pure Braking**

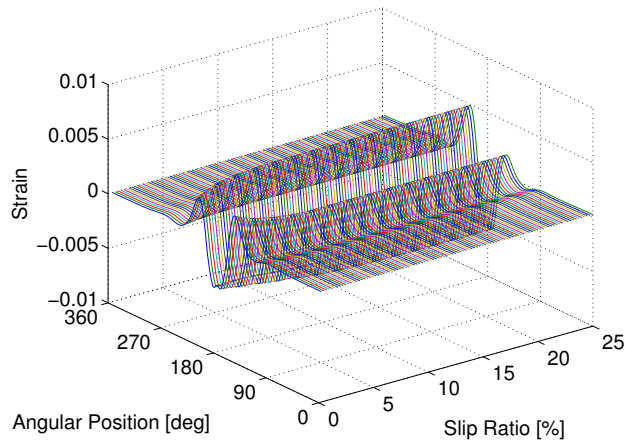


**Figure 4.3 – Training Data: Tread Centerline Lateral Strain in Pure Braking**

appear in Figures 4.10 through 4.15. Strain measurements taken from the left and right sidewalls are significantly different in the pure cornering case, as expected, with opposite side surfaces having an upside down appearance. These same pure cornering strain plots are presented in two dimensional strain versus angular position views in Appendix D.2.

### 4.3.3 Combined Slip Testing Data

Figures 4.16 through 4.21 show strain versus angular position for the testing cases. In the plots “SR” refers to slip ratio, which is associated with braking forces, and “SA” refers to

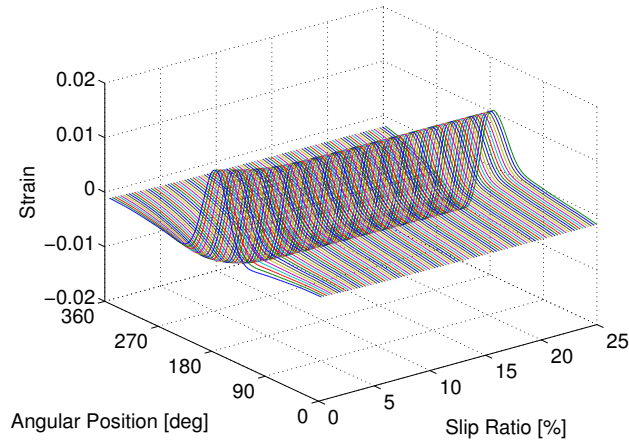


**Figure 4.4 – Training Data: Sidewall Left Longitudinal Strain in Pure Braking**

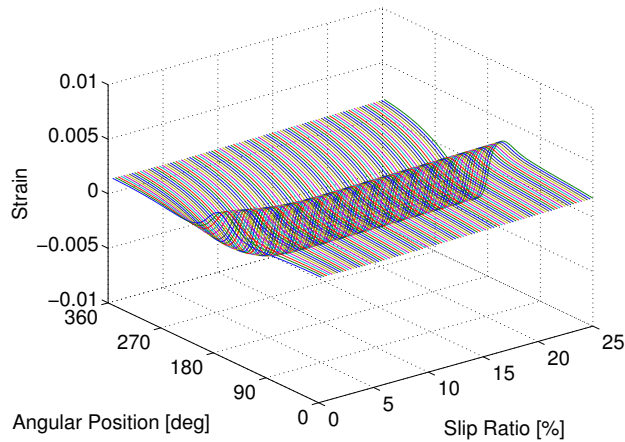


**Figure 4.5 – Training Data: Sidewall Left Radial Strain in Pure Braking**

slip angle, which is related to cornering forces. There are seven testing cases, all of which represent realistic combined slip scenarios that could occur during normal or moderate driving. Table 4.2 lists the combined slip testing cases that were simulated. The actual force and moment values for the testing cases are recorded in Table 4.3.

#### 4.3.4 Neural Network Data Preparation

Strain data were written by ABAQUS into text files, and dedicated MATLAB scripts were written and employed in order to read the strain data into MATLAB workspace variables

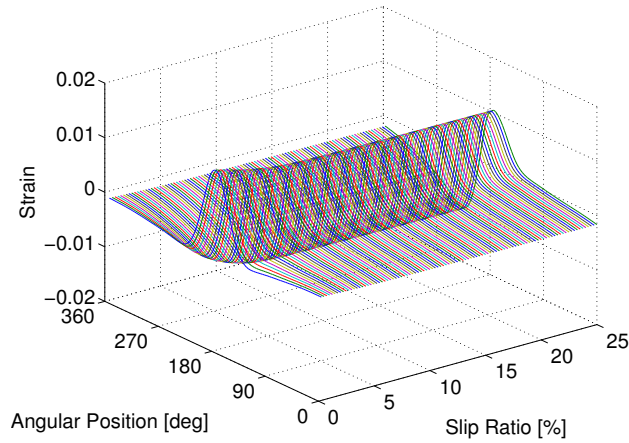


**Figure 4.6 – Training Data: Sidewall Right Longitudinal Strain in Pure Braking**

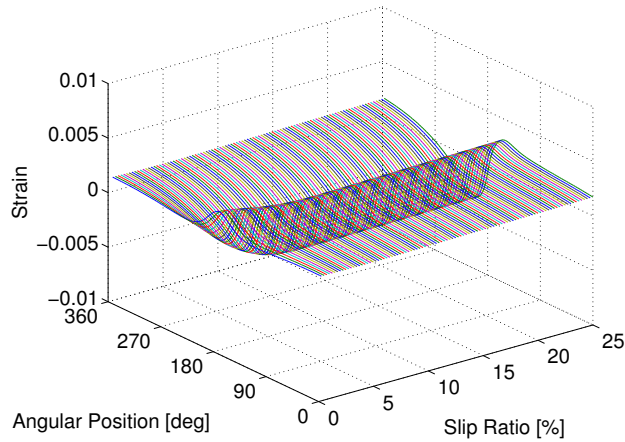


**Figure 4.7 – Training Data: Sidewall Right Radial Strain in Pure Braking**

for subsequent use with the neural networks. Each wheel revolution contained 120 strain samples at each of the six measurement locations. For use with the neural networks, these matrices were unfolded into column vectors of 720 length. Therefore, the size of the training input matrix was  $720 \times 200$ , since there were 200 training input vectors. That is, there were 200 training input samples, 100 from pure braking and 100 from pure cornering.

The size of the training target matrix was  $3 \times 200$ , since there were two target forces and one target moment associated with each training sample. The testing input matrix was  $720 \times 7$  in size, since there were seven testing vectors input to the neural networks associated with combined slip conditions. Training and testing matrices were in this form

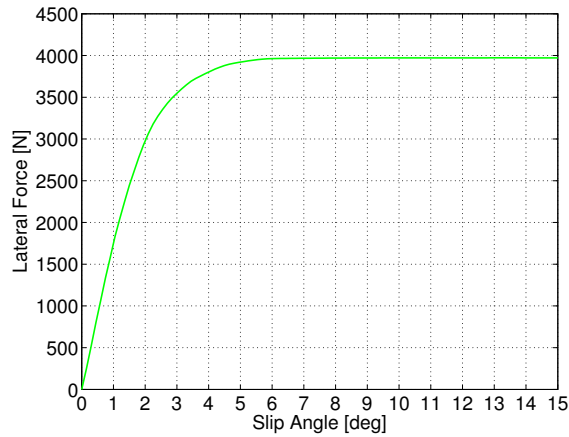


Figure 4.8 – Lateral Force versus Slip Ratio in Pure Cornering

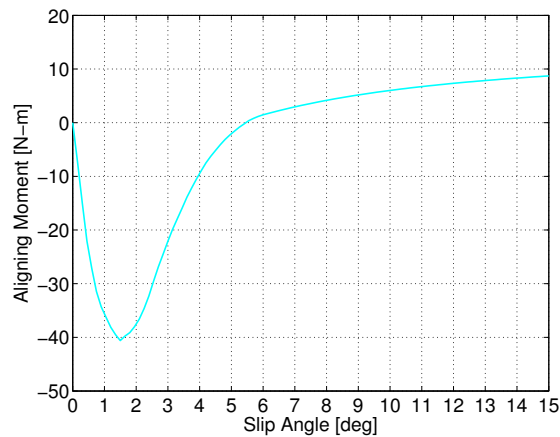
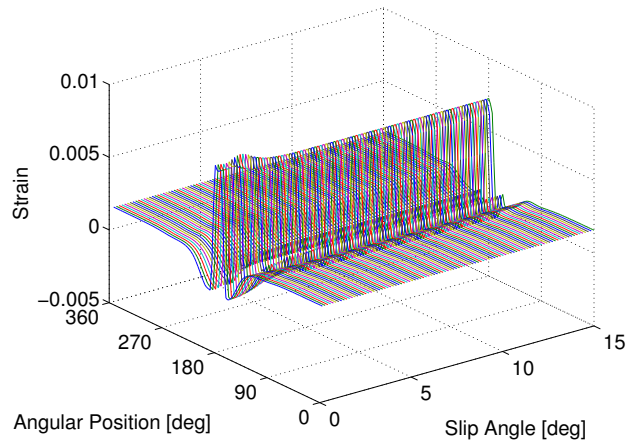


Figure 4.9 – Aligning Moment versus Slip Ratio in Pure Cornering

in the multilayer perceptron and radial basis function networks. The same training and testing data were used with both of the artificial intelligence tools investigated.

The problem as designed is large; it is a 720-to-3 mapping function. All of the features of the strain input training data were retained. It is assumed that the strain data as presented to the neural networks can actually be acquired in practice; to do so without aliasing would require a 2000 Hz sampling rate. Whether that can be realistically achieved in the vehicle is not the subject of this study. Rather, it is assumed that 120 strain samples can be obtained for each wheel revolution. These data were provided unmodified to the neural networks to see if the large mapping function can be fit with good results, and to find out if the mathematical models will “buckle at the knees” computationally in the process.



**Figure 4.10 – Training Data: Tread Centerline Longitudinal Strain in Pure Cornering**

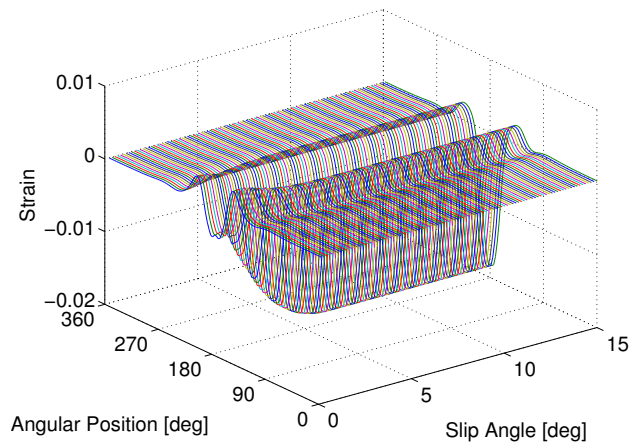


**Figure 4.11 – Training Data: Tread Centerline Lateral Strain in Pure Cornering**

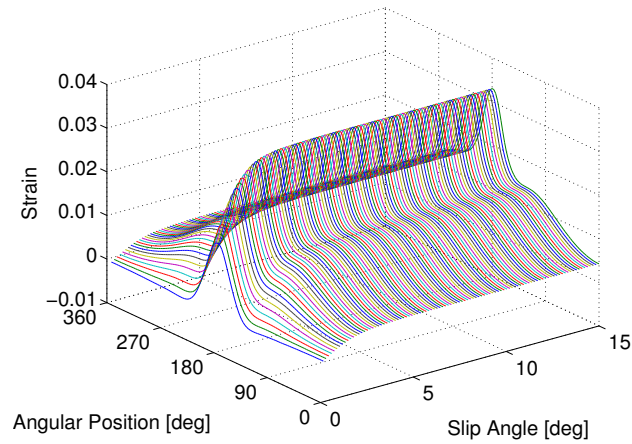


**Figure 4.12 – Training Data: Sidewall Left Longitudinal Strain in Pure Cornering**

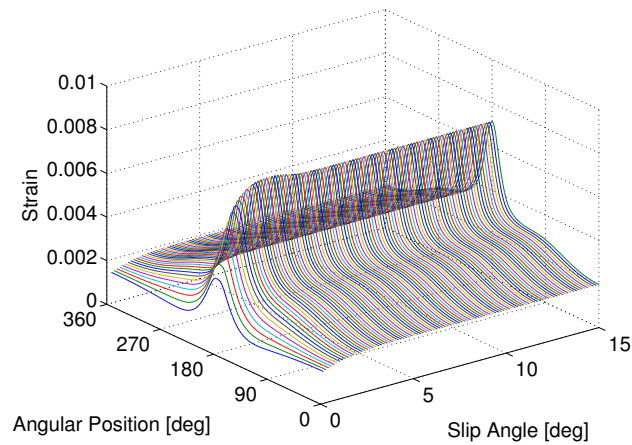


**Figure 4.13 – Training Data: Sidewall Left Radial Strain in Pure Cornering**

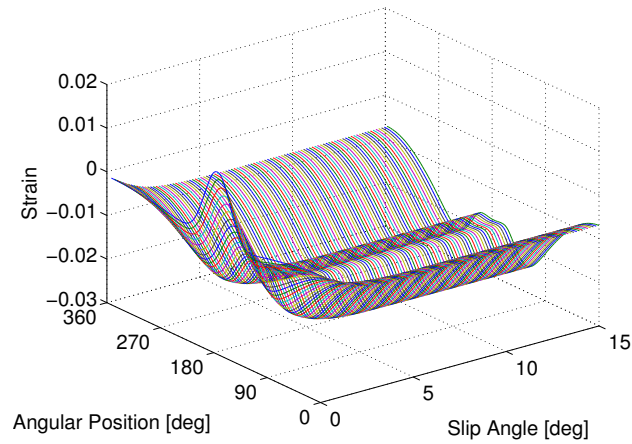


Figure 4.14 – Training Data: Sidewall Right Longitudinal Strain in Pure Cornering

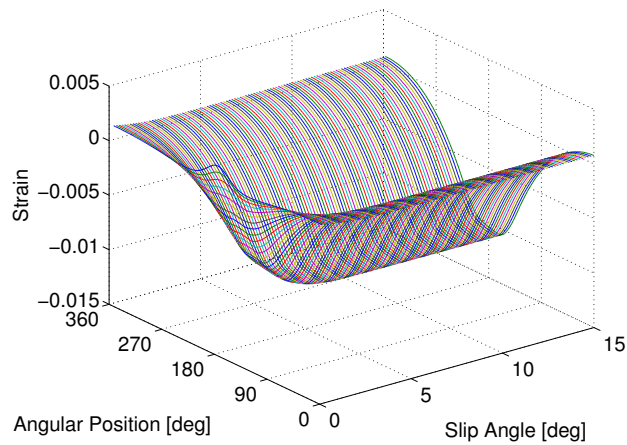


Figure 4.15 – Training Data: Sidewall Right Radial Strain in Pure Cornering

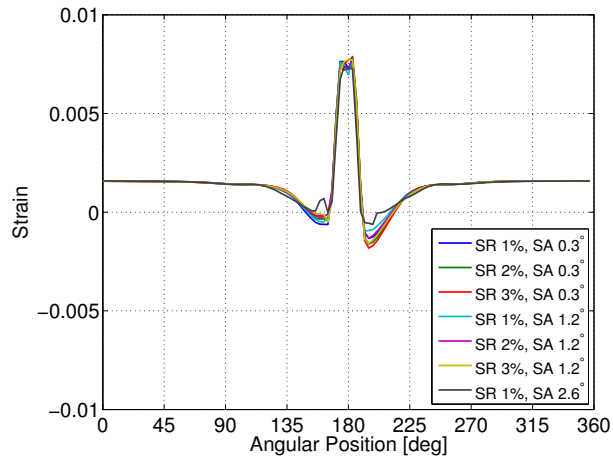


Figure 4.16 – Testing Data: Tread Centerline Longitudinal Strain versus Angular Position in Combined Slip

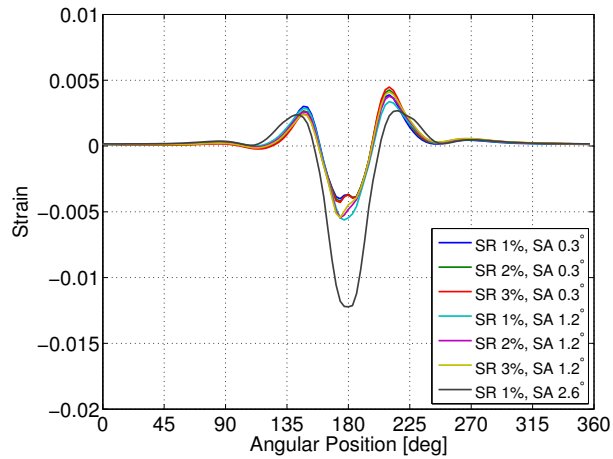


Figure 4.17 – Testing Data: Tread Centerline Lateral Strain versus Angular Position in Combined Slip



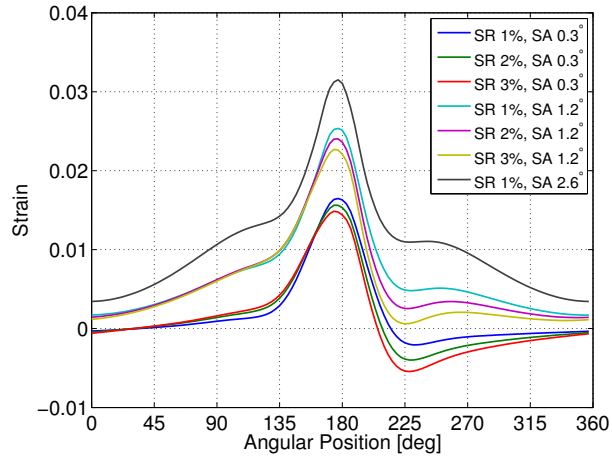


Figure 4.18 – Testing Data: Sidewall Left Longitudinal Strain versus Angular Position in Combined Slip

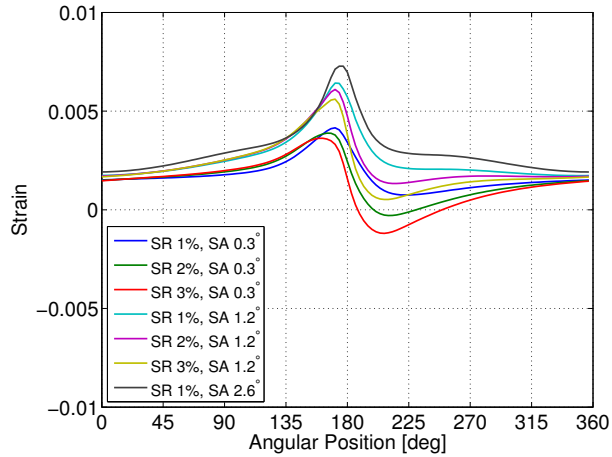


Figure 4.19 – Testing Data: Sidewall Left Radial Strain versus Angular Position in Combined Slip

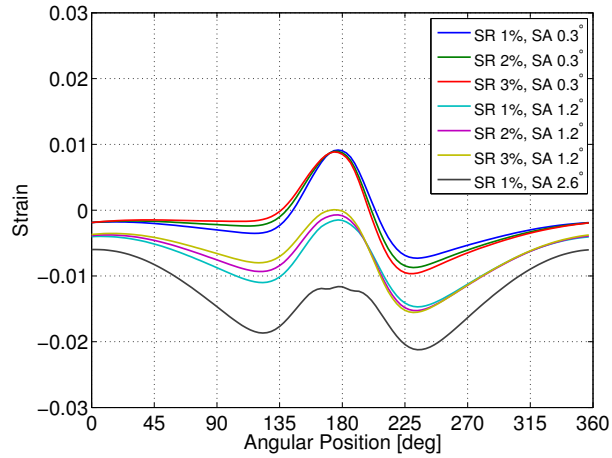


Figure 4.20 – Testing Data: Sidewall Right Longitudinal Strain versus Angular Position in Combined Slip

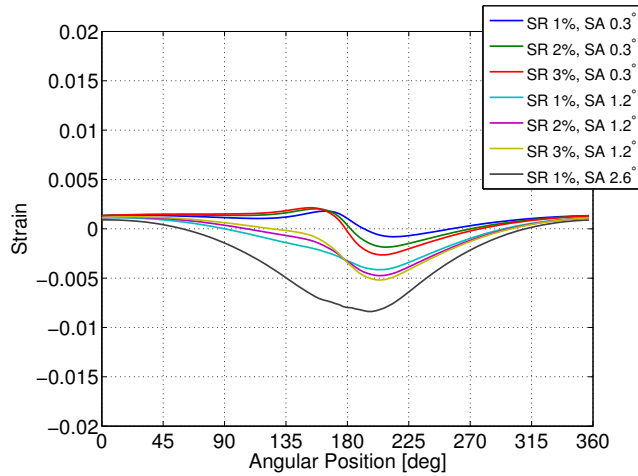


Figure 4.21 – Testing Data: Sidewall Right Radial Strain versus Angular Position in Combined Slip

## 4.4 Neural Network Categories

Two artificial intelligence methods were investigated during this study. These are enumerated as follows, along with their associated acronyms and brief forms. Both of these are feedforward neural networks that use supervised learning mechanisms.

1. Multilayer Perceptron Network (MLPN or MLP Network)
2. Radial Basis Function Network (RBFN or RBF Network)

**Table 4.2 – Combined Slip Testing Cases for Neural Networks**

Case No.	Longitudinal Slip Ratio [%]	Lateral Slip Angle [deg]
1	1.0	0.3
2	2.0	0.3
3	3.0	0.3
4	1.0	1.2
5	2.0	1.2
6	3.0	1.2
7	1.0	2.6

**Table 4.3 – Actual Values for Combined Slip Testing Cases**

Case No.	1	2	3	
$F_x$ [N]	1338.0	2288.8	2910.7	
$F_y$ [N]	505.3	465.2	421.3	
$M_z$ [N-m]	-17.4	-16.9	-15.3	
Case No.	4	5	6	7
$F_x$ [N]	1236.0	2084.0	2697.4	851.2
$F_y$ [N]	1913.4	1769.3	1621.7	3260.5
$M_z$ [N-m]	-54.4	-55.3	-52.0	-54.2

### 4.4.1 Multilayer Perceptron Neural Network

A MLP network with backpropagation learning is the most common type of neural network used in pattern recognition [68]; this type is also used extensively for function fitting problems. Furthermore, many tools are available in MATLAB for modeling and solving

MLP networks. According to the MATLAB documentation, the “multilayer feedforward neural network is the workhorse” of the neural network software [69]. During this study the “fitnet” function in MATLAB was used for implementation of the MLP networks.

The structure of a MLP network with two hidden layers is shown in Figure 4.22. MLP networks can have one or more hidden layers. There are no set rules about how many layers may be required for any given problem; however, one hidden layer with sigmoid activation functions is sufficient for approximating a continuous function, presuming an appropriate number of neurons [70]. The challenge is to select the appropriate number of neurons in the single hidden layer.

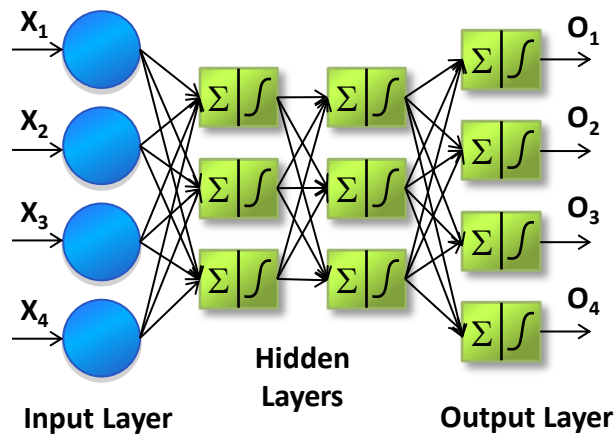


Figure 4.22 – MLP Network with Two Hidden layers

Tsoukalas [71] outlines a rule for designing a three layer neural network (with one hidden layer) that can map an input vector of size  $m$  to an output vector of size  $n$ . The network can perform this mapping problem assuming that the input layer has  $m$  neurons, the output layer has  $n$  neurons and the hidden layer has  $2m + 1$  neurons. It is easy to imagine how this rule could result in a very large neural network, in the event of a large input vector size. Additionally, the rule does not necessarily result in the most efficient network, and it does not imply that a smaller network cannot also solve the problem. Therefore, some trial and error is involved in the design of neural networks with respect to the selection of the hidden layer size.

MLP networks try to approximate a function with a sum of sigmoid functions [72]. In operation, a MLP network with backpropagation works by minimizing an error function,  $\epsilon$ , which is the sum of the squares of the error for each sample in the training data set, as follows:

$$\epsilon = \sum_i \sum_j (E_{ij} - O_{ij})^2 \quad (4.1)$$

where the first sum is over the input training vectors, the second sum is over the output neurons and  $E_{ij}$  and  $O_{ij}$  are the expected and obtained values of the  $j$ -th neuron for the  $i$ -th sample, respectively.

One practical problem with MLP networks is premature saturation [73]. The problem occurs when the values of input samples or weights are too large or too small. Thus, suitable initialization of the weights and proper input data scaling is required for training, especially for fast training with a reasonable number of iterations. Weights should be started at small random values. For sigmoid transfer functions a standard scaling of the input data is recommended, meaning zero mean and unit variance.

During this study the “trainlm” training algorithm was used in MATLAB when solving the MLP networks. This is the Levenberg-Marquardt backpropagation method. It should have fast performance on networks with a low number of weights when used for function approximation problems; performance is not expected to be as good when used in pattern recognition applications. The default “tansig” transfer function was employed; it is a conventional hyperbolic tangent sigmoid.

#### 4.4.2 Radial Basis Function Neural Network

A RBF network is one of the most powerful types of neural networks, especially for function fitting analysis. It is possible to attain almost zero error in a function representation using a RBF network. The structure of a RBF network is shown in Figure 4.23. In this example there are four receptive field units, or neurons, in the single hidden layer. RBF networks employ only one hidden layer, and there are no weights between the hidden layer and the input layer [68].

Training of a RBF network involves two stages. First, the centers and widths of individual neurons in the hidden layer are set using an unsupervised training method, usually one of several clustering algorithms [71]. Second, the connection weights between the hidden layer neurons and the output layer neurons are calculated, which is the supervised learning phase.

RBF networks usually employ a Gaussian function as the radial basis transfer function; this is true of the “newrb” function in MATLAB, which was used during this study. The Gaussian transfer function for the  $i$ -th hidden neuron is shown in Equation (4.2), which is sourced from [70]:

$$g_i(\mathbf{x}) = \exp\left(-\frac{\|\mathbf{x} - \mathbf{v}_i\|^2}{2\sigma_i^2}\right) \quad (4.2)$$

where  $\mathbf{x}$  is the input,  $\mathbf{v}_i$  is the center and  $\sigma_i$  is the width.

The output of the RBF network can be written as follows:

$$o_j(\mathbf{x}) = \sum_{i=1}^n w_{ij} g_i(\mathbf{x}) \quad j = 1, \dots, r \quad (4.3)$$

where  $n$  is the number of neurons in the hidden layer,  $r$  is the number of neurons in the output layer and  $w_{ij}$  is the connection weight between the  $i$ -th hidden neuron and the  $j$ -th output neuron.

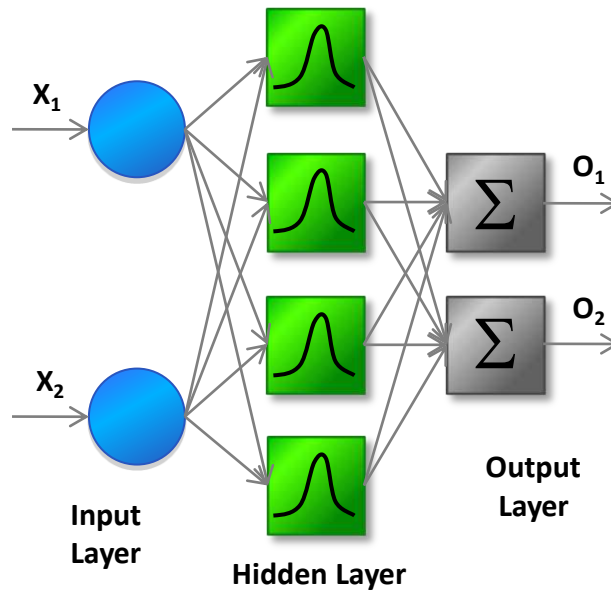


Figure 4.23 – RBF Network

The main drawback with RBF networks is that they may need a large number of neurons in the single hidden layer, often numbering in the hundreds [72]. Furthermore, they should not be as capable as MLP networks with respect to generalization, especially when subjected to noisy input vectors. When good generalization is needed from a RBF network in a function approximation problem, the training set samples must evenly represent the set of all possible input vectors [71].

## 4.5 Neural Network Selection

MATLAB software along with its Neural Network Toolbox was used to perform all of the neural network training and testing simulations during this study.

### 4.5.1 Computers

Three computers were used to solve the neural networks. The specifications for these computers appear in Appendix B. Three separate machines were employed in order to solve more than one model at once; this was required during the MLP network training procedures, since some of the training processes took many hours to complete. The computers used are referred to as Computer A, Computer B and Computer C. The first two are laptop models and the third is a desktop model.

The compute power required for training and testing of the networks is highly relevant to the STSS. If online training in the vehicle is required, the compute hardware available in the the vehicle will be limited. Therefore, training and testing times are reported, along with the computers used, in order to provide some insight into the practical computing requirements of the artificial intelligence methods.

### 4.5.2 Multilayer Perceptron Neural Network

#### 4.5.2.1 MLP Models and Training Error

Table 4.4 – MLP Networks Overview

Model No.	Model Name	Neurons in Hidden Layer 1	Neurons in Hidden Layer 2
1	fitnet1	10	0
2	fitnet2	5	5
3	fitnet3	15	0
4	fitnet4	20	0
5	fitnet5	5	0
6	fitnet6	25	0
7	fitnet7	10	5

Tables 4.4 through 4.6 summarize the structure and the training performance of the MLP networks analyzed. Seven MLP networks were analyzed; five of these had only one hidden layer and the remaining networks had two hidden layers. Most of the MLP networks stopped training at 1000 epochs, which was the maximum allowed. This value was reached for most networks before the training goals were achieved, which were set at either a zero mean squared error (MSE) or a minimum gradient. In the case of fitnet6 the training was user stopped at 26 hours due to unreasonable training time.

In general, training times for the MLP networks were very long, varying from around one hour to one day. This could present a problem in practice, assuming that training is

**Table 4.5 – MLP Networks Training Performance**

Model No.	Best Performance (MSE)	Epochs
1	6.50E-11	1000
2	6.79E-01	1000
3	1.48E-15	827
4	1.51E-14	157
5	4.64E+01	1000
6	5.15E-11	564
7	4.82E-05	1000

**Table 4.6 – MLP Networks Solve Time**

Model No.	Training Time [hr]	Testing Time per Case [sec]	Computer Used
1	4	0.071	B
2	1	0.035	A
3	11	0.101	A
4	4	0.003	C
5	1	0.003	C
6	26 (User Stop)	0.004	C
7	5	0.098	B



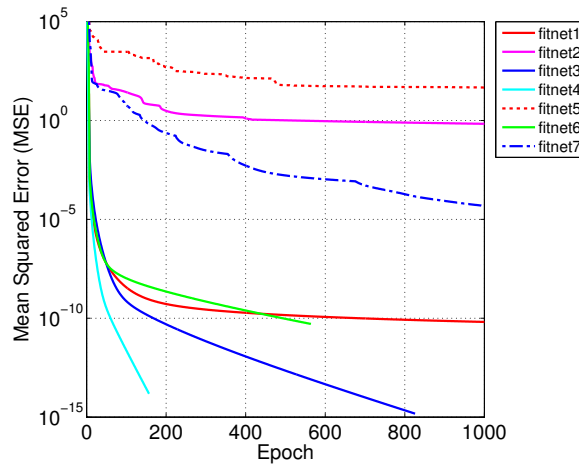


Figure 4.24 – Training Error for MLP Networks

performed online in the vehicle. However, solve times per test case were reasonable, since all were less than the time of one wheel revolution of about one-eighth of a second.

Training error versus epoch for the MPL networks analyzed is shown in Figure 4.24. It is interesting to note that the MLP networks with two hidden layers, fitnet2 and fitnet7, exhibited the worst training error performance, except for the simplest network tested with only five neurons in one hidden layer. According to Jang [68], two hidden layers may be required for approximation of a piecewise-continuous function, as opposed to the single layer that should be sufficient for fitting a standard continuous function. In the smart tire system, as presented to the networks, it appears that the function is effectively continuous and therefore a second hidden layer of neurons is not required (or desirable) in the MLP network.

#### 4.5.2.2 Best Model Testing Performance: fitnet1

Percent change in testing output values, compared to the actual values, were calculated for all neural networks analyzed. This comparison was used to determine the testing performance of the networks. A review of testing output from the seven MLP networks studied shows that the performance of the MLP network type was poor in the case of the smart tire system. The best testing results were obtained from fitnet1, which had a single hidden layer with ten neurons. Testing output from fitnet1 is shown in Table 4.7. Change from actual values for fitnet1 is shown in Table 4.8.

From Tables 4.7 and 4.8 it can be seen that fitnet1 predicted the combined slip forces within 33% and the moment within 56%. This performance is insufficient for use in practice in a smart tire sensor system. fitnet1 performed better than the other MLP networks, however. The testing results for the losing networks were surprisingly poor; in some

**Table 4.7 – Testing Output from fitnet1**

Case No.	1	2	3	
F <sub>x</sub> [N]	1516.7	2450.0	3039.8	
F <sub>y</sub> [N]	422.3	355.8	284.6	
M <sub>z</sub> [N-m]	-12.6	-9.4	-6.8	
Case No.	4	5	6	7
F <sub>x</sub> [N]	1208.7	1963.8	2577.1	891.0
F <sub>y</sub> [N]	1990.4	1836.1	1565.6	3243.9
M <sub>z</sub> [N-m]	-51.2	-49.5	-45.2	-51.2

**Table 4.8 – Change from Actual Values for fitnet1**

Case No.	1	2	3	
Change in F <sub>x</sub> [%]	13.4	7.0	4.4	
Change in F <sub>y</sub> [%]	-16.4	-23.5	-32.5	
Change in M <sub>z</sub> [%]	27.5	44.5	55.4	
Case No.	4	5	6	7
Change in F <sub>x</sub> [%]	-2.2	-5.8	-4.5	4.7
Change in F <sub>y</sub> [%]	4.0	3.8	-3.5	-0.5
Change in M <sub>z</sub> [%]	5.8	10.5	13.1	5.7

cases the predicted values were hundreds of percent different compared to the actual values. Therefore, the MLP networks as designed were not very good at extrapolating to combined slip scenarios given the pure slip scenarios they were trained on. This despite their reputation for generalization, which is supposed to be the “best” [72] when compared with RBF networks, although MLP networks are not known to be excellent for extrapolation.

The poor results of the MLP networks may be due to the relatively small number of neurons compared to the size of the input vectors. Significantly larger hidden layer sizes could not be investigated due to very long training times. However, it is possible that training times could be decreased if the input data were scaled as recommended. The strain data as calculated by ABAQUS were not scaled or normalized in any way, since the idea was to manipulate the raw data as little as possible in order to minimize the computational cost of the system. If the scaling procedure had been followed, it is possible that the MLP networks could have trained in shorter times. In that case more hidden layer neurons could be investigated.

### 4.5.3 Radial Basis Function Neural Network

#### 4.5.3.1 RBF Models and Training Error

Table 4.9 – RBF Networks Overview

Model No.	Model Name	Neurons in Hidden Layer	Spread
1	newrb1	200	1
2	newrb2	200	0.5
3	newrb3	200	3
4	newrb4	200	8
5	newrb5	200	10

Table 4.10 – RBF Networks Training Performance

Model No.	Best Performance (MSE)
1	2.44E-10
2	2.04E-10
3	6.80E-07
4	1.17E-05
5	1.32E-05

Tables 4.9 through 4.11 summarize the structure and the training performance of the RBF networks analyzed. Five RBF networks were analyzed; each had a different spread

Table 4.11 – RBF Networks Solve Time

Model No.	Training Time [sec]	Testing Time per Case [sec]	Computer Used
1	27	0.004	B
2	28	0.004	B
3	33	0.004	B
4	32	0.004	B
5	33	0.004	B

(i.e. width), as shown in Table 4.9. The number of neurons in the RBF networks studied was varied from 10 to 200 in steps of 10. The default maximum number of neurons is equal to the number of training samples; in the case of the smart tire system it is 200. A RBF network is expected to overfit if the number of neurons exceeds the number of input vectors [69].

Training times for the RBF networks were around 30 seconds, which was much shorter than the training times for the MLP networks. This means that training could likely be performed online in the vehicle. Solve times of 0.004 second per test case were also reasonable, since they were significantly less than the time of one wheel revolution of around one-eighth of a second. Low compute times for both training and testing suggest that the RBF networks are suitable for use in the STSS in actual practice.

The training goal for the RBF networks was set to 1E-20 mean squared error, which was not reached by any of the networks tested. Training error versus epoch (i.e. number of neurons) for the RBF networks analyzed is shown in Figure 4.25. Training error performance was very similar in terms of behavior and levels for the networks tested.

#### 4.5.3.2 Best Model Testing Performance: newrb4

A review of testing output from the five RBF networks studied shows that the performance of the RBF network type was consistently good in the case of the smart tire system. The best testing results were obtained from newrb4, which had a spread of 8. Testing output from newrb4 is shown in Table 4.12. Change from actual values for newrb4 is shown in Table 4.13.

From Tables 4.12 and 4.13 it can be seen that newrb4 predicted the combined slip forces within 1% and the moment within 14%. This performance is likely to be sufficient for use in practice in a smart tire sensor system, since knowledge of the forces is of primary importance, whereas knowledge of the moment is of secondary importance to vehicle dynamics.

All of the RBF networks performed in an effective manner. In general, the RBF networks fit the forces well; they performed less well when fitting the moment, although

**Table 4.12 – Testing Output from newrb4**

Case No.	1	2	3	
F <sub>x</sub> [N]	1333.3	2283.1	2905.0	
F <sub>y</sub> [N]	503.9	463.8	420.3	
M <sub>z</sub> [N-m]	-18.4	-18.6	-17.4	
Case No.	4	5	6	7
F <sub>x</sub> [N]	1224.8	2070.4	2684.4	845.9
F <sub>y</sub> [N]	1910.1	1765.0	1618.5	3255.1
M <sub>z</sub> [N-m]	-57.6	-61.0	-58.8	-57.8

**Table 4.13 – Change from Actual Values for newrb4**

Case No.	1	2	3	
Change in F <sub>x</sub> [%]	-0.3	-0.2	-0.2	
Change in F <sub>y</sub> [%]	-0.3	-0.3	-0.3	
Change in M <sub>z</sub> [%]	-5.7	-10.0	-13.4	
Case No.	4	5	6	7
Change in F <sub>x</sub> [%]	-0.9	-0.7	-0.5	-0.6
Change in F <sub>y</sub> [%]	-0.2	-0.2	-0.2	-0.2
Change in M <sub>z</sub> [%]	-5.8	-10.3	-13.2	-6.5

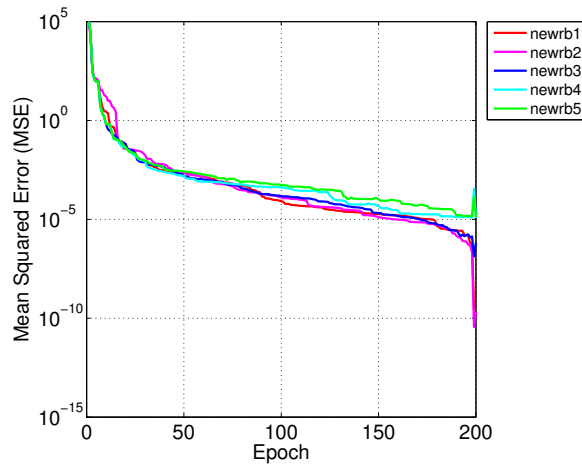


Figure 4.25 – Training Error for RBF Networks

this less accurate moment performance is still likely to be acceptable in the smart tire application. It is interesting that the RBF networks are capable of fitting the force curves well, which have a monotonically increasing character, whereas the moment curve, which is highly nonlinear, is more difficult for the RBF networks to fit.

In picking the winner among the RBF networks, a compromise was made between the prediction of the forces and the prediction of the moment. Slightly decreased performance in the prediction of the forces was selected in order to obtain improved performance in the moment prediction. However, most of the five RBF networks studied provided good testing performance. In general, though, the spread should be in the 8 to 10 range, since the best overall performance was produced by newrb4 and newrb5, which had these values for the spread.

#### 4.5.4 MLPN Generalization Investigation

Since the MLP networks performed poorly compared to the RBF networks, an investigation of the performance of the MLP networks was conducted. In particular, an easier problem was designed for the MLP networks, where easier means using pure slip data to both train and test the MLP networks, to find out if they are capable of generalization when limited to pure slip cases. This is a less challenging problem compared to the previous one, where the neural networks were trained on pure slip data and tested on combined slip data, forcing them to extrapolate from the pure slip scenarios they were trained on to the unknown combined slip situations they were tested on. The easier problem was also investigated using the RBF networks, for comparison.

In the pure slip training and testing study, the winning network configurations of fitnet1 (MLPN) and newrb4 (RBFN) were reused. The networks were trained on 80%

of the pure slip training vectors, for a total of 160 (out of the 200 possible) pure slip samples. Seven pure slip test cases were hand-selected from the remaining unused pure slip samples, representing an assortment of pure slip tire force scenarios. Worst case testing error from this pure slip training and testing study is summarized in Table 4.14. Previous worst case testing error from the pure slip training and combined slip testing study is summarized in Table 4.15.

**Table 4.14 – Generalization: Worst Case Test Error for Networks Trained and Tested on Pure Slip (All Six Strain Sensors Used in Training)**

Network Type	MLPN	RBFN
Change in $F_x$ [%]	4	1
Change in $F_y$ [%]	1	1
Change in $M_z$ [%]	2	1

**Table 4.15 – Extrapolation: Worst Case Test Error for Networks Trained on Pure Slip and Tested on Combined Slip (All Six Strain Sensors Used in Training)**

Network Type	MLPN	RBFN
Change in $F_x$ [%]	14	1
Change in $F_y$ [%]	33	1
Change in $M_z$ [%]	56	14

From Tables 4.14 and 4.15 it can be seen that the MLP network had significantly improved performance when presented with the pure slip generalization problem. When trained and tested on pure slip data, the tire forces were within 4% and the moment was within 2%. This is good performance, although not as good as the RBF network, which calculated all of the test outputs within 1%. Nevertheless, the results show that the MLP network type is capable of generalizing from training pure slip samples to testing pure slip samples, but it is not very good at extrapolating from training pure slip samples to testing combined slip samples. Thus, the RBF network type should be used in the STSS, since it is capable of both generalization and extrapolation in this context.

## 4.6 Neural Network Studies

In the smart tire problem as designed, the RBF networks calculated the testing outputs much faster and with much higher accuracy compared to the MLP networks. Therefore, the RBF neural network type is very suited to the STSS and this neural network type was selected and investigated further using the same training and testing data set, except modified to represent subsets of the data or to study other concerns. An overview of the

investigations performed using the best RBF neural network configuration, newrb4, and the associated results are summarized in Appendix E, with the exception of the number of sensors study that is outlined here. In all of the studies the neural networks were presented with the extrapolation problem, where they were trained on pure slip samples and tested on combined slip samples.

#### 4.6.1 Number of Sensors

This study is designed to determine the number of strain sensors, and also to identify their locations and orientations. The primary task is to find out if all six strain sensors are required in order to accurately estimate the tire forces. Table 4.16 summarizes the testing performance for eight sensor configuration trials, each involving a different combination of the six original sensors, with the worst case change from actual values shown. The first place trial has two sensors located at sidewall left; this configuration is illustrated in Figure 4.26. Using this sensor configuration, the neural network is capable of estimating all of the outputs within 1%. Therefore, only two of the strain sensors are required to accurately predict the tire forces, assuming the limited reduced system is in place (see Table 4.1).

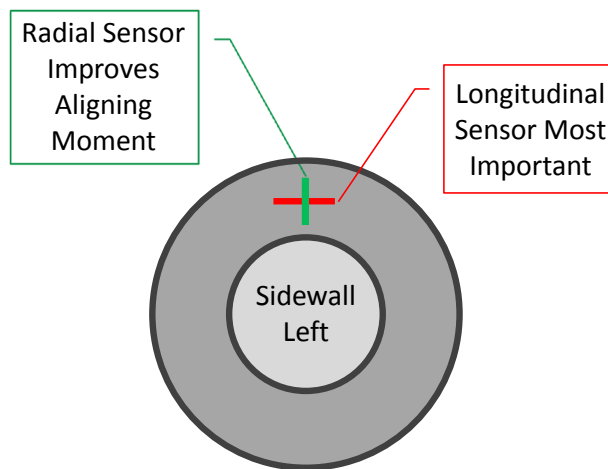


**Figure 4.26 – Location and Orientation of Two Sensors in First Place Testing Performance Trial**

Note that in the second place trial there is only one sidewall left longitudinal sensor; most of the force information can apparently be obtained from this strain measurement location. Performance of the second place trial is degraded compared to the first place trial mainly with respect to the moment calculation. The third place trial has all six



## CHAPTER 4. VIRTUAL STRAIN PROCESSING

---

sensors, and its performance is not improved compared to the first and second place trials. Some general observations based on the number of sensors study are as follows.

- Sidewall longitudinal is the most important sensor and provides the greatest overall force and moment information.
- Sidewall longitudinal by itself provides similar overall results when compared with results from all six sensors.
- Sidewall radial, when added to sidewall longitudinal, improves the accuracy of the moment calculation.
- Two orthogonal tread centerline sensors are inferior to two orthogonal sidewall sensors, in both force and (especially) moment calculations.
- Tread centerline lateral appears to provide more information than tread centerline longitudinal.
- Sidewall longitudinal appears to provide more information than sidewall radial.
- Sidewall longitudinal benefits more from combination with sidewall radial than pairing with centerline lateral.
- Further work should concentrate on sidewall strain measurements.

**Table 4.16 – Worst Case Test Error in Number of Sensors Study**

<b>Trial No.</b>	<b>1</b>	<b>2</b>	<b>3</b>	<b>4</b>	<b>5</b>	<b>6</b>	<b>7</b>	<b>8</b>
<b>Number of Sensors</b>	6	4	2	2	2	2	1	1
<b>Sensors Used</b>	<b>All</b>	<b>Both tread centerline and both sidewall left.</b>	<b>Both sidewall left.</b>	<b>Both tread centerline.</b>	<b>Tread centerline longitudinal and sidewall left radial.</b>	<b>Tread centerline lateral and sidewall left longitudinal.</b>	<b>Sidewall left longitudinal.</b>	<b>Sidewall left radial.</b>
<b>Change in <math>F_x</math> [%]</b>	1	3	1	2	9	4	2	13
<b>Change in <math>F_y</math> [%]</b>	1	3	1	9	2	2	0	12
<b>Change in <math>M_z</math> [%]</b>	14	22	1	41	110	14	9	130
<b>Rank</b>	3	5	1	6	7	4	2	8

---

## CHAPTER 4. VIRTUAL STRAIN PROCESSING

---

The sidewalls are good strain measurement locations, considering both the neural network results and a qualitative review of the strain data. It is interesting to consider the six strain signals in two very different pure slip conditions, shown in Figures 4.27 and 4.28. These graphs represent pure braking and pure cornering, respectively. In both cases the total force developed is 2.5 kN. The tread centerline strain measurements are shown in these plots with green and blue curves. In general, the tread strain measurements have lower peak strain levels, which is reasonable considering the much higher stiffness of the tread (reinforced with steel) compared to the sidewall (reinforced with polyester).

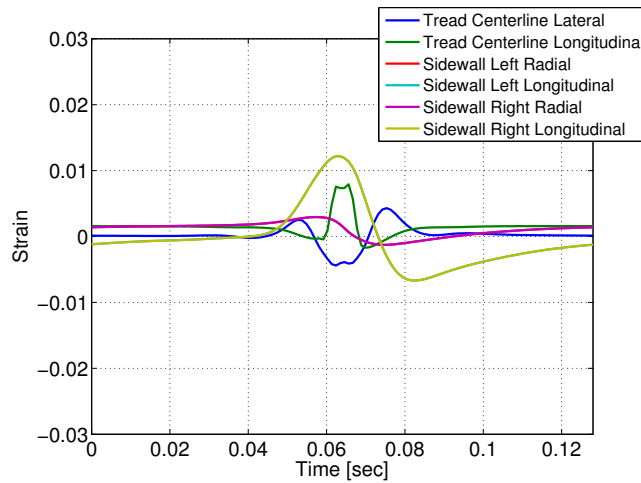


Figure 4.27 – Strain Data for Six Strain Sensors in Pure Braking,  $F_x = 2.5$  kN

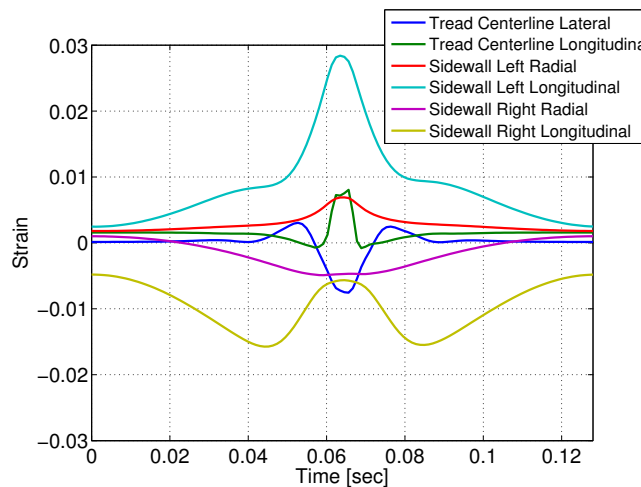


Figure 4.28 – Strain Data for Six Strain Sensors in Pure Cornering,  $F_y = 2.5$  kN

The tread centerline longitudinal strain measurements are plotted back-to-back in Figure 4.29. These two signals are remarkably similar given the fundamentally different force

conditions they represent. It can be seen that the peaks of these waveforms cannot be used to differentiate between the force conditions represented, since the peaks are almost the same. There is some difference in the waveforms, mainly at the rear of the contact patch, although this disparity would probably be difficult to detect in the real STSS, with real strain sensors that are noisy and affected by other issues such as temperature-induced amplitude modifications. Therefore, tread strain measurement locations are inferior to sidewall strain measurement locations in the STSS.

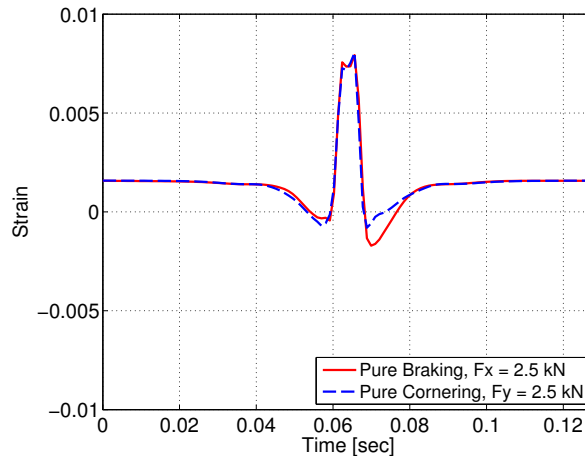


Figure 4.29 – Tread Centerline Longitudinal Signal in Pure Slip Conditions

The results of the number of sensors study show that the STSS should have two strain sensors located near one another at the left (outside in the tire FEM) sidewall, with one oriented longitudinally and the other oriented radially. It is important to note that this conclusion must be confirmed with the complete system, not just the reduced system. Fixed outputs in the reduced system, including vertical force, friction coefficient and inflation pressure, may depend on sensors that appear to be redundant. These outputs will not be fixed in the complete system; thus, apparently unnecessary sensors in the reduced system may ultimately be required in the complete system.

## 4.7 Summary

Based on the results of the virtual strain processing study, the following conclusions can be made.

1. MLP networks are capable of being trained on a full spectrum of pure slip virtual strain measurements, assuming 120 samples are obtained during each wheel revolution, although training times are very long, typically on the order of hours.

## CHAPTER 4. VIRTUAL STRAIN PROCESSING

---

2. A MLP network can determine longitudinal and lateral tire forces within 33% and tire aligning moment within 56%, in the case of extrapolation from pure slip training conditions to combined slip testing scenarios.
3. MLP networks should not be used in the STSS, since they are not suited to the extrapolation problem of training on pure slip and testing on combined slip.
4. RBF networks are capable of being trained on a full spectrum of pure slip virtual strain measurements, assuming 120 samples are obtained during each wheel revolution.
5. A RBF network can determine longitudinal and lateral tire forces within 1% and tire aligning moment within 1%, in the case of extrapolation from pure slip training conditions to combined slip testing scenarios.
6. RBF networks are suitable for use in the STSS, since they are capable of calculating accurate tire force and moment results quickly, including when required to extrapolate from pure slip to combined slip.
7. RBF networks train and test quickly; training times were less than one minute and testing times were about 0.004 second per case, which is a small fraction of the total time of one wheel revolution at 60 KPH.
8. Due to short training and testing times, RBF networks can likely be used in real time in a STSS.
9. RBF networks produce overall excellent results when trained on virtual strain data and they should be investigated further using physical strain data.
10. The STSS should have two in-tire strain sensors located near one another at the outside sidewall, with one oriented longitudinally and the other oriented radially.
11. Two methods to reduce the large size of the strain training vectors, including 1) using a footprint section or 2) using peaks and valleys, produce unacceptably inaccurate testing outputs from the neural networks; these methods should not be used in the STSS.
12. The reduced sample rate approach for reducing the large size of the strain training vectors shows some promise; testing outputs may have acceptable accuracy when a strain sampling frequency as low as 200 Hz is employed, but further investigation at high speeds is required.
13. Strain measurements exhibit some velocity dependence; if testing data are 40 KPH different from training data, tire forces are expected to be incorrect by about 15%.
14. A very good angular position sensor is required in the STSS; lateral shifting of the strain data with respect to correct angular position will lead to highly inaccurate tire forces.

## Chapter 5

# Smart Tire Prototyping and Testing

**Chapter Brief**—Two STSS prototypes are fabricated and tested, both of which include piezoelectric deformation sensors and an angular position measure. Smart tire revision 1 uses wheel angular position estimates based on vehicle ABS angular velocity measurements. Neural network analysis of smart tire revision 1 data shows that better angular position data are required than can be obtained from vehicle ABS, with a reliable once per wheel revolution angular position index being a necessity. Lessons learned in smart tire revision 1 are incorporated into smart tire revision 2, which includes a rotary encoder to directly measure wheel angular position including an angular position index. Data collected from revision 2 in standard vehicle dynamics events are stored for use in the physical deformation processing study.

---

### 5.1 In-Tire Piezoelectric Sensor

Durability bench testing of a commercially available piezoelectric sensor for in-tire deformation measurement was performed, which is summarized in Appendix F. A partial attachment method for the sensor was established for use in the STSS prototypes, which involved bonding the top third of the sensor to the tire rubber, retaining its free end with a paper clip and placing plastic film under the free end to prevent rubber abrasion. Using this method the sensor was expected to produce repeatable output for around one hour of continuous use assuming a vehicle speed of 30 KPH, with voltage levels maintained within 5% of the starting level. Beyond this time the sensor signals were expected to exhibit evidence of fatigue failure, including decreased voltage levels and increased noise.

### 5.2 Smart Tire Revision 1

Both smart tire revision 1 and revision 2 were designed for use at the left front corner of the research vehicle.

### 5.2.1 Prototype Fabrication

Six piezoelectric sensors were installed in smart tire revision 1. Their locations and orientations are listed in Table C.4. Figure 5.1 shows photographs of the instrumented tire used in smart tire revision 1, including images of the tread centerline and sidewall right sensors. Sidewall left sensors are not shown as they were simply a mirror of the sidewall right sensor layout. Smart tire revision 1 used a wired data transmission system, with the lead wires from the piezoelectric sensors routed through the rim. Dedicated holes were drilled in the rim for the purpose of passing the electrical cables.

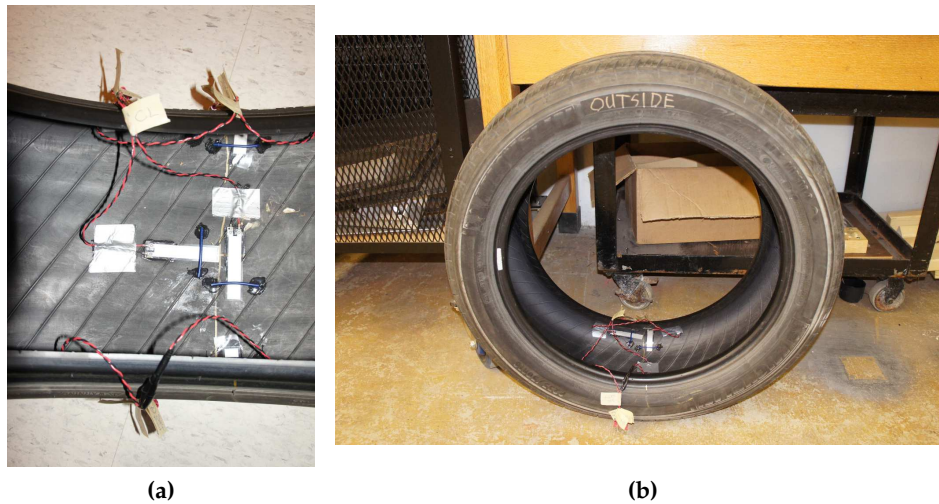


**Figure 5.1 – Instrumented Tire for Smart Tire Revision 1: (a) Tread Centerline Sensors (b) Sidewall Right Sensors**

The smart tire rim is shown in Figure 5.2, which was a custom modified 18"× 8" alloy wheel that was selected for its consistent, uninterrupted flange suitable for drilling tire valve bores. The four holes in the rim flange are circled. The rim was shipped with one of these holes already drilled. Three additional identical holes were drilled such that the four holes were evenly spaced around the rim. The original hole was intended for a conventional rubber tire valve; this hole retained that function.

The three additional holes were used for special cable conduit tire valves, shown in Figure 5.3. The valve cores were removed from the tire valves, allowing the piezoelectric sensor data to pass through. The cable threaded through the valves had 22 AWG telephone wire inside with four solid copper conductors per cable. The cable housings were bonded to the inside of the modified tire valves using "Lepage Stik 'N Seal Extreme Repair Adhesive", which was recommended for use in the construction of home fish aquariums and therefore assumed to be water (and air) tight when cured.



Figure 5.2 – Alloy Rim with Four Tire Valve Holes

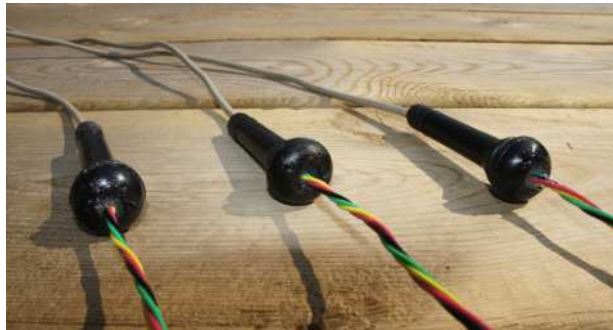


Figure 5.3 – Modified Tire Valve Electrical Cables

Data from the in-tire piezoelectric sensors were stored in a data logger mounted on the outside of the rim for later offline data analysis. The data logger was located inside an aluminum housing that was attached to the rim with an adapter plate, shown in Figure 5.4. The back of the adapter plate is shown. The adapter plate was made from 3/16" thickness aluminum; it had foam rubber pads at the back that were in contact with the rim for the purpose of isolating the adapter plate and its data logger from the rim. The adapter plate also had four threaded studs for attaching the data acquisition housing.

Figure 5.5 shows the instrumented rim with modified tire valve electrical cables and adapter plate. The assembled smart tire revision 1 prototype is shown in Figure 5.6. The complete prototype except for the data acquisition box appears in Figure 5.6a. The prototype smart tire revision 1 was put on the test vehicle first; then the data acquisition box was attached to the prototype. This installation order was necessary because the data acquisition box blocked access to the wheel lug nuts used to secure the smart tire to the vehicle. The base of the data acquisition housing is shown in Figure 5.6b at its attachment location.



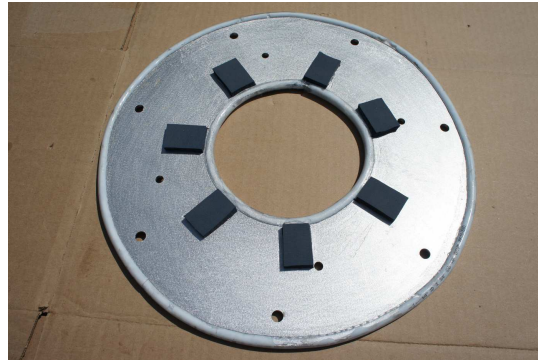


Figure 5.4 – Back of Adapter Plate

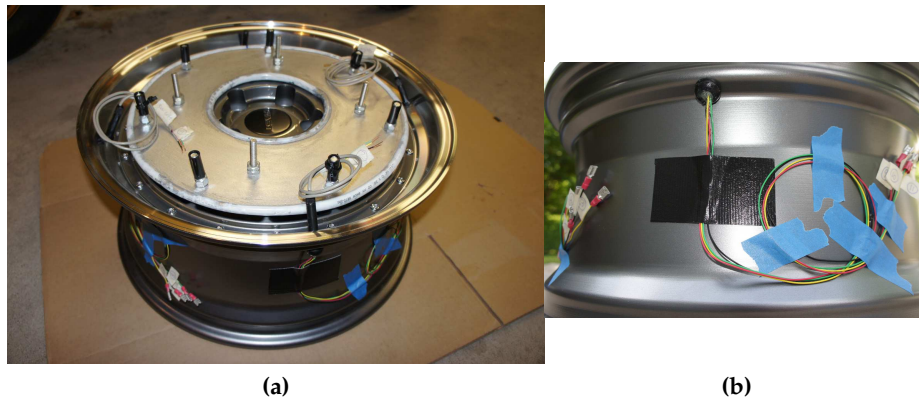


Figure 5.5 – Instrumented Rim with Modified Tire Valves and Adapter Plate: (a) Oblique View (b) Detail of Electrical Cable

When fabrication of smart tire revision 1 was complete, the function of the piezoelectric sensors was tested in the laboratory, since it was possible that they could have been damaged during the tire mounting process. The confirmation test simply involved striking the smart tire with a construction hammer at a tread location in the radial direction and recording the output signals from the piezoelectric sensors. This test confirmed that all of the sensors survived the tire mounting process, as all of them had reasonable responses to the hammer strike. However, one of the sensors, the sidewall left radial sensor, had very low output voltage levels, and therefore the data from this sensor were not used in all of the post-processing procedures. The sensor responses due to the hammer strike are shown in Figure 5.7.

One important note regarding smart tire revision 1 is that it did not have a dedicated angular position sensor, even though this was a known requirement based on previous work using the tire FEM. In smart tire revision 1, estimates of wheel position were made



Figure 5.6 – Smart Tire Prototype Revision 1: (a) Without Data Acquisition Box (b) With Bottom Part of Data Acquisition Box Housing

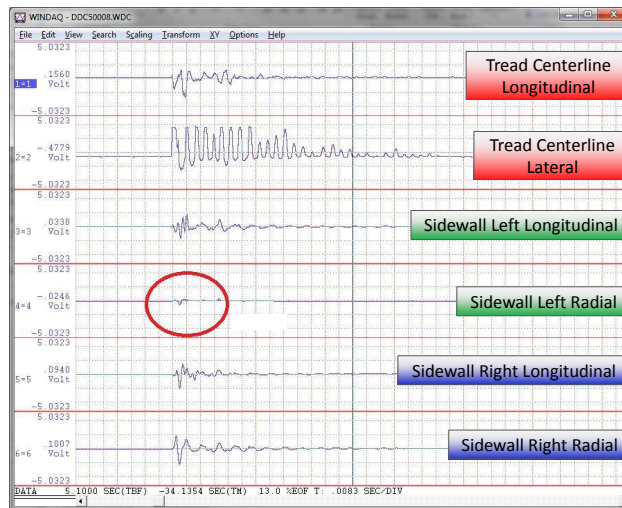


Figure 5.7 – Piezoelectric Sensor Voltage versus Time for Smart Tire Revision 1 in Hammer Strike

based on the wheel angular velocity data available from the vehicle anti-lock braking system. Wheel angular position was not available from the ABS system.

### 5.2.2 Electromagnetic Field Interference Test

The research vehicle used to test the smart tire prototypes was itself a prototype, not a production vehicle. The vehicle was a series drive electric vehicle based on a modified 2011 Chevrolet Equinox. This was a four door sport utility vehicle with the 18" wheel option. The vehicle was fitted with the same tires as the smart tire, with respect to make,

## CHAPTER 5. SMART TIRE PROTOTYPING AND TESTING

---

model, size and mileage (see Table A.3 for details). Therefore, there was consistency at all four corners of the vehicle with respect to its tires.

The Equinox electric drive system consisted of a DC battery pack connected to four power inverters; the inverters were linked to four three-phase Alternating Current (AC) electric corner motors. The input voltage was 360 VDC. The vehicle could be operated in four wheel drive mode or rear wheel drive mode. In the four wheel drive case, the highest possible power output was  $4 \times 85$  kW, but in practical four wheel drive usage,  $4 \times 25$  kW was typical. The most frequently used drive scenario was rear wheel drive, with  $2 \times 50$  kW being the power condition.

Since the research vehicle was known to produce significant electromagnetic fields, an electromagnetic field (EMF) interference test was performed to quantify the effect that these fields would have on the piezoelectric sensors. Since the sensors were located in-tire, they could possibly be deformed (effectively pre-loaded) by the vehicle's own electromagnetic field, even in the absence of tire mechanical deformation. To study this possibility, an in-laboratory test was designed, the setup for which is shown in Figure 5.8.

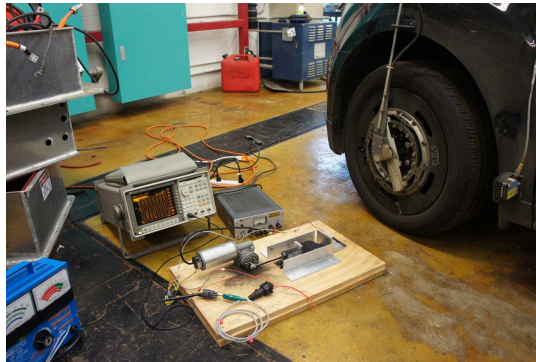


**Figure 5.8 – Test Setup for EMF Interference Test**

In the EMF interference test the vehicle was parked and stationary. The durability bench testing machine was used, along with a tire samples that was fabricated for the EMF interference test. The bench test was operated at its usual 4 Hz during all of the tests. The entire smart tire measurement chain was tested, including custom electric cables, except for the data acquisition box. The test setup was physically close to the front left tire of the electric vehicle, such that the tire sample and its piezoelectric sensor were subjected to the vehicle's electromagnetic field. Three vehicle stationary operating conditions were tested, enumerated below, along with their resulting effect on the averaged piezoelectric sensor maximum voltage level.

1. Off: Baseline
2. Idle: +24%
3. Brake Torque: +15%

In the off condition, the vehicle batteries were disconnected. In the idle condition, the vehicle was on and ready to move, although it was still motionless. In the brake torque condition, the accelerator pedal was in the maximum position, as was the brake pedal at the same time. The vehicle remained stationary in this condition since the brakes were more powerful than the electric motors, which was true of the research vehicle and every other (safe to operate) vehicle. In all test conditions the durability bench testing machine was operating, including when testing the off condition, which was used as the baseline. Two data sets were collected for each test condition.

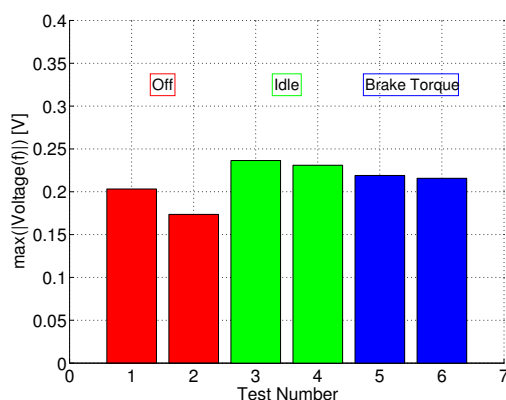


Figure 5.9 – Maximum Voltage versus Test Number in EMF Interference Test

A review of the time histories collected during the EMF interference test shows that the shape of the signals output from the piezoelectric sensor did not change with the different vehicle conditions tested. The waveforms were similar and did not exhibit obvious noise when the vehicle was on. However, the maximum voltage levels increased in the idle and brake torque vehicle operating conditions, as shown in Figure 5.9. Idle voltage levels were higher than brake torque levels, and both were higher than off levels. These results were consistent with previous (unrelated) EMF interference testing performed by UW employees, who studied the influence of the research vehicle on its own built-in data acquisition systems.

The custom electrical cables were likely to be affected little by the vehicle’s electromagnetic field, due to their spiral wound wires. Therefore, it is probable that the piezoelectric sensor experienced EMF interference during the testing, whereby the additional output voltage from the sensor was a direct result of a strain pre-load created by the vehicle’s electromagnetic field. Due to this undesirable influence, the vehicle was usually used in rear wheel drive mode during smart tire on-road testing, since the electromagnetic field was presumed to be weaker at the front left smart tire location in rear wheel drive mode compared to the four wheel drive scenario. In a few cases, the vehicle was operated in four wheel drive mode in order to generate and measure drive torques at the front wheels.

In these cases, the four wheel drive mode of operation is noted, although no attempt was made to compensate for the EMF interference in the sensor output.

### 5.2.3 On-Road Test Overview and Results

Piezoelectric sensor data collected from smart tire revision 1 were not used to draw overall conclusions about smart tire feasibility. Instead, data from smart tire revision 1 were analyzed in order to identify improvements to the STSS that could be implemented in smart tire revision 2. Therefore, test results from smart tire revision 1 are reported here in order to chronicle the process used to design smart tire revision 2.

#### 5.2.3.1 Vehicle Test Setup for Revision 1

**Research Vehicle.** A photograph of the research vehicle with smart tire revision 1 on a summer of 2014 test day appears in Figure 5.10. Images showing the front corners of the vehicle appear in Figure 5.11. Smart tire revision 1 was located at the left front corner. A Michigan Scientific 6-axis wheel load transducer was installed at the right front corner. The wheel load transducer was capable of measuring all six tire forces developed at the right front wheel center, including three forces and three moments.



Figure 5.10 – On-Road Test of Smart Tire Revision 1

**Data Acquisition Systems.** The data from the wheel load transducer, and also the vehicle's own ABS wheel angular velocity signals, were recorded using a research data acquisition system that was installed in the vehicle. This dSPACE system had a standard sampling frequency of 200 Hz, which was acceptable considering the manner in which the tire force data were averaged over complete wheel revolutions in the smart tire research



**Figure 5.11 – Research Vehicle Front Corners: (a) Left Front with Smart Tire Revision 1 (b) Right Front with Wheel Load Transducer**

project. The vehicle data acquisition sampling rate was much slower than the target sampling rate for the piezoelectric sensor data from the smart tire, which was set at 2000 Hz, given the planned road and wheel angular speeds and the need for unaliased deformation data. The sensor data could be downsampled if necessary.



**Figure 5.12 – Smart Tire Data Acquisition Box**

The smart tire data acquisition system without its top cover is shown in Figure 5.12. The main components were the data logger (beige color) and a battery (black color). The design, maintenance and operation of the data acquisition system was assigned to an independent contributor, which made this system one of the few aspects of the research project that was outside of the control of the author. In the on-road vehicle testing, the data acquisition system had three major problems.

1. Data Clipping of Piezoelectric Sensor Measurements at +/- 4V
2. Incorrect Sampling Frequency of 2057.143 Hz

### 3. Smart Tire Data Acquisition System Not Synchronized With Vehicle Data Acquisition System

Of these three problems, the only one that was rectified was the data clipping issue. The input voltage range to the data logger was increased to + / - 10V for the smart tire revision 2 testing, which was sufficient to record the piezoelectric sensor output in all of the vehicle tests without clipping. No support was provided for resolving the other issues, however. The very strange sampling rate required resampling and interpolation of the data using MATLAB, in order to create data with a 2000 Hz sampling rate and a consistent time step of 0.0005 s, required for other subsequent signal processing procedures.

More serious was the lack of synchronization between the two separate data acquisition systems (smart tire and vehicle), as they were operated independently for each vehicle event. Thus, data acquisition was started at two different times in two different systems with very different sampling rates (2057.143 Hz and 200 Hz) for each event. These time data sets were “lined up” in MATLAB using a peak-picking and lateral shifting procedure that was necessarily approximate and introduced timing errors into the data. For example, timing inconsistencies were introduced between the in-tire sensor data and the wheel speeds from the vehicle ABS system. Both data acquisition systems should have recorded some type of event marker in order to determine the proper time relationship between the systems.

**Test Events.** On-road vehicle test events were performed with the goal of developing a range of forces in the tires. The tests were performed at one tire pressure of 220 kPa (32 psi) and one dry road, high friction condition. Tire pressures at all four tires were measured and adjusted before the tests and measured again at the end of the tests, to confirm that air pressures were maintained throughout the tests. The following events were performed during every smart tire vehicle test session. These are standard vehicle dynamics events. In the pure lateral slip events, “low-G” steering refers to a normal cornering state associated with low vehicle lateral acceleration, especially in comparison with the high vehicle lateral acceleration levels that arise during emergency steering maneuvers.

- Pure longitudinal slip, straight line acceleration, 10 to 50 KPH.
- Pure longitudinal slip, straight line braking, 50 to 0 KPH.
- Pure lateral slip, low-G steering (throttle off, coasting), 20 KPH, left direction.
- Pure lateral slip, low-G steering (throttle off, coasting), 20 KPH, right direction.
- Combined slip, braking in a turn (turn initiated before brake application), 20 KPH, left direction.
- Combined slip, braking in a turn (turn initiated before brake application), 20 KPH, right direction.

**Physical Prototype System.** Similar to the analysis of virtual strain, the physical parking lot tests as designed had a reduced set of STSS outputs. The virtual prototype system had three outputs as listed in Table 4.1. The physical prototype system had four outputs as listed in Table 5.1. The difference was the vertical force, which varied in the parking lot tests due to vehicle weight transfer in the events, both from front-to-rear pitching motions and side-to-side rolling motions. In the physical prototype system there were two outputs – the friction coefficient and air inflation pressure – that were fixed to constant values. The remaining output variables including the longitudinal force, lateral force, vertical force and aligning moment were calculated by the STSS. Note that the vehicle speeds varied in the physical tests from 0 to 50 KPH, unlike in the tire FEM simulations in which the translational wheel speed was fixed to a steady 60 KPH.

**Table 5.1 – Complete System and Physical Prototype System Outputs**

Complete System Output	Physical Prototype System Output?
$F_x$	Yes
$F_y$	Yes
$F_z$	Yes (New)
$\mu$	No (Fixed to c. 0.9)
$p$	No (Fixed to 220 kPa)
$M_z$	Yes

**Parking Lot Tests.** Eleven vehicle parking lot events were performed using smart tire revision 1. These tests are described in Table 5.2, along with the number of complete wheel revolutions recorded during each event. In the vehicle turning tests, steering wheel angle is abbreviated as “SWA”. Each complete wheel revolution was a single sample from the perspective of the neural networks. Whether each test was used as a training event or a testing event with the neural networks varied. The total number of complete samples from the smart tire revision 1 parking lot tests was 390. The time required to perform the on-road vehicle testing described in Table 5.2 was half a day.

### 5.2.3.2 Raw and Filtered Time Domain Data

**Raw Time Data.** Raw piezoelectric sensor time histories from smart tire revision 1 appear in Figure 5.13. The voltage data were recorded in hard straight line acceleration test number 3. The scales are the same in all of the plots. Evidence of data clipping by the smart tire data acquisition system is obvious in the measurements, where the data are cut off abruptly above +4V and below -4V. Since this was a straight line acceleration test, data from the left and right sidewalls should be similar. A comparison of the sidewall radial data from left and right sidewalls shows that the sidewall left radial sensor had low output levels, confirming the laboratory hammer test results. Each sinusoidal-like



**Table 5.2 – UW Parking Lot Tests for Smart Tire Revision 1**

<b>Test No.</b>	<b>Number of Complete Wheel Revolutions / Samples</b>	<b>Test Description</b>
1	41	Straight Line Acceleration, 10 to 40 KPH, Light
2	41	Straight Line Acceleration, 10 to 40 KPH, Moderate
3	41	Straight Line Acceleration, 10 to 40 KPH, Hard
4	43	Straight Line Braking, 40 to 0 KPH, Light
5	20	Straight Line Braking, 40 to 0 KPH, Hard
6	44	Step Steer, SWA = 180°, Coasting 30 KPH, Left Direction, Some Combined Steering and Braking at End of Test Record
7	N/A	Aborted Test Due to Parking Lot Collision Avoidance
8	52	Step Steer, SWA = 180°, Coasting 30 KPH, Left Direction
9	32	Braking in a Turn, SWA = 180°, 30 KPH, Left Direction
10	28	Braking in a Turn, SWA = 180°, 30 KPH, Right Direction
11	48	Step Steer, SWA = 180°, Coasting 30 KPH, Right Direction
<b>TOTAL</b>	<b>390</b>	

## CHAPTER 5. SMART TIRE PROTOTYPING AND TESTING

---

period in the sensor data, with one peak and one valley, represented one complete wheel revolution. Therefore, peaks and valleys could be counted to determine the number of wheel revolutions experienced by the piezoelectric sensors during each test.

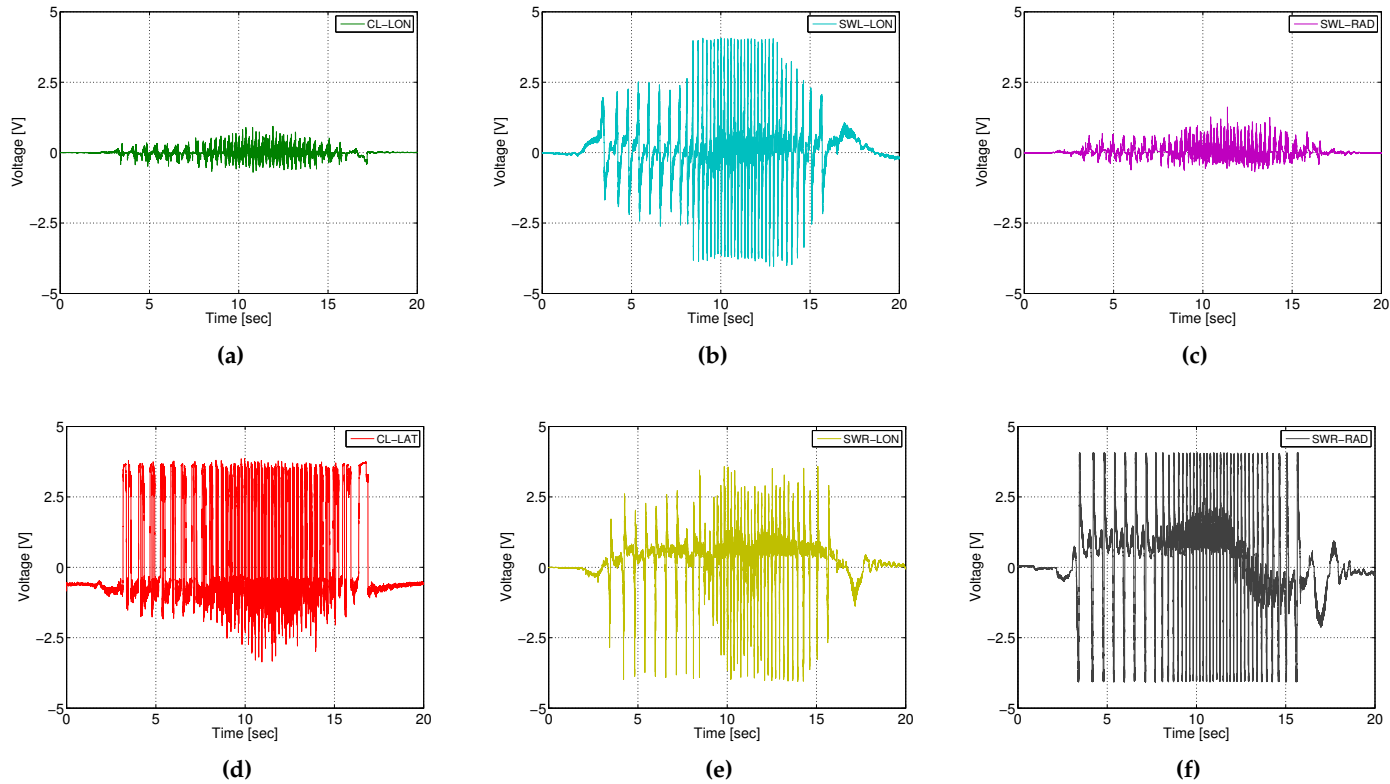


**Figure 5.13 – Piezoelectric Sensor Output in Hard Straight Line Acceleration Test No. 3 From Smart Tire Revision 1: (a) Tread Centerline Longitudinal (b) Sidewall Left Longitudinal (c) Sidewall Left Radial (d) Tread Centerline Lateral (e) Sidewall Right Longitudinal (f) Sidewall Right Radial**

**Vibration in Time Data.** A significant vibration was identified in the raw time data output from the piezoelectric sensors. This vibration is well illustrated by looking at the sensor output data in hard straight line braking test number 5 from smart tire revision 1. The nature of test number 5 from an overall vehicle perspective can be determined from reviewing some vehicle sensor output. Figure 5.14a shows the vehicle center of gravity (CG) acceleration measurement during hard straight line braking test number 5. This measurement was the output of an accelerometer located inside the vehicle at its estimated CG location, on the vehicle centerline just behind the front seats. The vehicle CG accelerometer was recorded using the vehicle data acquisition system.

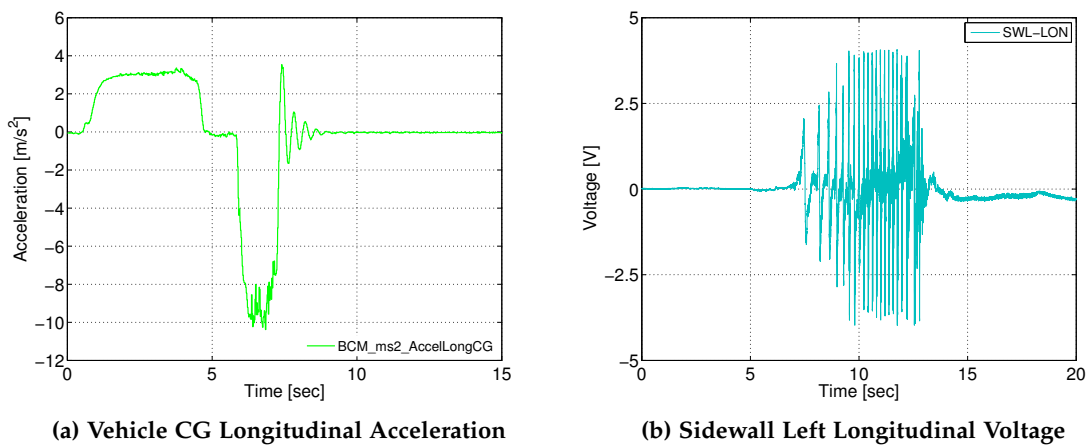
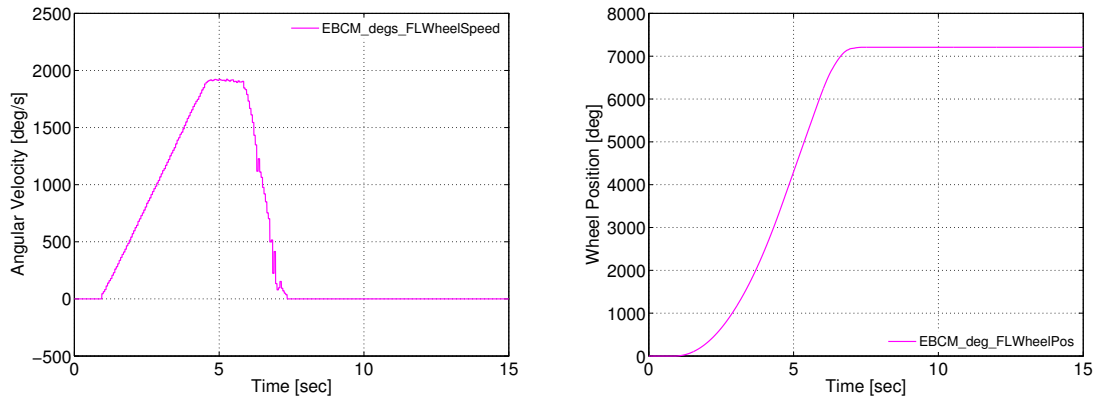


**Figure 5.14 – Sensor Output in Hard Straight Line Braking Test No. 5 From Smart Tire Revision 1**

The hard straight line braking event had three main parts, shown in Figure 5.14a. First, there was a positive acceleration section of around  $3 \frac{m}{s^2}$  in which the vehicle was increasing in speed. Second, there was a short section of zero acceleration in which the vehicle was maintaining a steady speed (of approximately 40 KPH). Third, there was a large negative acceleration section in which the vehicle was braking and decreasing in speed. It can be seen that this was a very hard braking event, as the peak braking acceleration was about  $-10 \frac{m}{s^2}$  (-1 G). The piezoelectric sensor output from the sidewall left longitudinal sensor, shown in Figure 5.14b, was recorded using the smart tire data acquisition system and therefore is out of sync with the timeframe of the accelerometer output. It can be seen from Figures 5.14a and 5.14b that the vehicle accelerometer recording started more than five seconds after the start of the piezoelectric sensor recording. Adjustment of the timelines in an attempt to correct this offset was performed using MATLAB.

Figure 5.15 shows the vehicle ABS sensor signals in hard straight line braking test number 5. Figure 5.15a is the measured angular velocity for the front left wheel. Figure 5.15b is the estimated angular position for the front left wheel. The angular position



(a) Measured Front Left Wheel Angular Velocity      (b) Estimated Front Left Wheel Angular Position  
**Figure 5.15 – Vehicle ABS Sensor Output in Hard Straight Line Braking Test No. 5 From Smart Tire Revision 1**

estimate was made using a simple numerical integration technique. The cumulative sum of the angular position increments is plotted in Figure 5.15b.

The vibration of interest can be seen in the time domain piezoelectric signals of Figure 5.16. These data are from the sidewall left longitudinal piezoelectric sensor in hard straight line braking test number 5. The plots show two complete wheel revolutions that are from the acceleration section of the test. The vibration can be clearly seen in the time histories after the first large peak. The vibration occurred in the acceleration and braking sections of the test. Therefore, the vibration was not associated with a vehicle control function such as ABS, since that system would have had an effect only in the braking section of the test and not in the acceleration section.

A frequency domain analysis of the piezoelectric sensor data showed that the frequency of the vibration was 67 Hz. It was consistently at the same frequency for each wheel revolution and therefore independent of wheel speed. A review of the tire modal analysis results, both simulated using FEA and in the physical tests, showed that the longitudinal translational mode of the tire occurred at either 72 Hz (analysis) or 74 Hz (test) at an air inflation pressure of 220 kPa. This longitudinal tire mode was most likely being excited by the longitudinal acceleration and braking forces developed during the hard straight line braking test.

This suspicion was confirmed by a special vehicle test. A straight line rolling test was performed in which the vehicle was pushed by two people at very low / walking speeds. The vehicle was not self-powered. This was to simulate a slow, steady-state rolling condition in which no significant forces were present. In this slow rolling state the modes of the tire should not have been excited. As expected, the piezoelectric sensor data measured in the straight line rolling test did not exhibit the 67 Hz vibration, confirming

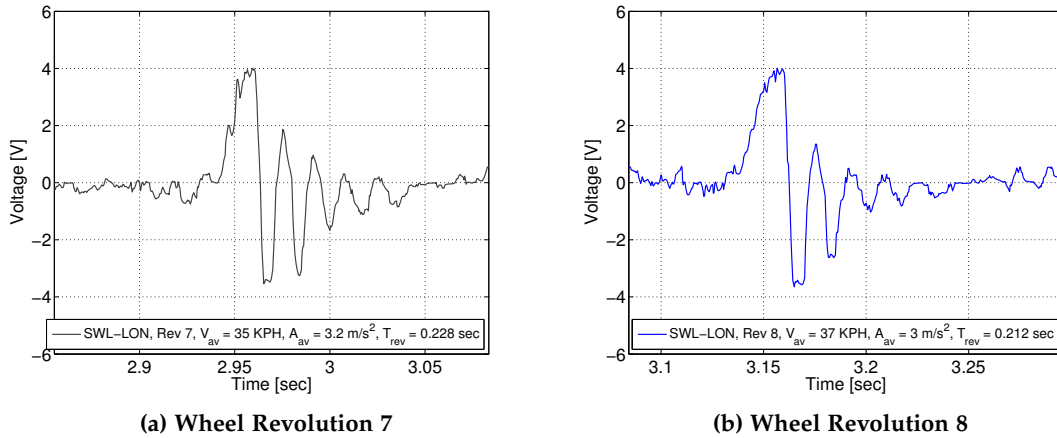


**Figure 5.16 – Sidewall Left Longitudinal Piezoelectric Sensor Output in Hard Straight Line Braking Test No. 5 From Smart Tire Revision 1**

that it was a vibrational mode being excited in the vehicle dynamic tests. Related to this, the reason that the 67 Hz vibration did not appear in the virtual strain measurements as calculated by the tire FEM is that the model was used in static simulations that did not consider the dynamic behavior of the tire.

**Frequency Domain Data.** Piezoelectric deformation data from the sidewall right radial sensor in hard straight line braking test number 5 from smart tire revision 1 appear in Figure 5.17. The data shown are taken from an approximately 40 KPH steady speed section of the test. Figure 5.17a shows the time domain data and Figure 5.17b shows the frequency domain data. Significant frequencies identified in steady speed driving are listed in Table 5.3. The wheel fundamental frequency at this driving speed is 5 Hz, which appears as the first peak in the frequency spectrum. The remaining frequencies are harmonics, up until 36.7 Hz, which is the first vibration mode of the tire, identified in laboratory physical modal analysis testing as occurring at a frequency of 37 Hz.

**Table 5.3 – Significant Response Frequencies in Piezoelectric Sensor Output in Steady Speed 40 KPH Driving**

Peak No.	Frequency [Hz]
1	5.0
2	10.3
3	15.8
4	20.6
5	26.4
6	31.6
7	36.7

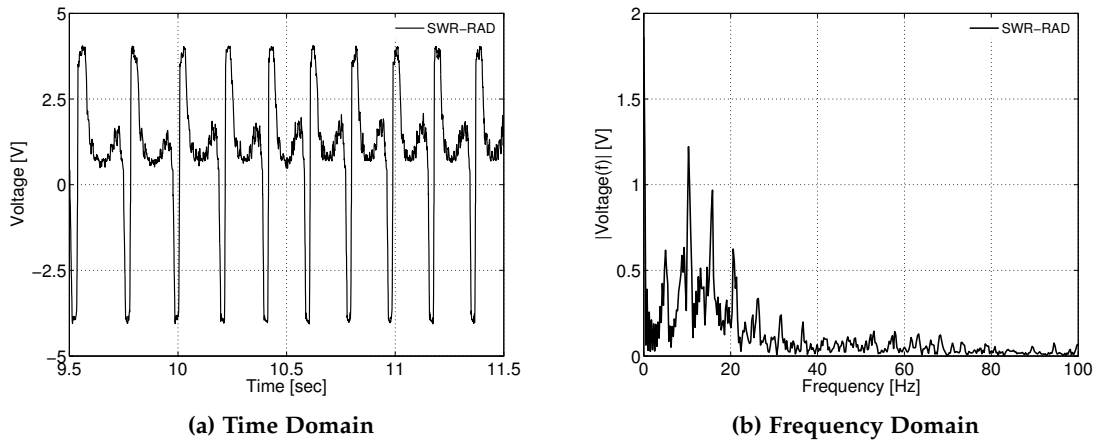


**Figure 5.17 – Sidewall Right Radial Piezoelectric Sensor Output in Steady Speed 40 KPH Driving From Smart Tire Revision 1**

**Filtered Time Data.** Piezoelectric sensor time data were low-pass filtered in order to retain frequencies below the tire modal frequencies and to significantly reduce the influence of frequencies associated with modal activity. A preliminary conventional filter with phase distortion and a cutoff frequency of 35 Hz was designed in MATLAB. The purpose of applying this filter was to remove all tire vibration modes and measurement noise from the test data (see Section C.1.3 for a discussion of tire natural frequencies). Sidewall piezoelectric sensor output with this filter applied appear in Figures 5.18 and 5.19, where approximately four wheel revolutions of the unfiltered and filtered data are shown in each graph.

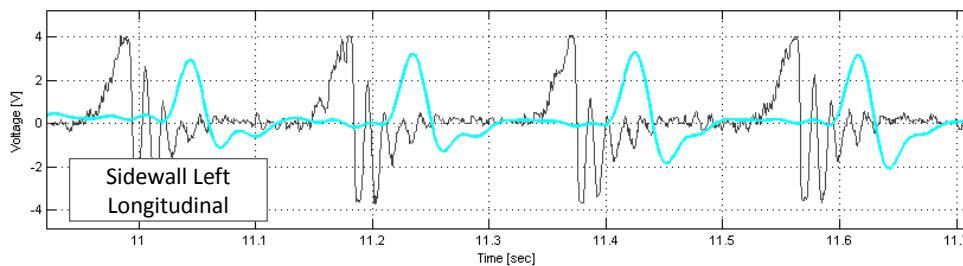


**Figure 5.18 – Filtered Sidewall Left Longitudinal Piezoelectric Sensor Output in Hard Straight Line Braking Test No. 5 From Smart Tire Revision 1**

The filtered piezoelectric sensor data resembled the virtual strain data as calculated by the tire FEM. The sidewall longitudinal piezoelectric sensor measurement was very similar to the analogous strain measurement in the tire FEM, in terms of overall waveform shape. The sidewall radial sensor measurement differed more; the tire FEM predicted

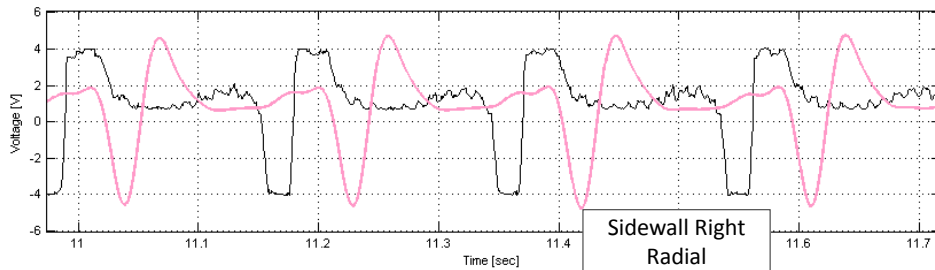


**Figure 5.19 – Filtered Sidewall Right Radial Piezoelectric Sensor Output in Hard Straight Line Braking Test No. 5 From Smart Tire Revision 1**

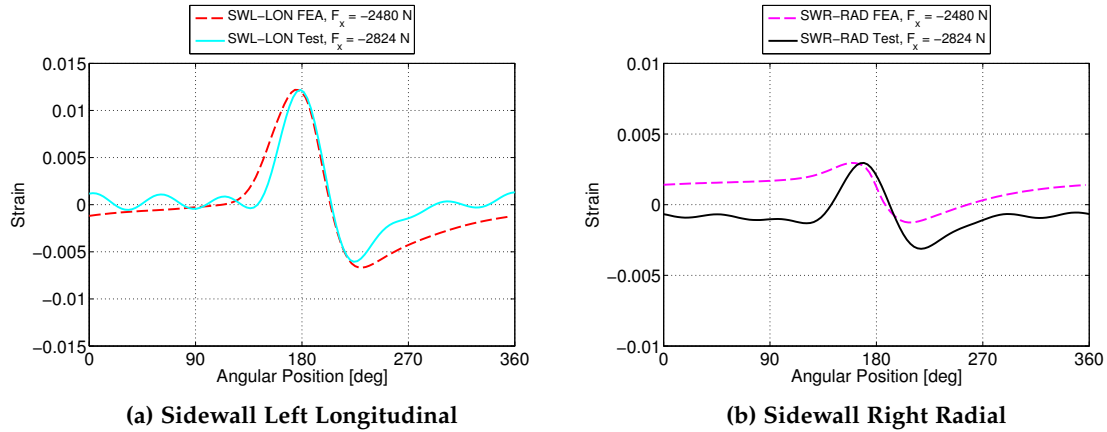
that the sidewall longitudinal strain levels would be higher than the radial strain levels, whereas the opposite was true in the physical test. The sidewall radial sensors may have been in different radial positions in the physical test compared to the tire FEM, as a possible reason for this discrepancy, along with a longer radial sensor length in the test that both strained and bent the radial sensors. Since the piezoelectric sensors in the physical test were sensitive to both straining and bending deformation modes, their output should have been relatively high compared to the tire FEA, where pure radial strain was calculated.

Figure 5.20 shows comparisons between the strain as calculated in the tire FEA (dashed lines) and physically measured “strain” from the piezoelectric sensors (solid lines). Braking strain versus angular position was measured in a pure braking event for both the analysis and the test; brake force levels were around 15% different in the analysis compared to the test. Virtual strain was unmodified, but piezoelectric sensor voltage outputs were modified with a false “calibration” scale factor that compressed the vertical height of the physical waveforms for comparison with the analysis results. The physical sensor peaks were aligned with the analysis peaks, in terms of maximum strain level, when calculating the calibration values. The angular position scales were not modified.

Note that the calibration scale factors used to produce Figures 5.20a and 5.20b were different. Figure 5.20a confirms that the physical sidewall longitudinal piezoelectric sensor measured strain similarly to the tire FEM, except for a ripple with a frequency of approximately 25 Hz (in the filtered measurement). The physical sidewall radial sensor differed more compared to the virtual strain, as seen in Figure 5.20b. The radial curves have similar shapes, but the physical measurement is offset in the direction of negative, compressive strains in comparison to the virtual measurement. Therefore, the longitudinal piezoelectric sensor practically replicated the pure longitudinal strain measurement in the tire FEM, but the radial sensor made a comparatively different measurement, probably due to its sensitivity to combined strain and bending in the physical test.

A second low-pass filter was designed in MATLAB that was used in all of the smart tire data processing. The cutoff frequency was still 35 Hz; however, this was a 7<sup>th</sup> order





**Figure 5.20 – Sidewall Strain in Hard Straight Line Braking Test No. 5 From Smart Tire Revision 1 for Wheel Revolution 17**

zero-phase (i.e. no time delay) elliptic filter. The frequency response of this filter is plotted in Figure 5.21. The piezoelectric sensor output from the sidewall left longitudinal sensor in hard straight line acceleration test number 3 is shown in Figure 5.22, for both the original and the filtered data. The filter was effective at smoothing the raw data, as seen in the plots.

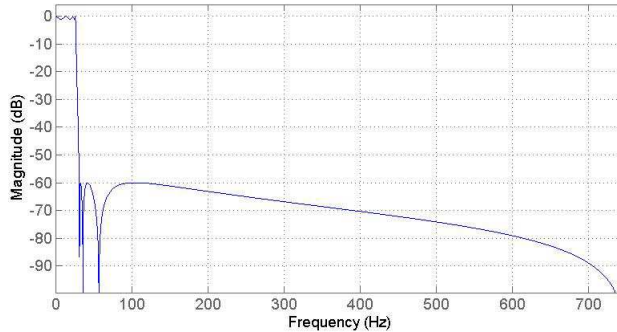


**Figure 5.21 – Elliptic Filter Frequency Response**

Raw data were processed into the three-dimensional form shown in Figure 5.22 for subsequent use in the neural networks. In these plots the wheel revolution number is plotted on the X-axis, the angular position of the wheel is plotted on the Y-axis and the piezoelectric sensor output voltage is plotted on the Z-axis. Each wheel revolution contained 120 evenly distributed piezoelectric sensor samples at each measurement location, which was the same amount of data resolution in reference to angular position compared to the tire FEM. By processing the piezoelectric sensor data with respect to angular po-

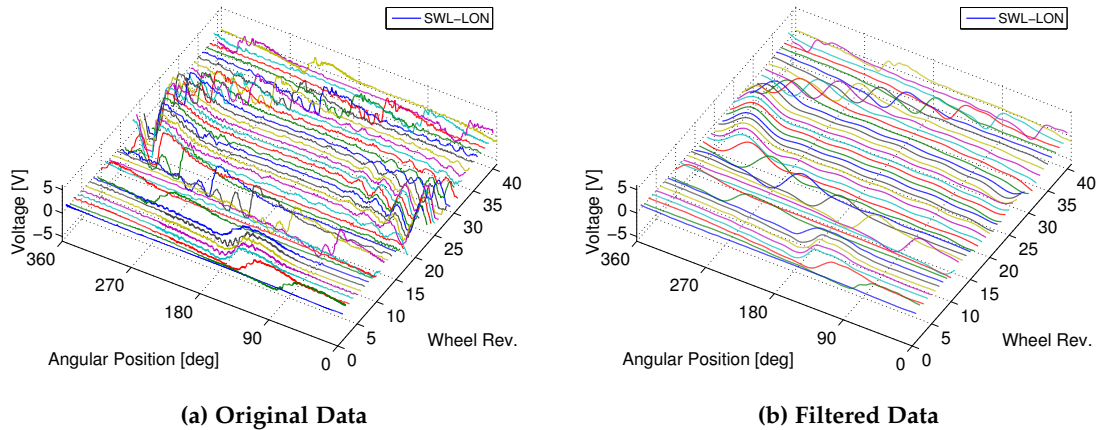


**Figure 5.22 – Sidewall Left Longitudinal Piezoelectric Sensor Output in Hard Straight Line Acceleration Test No. 3 From Smart Tire Revision 1**

sition rather than time, the explicit time dependence of the problem is taken away, and the problem is effectively analyzed in the order domain. This is equivalent to the way in which the tire FEM was analyzed, as the static simulations that were performed produced virtual strain measurements with respect to angular position, not time.

### 5.2.3.3 Neural Network Data Analysis

All of the data from the smart tire revision 1 on-road vehicle tests were processed into the forms required for training and testing of the neural networks. This included the data from all six piezoelectric sensors. Based on the tire FEA results, only two sensors should be required in the STSS, located in the left (outside) sidewall. Six sensors were used in the physical tests, however, both to confirm the tire FEA results and also to provide some redundancy, in case of a sensor failure.

**Step Steer Left.** Piezoelectric sensor data from smart tire revision 1 appear in Figure 5.23. These data were recorded in step steer left test number 8. As shown in Figure 5.23c, the sidewall left radial sensor was poor, producing very low voltage levels. Therefore, the sidewall right sensors, both longitudinal and radial, were used in the neural networks when they were trained on one of the sidewall pairs. The voltage levels from the tread centerline longitudinal sensor, as shown in Figure 5.23a, were also low, although it is unclear if this was due to a sensor malfunction, or if the levels from this sensor were low due to the high longitudinal stiffness (and associated low deformation) of the tread area.

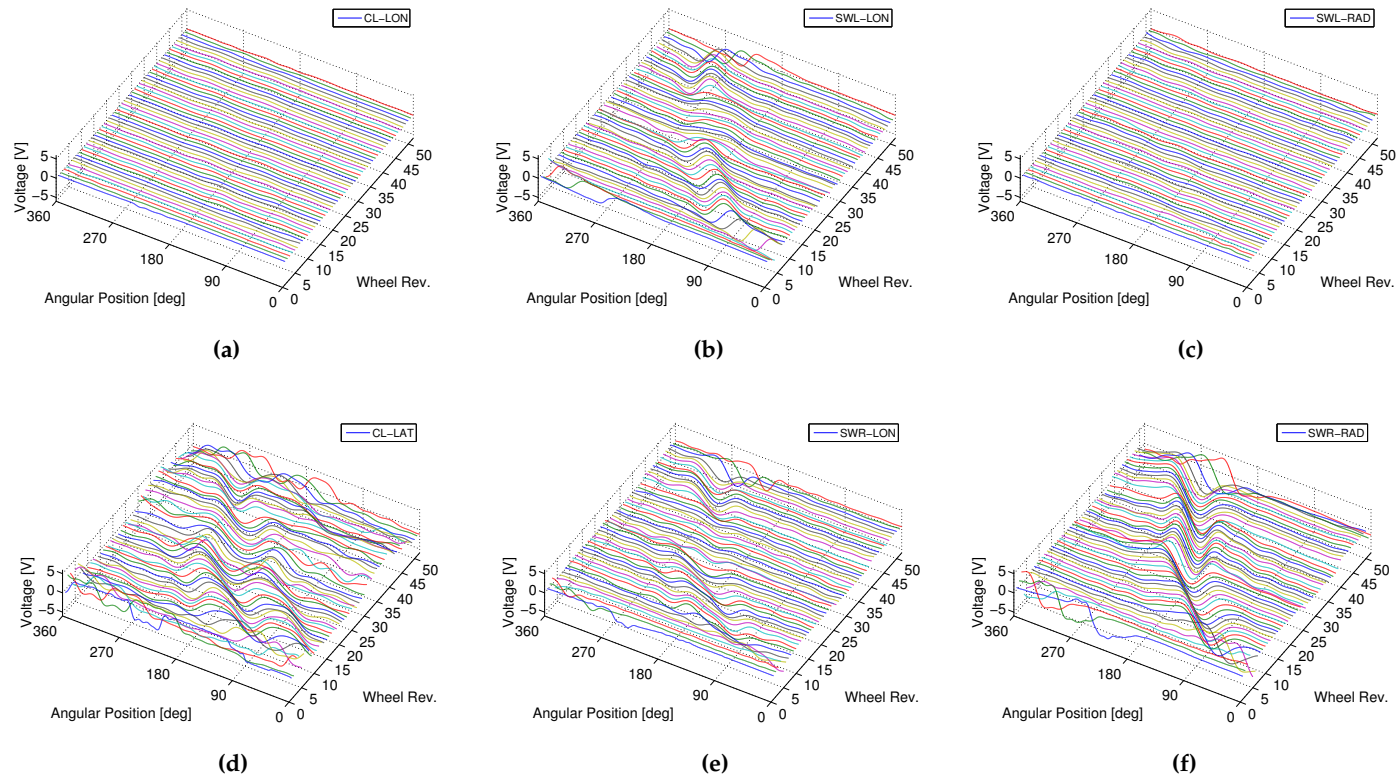


**Figure 5.23 – Piezoelectric Sensor Data Surfaces in Step Steer Left Test No. 8 From Smart Tire Revision 1: (a) Tread Centerline Longitudinal (b) Sidewall Left Longitudinal (c) Sidewall Left Radial (d) Tread Centerline Lateral (e) Sidewall Right Longitudinal (f) Sidewall Right Radial**

The tire force signals from the right front wheel load transducer are shown in Figure 5.24 for step steer left test number 8. Three tire forces and one tire moment are shown. The large changes in lateral force and aligning moment that occurred during the step steer test can be easily seen in the data surfaces, as a trough or a ridge. A similar depression exists in the vertical force data, which was the result of a side-to-side weight transfer during the step steer test. Longitudinal forces did not change as much during this pure lateral slip test, which was expected, except for the end when the vehicle was braked and stopped.

In general, the tire forces did not vary much over each complete wheel revolution. Therefore, an average tire force was calculated for each wheel revolution. These average forces were used as the targets in the neural networks. Thus, the STSS was designed to estimate the tire forces once per wheel revolution. The voltage output from each piezoelectric deformation sensor was sampled 120 times over one revolution, and these data were mapped to the once per revolution average tire forces. This data configuration was selected for early prototyping. The frequency of the tire force outputs could be increased by sampling the measured tire forces multiple times per revolution and mapping the piezoelectric sensor data to these multiple samples. In this way the STSS could estimate tire forces as they evolve in time over each revolution. However, this approach was not investigated as it would have markedly increased the size of the problem that the neural networks were subjected to.

It is important to note that the target tire forces were measured at the right front tire, whereas the tire deformation was measured using the in-tire piezoelectric sensors in the left front tire. The tire forces should be very similar at the front corners during a pure longitudinal slip test, but they will be somewhat different in a pure lateral slip and a combined slip test. This is illustrated in Figure 5.25, which shows the measured front wheel velocities from the ABS system in two different events. Sections where the front wheel speeds differ are expected to have different front tire forces and moments.

The neural network problem, as applied to the physical test data, was to map the in-tire strain measured in the left front tire to the tire forces developed in the right front tire. This was certainly not an ideal situation, but the most practical approach. The physical tests were designed this way to create an economical smart tire feasibility study. The special rims that were part of the wheel load transducer assemblies were limited production items; the research project could not justify drilling cable pass-through holes and making other modifications that would destroy one. In future STSS development work, however, the wheel load sensor system should be moved to the left front vehicle corner, and the smart tire should be mounted on it. In that case the deformation measured in the left front tire could be used to estimate the left front tire forces.

The average tire force signals from the right front wheel load transducer are shown in Figure 5.26 for step steer left test number 8. These calculated target force levels are an averaged version of the side view, or side projection, of the force surfaces, where the side view is a plot of force versus wheel revolution.

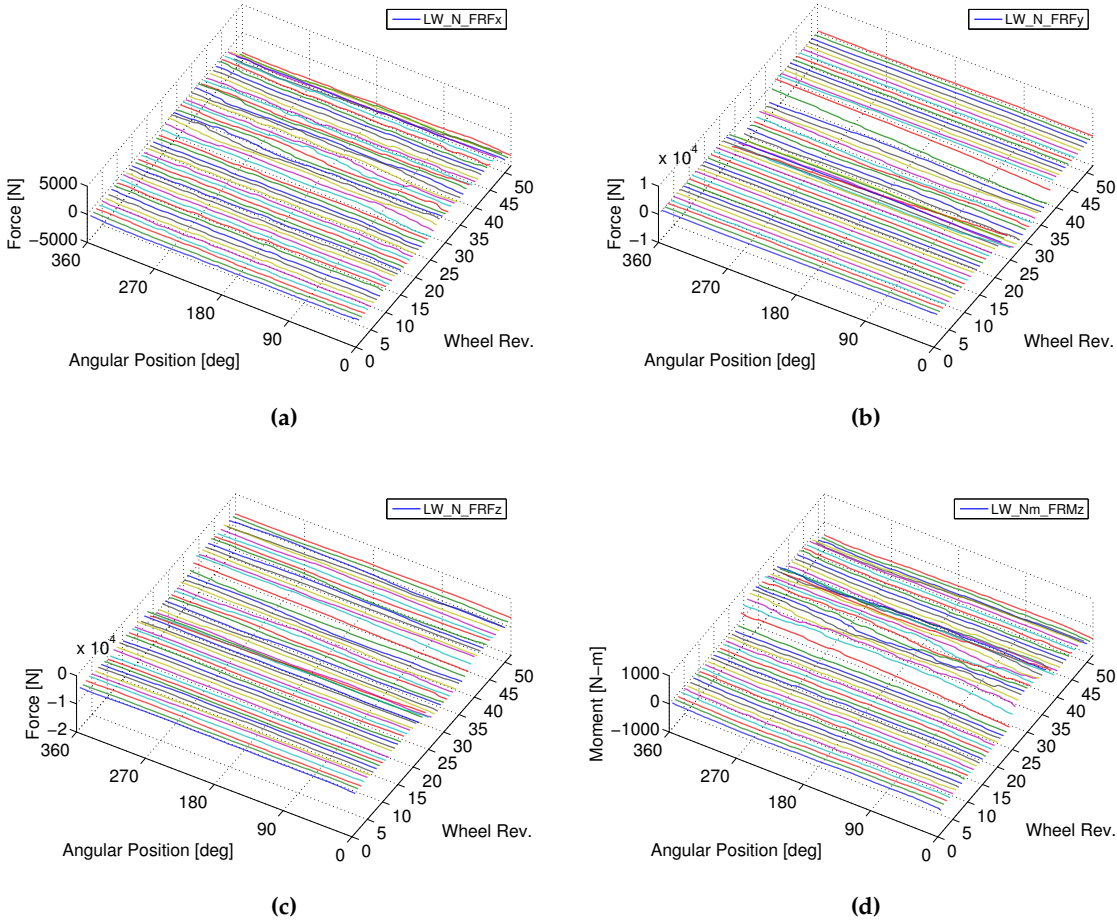
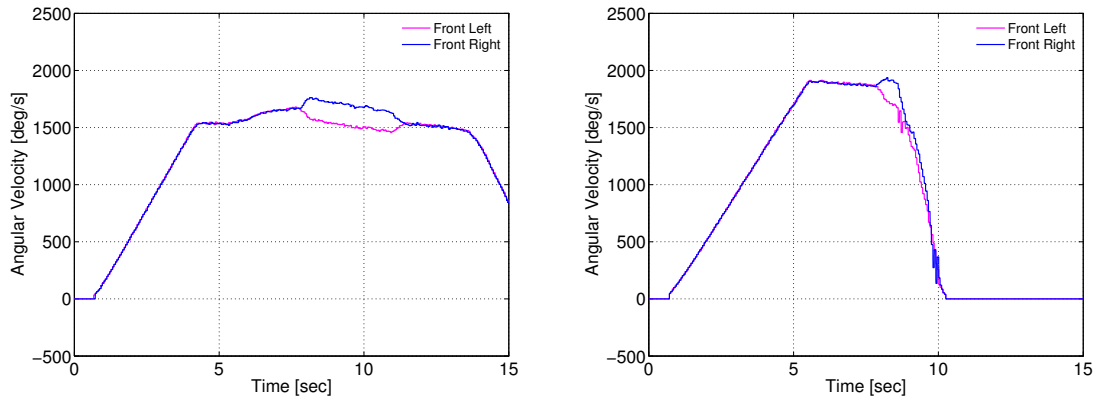


Figure 5.24 – Wheel Load Transducer Data Surfaces in Step Steer Left Test No. 8 From Smart Tire Revision 1: (a) Longitudinal Force (b) Lateral Force (c) Vertical Force (d) Aligning Moment



(a) Pure Slip: Step Steer Left Test No. 8      (b) Combined Slip: Braking in a Turn Left Test No. 9  
**Figure 5.25 – Measured Front Wheel Angular Velocities From Vehicle ABS Sensors in Smart Tire Revision 1**

**Braking in a Turn Left.** Data from braking in a turn left test number 9, a combined slip test, is shown here for comparison with step steer left test number 8, a pure lateral slip test. Piezoelectric sensor data appear in Figure 5.27. The tire force signals are shown in Figure 5.28, and the average tire forces are shown in Figure 5.29. The piezoelectric sensor data exhibit the same trends regarding the bad / low voltage sensors, where the sidewall left radial and the tread centerline longitudinal sensors did not produce useful output. This was true for all the events performed during smart tire revision 1 testing.

A review of the tire force measurements for braking in a turn left test number 9 shows that the combined braking and steering occurred near the end of the test, where all of the forces have their highest absolute magnitudes. All of the data obtained during testing of smart tire revision 1 were processed in the same manner, with data surfaces calculated for piezoelectric sensor output and wheel force transducer output, as well as average forces calculated from the wheel force transducer measurements. The processed data were used to train and test the neural networks.

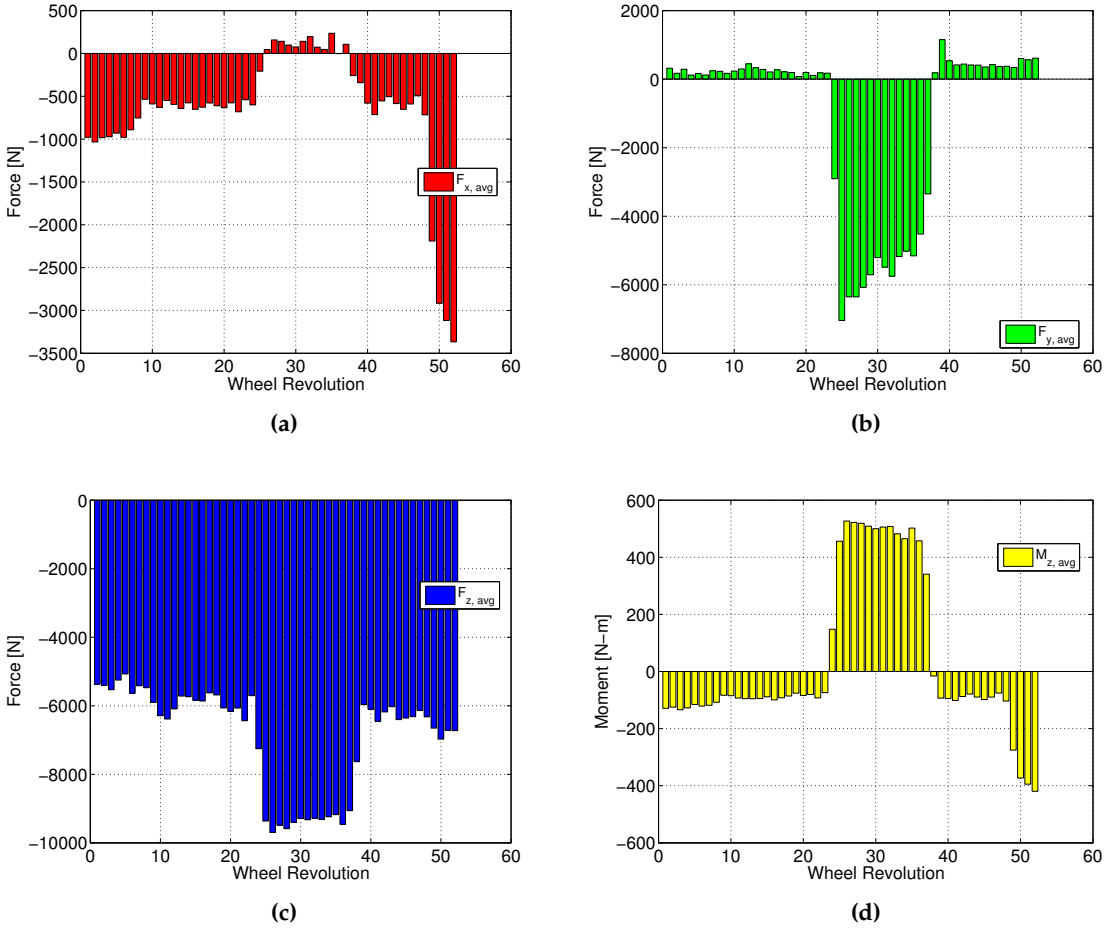
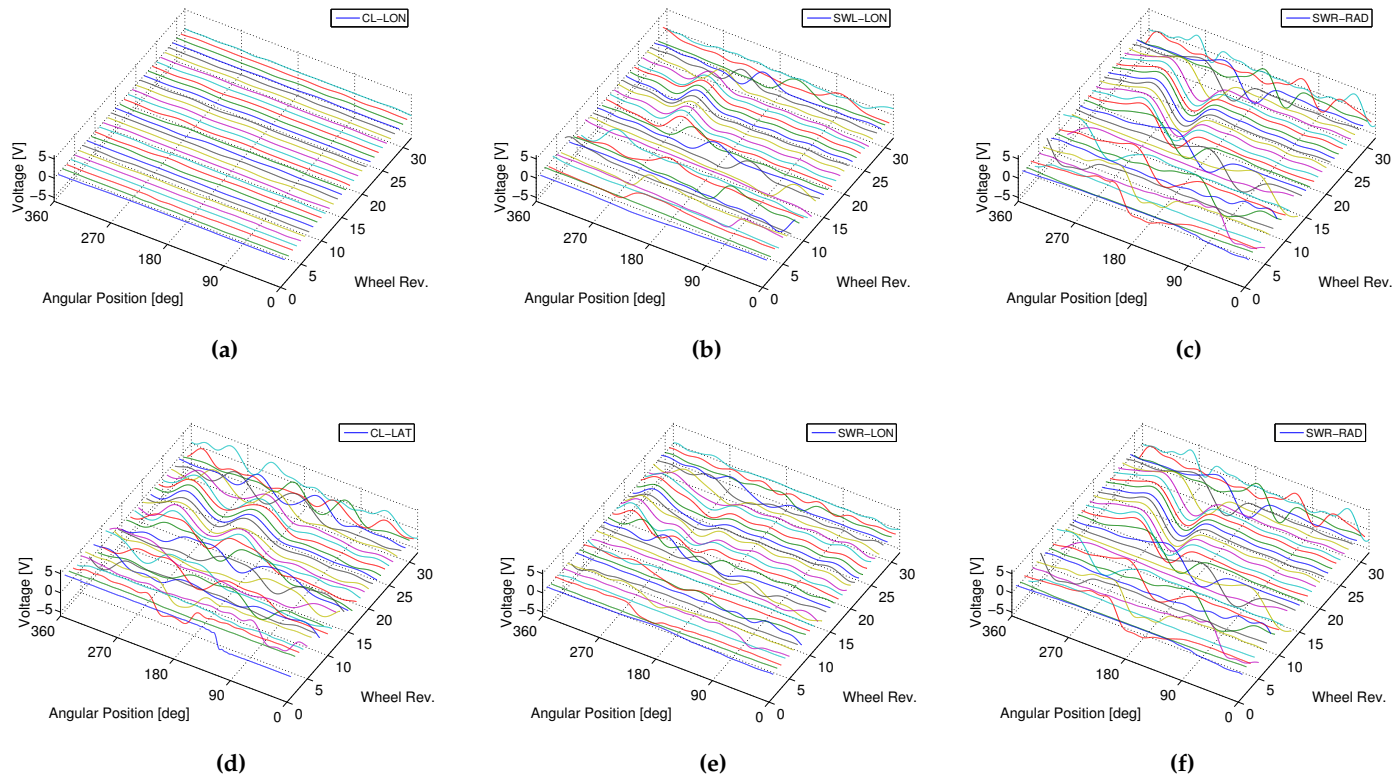


Figure 5.26 – Wheel Load Transducer Averages in Step Steer Left Test No. 8 From Smart Tire Revision 1: (a) Longitudinal Force (b) Lateral Force (c) Vertical Force (d) Aligning Moment



**Figure 5.27 – Piezoelectric Sensor Data Surfaces in Braking in a Turn Left Test No. 9 From Smart Tire Revision 1: (a) Tread Centerline Longitudinal (b) Sidewall Left Longitudinal (c) Sidewall Left Radial (d) Tread Centerline Lateral (e) Sidewall Right Longitudinal (f) Sidewall Right Radial**



**Neural Network Results.** Physical test data from smart tire revision 1 were analyzed using the winning neural network configuration in the virtual strain analysis. This was a radial basis function neural network with the “newrb4” setup; see Table 4.9 for details. In the case of the smart tire revision 1 data set, the following training and testing combination was used.

- *Training Data.* Taken from all “good” parking lot events. Excluded events 6 and 7. Total number of training samples (full wheel revolutions) = 346. Included pure slip and combined slip tests.
- *Testing Data.* Taken from event 6, a mostly pure slip steering event with some combined steering and braking at the end of the test. Total number of testing samples (full wheel revolutions) = 7.

Seven test cases were selected from step steer left test number 6, which had 44 complete wheel revolutions to choose from. The wheel revolution numbers associated with these test cases are listed in Table 5.4. The tire force values for each of the test cases are listed in Table 5.5. Percent change in testing output values, compared to the actual values, were calculated for the neural networks analyzed. Change from actual values for the network trained on all six sensors is shown in Table 5.6; similar results for the network trained on two sidewall right sensors appear on Table 5.7.

**Table 5.4 – Test Cases From Step Steer Left Test No. 6**

Test Case No.	Wheel Revolution No.
1	5
2	10
3	15
4	25
5	30
6	40
7	43

From Tables 5.6 and 5.7 it can be seen that the tire force estimates from smart tire revision 1 did not have acceptable accuracy. The two sensors case (forces within 152%) was better than the six sensors case (forces within 549%), but neither was satisfactory. Similar to the results of the virtual strain processing study, the networks had worse performance when trained on all six sensors compared to when trained on only two sidewall sensors. Additionally, results for the six sensor scenario may have been relatively worse in the physical tests because two of the six sensors were probably malfunctioning. Other neural network trials were attempted, including training the networks on unfiltered piezoelectric sensor data, adding the wheel angular velocity to the training data and training on just one single sidewall right longitudinal sensor, but all of these trials resulted in force estimates that were inaccurate by hundreds of percent.

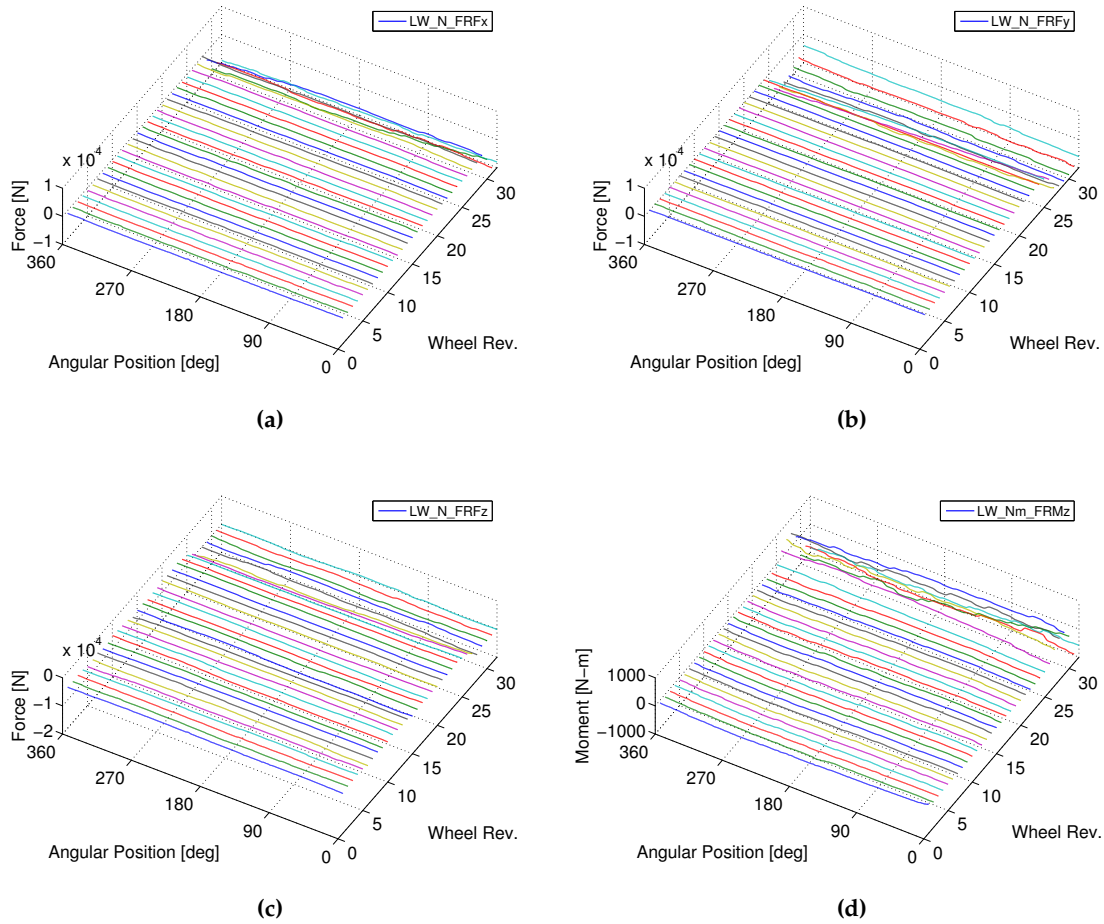


Figure 5.28 – Wheel Load Transducer Data Surfaces in Braking in a Turn Left Test No. 9 From Smart Tire Revision 1: (a) Longitudinal Force (b) Lateral Force (c) Vertical Force (d) Aligning Moment

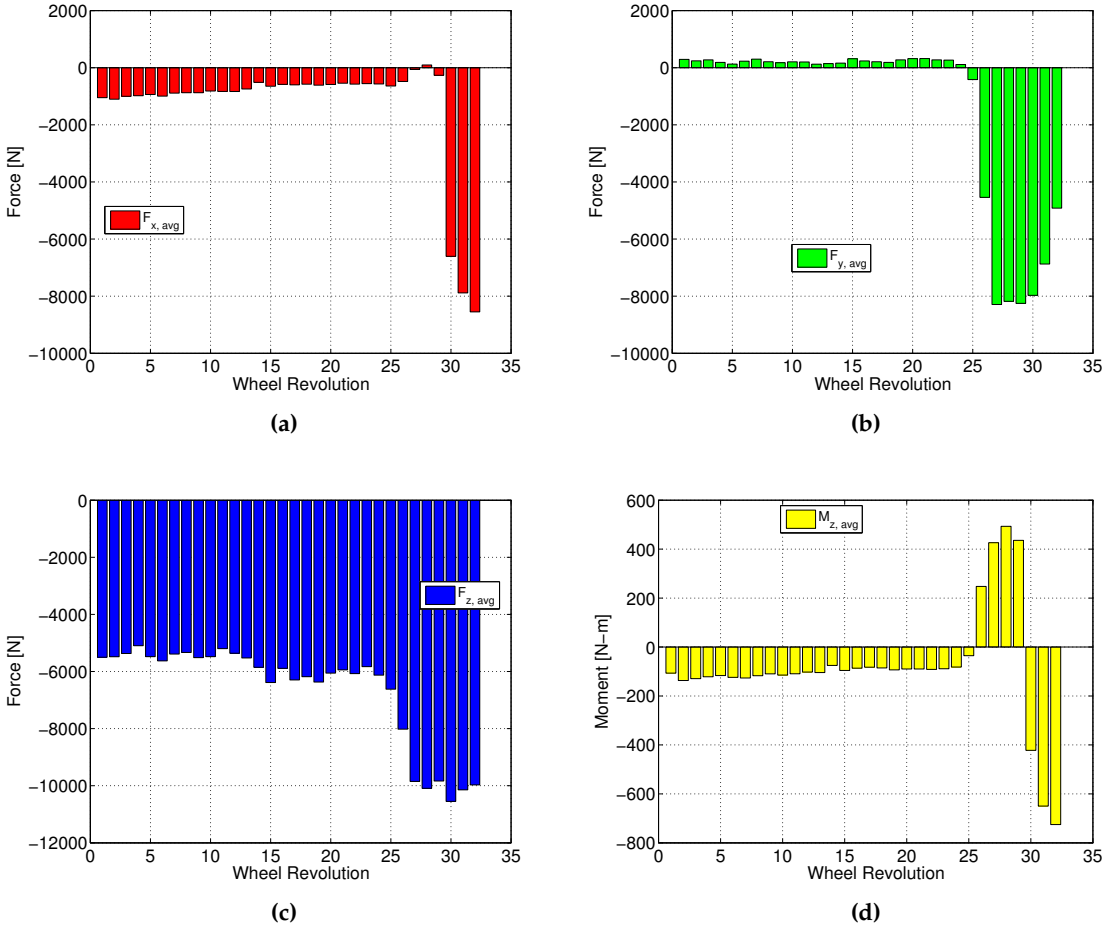


Figure 5.29 – Wheel Load Transducer Averages in Braking in a Turn Left Test No. 9 From Smart Tire Revision 1: (a) Longitudinal Force (b) Lateral Force (c) Vertical Force (d) Aligning Moment

**Table 5.5 – Actual Values for Event 6 Testing Cases**

Case No.	1	2	3
F <sub>x</sub> [N]	-1000	-538	-503
F <sub>y</sub> [N]	278	383	325
F <sub>z</sub> [N]	-5468	-5897	-5826
M <sub>z</sub> [N-m]	-135	-97	-83

---

Case No.	4	5	6	7
F <sub>x</sub> [N]	-292	-258	-868	-2300
F <sub>y</sub> [N]	-2455	-1500	-1433	-898
F <sub>z</sub> [N]	-8394	-8151	-8078	-7689
M <sub>z</sub> [N-m]	200	140	70	-163

**Table 5.6 – Change from Actual Values for 6 Sensors (Within 549%)**

Case No.	1	2	3
Change in F <sub>x</sub> [%]	72	18	-8
Change in F <sub>y</sub> [%]	276	60	9
Change in F <sub>z</sub> [%]	21	13	6
Change in M <sub>z</sub> [%]	69	31	3

---

Case No.	4	5	6	7
Change in F <sub>x</sub> [%]	418	549	243	155
Change in F <sub>y</sub> [%]	177	235	248	337
Change in F <sub>z</sub> [%]	77	80	83	82
Change in M <sub>z</sub> [%]	-37	8	134	202

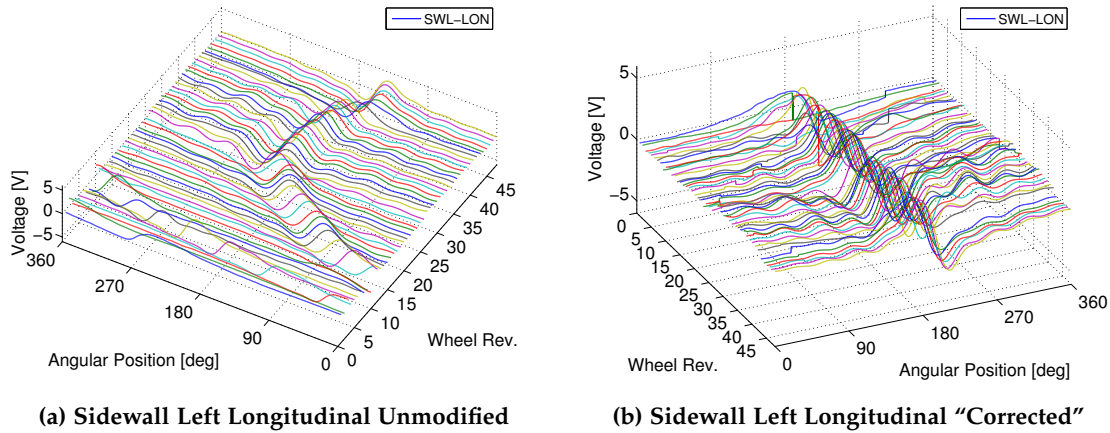
**Table 5.7 – Change from Actual Values for 2 Sensors (Within 152%)**

Case No.	1	2	3
Change in F <sub>x</sub> [%]	11	-77	-40
Change in F <sub>y</sub> [%]	-79	-28	-131
Change in F <sub>z</sub> [%]	3	2	-1
Change in M <sub>z</sub> [%]	2	-36	-27

---

Case No.	4	5	6	7
Change in F <sub>x</sub> [%]	-17	4	77	102
Change in F <sub>y</sub> [%]	-32	115	109	116
Change in F <sub>z</sub> [%]	-4	63	66	69
Change in M <sub>z</sub> [%]	40	-135	-152	97

A review of the piezoelectric sensor data surfaces in Figures 5.23 and 5.27 shows that the lateral position (on the angular position scale) of the waveforms is irregular in the data surfaces. Compared to the virtual strain data surfaces, which had their peaks and valleys of greatest size near the center of the contact patch ( $180^\circ$ ) as expected, the peaks and valleys in the physical deformation data were located over the entire  $360^\circ$  angular position range, depending on the wheel revolution. This indicates that something was wrong with the angular position estimation scheme based on the vehicle ABS wheel speed measurements, since the data processing scheme as implemented should have triggered the data acquisition once for each wheel revolution based on an estimated angular index position.



(a) Sidewall Left Longitudinal Unmodified (b) Sidewall Left Longitudinal "Corrected"  
**Figure 5.30 – Piezoelectric Sensor Data Surfaces in Step Steer Right Test No. 11 From Smart Tire Revision 1**

To illustrate what the data should look like, Figure 5.30 shows the sidewall left longitudinal piezoelectric sensor data surface in step steer right test number 11, along with a manipulated version intended to simulate the expected appearance. To create the "corrected" data surface, the individual wheel revolution curves were shifted to align the peaks with the  $180^\circ$  angular position. In practice, the peaks do not exactly align with the center of the contact patch, but the data have been modified in this way for visualization of their approximately correct appearance. Since a good angular position sensor was a known requirement in the STSS, a dedicated rotary encoder was incorporated into smart tire revision 2. No further investigation of the angular position estimates using the vehicle ABS sensors was attempted.

## 5.3 Smart Tire Revision 2

### 5.3.1 Prototype Fabrication

The smart tire custom rim was reused in smart tire revision 2, but the rest was new compared to revision 1. A new tire was fitted with new piezoelectric sensors in a new layout in smart tire revision 2. This required the dismounting of the revision 1 tire from the rim, since the rim was required in the new revision but the tire was not. Due to the possibility of damage to the tire valve electrical cables during the dismounting process, new cables were fabricated and installed in smart tire revision 2. An additional hole was drilled in the rim to allow for another electrical cable to pass through. The new cable allowed eight sensors to be installed and recorded in smart tire revision 2. There were four pairs of sidewall sensors installed, each set having a longitudinally oriented and a radially oriented sensor.



Figure 5.31 – Instrumented Tire for Smart Tire Revision 2: (a) Inside (b) Outside

Figure 5.31 shows photographs of the instrumented tire used in smart tire revision 2, incorporating views of some of the sidewall sensors. The reference lines drawn and etched into the exterior of the tire can be seen in the images. These reference lines were used to determine where each sensor was located inside the tire relative to the reference lines and each other. Three sensor pairs were bonded to the inside of the tire using the “best” method as determined during durability bench testing; this attachment method was the same as that used in revision 1, as shown in Figure 5.32. One sensor pair was attached using “Amazing Goop” adhesive, to have a different sensor attachment method available for comparison in the on-road vehicle testing. The Amazing Goop sensor pair was not recorded during on-road testing, though, due to limitations in the number of channels that could be recorded in the smart tire data acquisition system.

There were four sensor groups installed in smart tire revision 2, enumerated below, along with an explanation of how they were used. Sketches showing the locations and ori-



**Figure 5.32 – Detail of Sidewall Sensor Pair in Smart Tire Revision 2**

entations of the groups that were recorded, Group 1 and Group 4, appear in Figure 5.33. The recorded groups were located on opposite sidewalls and they were diametrically opposed inside the tire.

1. *Group 1.* At sidewall left “bottom”. Attached using best method. Recorded during testing.
2. *Group 2.* Not used. Destroyed during tire mounting process.
3. *Group 3.* Not recorded. Attached using “Amazing Goop” adhesive.
4. *Group 4.* At sidewall right “top”. Attached using best method. Recorded during testing.

After smart tire revision 2 was completely assembled, piezoelectric sensor outputs for Groups 1 and 4 were tested and confirmed by hitting the tire with a hammer, similar to the sensor confirmation procedure of revision 1. Both of the sensor groups produced the expected output. Figure 5.34 shows sensor output from Group 1 in the hammer tests, for different time histories each with multiple hammer strikes. The time histories were the result of radial direction strikes near the sensors. The sensors clearly exhibit the expected transient response to each hammer excitation event, with an initial peak followed by decaying oscillations. It is possible that the piezoelectric sensors could be used in a modal analysis of the tire, in place of the usual accelerometers.

Figure 5.35 shows the complete smart tire revision 2 as installed on the research vehicle. Smart tire revision 2 had a rotary encoder incorporated into it that included a built-in slip ring function. This device was used to record the angular reference index marked on the tire, in addition to passing the in-tire strain signals via cable to the inside of the vehicle. Table 5.8 lists information about the encoder, leased specifically for the smart tire research project.

The encoder device could measure the once per revolution angular position index in two different ways. The first was by using a tachometer function that had an analog voltage output. The second was by using the encoder function to produce a digital output.

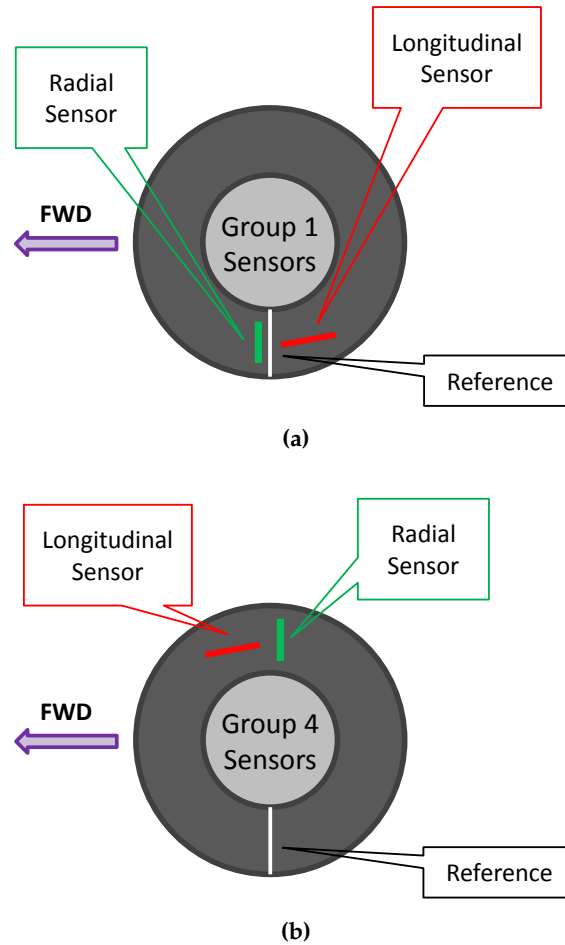


**Figure 5.33 – Location and Orientation of Sensor Groups in Smart Tire Revision 2: (a) Group 1 at Sidewall Left “Bottom” (b) Group 4 at Sidewall Right “Top”**

These two signals are plotted in Figure 5.36 from a laboratory test. The research vehicle was lifted on a hoist such that its wheels were clear of the floor and they could turn freely. The left front wheel was turned by hand in the test. Four complete wheel revolutions can be seen in the recording, which was made using a signal analyzer. In the on-road vehicle tests, the analog voltage signal was recorded only, as the smart tire data logger was suitable for measuring analog signals, not digital signals.

Since the in-tire piezoelectric signals were routed through the slip ring / encoder device, the smart tire data acquisition system was moved inside the research vehicle. Figure 5.37 is a photograph showing the data acquisition equipment inside the vehicle during the on-road testing of smart tire revision 2. The smart tire data acquisition system can be seen on the right, next to the existing vehicle data acquisition system.



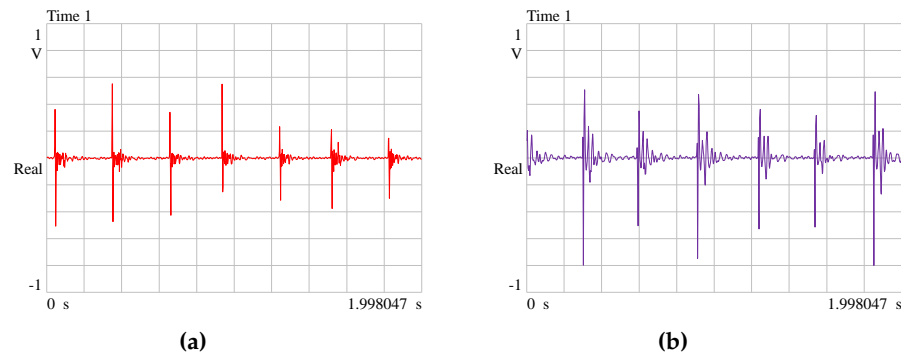


Figure 5.34 – Group 1 Piezoelectric Sensor Voltage versus Time for Smart Tire Revision 2 in Hammer Strikes – Different Time Histories Shown: (a) Longitudinal Sensor (b) Radial Sensor



Figure 5.35 – Smart Tire Prototype Revision 2

## 5.3.2 On-Road Test Overview

### 5.3.2.1 Vehicle Test Setup for Revision 2

**Research Vehicle.** A photograph of the research vehicle with smart tire revision 2 on a spring of 2015 test day appears in Figure 5.38. Images showing the left front corner and right side of the vehicle appear in Figure 5.39. Smart tire revision 2 was located at the left front corner, in the same position as revision 1. The same Michigan Scientific 6-axis wheel load transducer was installed at the right front corner.

**Test Events.** The same test events and conditions were used during the on-road vehicle testing of smart tire revision 2 compared to revision 1. Some additional events were added, however, described below.

- Pure longitudinal slip, straight line driving, 5 KPH.

**Table 5.8 – Rotary Encoder Information**

Manufacturer	Michigan Scientific Corporation
Model	SR/ERT Series Slip Ring & Rotation Sensor
Pulse Count	512
Serial Number	2650

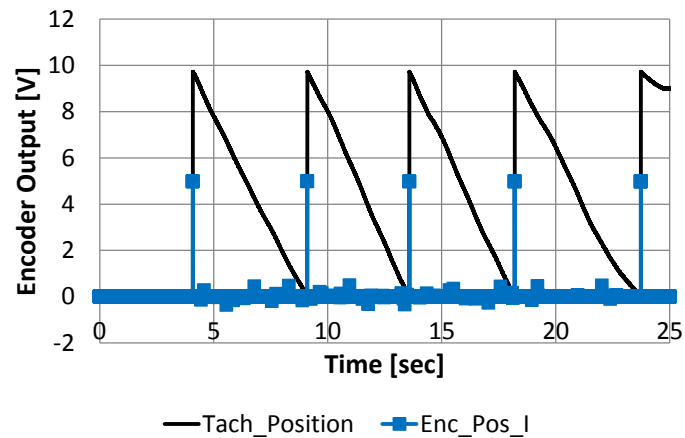


**Figure 5.36 – Encoder Position Index Measurements versus Time**

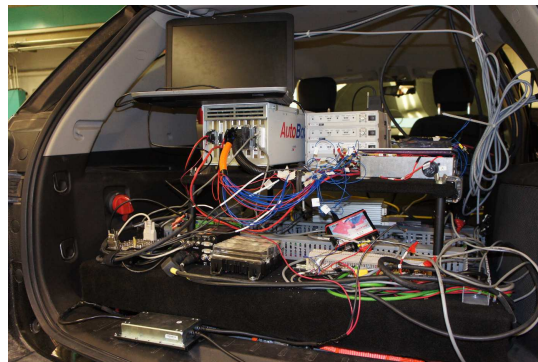


**Figure 5.37 – Inside Data Acquisition Systems for Smart Tire Revision 2**

- Pure longitudinal slip, accelerator pedal punches, 20 KPH.
- Pure longitudinal slip, brake pedal punches, 40 KPH.
- Pure lateral slip, sinusoidal steering (throttle off, coasting), 30 KPH.



Figure 5.38 – On-Road Test of Smart Tire Revision 2



Figure 5.39 – Research Vehicle Views: (a) Left Front Corner with Smart Tire Revision 2 (b) Right Side

**Parking Lot Tests.** Three rounds of vehicle parking lot events were performed using smart tire revision 2. These rounds were conducted on three separate days. An overview of each testing round is listed below. Conclusions about the STSS were based primarily on Round 1 testing results, as Round 2 did not result in useful data, and sensor deterioration had reached unacceptable levels by Round 3. Therefore, data collected for use in the physical deformation processing study were mostly collected during Round 1, but some of the Round 3 data were analyzed for comparison. The thirty-one vehicle parking lot events performed using smart tire revision 2 during Round 1 are summarized in Table 5.9.

1. *Round 1.* Piezoelectric in-tire sensors were recorded using the smart tire data acquisition system with 2057.143 Hz as the sampling frequency. Wheel load transducer signals and the encoder angular position signal were recorded using the vehicle data acquisition system with a sampling frequency of 200 Hz. Technical issues with the smart tire data acquisition system prevented the encoder angular position signal from being recorded properly on it, leaving the slower sampled version of this signal as recorded by the vehicle data acquisition system to be used in the data analysis. Total number of events performed and recorded in Round 1 = 31.
2. *Round 2.* The second round of testing was performed in an attempt to fix issues surrounding the recording of the encoder angular position signal in the smart tire data acquisition system, since it was desirable to record it at a higher sampling frequency. Round 2 was also performed in order to collect more training and testing data for the neural networks, to be added to the Round 1 data. A major malfunction in the smart tire data acquisition system occurred during Round 2, in which the system recorded only a small fraction of the signal time histories at the end of each event. None of the data were useful for post-processing. Total number of events performed and recorded in Round 2 = 34.
3. *Round 3.* The third round of testing was performed in order to address ongoing issues with the smart tire data acquisition system. The vehicle data acquisition system was modified such that its sampling frequency was increased to 2000 Hz, rendering the smart tire system redundant. All of the signals in Round 3 were recorded using the modified vehicle data acquisition system with the higher sample rate. The vehicle drive configuration was four wheel drive, which was unique, as all other vehicle testing was performed in rear wheel drive mode. Recorded data were not very useful due to significant piezoelectric sensor fatigue as evidenced by deteriorated signals compared to Round 1. Total number of events performed and recorded in Round 3 = 35.

**CHAPTER 5. SMART TIRE PROTOTYPING AND TESTING**

---

**Table 5.9 – UW Parking Lot Tests for Smart Tire Revision 2 in Round 1**

Test No.	Number of Complete Wheel Revolutions / Samples	Test Description	Notes
1	36	Straight Line Driving	30 KPH
2	42	Straight Line Driving	30 KPH
3	40	Straight Line Driving	30 KPH
4	43	Straight Line Driving	30 KPH
5	35	Straight Line Driving	Creeping Downhill
6	20	Straight Line Driving	Creeping Uphill
7	44	Straight Line Acceleration	Light
8	36	Straight Line Acceleration	Light
9	38	Straight Line Acceleration	Moderate
10	36	Straight Line Acceleration	Moderate
11	32	Straight Line Braking	Light
12	35	Straight Line Braking	Light
13	30	Straight Line Braking	Moderate
14	31	Straight Line Braking	Moderate
15	46	Step Steer Left	20 KPH, 180° SWA
16	43	Step Steer Left	20 KPH, 180° SWA
17	41	Step Steer Left	20 KPH, 180° SWA
18	42	Step Steer Right	20 KPH, 180° SWA
19	39	Step Steer Right	20 KPH, 180° SWA
20	44	Step Steer Right	20 KPH, 180° SWA
21	26	Braking in a Turn Left	35 KPH
22	24	Braking in a Turn Left	35 KPH
23	25	Braking in a Turn Left	35 KPH
24	36	Braking in a Turn Right	35 KPH
25	40	Braking in a Turn Right	35 KPH
26	41	Braking in a Turn Right	35 KPH
27	64	Step Steer Left	40 KPH, 180° SWA
28	64	Step Steer Right	40 KPH, 180° SWA
29	48	Sinusoidal Steer	180° SWA
30	49	Sinusoidal Steer	180° SWA
31	50	Sinusoidal Steer	180° SWA
<b>TOTAL</b>	<b>1220</b>		

## 5.4 Summary

The following summary can be made based on the results of the smart tire prototyping and testing activities.

1. A physical durability bench test of a commercially available piezoelectric sensor was conducted.
2. The piezoelectric sensor was a dimensionally large deformation sensor that had a composite construction consisting of a thin compound PVDF and polyester beam layer sandwiched between two silver electrode layers, with the entire stack-up coated in urethane.
3. Low cost, mechanical flexibility and independence from power supplies and amplifiers were the main advantages of the piezoelectric sensor.
4. A lack of information regarding the strain range and fatigue life of the piezoelectric sensor was its biggest disadvantage.
5. A tire sample durability bench testing machine was fabricated that operated at a frequency of 4 Hz, simulating vehicle travel at 30 KPH, and subjected the sample to 10,000 deformation cycles in 45 minutes.
6. Tire sidewall samples were cut such that they were deformed in the radial direction; piezoelectric sensors were bonded to these samples in the radial direction using adhesives.
7. Four tire sidewall samples with sensors bonded entirely to the rubber were found to experience degradation in sensor output over durability test time, including a decrease in voltage levels and an increase in noise; ultimately this attachment method resulted in permanent buckling of the sensors.
8. A fifth tire sidewall sample with a sensor partially bonded to the rubber at its top third had the “best” durability results; the sensor also had a paper clip retaining its free end and a piece of plastic film under its free end to prevent abrasion of the rubber.
9. The fifth tire sidewall sample was ranked first in the durability testing results, but it too suffered from the problems of decreased voltage levels and increased noise with time; it cannot be used in the STSS.
10. The fifth tire sidewall sample was found to maintain its starting output voltage within 5% for the first hour of operation; beyond one hour of continuous operation on the same test day, voltage levels were determined to be within 10%, which was considered an overall adequate performance and therefore the attachment method was adopted for use in the smart tire prototypes.

11. In future work on the STSS, a deformation sensor for in-tire use must be identified that has similar flexibility compared to tire rubber; in that case it is likely to be sufficiently durable.
12. Smart tire revision 1 was fabricated with six in-tire piezoelectric sensors and a dedicated wired smart tire data acquisition system that stored sensor output in a rim mounted data logger.
13. Physical on-road vehicle testing of smart tire revision 1 identified a longitudinal tire mode of vibration at 67 Hz that was removed from the data through low-pass filtering along with the attenuation of all other tire modes and measurement noise using the filter.
14. Piezoelectric sensor data as measured at the tire sidewall were found to resemble the virtual sidewall strain data with respect to shape of the waveforms.
15. Piezoelectric sensor data measured at the left front tire was mapped to tire forces at the right front tire as measured by a wheel load transducer; tire forces were averaged to produce once per revolution target force values.
16. Neural networks configured per the virtual strain processing study were used to analyze data collected in smart tire revision 1 on-road vehicle testing, where standard vehicle dynamic events were performed to bring about pure and combined slip tire force conditions.
17. Results of the neural networks when processing data from smart tire revision 1 were unacceptable, with tire force estimates that were inaccurate by hundreds of percent.
18. A problem with the left front wheel angular position estimate, itself based on measured wheel angular velocity from the vehicle ABS system, was identified where incorrect triggering of data acquisition based on an estimated wheel angular position index resulted in incorrect angular positioning of the piezoelectric sensor data as the wheel revolutions evolved in each test event.
19. Smart tire revision 2 was fabricated with two pairs of sidewall sensors that were recorded during testing; it incorporated a slip ring / encoder device that was used to pass the in-tire piezoelectric sensor signals into the vehicle for data storage and also to output a once per revolution angular position index for the left front wheel.
20. Three rounds of on-road vehicle testing were conducted using smart tire revision 2; only the first round produced usable data, as the data acquisition equipment malfunctioned in the second round and the piezoelectric sensors were too deteriorated for use by the third round.
21. Data collected from smart tire revision 2 were used in the physical deformation processing study.

## Chapter 6

# Smart Tire Outputs Estimation

**Chapter Brief**—Piezoelectric sensor data from smart tire revision 2 are used with neural networks to estimate the three orthogonal tire forces and the tire aligning moment that are required outputs from the STSS. Data from two sidewall left sensors are used to estimate tire forces. The neural networks are capable of predicting the correct trends in the tire force data over several testing events. Estimates for fixed STSS outputs in the physical tests, including the air inflation pressure and the tire / road friction coefficient, are investigated using tire FEA. Analysis results show that air inflation pressure can be determined from strain waveform offsets assuming a linear relationship between the two; the neural networks are expected to be capable of inflation pressure estimation based on fitting this functional relationship. Tire / road friction coefficient can be obtained by processing the tensile strain at the center of the contact patch.

---

### 6.1 Estimation of Tire Forces

Piezoelectric sensor data collected from smart tire revision 2 were used to draw overall conclusions about the STSS; in particular, the performance of the STSS regarding estimation of the three orthogonal tire forces and tire aligning moment. Analysis of data collected during the first and third testing rounds is presented here. Division of the testing rounds with respect to event types appears in Table 6.1. Data analysis was focused on Group 1 sensors located at the outside (left) sidewall, as Group 4 sensors located at the inside (right) sidewall produced similar signals and were considered to provide a backup data set. In addition, Group 1 was located adjacent to the tire reference index mark. Therefore, the position of its sensors relative to the index was easier to measure and more certain.

#### 6.1.1 Round 1 Testing

The research vehicle was operated in rear wheel drive mode in Round 1 testing.



Table 6.1 – Statistics for Testing Rounds 1 and 3 for Smart Tire Revision 2

Test- ing Round No.	No. of Tests	No. of Lon- gitudinal Pure Slip Tests	No. of Lateral Pure Slip Tests	No. of Com- bined Slip Tests	No. of Training Samples (Complete Wheel Revolutions)
1	31	14	11	6	1220
3	35	16	12	7	1264

6.1.1.1 Order Domain Data

The rotary encoder incorporated into smart tire revision 2 fixed the angular position issue observed in revision 1, as can be seen in the piezoelectric sensor measurements of Figure 6.1 for sinusoidal steering test number 31, where the data are clearly consistent in each wheel revolution with respect to angular position. It is interesting that the steering motion can be easily identified in the data surfaces as rounded “hills”. The longitudinal and radial sensor measurements at the left sidewall are shown, as data from these sensor locations were used to train the neural networks.

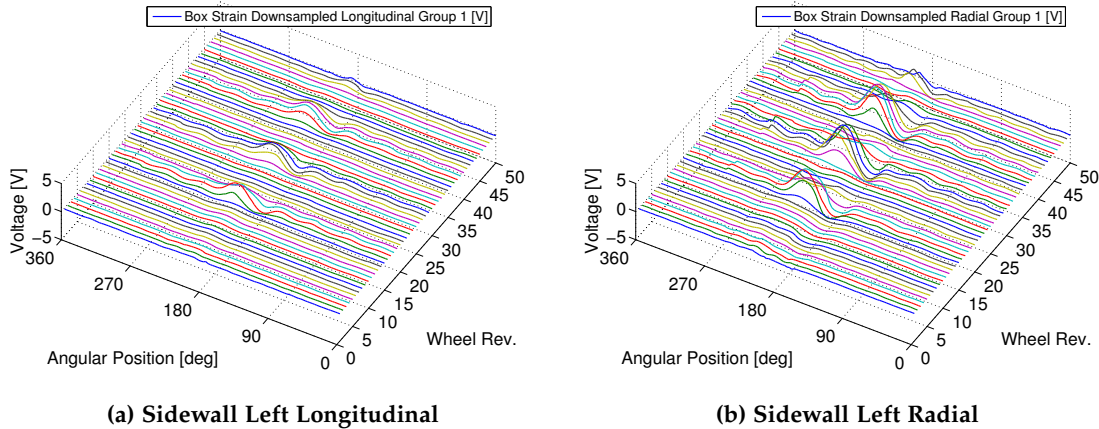


Figure 6.1 – Piezoelectric Sensor Data Surfaces in Sinusoidal Steering Test No. 31 From Smart Tire Revision 2

The tire force signals from the right front wheel load transducer are shown in Figure 6.2 for sinusoidal steering test number 31. Three tire forces and one tire moment are shown as data surfaces. The average tire force signals are shown in Figure 6.3. The sinusoidal nature of the steering motion during the test is apparent in the tire force data surfaces and averages, similar to the piezoelectric sensor data. For reference, piezoelectric sensor measurements and wheel load transducer measurements for some events in

Round 1 testing are shown in Appendix G. One set of plots for each test type is included. For example, four straight line braking tests were performed in Round 1 testing, but only one of these is plotted as an example of the type. Each test has two piezoelectric sensor data surfaces plotted and four graphs showing average tire forces. The piezoelectric sensor measurements were the training data for the neural networks, and the average forces were the targets.

#### 6.1.1.2 Neural Network Data Analysis

**Points Study.** A points study of the Round 1 physical test data was conducted that was similar to the sample rate study using the virtual strain as calculated by the tire FEM. In the points study, all of the data were used for training except for braking in a turn left test number 22, which was used as the testing case. Each piezoelectric sensor waveform representing one complete wheel revolution was sampled evenly over 360 degrees using a certain number of points. There were 10, 20, 30, 40, 60 and 120 points trials investigated. Figure 6.4 shows the training error in the neural networks during these trials.

From Figure 6.4 it can be seen that the 120 points trial had the lowest overall training error compared to all of the trials. MSE at the end of training, however, was insufficient to expect very good testing results from the trained network (compare training error in Figure 4.25 for the virtual strain case). Overall training behavior with physical deformation data was good; however, with smoothly decreasing training error. To decrease the error further, more training samples would be required.

Figures 6.5 through 6.8 show the neural network results in the points study. Target (bar graph) and estimated (line graph) tire forces are shown for all trials except for the 10 points trial, since performance was so poor in that case that the vertical force scales were too compressed to see any detail in the other trials. A review of the tire force estimates from the 120 points trial shows that the neural networks were able to predict the generally correct trends in the tire forces with 120 points per revolution of piezoelectric sensor deformation data.

Table 6.2 lists the average change in estimated tire force values compared to actual tire force values in the points study. The average change is the average error in the estimates over the entire braking in a turn left test number 22. From Table 6.2 it can be seen that 120 points per waveform are required, as the tire force estimates had the least overall error at this data resolution. This result was different compared to the results of the sample rate study using virtual strain, where 26 points per waveform were found to produce reasonably accurate results.

However, that comparison is not valid since the neural network was insufficiently trained in the case of the physical test data. The testing case, braking in a turn left test number 22, was a combined slip event. There were only five other combined slip tests to train the neural networks with in Round 1. In addition, the combined slip test events did

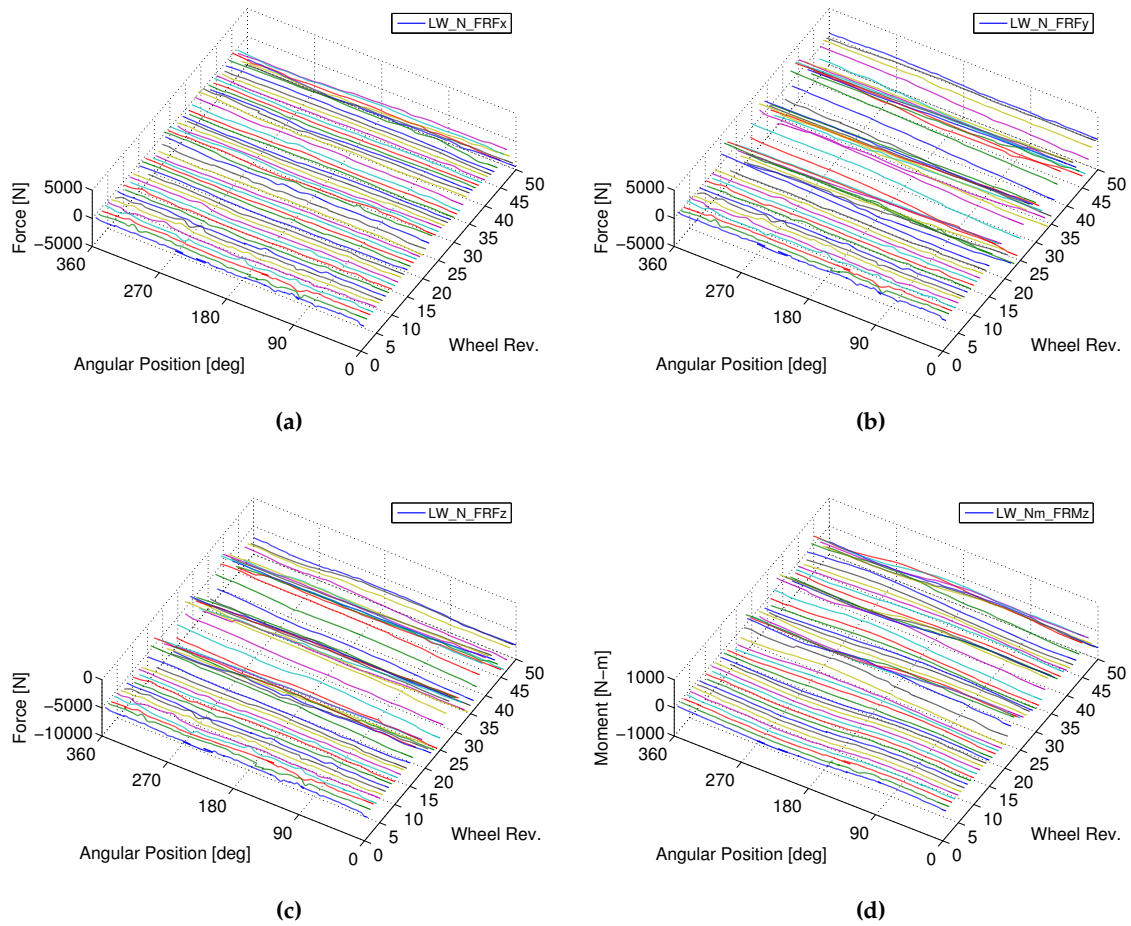


Figure 6.2 – Wheel Load Transducer Data Surfaces in Sinusoidal Steering Test No. 31 From Smart Tire Revision 2: (a) Longitudinal Force (b) Lateral Force (c) Vertical Force (d) Aligning Moment

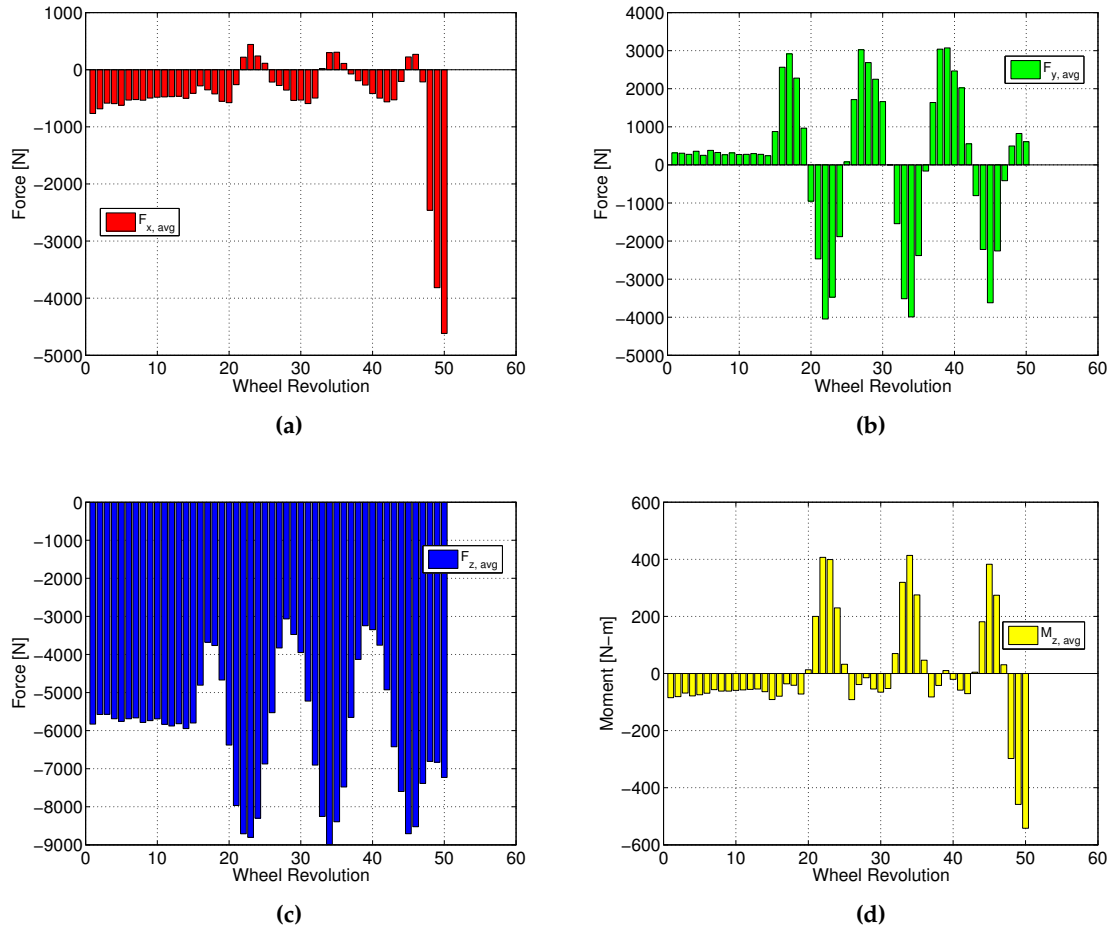


Figure 6.3 – Wheel Load Transducer Averages in Sinusoidal Steering Test No. 31 From Smart Tire Revision 2: (a) Longitudinal Force (b) Lateral Force (c) Vertical Force (d) Aligning Moment

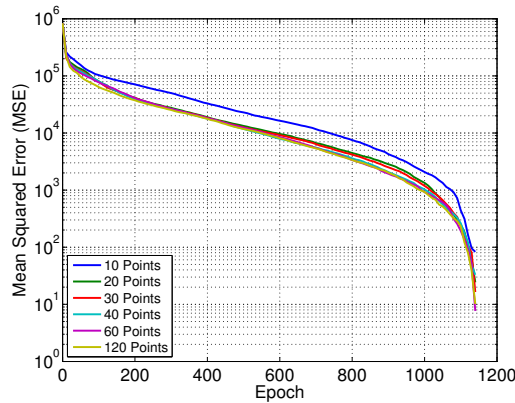
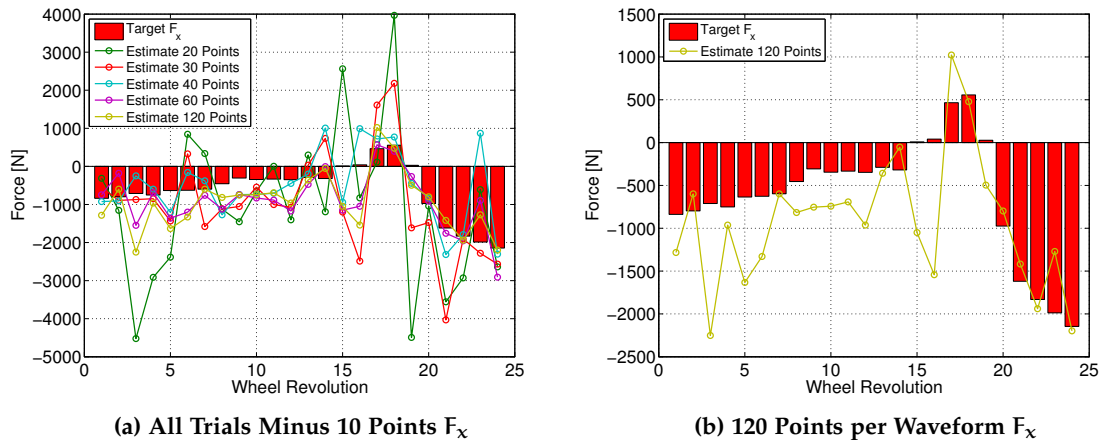


Figure 6.4 – Training Error for Networks in Points Study



(a) All Trials Minus 10 Points  $F_x$

(b) 120 Points per Waveform  $F_x$

Figure 6.5 – Target and Estimated Longitudinal Tire Force in Braking in a Turn Left Test No. 22 From Smart Tire Revision 2 – Points Study

not consist entirely of combined slip samples. For example, Figure G.5 shows tire force targets for braking in a turn right test number 26. When considering longitudinal and lateral tire forces, it can be seen that there were only a few complete revolutions in the test that combined high forces of both types. Therefore, the Round 1 physical test data set did not contain enough samples to train the networks properly. But longer test days performed to collect more samples resulted in deterioration of the piezoelectric sensors, which limited the total amount of testing time.

The neural networks were most effective at estimating vertical force, least effective at estimating longitudinal force and good at estimating lateral force and aligning moment. In the plot of Figure 6.5b it can be seen that the networks made poor estimates at wheel

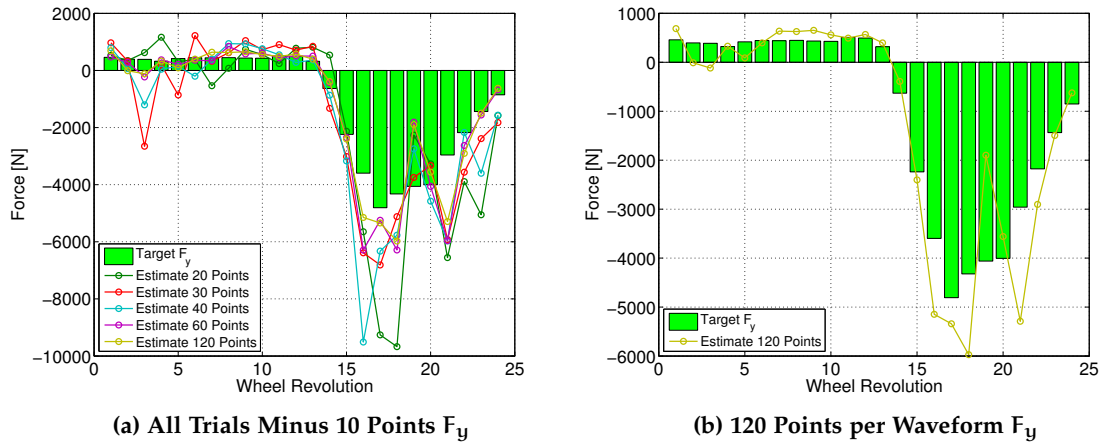


Figure 6.6 – Target and Estimated Lateral Tire Force in Braking in a Turn Left Test No. 22 From Smart Tire Revision 2 – Points Study

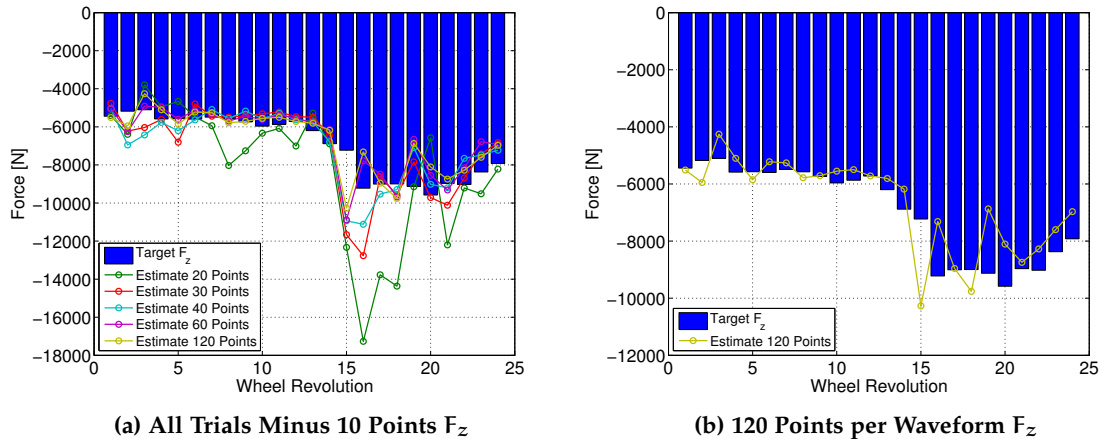


Figure 6.7 – Target and Estimated Vertical Tire Force in Braking in a Turn Left Test No. 22 From Smart Tire Revision 2 – Points Study

revolutions 15 and 16, when the longitudinal force was nearly zero. This indicates that the two straight line creeping tests did not provide enough, or any, training data to the networks in the near-zero longitudinal force case.

**Sector Study.** The sector study was performed to determine the effect of using the center third of the piezoelectric deformation data, similar to the footprint study of virtual strain. In the sector study the data from 120 to 240 degrees were retained, while the data outside this 120 degree segment were discarded. The sector study was not an attempt at

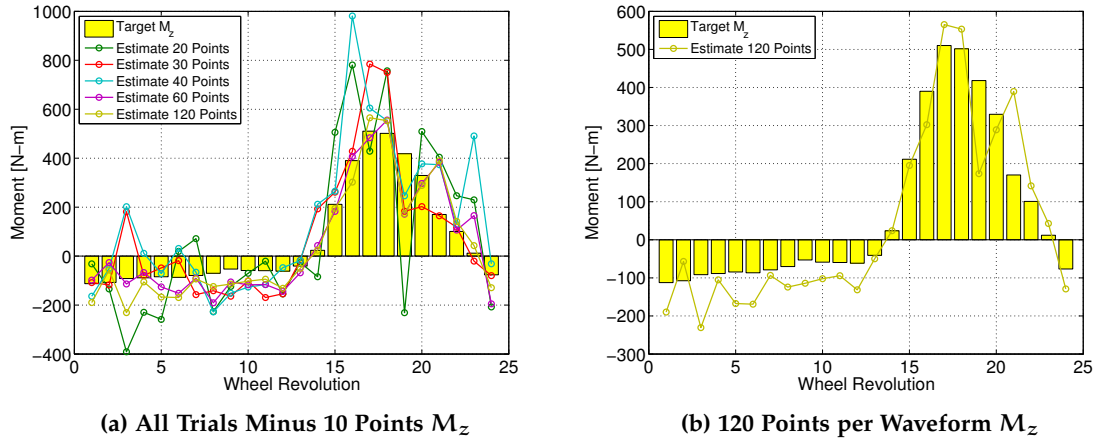


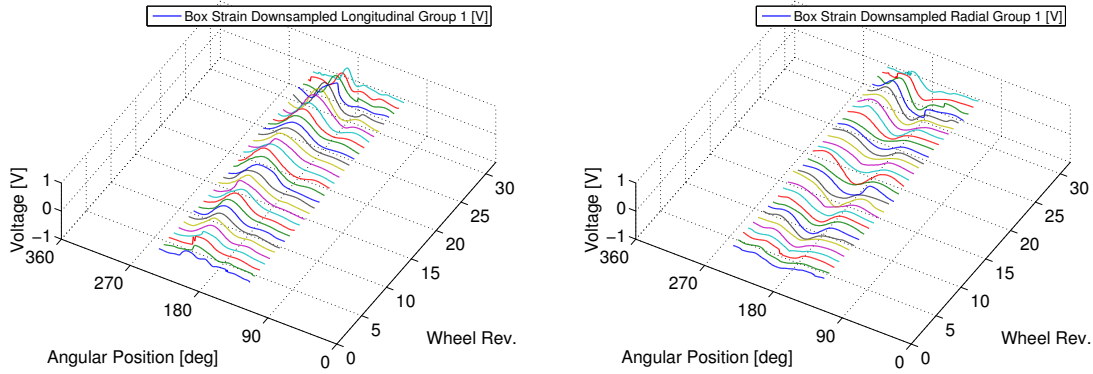
Figure 6.8 – Target and Estimated Aligning Tire Moment in Braking in a Turn Left Test No. 22 From Smart Tire Revision 2 – Points Study

Table 6.2 – Average Error in Tire Force Estimates From Neural Networks for Braking in a Turn Left Test No. 22 – Points Study

Tire Force	Number of Points per Waveform					
	10	20	30	40	60	120
$F_x$	55,842%	2,223%	1,222%	714%	804%	837%
$F_y$	329%	89%	110%	81%	38%	39%
$F_z$	111%	23%	13%	11%	11%	10%
$M_z$	3,034%	207%	107%	278%	112%	66%

problem reduction size, as the segments contained 120 data points, the same as the baseline case in which 120 points were taken from the entire wheel revolution range. Rather, the purpose was to investigate the effect of using the center portion of the physical test data to train and test the neural networks, independent of the data size issue. Figure 6.9 illustrates the appearance of the sectorized data surfaces in the case of straight line braking test number 11.

Figure 6.10 shows the neural network results in the sector study. The performance of the networks was worse when trained on the data sector, which confirms the similar result from the comparable footprint study of virtual strain, as shown in Table 6.3. Note the poor performance of the sector-trained networks at wheel revolution 23, which had low lateral force and near zero aligning moment. This result is consistent with the footprint study of virtual strain, which found that the aligning moment estimates should suffer when the networks are trained on data centered on the footprint only.



(a) Sidewall Left Longitudinal

(b) Sidewall Left Radial

Figure 6.9 – Piezoelectric Sensor Data Surfaces in Straight Line Braking Test No. 11 From Smart Tire Revision 2 – Sectored

Table 6.3 – Average Error in Tire Force Estimates From Neural Networks for Braking in a Turn Left Test No. 22 – Sector Study

Tire Force	Entire 360° Cycle	Centered 120° Sector
$F_x$	837%	1306%
$F_y$	39%	183%
$F_z$	10%	16%
$M_z$	66%	248%

**Reduced Size Training Data Set Study.** A points study of the Round 1 physical test data was performed that was intended to test the effect of a reduced training data set size. In the previous studies, the neural networks were trained on the entire Round 1 data set except for the testing case, which was braking in a turn left test number 22. In that case the networks were trained on 98% of the data set. Table 6.4 describes the configuration of the two reduced size training data set trials. The networks were trained on 92% of the data set in the first trial and 71% of the data set in the second trial.

Figures 6.11 through 6.13 show the neural network results in the reduced training data set study. The performance of the networks was similar given the two different size training data sets; it is presumed that neither contained a sufficient number of samples to fully train the networks. The rear wheel drive configuration of the research vehicle can be seen in the target, or measured, tire force values of Figure 6.11, which shows the straight line braking test number 11 event.



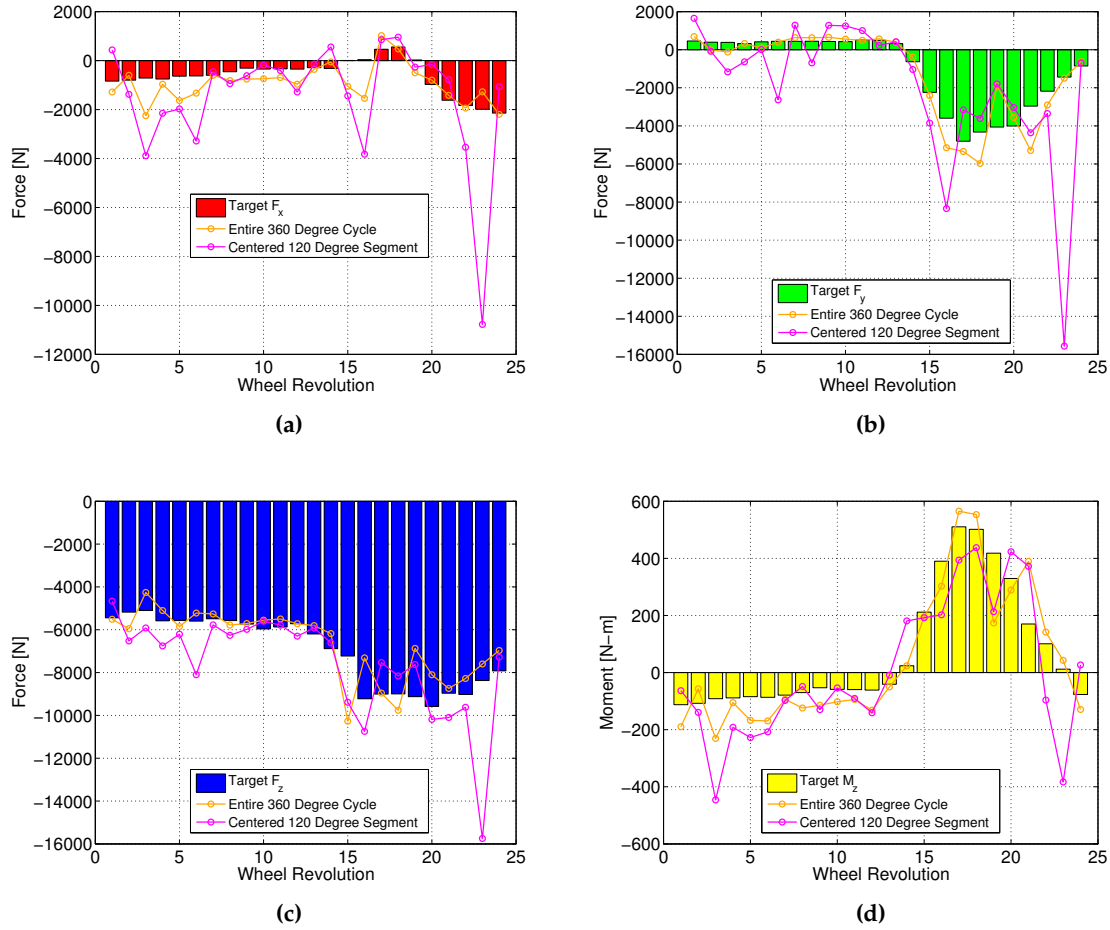


Figure 6.10 – Target and Estimated Tire Forces in Braking in a Turn Left Test No. 22 From Smart Tire Revision 2 – Sector Study: (a)  $F_x$  (b)  $F_y$  (c)  $F_z$  (d)  $M_z$

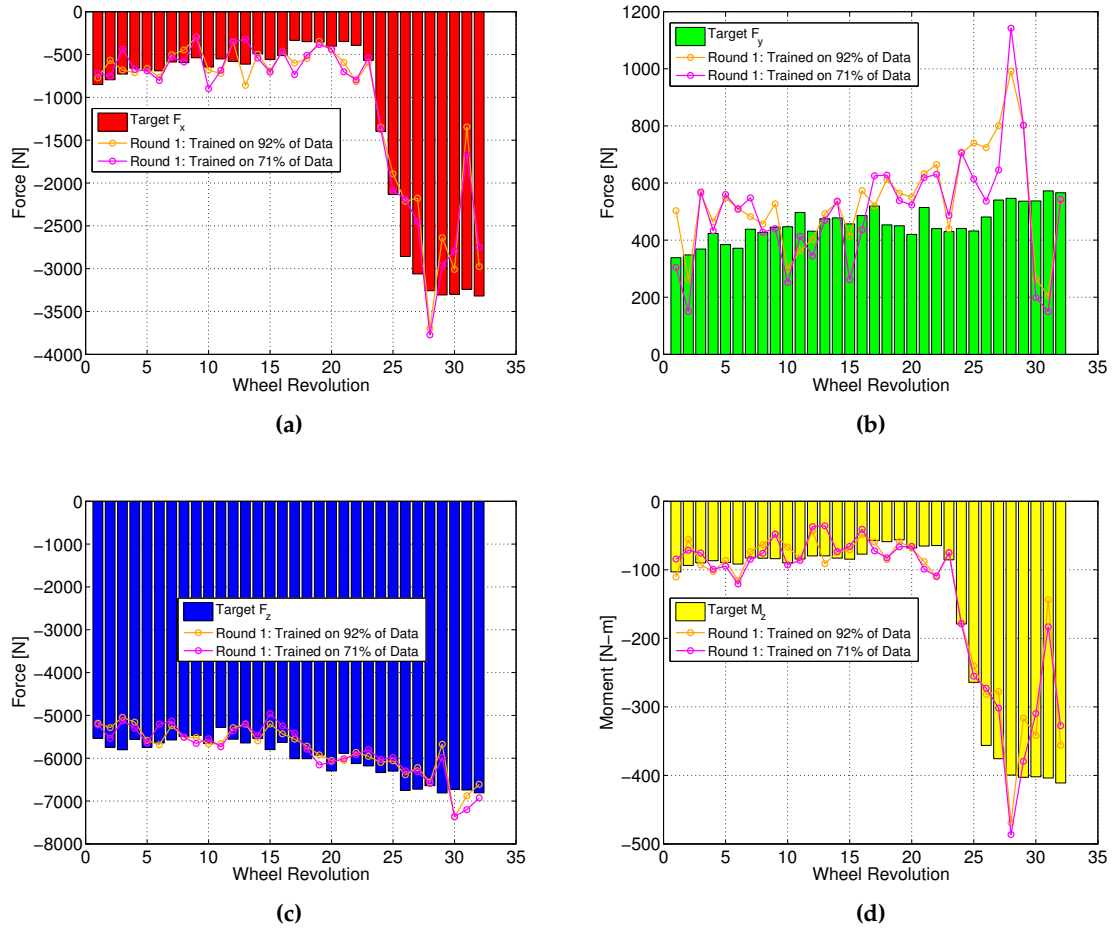


Figure 6.11 – Target and Estimated Tire Forces in Light Straight Line Braking Test No. 11 From Smart Tire Revision 2 – Training Size Study: (a)  $F_x$  (b)  $F_y$  (c)  $F_z$  (d)  $M_z$

---

**CHAPTER 6. SMART TIRE OUTPUTS ESTIMATION**

---

**Table 6.4 – Round 1 Data in Reduced Size Training Data Set Study**

Trial No.	Testing Data	Training Data	Fraction of Data Set Used for Training
I	<ul style="list-style-type: none"> <li>• Straight Line Braking Test No. 11</li> <li>• Step Steer Left Test No. 17</li> <li>• Brake in Turn Left Test No. 22</li> </ul>	All events except the three testing cases.	92%
II	Same as I.	Same as I except for test number 3, 8, 14, 15, 19 and 31 not used.	71%

Table 6.5 lists the average change in estimated tire force values compared to actual tire force values in the reduced size training data set study. Tire force accuracy from the networks in straight line braking test number 11 was good, with an average tire force error of 31% or less. Accuracy was not as high in the step steer left number 17 test or in the brake in a turn left test number 22. Accuracy of longitudinal tire force estimates was especially poor in the presence of large lateral forces.

**Table 6.5 – Average Error in Tire Force Estimates From Neural Networks – Training Size Study**

Testing Case	Tire Force	Trial I (92%)	Trial II (71%)
Straight Line Braking Test No. 11	$F_x$	25%	28%
	$F_y$	32%	31%
	$F_z$	5%	6%
	$M_z$	21%	23%
Step Steer Left Test No. 17	$F_x$	133%	105%
	$F_y$	47%	51%
	$F_z$	6%	5%
	$M_z$	84%	73%
Brake in Turn Left Test No. 22	$F_x$	676%	728%
	$F_y$	40%	40%
	$F_z$	12%	12%
	$M_z$	82%	63%

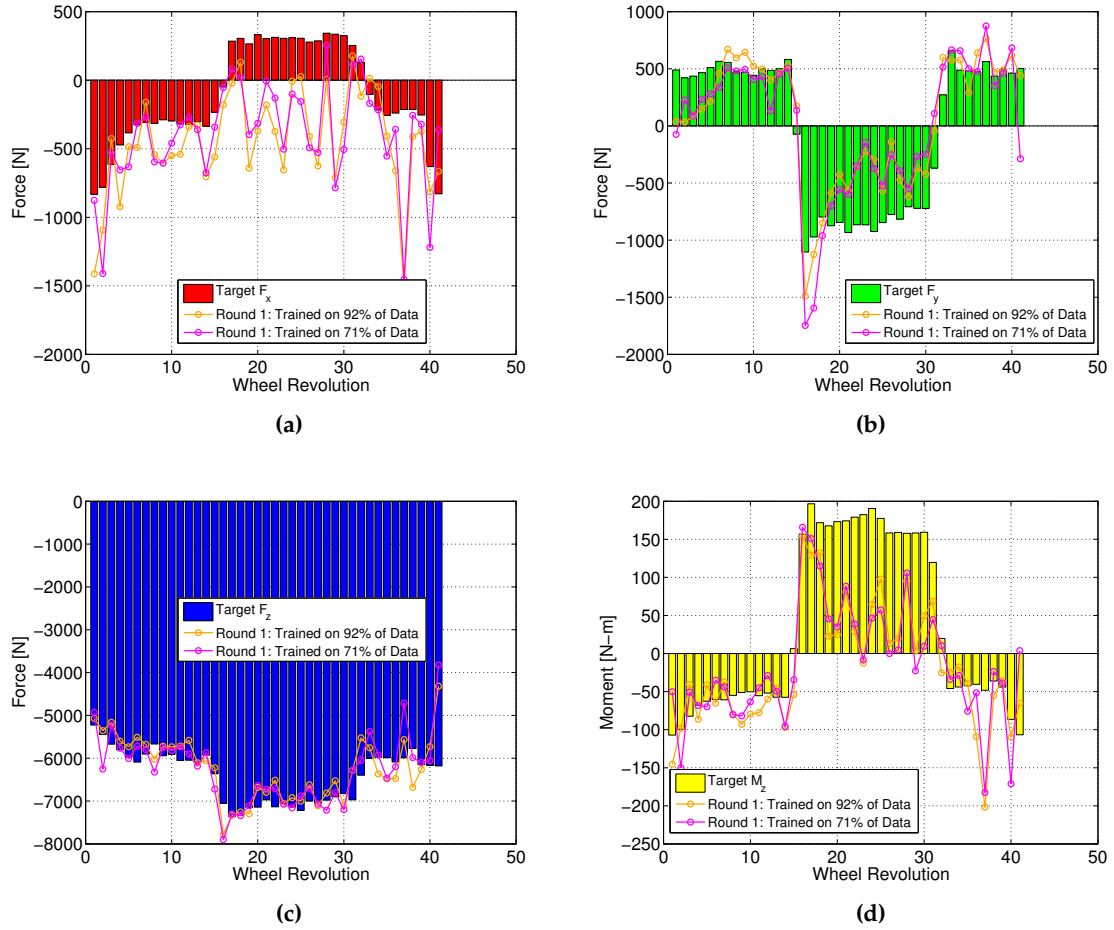


Figure 6.12 – Target and Estimated Tire Forces in Step Steer Left Test No. 17 From Smart Tire Revision 2 – Training Size Study: (a)  $F_x$  (b)  $F_y$  (c)  $F_z$  (d)  $M_z$

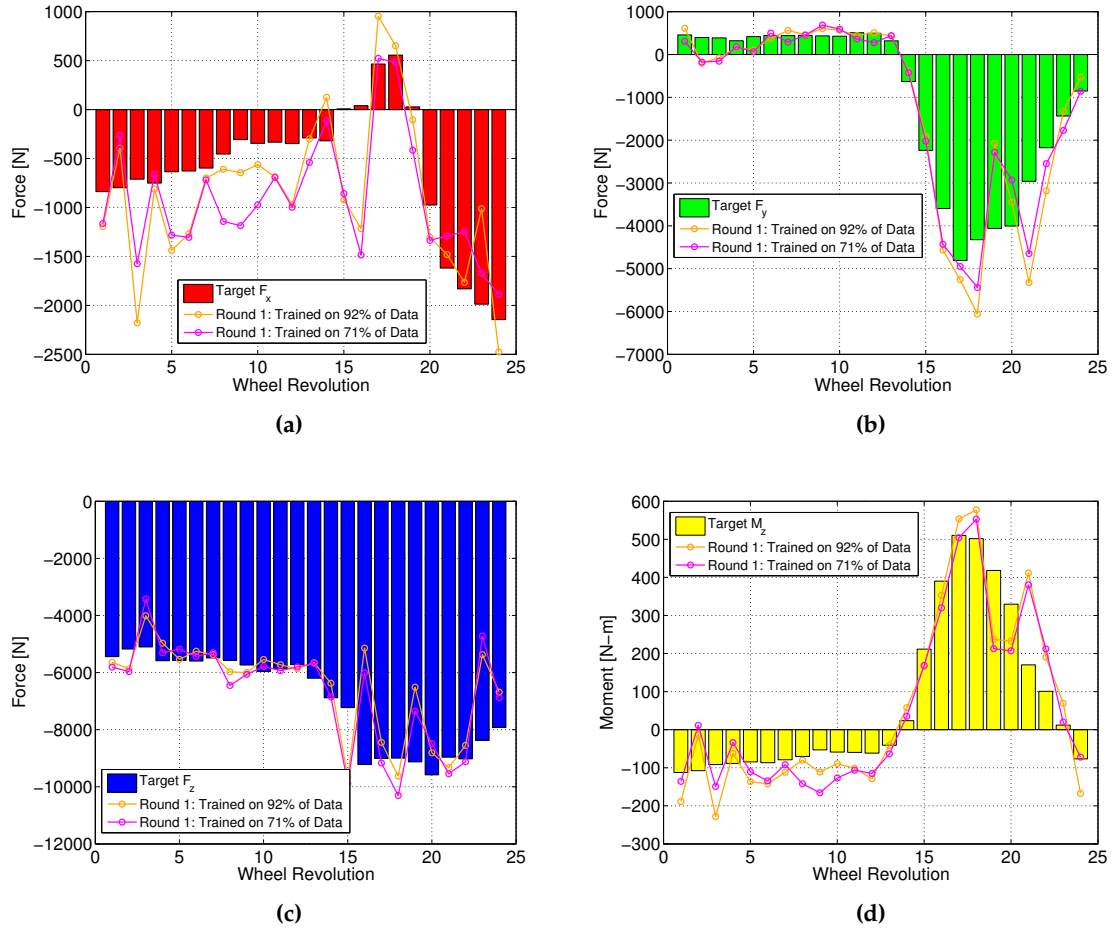


Figure 6.13 – Target and Estimated Tire Forces in Braking in a Turn Left Test No. 22 From Smart Tire Revision 2 – Training Size Study: (a)  $F_x$  (b)  $F_y$  (c)  $F_z$  (d)  $M_z$

Table 6.6 summarizes the overall performance of the neural networks, in both the physical test and the simulations. The overall performance in the physical tests is taken from the worst case estimates of Table 6.5 in the Trial II case. While the overall tire force trends were properly predicted by the neural networks, the tire force estimates were not especially accurate, especially in comparison to the results from the tire FEA.

The single most important difference between the analysis and the test was that the networks were presented with an evenly distributed set of training samples representing a broad range of tire forces in the analysis. The Round 1 training set in the physical test did not have this advantage, as the training data samples were skewed towards the low to moderate tire forces developed in light acceleration and slow steady-state cruising conditions. Training samples consisting of combined high tire forces made up a small fraction of the physical testing training data, less than 10%. Better performance from the neural networks in the physical test would require more training data, especially more data collected from high tire force conditions.

**Table 6.6 – Average Error in Tire Force Estimates**

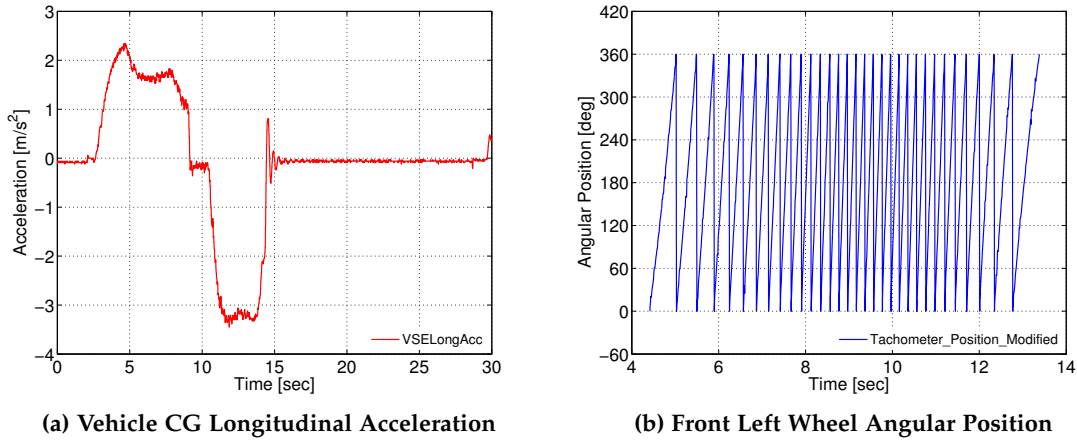
Tire Force	Analysis	Test
Fx	1%	728%
Fy	1%	51%
Fz	N/A	12%
Mz	1%	73%

Some time domain data collected from straight line braking test number 11 event are shown in Figure 6.14. The vehicle longitudinal acceleration appears in Figure 6.14a and the wheel angular position is shown in Figure 6.14b. The entire time record is graphed in the case of the longitudinal acceleration, whereas only the analysis time section (used in the piezoelectric sensor data surfaces) is plotted in case of the the wheel angular position.

Comparing the acceleration section at the beginning of the time history with the right front tire longitudinal forces developed in Figure 6.11a, it can be seen that even though positive longitudinal forces were required to produce forward acceleration of the vehicle, only negative longitudinal forces were recorded. This is because the vehicle was tested in rear wheel drive mode, and the drive torques (and associated positive longitudinal tire forces) were developed at the rear wheels. The negative tire forces recorded at the front wheels during positive vehicle acceleration were associated with the rolling resistance of the tires.

### **6.1.2 Round 3 Testing**

The research vehicle was operated in four wheel drive mode in Round 3 testing.



(a) Vehicle CG Longitudinal Acceleration (b) Front Left Wheel Angular Position  
**Figure 6.14 – Time Domain Data in Light Straight Line Braking Test No. 11 From Smart Tire Revision 2**

### 6.1.2.1 Neural Network Data Analysis

**Piezoelectric Sensor Deterioration.** Data collected in Round 2 testing were not usable. Unfortunately, the piezoelectric deformation sensors had been subjected to too many strain cycles by Round 3, by which time they exhibited a substantial noise increase. Both sidewall sensors data sets were also shifted with respect to angular position, and consistently so for each wheel revolution in the test events. Figure 6.15 shows some of the deteriorated piezoelectric data from the Group 1 sensors, both as measured and modified with angular position shifts applied. Data from the longitudinal piezoelectric sensor shifted 10 degrees and data from the radial sensor shifted 85 degrees, compared to Round 1. This indicates durability failures of the sensors, especially in the case of the radial sensor, where either adhesive failure or permanent deformation of the sensor itself likely took place.

The longitudinal sensor was also found to have reduced overall levels in Round 3 testing compared to Round 1; therefore, the voltage output from this sensor was multiplied by 1.3 to compensate. These modifications to the piezoelectric sensors, including the separate lateral shifts in angular position, and the multiplication of the longitudinal sensor voltage levels, constituted the modifications made to all of the piezoelectric sensor data in the Round 3 data set for subsequent use with the neural networks.

**Modified Piezoelectric Sensor Data Study.** All of the Round 3 data were used to train the neural network, except for straight line acceleration and braking test number 9, which was used for testing. The results from the neural network are shown in Figure 6.16. The neural network had very poor results when estimating lateral force and aligning moment as expected, since both are highly dependent on the radial deformation measurement,

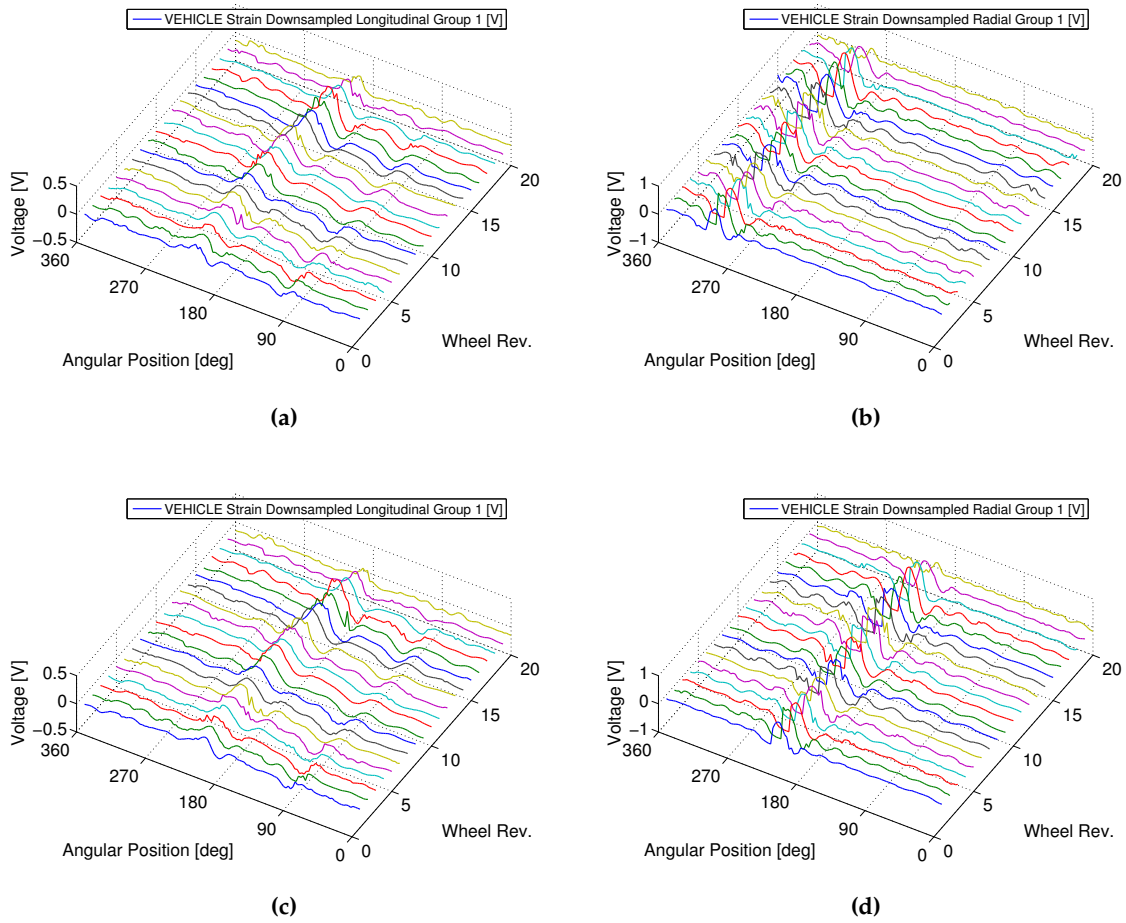


Figure 6.15 – Piezoelectric Sensor Data Surfaces in Round 3 Straight Line Acceleration and Braking Test No. 3 From Smart Tire Revision 2: (a) Longitudinal Sensor Unmodified (b) Radial Sensor Unmodified (c) Longitudinal Sensor Shifted  $-10^\circ$  (d) Radial Sensor Shifted  $-85^\circ$



which was seriously compromised by sensor fatigue in Round 3 testing. A review of Figure 6.16a shows that the network was quite effective at estimating longitudinal force. Significant positive longitudinal forces were developed at the beginning of the test event, as can be seen from the plot, as the research vehicle was operated in four wheel drive mode in Round 3 testing.

Table 6.7 lists the average change in estimated tire force values compared to actual tire force values for Round 1 and Round 3. The neural networks made worse estimates in Round 3 compared to Round 1, except in the case of longitudinal force. The improved longitudinal force results were mainly due to a broad spectrum of longitudinal tire force training samples in Round 3, including positive longitudinal forces. In future work, smart tire prototypes should be tested using a four wheel drive vehicle in order to generate a range of longitudinal forces at the front wheels. Future smart tire prototypes should remain at the front wheels in order to maintain a large range of lateral forces produced from the large steering angles at the front wheels, in addition to gaining positive longitudinal forces from the drive torques.

**Table 6.7 – Average Error in Tire Force Test Estimates**

<b>Tire Force</b>	<b>Round 1</b>	<b>Round 3</b>
F <sub>x</sub>	728%	45%
F <sub>y</sub>	51%	1817%
F <sub>z</sub>	12%	22%
M <sub>z</sub>	73%	142%

Since the piezoelectric sensors in Round 3 testing had fatigued, data from Round 3 could not be combined with data from Round 1 to form a large single training data set for the neural networks. The collection of a large data set is the subject of future work, when a smart tire prototype can be fabricated with more suitable deformation sensors with a much longer durability life compared to the piezoelectric sensors.

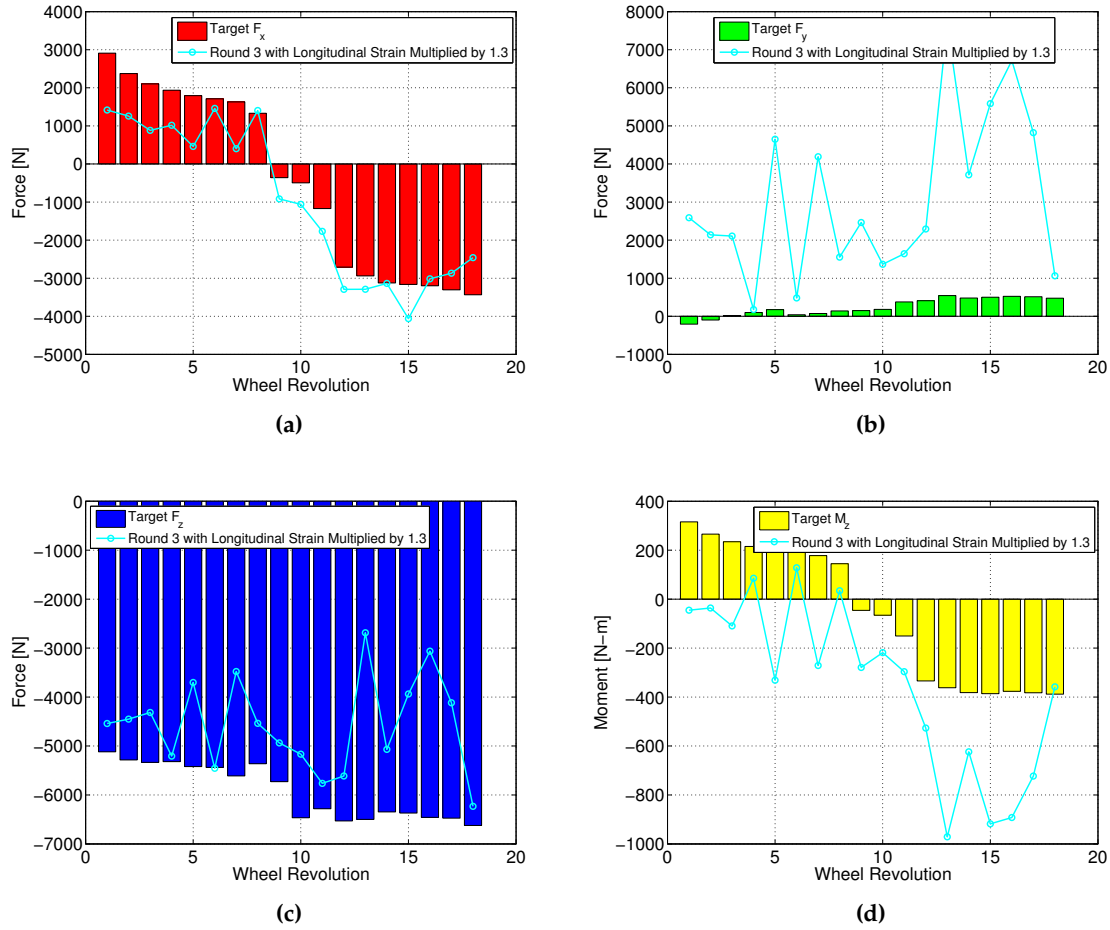


Figure 6.16 – Target and Estimated Tire Forces in Round 3 Straight Line Acceleration and Braking Test No. 9 From Smart Tire Revision 2: (a)  $F_x$  (b)  $F_y$  (c)  $F_z$  (d)  $M_z$

## 6.2 Estimation of Other Outputs

Smart tire prototypes were physically tested with with the air inflation pressure and the friction coefficient fixed. The testing and data analysis focused on estimating longitudinal force, lateral force, vertical force and aligning moment. Fatigue failure of the piezoelectric sensors prevented further testing into the fixed quantities. In this section, analysis of the fixed quantities is discussed, using tire FEM strain curves, as physical test results are not available.

### 6.2.1 Air Inflation Pressure

A preliminary tire FEM of a P 155/80 R 13 79 S tire was built and exercised as part of the STSS research project [74]. The preliminary tire FEM had air inflation pressure applied as distributed surface loads to element faces on the tire inside surface, the same as in all the tire models. Five different air inflation pressure cases were studied, all with a constant translational speed of 60 KPH and a constant vertical force of 4 kN. The inflation pressures ranged from 110 kPa (16 psi) to 440 kPa (64 psi).

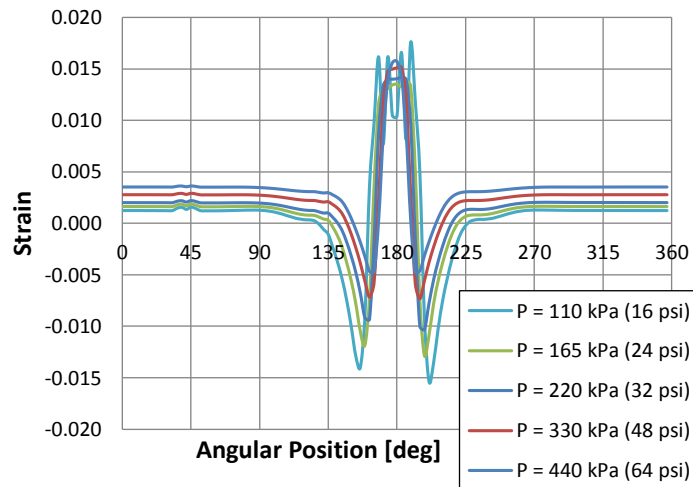


**Figure 6.17 – Longitudinal Strain at Tire Inner Liner Centerline versus Angular Position for Free Rolling From the Preliminary Tire FEM**

Figure 6.17 shows tread centerline longitudinal strain versus angular position. From this plot it can be seen that the strain offset increases with increasing inflation pressure; this can be seen by looking at the individual traces opposite the contact patch, at 0 degrees angular position. In contrast, the center of the contact patch at 180 degrees is predicted

to have non-linear behavior in its tread centerline longitudinal strain levels, especially at low inflation pressures.

The tread centerline lateral strain versus angular position is shown in Figure 6.18. The strain offset decreases with increasing inflation pressure, which can be seen at 0 degrees angular position. A plot of strain opposite the contact patch (at 0 degrees) versus inflation pressure is shown in Figure 6.19, for both longitudinal and lateral directions at the tread centerline location.

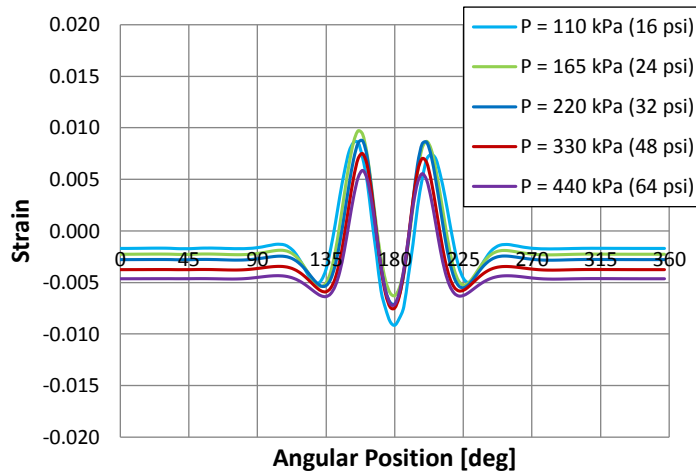


**Figure 6.18 – Lateral Strain at Tire Inner Liner Centerline versus Angular Position for Free Rolling From the Preliminary Tire FEM**

From Figure 6.19 it can be seen that there is a linear relationship between the longitudinal centerline strain opposite the contact patch and the inflation pressure. A similar linear relationship is obtained in the lateral direction as well. Therefore, the tire inner liner centerline strain can be used to determine inflation pressure by assuming a simple linear relationship. It is presumed that sidewall strain measurements can also be used to determine inflation pressure. Furthermore, it is anticipated that the neural networks can fit the functional relationship between measured strain offset levels opposite the contact patch and air inflation pressure. This expectation will be easy to physically test in future work, since the on-road vehicle events will simply be repeated for different air inflation pressures.

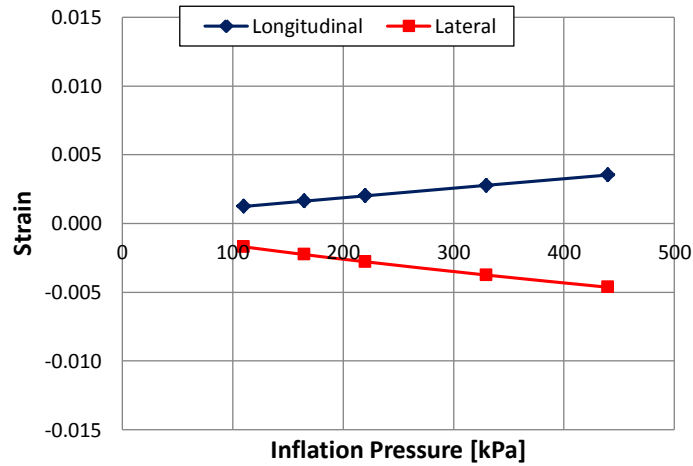


Figure 6.19 – Free Rolling Tread Centerline Strain Offset (Measured at  $0^\circ$ ) versus Inflation Pressure

## 6.2.2 Tire / Road Friction Coefficient

The preliminary tire FEM was solved in order to identify possible ways of estimating the tire / road friction coefficient. The model was used to calculate strain waveforms for different pure braking, pure cornering and combined slip events. In every case the total horizontal tire force developed was 1,800 N. Table 6.8 lists the pure and combined slip friction scenarios simulated using the preliminary tire FEM.

A review of sidewall strain as calculated by the model shows that the sidewall longitudinal strain measurements exhibit very little influence from differing friction coefficients given the same horizontal tire force. Figure 6.20 is a plot of sidewall left radial strain in three combined slip scenarios, with three different friction coefficients, as outlined in Table 6.8. Figure 6.20 illustrates one of the results of the friction investigation using the model; namely, that the friction coefficient had an effect in the strain waveforms at the rear of the contact patch, around 200 degrees. The minimum value at this location decreased with increasing friction coefficient. It may be possible to use the minimum strain level in this “valley” to estimate the friction coefficient. Note, however, that there is only approximately  $100 \mu\epsilon$  separating the valleys at this location. In practice, the physical measurement may obscure such a relatively small difference due to measurement noise alone.

Since the friction coefficient is a tire / road contact phenomenon, the tread may be a better location for strain measurement and identification of friction conditions. Even

**CHAPTER 6. SMART TIRE OUTPUTS ESTIMATION**

---

**Table 6.8 – Friction Scenarios in Preliminary Tire FEA**

Tire Loading Conditions	Inflation Pressure = 220 kPa, Vertical Force = 4 kN, Speed = 60 KPH		
Longitudinal, Lateral or Horizontal Force	1,800 N in Every Case		
Friction Scenario	Friction Coefficient, $\mu$ or $\mu u$		
	1	0.75	0.5
<b>Pure Braking</b>	SR 1.68%, SA 0°	SR 2.12%, SA 0°	SR 4.13%, SA 0°
<b>Pure Cornering</b>	SR 0%, SA 1.80°	SR 0%, SA 2.18°	SR 0%, SA 3.83°
<b>Combined Slip</b>	SR 1.00%, SA 1.20°	SR 1.17%, SA 1.25°	SR 2.00%, SA 1.71°

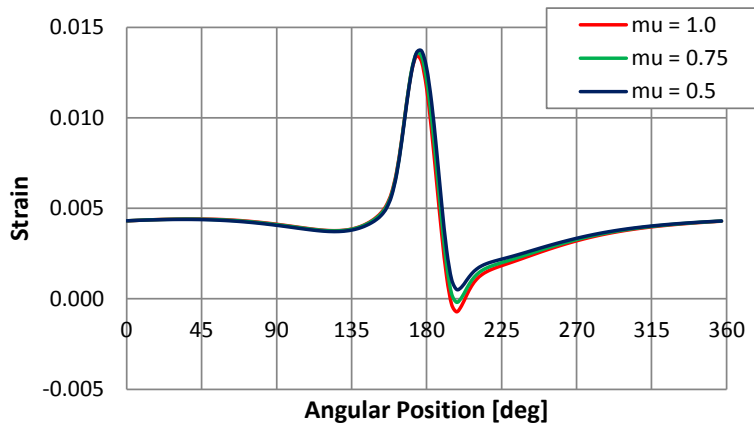


**Figure 6.20 – Sidewall Left Radial Strain at Tire Inner Liner versus Angular Position in Combined Slip, Horizontal Tire Force = 1800 N, From the Preliminary Tire FEM**

though the physical measurement would be made on the inside of the tire, that location is still closer to the contact interface than the sidewall, and therefore it is a more promising location for friction estimation. Figures 6.21 and 6.22 show tire FEA magnitude of displacement contours in pure braking for three different friction conditions. These plots indicate that different tire /road friction coefficients result in different displacement contours at the contact patch, even though the braking force is the same. Therefore, it should be possible to measure deformation, or strain, at the contact patch and estimate the friction coefficient.

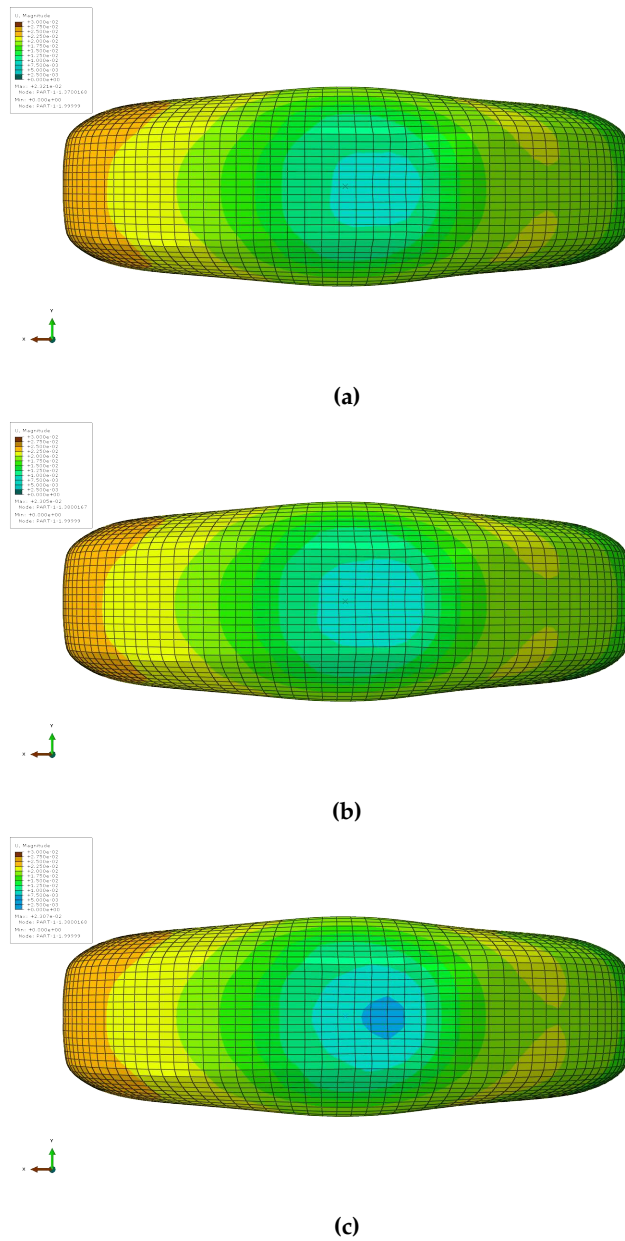
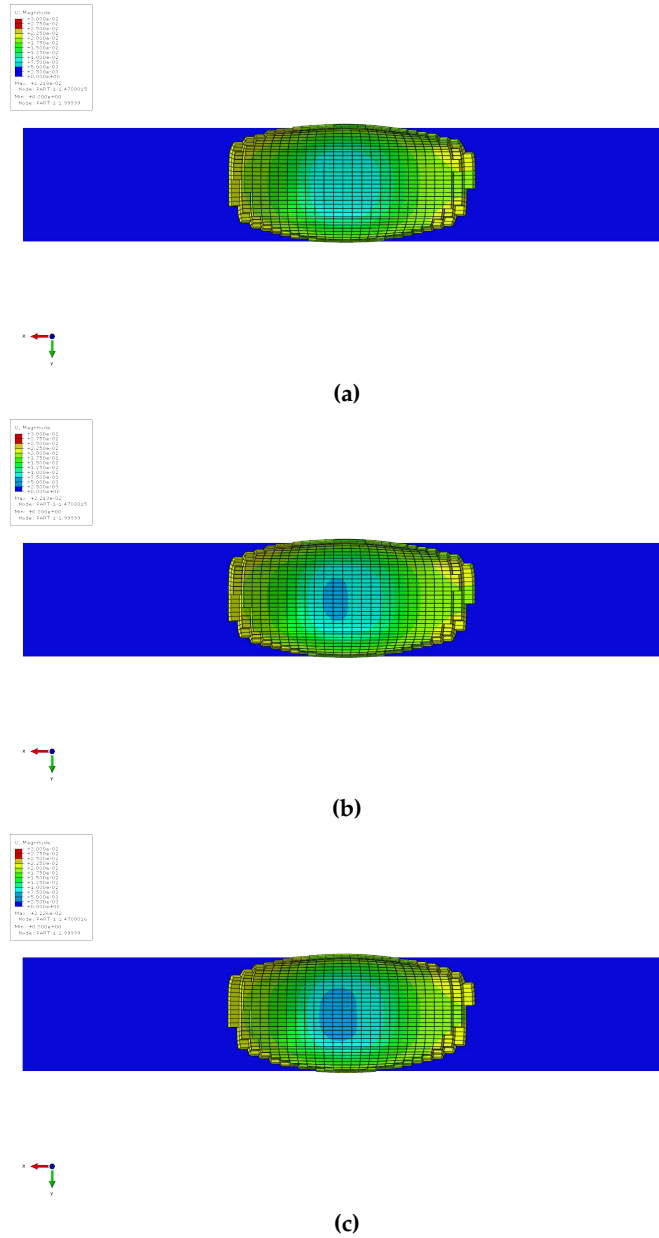


Figure 6.21 – Magnitude of Displacement Contours in Pure Braking, Same Scale in All Cases, Bottom View with Road Masked, Longitudinal Tire Force = 1800 N, From the Preliminary Tire FEM: (a)  $\mu = 1.0$  (b)  $\mu = 0.75$  (c)  $\mu = 0.5$

Figure 6.23 shows tread centerline longitudinal strain in pure cornering and pure braking. A comparison of Figures 6.23a and 6.23b shows that the braking condition is

## CHAPTER 6. SMART TIRE OUTPUTS ESTIMATION

---



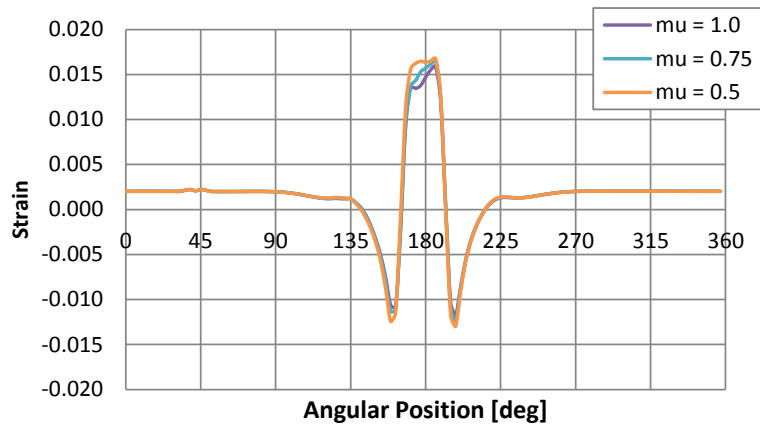
**Figure 6.22 – Magnitude of Displacement Contours in Pure Braking, Same Scale in All Cases, Top View with Upper Part of Tire Masked, Longitudinal Tire Force = 1800 N, From the Preliminary Tire FEM: (a)  $\mu = 1.0$  (b)  $\mu = 0.75$  (c)  $\mu = 0.5$**

indicated by increased compressive strain at the rear of the contact patch (around 200 degrees). It can be seen that the different friction conditions modified the tensile strains

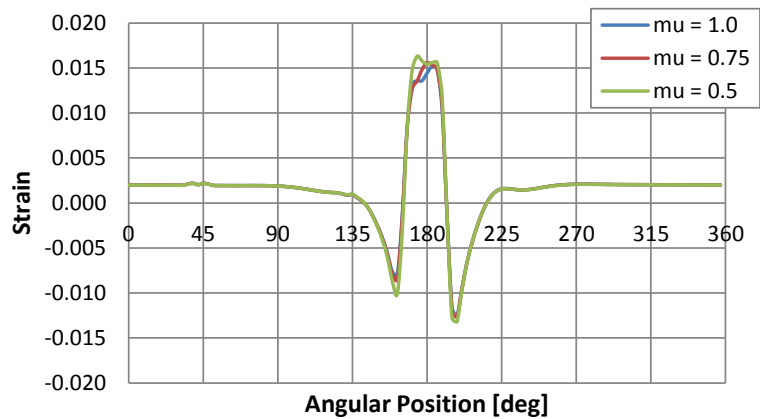


at the center of the contact patch. The peak tensile strain levels at 180 degrees were practically unmodified by braking forces; therefore, it is conceivable that strain levels at this location in the waveform can be used to estimate the friction coefficient without compensating for the influence of braking force.

Additionally, the slope of the strain waveforms just before the center of the contact patch could be used to estimate the friction coefficient, as there appears to be a relationship between the slope and the friction coefficient. Identification of the tire / road friction coefficient estimation method, assuming the tread centerline longitudinal strain measurement is used, is the subject of future work.



(a)



(b)

Figure 6.23 – Tread Centerline Longitudinal Strain at Tire Inner Liner versus Angular Position, Horizontal Tire Force = 1800 N, From the Preliminary Tire FEM: (a) Pure Cornering (b) Pure Braking

### 6.3 Summary

The following summary can be made based on the results of the smart tire outputs estimation study.

## CHAPTER 6. SMART TIRE OUTPUTS ESTIMATION

---

1. Piezoelectric sensor data from smart tire revision 2 were used to estimate the three orthogonal tire forces and the tire aligning moment.
2. Two piezoelectric sensors from the left (outside) sidewall were used to estimate tire forces, the first in a longitudinal orientation and the second in a radial orientation.
3. A points study of the piezoelectric sensor data found that at least 120 points sampled evenly over each complete wheel revolution are required in the STSS.
4. A sector study of the piezoelectric sensor data found that data from the entire wheel revolution are required in the STSS, rather than just a sector of the data centered on the footprint.
5. A reduced size training data set study found that the trends in the tire forces could be properly predicted by the neural networks, but a training data set consisting of 71% of the piezoelectric sensor data produced tire force estimates that were on average tens to hundreds of percent in error.
6. Neural network training error results show that not enough training samples were obtained during Round 1 testing, which lasted around half a day; training samples consisting of combined high forces accounted for less than 10% of the data set, an insufficient fraction.
7. The neural networks had their best performance when estimating vertical force (within 12%), their worst performance when estimating longitudinal force (within 728%) and middling performance when estimating lateral force (within 51%) and aligning moment (within 73%).
8. Modified piezoelectric data from the deteriorated Round 3 data set produced better longitudinal force estimates (within 45%) compared to Round 1, primarily due to a training data set that included positive longitudinal force samples obtained with the four wheel drive configuration of the research vehicle.
9. Future smart tire prototypes should remain at the front of the research vehicle due to the large lateral tire forces developed from steering; in addition, the front wheels should also be drive wheels in order to develop a range of longitudinal forces, both positive and negative.
10. A larger training data set is required in order to increase the accuracy of tire force estimates from the neural networks, the acquisition of which will require the identification and installation of in-tire strain sensors with much longer durability life compared to the piezoelectric sensors.
11. Virtual strain data from the preliminary tire FEM were used to investigate the estimation of the air inflation pressure and the tire / road friction coefficient, both of which were fixed to a single value in the physical tests.

12. Based on the tire FEA results, there is a linear relationship between the strain waveform offsets, as measured opposite the contact patch, and air inflation pressure.
13. It is assumed that the neural networks will be able to successfully fit the linear relationship between measured strain offsets and air inflation pressure.
14. Based on the tire FEA results, it will be difficult to use sidewall strain measurements to estimate friction coefficient, since sidewall longitudinal waveforms are not influenced by friction conditions.
15. Sidewall radial strain waveforms from the tire FEA show a relationship between strain minima and friction coefficient at the rear of the contact patch; the small strain differences at this location may be hard to distinguish in practice.
16. Displacement contours in the tire FEA show that displacement and strain patterns at the footprint vary depending on the friction condition, given the same tire force levels.
17. The tread centerline longitudinal strain measurement location shows promise for predicting the tire / road friction coefficient.
18. Processing of tensile strain at the footprint, assuming a tread centerline longitudinal strain measurement on the tire inner surface, may be a way of estimating tire / road friction coefficient, either through measuring peak strain levels or by calculating the slope of the curve just ahead of the center of the contact patch.

## Chapter 7

# Conclusion

### 7.1 System Description

The STSS is described, including sensor quantity, locations and orientations. Post-processing procedures are summarized, and an overview of STSS usage in the vehicle is included in flow chart form. Scientific contributions of the STSS research project are outlined.

#### 7.1.1 Development Challenges

The objective was to design a STSS that can determine six tire characteristics, including tire longitudinal force, tire lateral force, tire vertical force, tire aligning moment, tire / road friction coefficient and tire air inflation pressure. These STSS outputs can ultimately be used in more effective vehicle safety controllers as well as provide information about road conditions to the driver. Specific development challenges included the following items.

- Optimization of the number, locations and orientations of in-tire strain sensors to be used.
- Discovery of a method for post-processing in-tire strain measurements that can estimate the desired tire characteristics, especially tire forces, with high accuracy.
- Identification of a post-processing calculation method fast enough for use in real-time in an on-highway vehicle that can update its estimates at least once per wheel revolution.

#### 7.1.2 Construction and Operation

The STSS is a technology that can determine six tire characteristics. In a first embodiment, all six STSS outputs are calculated by post-processing the raw output from two

## CHAPTER 7. CONCLUSION

---

in-tire strain sensors and a wheel angular position sensor using artificial intelligence. The two strain sensors are located near one another on the tire inside surface at one of the sidewalls (either outside sidewall or inside sidewall, but preferably on the outside); the first is oriented longitudinally and the second is oriented radially. The wheel angular position sensor is a dedicated rotary encoder that can output at least 128 pulses per wheel revolution. It is possible that the wheel angular position may be obtained from the vehicle ABS, but only in the event that it has enough angular resolution, as well as a method for indicating a once per wheel revolution angular position index. Table 7.1 lists all of the sensors used in the STSS.

**Table 7.1 – STSS Sensors: Strain Sensors Attached to Tire Inside Surface**

Sensor Label	Sensor / Measurement Description	Notes
$\epsilon_1$	In-Tire Sidewall Longitudinal Strain	Outside Sidewall Preferred
$\epsilon_2$	In-Tire Sidewall Radial Strain	
$\theta$	Wheel Angular Position	May Be Possible to Obtain From Vehicle ABS System
$\epsilon_3$	In-Tire Tread Centerline Longitudinal Strain	In Embodiment 2 Only

In a second embodiment, all of the sensors from the first embodiment are retained. A third in-tire strain sensor is added at the tread centerline location and oriented longitudinally. The third strain sensor is located near the first two sensors, in the same angular (i.e. circumferential) position as the sidewall longitudinal sensor. The STSS of the second embodiment can estimate tire / road friction coefficient with improved accuracy compared to the first embodiment. The functional relationship between tensile strain conditions at the center of the contact patch (on the inside surface of the tire) and the friction condition is used to estimate the friction coefficient. The slope of the strain waveform before the center of the contact patch, along with peak strain levels at the center of the contact patch, are used to estimate friction coefficients. A sketch showing the STSS sensors in the tire cross-section appears in Figure 7.1.

In the STSS, tire characteristics are determined with high accuracy and calculations are made at least once per wheel revolution, up to and including highway speeds. Determination of the desired tire outputs with high accuracy and high speed is accomplished by post-processing the raw in-tire strain measurements using a form of artificial intelligence. The artificial intelligence used in the smart tire technology is a radial basis function neural network. The post-processing methodology for the raw in-tire strain measurements was formulated first using virtual strain as computed by a tire finite element model. The

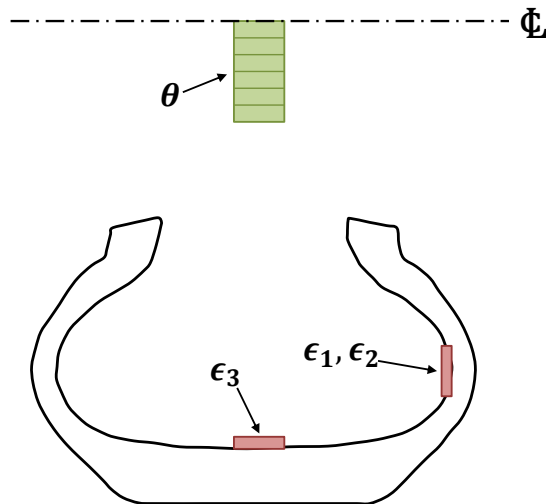


Figure 7.1 – STSS Sensors in Tire Cross-Section, Front View, Not to Scale

post-processing technique was confirmed through examination of physical strain measurements collected from a prototype STSS during on-road vehicle testing.

The STSS technology is in the early stages of development. The system has excellent performance when using virtual strain measurements as calculated by a tire FEM. In that case the tire forces and the tire aligning moment can be determined to within 1% of actual values using the STSS technology. More research must be done, however, in validating the outputs in a real vehicle. Despite imperfect physical strain data in the real world, including noisy signals and the influence of tire resonances in the strain data (not considered in the tire FEM), the STSS is ultimately expected to estimate its six tire characteristics to within 5% of their actual values. A flow chart providing a high level overview of STSS usage in vehicle appears in Figure 7.2.

### 7.1.3 Scientific Contributions

The STSS research project has resulted in new scientific knowledge regarding smart tires. A production-ready system has not been devised. However, the STSS research project has paved the way for future smart tire work, which will build on the following scientific contributions.

1. In-tire sensor quantity, locations and orientations identified.
2. Necessity of angular position measurement confirmed.
3. Architecture of artificial neural network established.

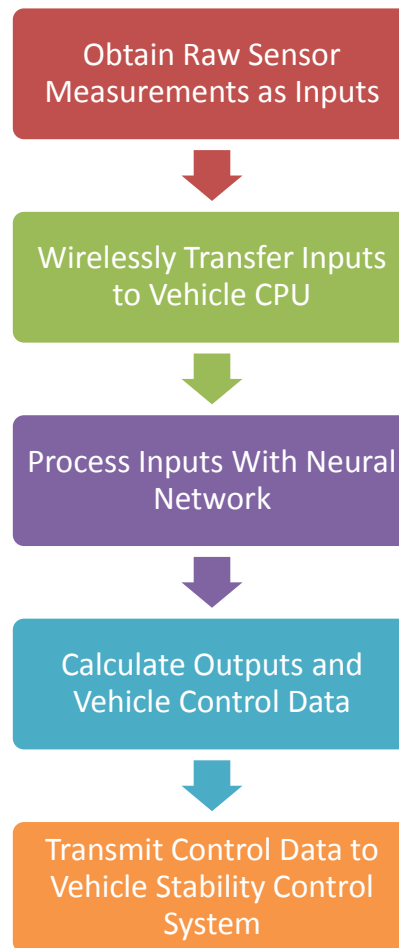


Figure 7.2 – Flow Chart for STSS in Vehicle

## 7.2 Future Work

The STSS technology is still immature. Major developments and innovations that are required are listed below. Investigation of these items is included in future research. The most significant of the technical issues still to be addressed is the identification of a sufficiently durable strain sensor for in-tire use. In addition, other future tasks include the following.



### **7.2.1 Validation of Non-Force Tire Outputs**

The three tire forces and the tire aligning moment have received particular attention in the early design phase since these characteristics are the most important from a vehicle dynamics and control perspective. Validation of the tire / road friction coefficient and air inflation pressure estimation methods requires a physical testing program designed specifically to test the accuracy of these outputs. The goal of having a STSS with six outputs remains, since a multi-use system is more desirable than a system that is narrowly focused.

### **7.2.2 Investigation of Temperature Dependence**

Tires have a wide range of operating temperatures. On a cold driving day, a tire may experience temperatures from  $-30^{\circ}\text{C}$  to  $130^{\circ}\text{C}$ , or possibly an even wider temperature range. All of the materials in the smart tire system have a deformation response to temperature loads, including the tire rubber, the sensor component materials and the wires attached to the sensors. The extent to which the strain measurements in the STSS are affected by temperature must be quantified and understood in order to compensate for this effect. The object is to measure in-tire strain associated with mechanical loads, not thermal loads.

### **7.2.3 Design of Wireless Data Transmission System**

Both STSS tire prototypes had a wired data transmission system, where signals from inside the tire were routed to the outside via cables that passed through the wheel. The STSS wheel was a dedicated prototype, with special bores drilled solely for the purpose of passing cables that connected the inside of the tire to an outside data acquisition system. This setup was for prototype validation testing only. Ultimately, the STSS will send its signals to the vehicle using a wireless transceiver. The conception and optimization of this transceiver module is required, considering in-tire requirements including low mass, small size and minimal power consumption.

### **7.2.4 Study of Energy Harvesting Methods**

Conventional batteries are an inconvenient energy storage method for in-tire use, mainly due to long tire maintenance intervals. Most tires are removed only when they require replacement, which can be five years or more in the case of passenger cars. A conventional battery would probably be depleted before the average tire needs replacement. Since the STSS wireless data transmission system must operate during the entire service life of a tire, the power supplied to it will ideally be sourced using an energy harvesting system,

## CHAPTER 7. CONCLUSION

---

where the energy required by the transceiver will be collected from a freely available source. For example, the kinetic energy associated with the motion of the tire and wheel could be transferred to electrical energy for use by the transceiver. The exact nature of the energy harvesting method, and an analysis of its limitations, is the subject of future research.

# References

- [1] Koskinen, S. and Peussa, P., 2009, "FRICTION Final Report", Technical Report No. FP6-IST-2004-4-027006, Information Society Technologies (IST) Programme, European Union (Finland).
- [2] Erdogan, G., Alexander, L. and Rajamani, R., 2011, "Estimation of Tire-Road Friction Coefficient Using a Novel Wireless Piezoelectric Tire Sensor", *IEEE Sensors Journal*, **11**(2), pp. 267–279.
- [3] Pisano, P. A., Goodwin, L. C. and Rossetti, M. A., 2009, "U.S. Highway Crashes in Adverse Road Weather Conditions", Technical Report, United States Department of Transportation, Washington, DC.
- [4] National Highway Traffic Safety Administration, 1981, *Mechanics of Pneumatic Tires*, United States Department of Transportation, Washington, DC, Chap. 9.
- [5] Bertrand, D., 2007, "Method of Determining Components of Forces Exerted on a Tire and Determining the Self-Alignment Torque", U.S. Patent No. 7,203,603 B2.
- [6] Matsuzaki, R., Keating, T., Todoroki, A. and Hiraoka, N., 2008, "Rubber-Based Strain Sensor Fabricated Using Photolithography for Intelligent Tires", *Sensors & Actuators A: Physical*, **148**(1), pp. 1–9.
- [7] Miyoshi, A., 2010, "Method for Estimating Tire Force Acting on Rolling Tire", U.S. Patent No. 7,707,876 B2.
- [8] Gillespie, T. D., 1992, *Fundamentals of Vehicle Dynamics*, Society of Automotive Engineers, Warrendale, PA, Chap. 10.
- [9] Rajamani, R., 2006, *Vehicle Dynamics and Control*, Springer Science+Business Media, New York, NY.
- [10] Fiala, E., 1954, "Seitenkraefte am rollenden Luftreifen [Lateral Forces Acting on Pneumatic Tire]", *Verein Deutscher Ingenieure – VDI Zeitschrift*, **96**(29), pp. 973–979.

## REFERENCES

---

- [11] Pacejka, H. B. and Bakker, E., 1993, "The Magic Formula Tyre Model", *Proceedings of the 1st International Colloquium on Tyre Models for Vehicle Dynamics Analysis*, Swets & Zeitlinger, Amsterdam, pp. 1–18.
- [12] Blundell, M. and Harty, D., 2004, *The Multibody Systems Approach to Vehicle Dynamics*, Society of Automotive Engineers, Warrendale, PA, Chap. 5.
- [13] Vehicle Dynamics Standards Committee, ed., 1976, *SAE J670e: Vehicle Dynamics Terminology*, Society of Automotive Engineers, Warrendale, PA.
- [14] MSC Software, 2008, "MD ADAMS/Tire R3 User Documentation", Technical Report, Santa Ana, CA.
- [15] Kiebre, R., Anstett-Collin, F. and Basset, M., 2011, "Sensitivity Analysis for the Study of Influential Parameters in Tyre Models", *International Journal of Vehicle Systems Modelling and Testing*, 6(1), pp. 72–87.
- [16] Wei, Y., 2008, "Modeling of Tire Rolling Contact Response by REF Model", SAE Paper No. 2008-01-1409.
- [17] Velenis, E., Tsiotras, P., Canudas-de-Wit, C. and Sorine, M., 2005, "Dynamic Tyre Friction Models for Combined Longitudinal and Lateral Vehicle Motion", *Vehicle System Dynamics*, 43(1), pp. 3–29.
- [18] Van Oosten, J., 2004, "Tire Testing Requirements for ADAMS/Tire PAC2002 Parameters", Technical Report, MSC Software, Santa Ana, CA.
- [19] Van Oosten, J. J. M. and Bakker, E., 1993, "Determination of Magic Tyre Model Parameters", *Proceedings of the 1st International Colloquium on Tyre Models for Vehicle Dynamics Analysis*, Swets & Zeitlinger, Amsterdam, pp. 19–29.
- [20] Lidner, L., 1993, "Experience with the Magic Formula Tyre Model", *Proceedings of the 1st International Colloquium on Tyre Models for Vehicle Dynamics Analysis*, Swets & Zeitlinger, Amsterdam, pp. 30–46.
- [21] Salaani, M. K., Heydinger, G. J. and Grygier, P. A., 2006, "Measurement and Modeling of Tire Forces on a Low Coefficient Surface", SAE Paper No. 2006-01-0559.
- [22] Dora, K. B., Karthikeyan, S., Rajasekaran, T. and Pacejka, H. B., 2006, "Design and Development of Innovative Tyre Test Facilities for Measuring Tyre Characteristics", SAE Paper No. 2006-32-0028.
- [23] Cossalter, V., Doria, A., Lot, R., Ruffo, N. and Salvador, M., 2003, "Dynamic Properties of Motorcycle and Scooter Tires: Measurement and Comparison", *Vehicle System Dynamics*, 39(5), pp. 329–352.
- [24] Dassault Systèmes Simulia, 2012, "Abaqus 6.12 Example Problems Manual", Technical Report, Providence, RI.

## REFERENCES

---

- [25] Chargin, M. and Bella, D., 2005, "Tire Models for Use in Dynamic Analyses", SAE Paper No. 2005-01-2382.
- [26] Ardeh, H. A., Datar, M., Jagadeesan, M. K. and Negrut, D., 2011, "An Expeditious High Fidelity ABAQUS-Based Surrogate Tire Model for Full Vehicle Durability Analysis in ADAMS", SAE International Journal of Materials and Manufacturing, 4(1), pp. 263–277.
- [27] Duni, E., Toniato, G., Saponaro, R., Smeriglio, P. and Puleo, V., 2010, "Vehicle Dynamic Solution Based on Finite Element Tire/Road Interaction Implemented through Implicit/Explicit Sequential and Co-Simulation Approach", SAE Paper No. 2010-01-1138.
- [28] Berzeri, M., Dhir, A., Ranganathan, R., Balendran, B., Jayakumar, P. and O'Heron, P. J., 2004, "A New Tire Model for Road Loads Simulation: Full Vehicle Validation", SAE Paper No. 2004-01-1579.
- [29] Rao, K. V. N., Kumar, R. K. and Bohara, P. C., 2004, "Prediction Of Tyre Force And Moment Characteristics During Vehicle Cornering Using Finite Element Techniques", SAE Paper No. 2004-28-0004.
- [30] Rao, K. V. N., Kumar, R. K., Mukhopadhyay, R. and Misra, V. K., 2006, "A Study of the Relationship Between Magic Formula Coefficients and Tyre Design Attributes through Finite Element Analysis", Vehicle System Dynamics, 44(1), pp. 33–63.
- [31] Balaramakrishna, N. and Kumar, R. K., 2009, "A Study on the Estimation of SWIFT Model Parameters by Finite Element Analysis", *Proceedings of the Institution of Mechanical Engineers, Part D: Journal of Automobile Engineering*, Professional Engineering Publishing, Westminister, UK, 223, pp. 1283–1300.
- [32] Ju, J., Ananthasayanam, B., Summers, J. D. and Joseph, P., 2010, "Design of Cellular Shear Bands of a Non-Pneumatic Tire - Investigation of Contact Pressure", SAE International Journal of Passenger Cars - Mechanical Systems, 3(1), pp. 598–606.
- [33] Veeramurthy, M., Ju, J., Thompson, L. L. and Summers, J. D., 2011, "Optimization of a Non-Pneumatic Tire for Reduced Rolling Resistance", *Proceedings of the ASME 2011 International Design Engineering Technical Conferences & Computers and Information in Engineering Conference*, ASME Paper No. DETC2011-48730.
- [34] Narasimhan, A., Ziegert, J. and Thompson, L., 2011, "Effects of Material Properties on Static Load-Deflection and Vibration of a Non-Pneumatic Tire During High-Speed Rolling", SAE International Journal of Passenger Cars - Mechanical Systems, 4(1), pp. 59–72.
- [35] Ryu, S., Kim, D., Ju, J. and Heo, H., 2011, "Separable Polyurethane Solid Tires for a Folding Bike", *Proceedings of the ASME 2011 International Design Engineering Technical*

## REFERENCES

---

- Conferences & Computers and Information in Engineering Conference*, ASME Paper No. DETC2011-47293.
- [36] Mohsenimanesh, A., Ward, S. M. and Gilchrist, M. D., 2008, "Stress Analysis of a Multi-Laminated Tractor Tyre using Non-Linear 3D Finite Element Analysis", *Materials and Design*, **30**(4), pp. 1124–1132.
- [37] Yang, X., Olatunbosun, O. and Bolarinwa, E., 2010, "Materials Testing for Finite Element Tire Model", *SAE International Journal of Materials and Manufacturing*, **3**(1), pp. 211–220.
- [38] Behroozi, M., Olatunbosun, O. A. and Ding, W., 2011, "Finite Element Analysis of Aircraft Tyre - Effect of Model Complexity on Tyre Performance Characteristics", *Materials and Design*, Corrected Proof.
- [39] Kim, K., Ju, J., Kim, D. and Rhie, S., 2011, "Finite Element Analysis of Tire and Pavement Interaction", *Proceedings of the ASME 2011 International Design Engineering Technical Conferences & Computers and Information in Engineering Conference*, ASME Paper No. DETC2011-47290.
- [40] National Highway Traffic Safety Administration, 2005, "Tire Pressure Monitoring Systems, Controls and Displays, Final Rule", Technical Report No. RIN 2127-AJ23, United States Department of Transportation, Washington, DC.
- [41] Zhang, X., Wang, F., Wang, Z., Li, W. and He, D., 2004, "Intelligent Tires Based on Wireless Passive Surface Acoustic Wave Sensors", *Proceedings of the 2004 IEEE Intelligent Transportation Systems Conference*, pp. 960–964.
- [42] Flatscher, M., Dielacher, M., Herndl, T., Lentsch, T., Matischek, R., Prainsack, J., Pribyl, W., Theuss, H. and Weber, W., 2010, "A Bulk Acoustic Wave (BAW) Based Transceiver for an In-Tire-Pressure Monitoring Sensor Node", *IEEE Journal of Solid-State Circuits*, **45**(1), pp. 167–177.
- [43] Holscher, H., Tewes, M., Botkin, N., Lohndorf, M., Hoffmann, K. H. and Quandt, E., 2004, "Modeling of Pneumatic Tires by a Finite Element Model for the Development a Tire Friction Remote Sensor", Preprint Submitted to *Computers & Structures*.
- [44] Sergio, M., Manaresi, N., Tartagni, M., Canegallo, R. and Guerrieri, R., 2006, "On a Road Tire Deformation Measurement System Using a Capacitive-Resistive Sensor", *Smart Materials and Structures*, **15**(6), pp. 1700–1706.
- [45] Yi, J., 2008, "A Piezo-Sensor-Based "Smart Tire" System for Mobile Robots and Vehicles", *IEEE/ASME Transactions on Mechatronics*, **13**(1), pp. 95–103.
- [46] Dennehy, D. J., Jones, R. P. and Mottram, J. T., 2002, "Foresight Vehicle: Drive-by-Tyre", SAE Paper No. 2002-01-1872.

## REFERENCES

---

- [47] Ohori, M., Ishizuka, T., Fujita, T., Masaki, N. and Suizu, Y., 2006, "Fundamental Study of Smart Tire System", *Proceedings of the IEEE 2006 Intelligent Transportation Systems Conference*, pp. 1519–1524.
- [48] Matsuzaki, R. and Todoroki, A., 2008, "Wireless Monitoring of Automobile Tires for Intelligent Tires", *Sensors*, **8**(12), pp. 8123–8138.
- [49] Matsuzaki, R. and Todoroki, A., 2008, "Intelligent Tires for Improved Tire Safety Using Wireless Strain Measurement", *Proceedings of SPIE 2008: Sensors and Smart Structure Technologies for Civil, Mechanical, and Aerospace Systems*, Society of Photo-Optical Instrumentation Engineers, Bellingham, WA, **6932**, pp. 1–11.
- [50] Nepote, A., Pierre, P. D. L., Varpula, T., Rautiainen, A. and Jaakkola, K., 2005, "The Intelligent Tire: Acceleration Sensors Data Acquisition", SAE Paper No. 2005-01-1481.
- [51] Savaresi, S. M., Tanelli, M., Langthaler, P. and Re, L. D., 2008, "New Regressors for the Direct Identification of Tire Deformation in Road Vehicles Via "In-Tire" Accelerometers", *IEEE Transactions on Control Systems Technology*, **16**(4), pp. 769–780.
- [52] Ergen, S. C., Sangiovanni-Vincentelli, A., Sun, X., Tebano, R., Alalusi, S., Audisio, G. and Sabatini, M., 2009, "The Tire as an Intelligent Sensor", *IEEE Transactions on Computer-Aided Design of Integrated Circuits and Systems*, **28**(7), pp. 941–955.
- [53] Erdogan, G., Hong, S., Borrelli, F. and Hedrick, K., 2011, "Tire Sensors for the Measurement of Slip Angle and Friction Coefficient and Their Use in Stability Control Systems", *SAE International Journal of Passenger Cars - Mechanical Systems*, **4**(1), pp. 44–58.
- [54] Morinaga, H., Wakao, Y. and Kobayakawa, A., 2009, "Estimation Method and Apparatus of Tire Dynamic State Amount and Tire with Sensors", U.S. Patent No. 7,546,764 B2.
- [55] Savaresi, S., Tanelli, M. and Langthaler, P., 2012, "Method for Calculating Forces Acting on the Footprint Area of a Tyre and Apparatus for Calculating said Forces", U.S. Patent No. 8,165,827 B2.
- [56] Tebano, R. and Audisio, G., 2014, "Method and System for Determining the Potential Friction Between a Tyre for Vehicles and a Rolling Surface", U.S. Patent No. 8,626,454 B2.
- [57] Tebano, R., Audisio, G. and Fioravanti, A., 2014, "Method and System for Estimating the Inflation Pressure of a Tire", U.S. Patent No. 8,833,151 B2.
- [58] Brusarosco, M., Mancosu, F. and Arosio, D., 2014, "Method and System for Determining a Tyre Load During the Running of a Motor Vehicle", U.S. Patent No. 8,874,386 B2.

---

## REFERENCES

---

- [59] Treloar, L. R. G., 1944, "Stress-Strain Data for Vulcanised Rubber Under Various Types of Deformation", *Transactions of the Faraday Society*, **40**(1), pp. 59–70.
- [60] MSC Software, 2010, "Nonlinear Finite Element Analysis of Elastomers", Technical Report, Santa Ana, CA.
- [61] Shabana, A. A., 2012, *Computational Continuum Mechanics*, Cambridge University Press, New York, NY, 2nd ed.
- [62] Dassault Systèmes Simulia, 2012, "Abaqus 6.12 Analysis User's Manual", Technical Report, Providence, RI.
- [63] Boyce, M. C. and Arruda, E. M., 2000, "Constitutive Models of Rubber Elasticity: A Review", *Rubber Chemistry and Technology*, **73**(3), pp. 504–523.
- [64] Govindarajan, S. M. and Hurtado, J. A., 2010, "Anisotropic Hyperelastic Models in Abaqus", *Proceedings of the 6th European Conference on Constitutive Models for Rubber*, German Research Foundation (DFG), Bonn, DE, pp. 365–369.
- [65] National Highway Traffic Safety Administration, 1981, *Mechanics of Pneumatic Tires*, United States Department of Transportation, Washington, DC, Chap. 10.
- [66] Rao, S. S., 1990, *Mechanical Vibrations*, Addison-Wesley Publishing, Reading, MA, 2nd ed.
- [67] Negnevitsky, M., 2005, *Artificial Intelligence: A Guide to Intelligent Systems*, Addison-Wesley, New York, NY.
- [68] Jang, R., Sun, C. and Mizutani, E., 1997, *Neuro-Fuzzy and Soft Computing: A Computational Approach to Learning and Machine Intelligence*, Prentice Hall, Upper Saddle River, NJ.
- [69] The MathWorks, 2013, "MATLAB R2013a Documentation", Technical Report, Natick, MA.
- [70] Karray, F. and De Silva, C., 2004, *Soft Computing and Intelligent Systems Design: Theory, Tools and Applications*, Addison-Wesley, New York, NY.
- [71] Tsoukalas, L. and Uhrig, R., 1997, *Fuzzy and Neural Approaches in Engineering*, John Wiley & Sons, New York, NY.
- [72] Tufféry, S., 2011, *Data Mining and Statistics for Decision Making*, John Wiley & Sons, Hoboken, NJ.
- [73] Cherkassky, V. and Mulier, F., 2007, *Learning from Data: Concepts, Theory, and Methods*, John Wiley & Sons, Hoboken, NJ.



## REFERENCES

---

- [74] Bastiaan, J. M., 2013, "Design of a Smart Tire Sensor System – Research Proposal", Technical Report, University of Waterloo, Waterloo, ON.
- [75] Rao, S. S., 2011, *The Finite Element Method in Engineering*, Elsevier / Butterworth-Heinemann, Boston, MA, 5th ed.
- [76] Ballas, R. G., 2007, *Piezoelectric Multilayer Beam Bending Actuators*, Springer Science+Business Media, New York, NY.
- [77] Sirohi, J. and Chopra, I., 2000, "Fundamental Understanding of Piezoelectric Strain Sensors", *Journal of Intelligent Material Systems and Structures*, **11**(4), pp. 246–257.
- [78] Measurement Specialties, 2008, "Piezo Film Product Guide and Price List", Technical Report, Hampton, VA.
- [79] Vishay Precision Group, 2010, "Fatigue Characteristics of Micro-Measurements Strain Gages", Technical Report No. TN-508-1, Malvern, PA.
- [80] National Highway Traffic Safety Administration, 2006, "The Pneumatic Tire", Technical Report No. HS-810-561, United States Department of Transportation, Washington, DC.

# APPENDICES

## Appendix A

# Tire FEM Procedures and Geometry

### A.1 Numerical Method

Finite element analysis is a numerical method that can be used to find approximate solutions to problems in solid mechanics. From the point of view of the STSS research project, the “solid” is a tire. The finite element representation of a solid is discontinuous, in the sense that it is made up of discrete subdivisions called finite elements, which in turn are related to one another through joints called nodes. Often the accuracy of a finite element analysis solution can be improved with an increase in the number of finite elements, albeit at the expense of increased computational costs.

In a static finite element analysis, the equilibrium equations of a structure can be written as:

$$\mathbf{K} \mathbf{Q} = \mathbf{P} \quad (\text{A.1})$$

where  $\mathbf{K}$  is the stiffness matrix,  $\mathbf{Q}$  is the vector of nodal displacements and  $\mathbf{P}$  is the nodal load vector [75]. Once the boundary conditions are incorporated into the static problem, the equilibrium equations are solved for the nodal displacements. The element strains are computed based on the nodal displacements.

In a transient dynamic finite element analysis, the equations of motion of a structure can be represented by:

$$\mathbf{M} \ddot{\mathbf{Q}}(t) + \mathbf{C} \dot{\mathbf{Q}}(t) + \mathbf{K} \mathbf{Q}(t) = \mathbf{P}(t) \quad (\text{A.2})$$

where  $\mathbf{K}$ ,  $\mathbf{Q}$  and  $\mathbf{P}$  have the same meaning as in Equation (A.1),  $\mathbf{M}$  is the mass matrix,  $\mathbf{C}$  is the damping matrix,  $\ddot{\mathbf{Q}}$  is the nodal accelerations vector and  $\dot{\mathbf{Q}}$  is the vector of nodal velocities. In Equation (A.2) the loads and nodal quantities are functions of time  $t$ . Boundary

and initial conditions are applied in the transient dynamic problem, resulting in nodal displacement time histories. Element strains as a function of time are determined based on nodal displacements, as in the static case. Transient dynamic finite element analysis can be performed using both implicit and explicit time integration procedures.

The STSS research project employed finite element analysis as a design tool. A tire finite element model was used to simulate various loading conditions, including both static and dynamic events. Static loads are comprised of air inflation pressure and vehicle corner weight. Dynamic cases include relatively simple steady-state dynamic events, such as free rolling on a flat, consistent surface or steady-state braking, steady-state cornering or a combination of the two.

Transient dynamic events are also of interest, including analysis of travel over geometrically uneven roads, investigation of rapidly changing tire / road friction conditions and determination of vehicle acceleration effects. During the STSS research project, however, transient events were not simulated using finite element analysis. Instead, finite element analysis studies were restricted to analysis of static and steady-state dynamic events, primarily due to computer hardware limitations.

## A.2 Analysis Procedures

Tire finite element models were created for and solved with ABAQUS version 6.12-3. A true SI metric system of units (i.e. kg, m, N) was used in the finite element models; when results are presented in other units, they have been converted from the original SI analysis output. All of the finite element models represent solid rubber components using first-order bricks of “hybrid” element type C3D8H. This is the recommended continuum element type for incompressible (or nearly incompressible) materials in ABAQUS/Standard.

Fiber reinforcement layers are represented using surface element type SFM3D4R, the properties of which are defined using the \*REBAR LAYER definition. The \*EMBEDDED ELEMENT feature is used to attach the fiber reinforcement layer to the rubber substrate. The translational degrees of freedom of the embedded reinforcement elements are constrained to the analogous degrees of freedom of the host rubber elements. Therefore, the nodes of the reinforcement elements are effectively tied to the nodes of the rubber elements and the translational degrees of freedom of the embedded nodes are removed from the analysis.

The finite element model is built by first defining a two-dimensional cross-section. The cross-section consisting of CGAX4R and SFMGAX1 axi-symmetric elements is revolved and extruded in order to create a three-dimensional tire finite element model consisting of solid elements (rubber) and surface elements (reinforcements). Using this modeling approach, nodal streamlines are formed in the finite element model of the tire. The tire

**APPENDIX A. TIRE FEM PROCEDURES AND GEOMETRY**

---

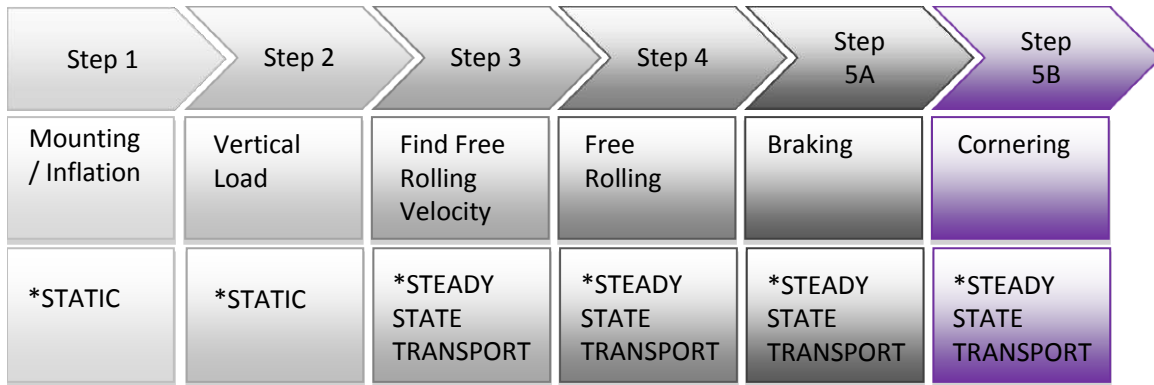


**Figure A.1 – Tire Finite Element Analysis Steps Flowchart**

is put into contact with a rigid road in the simulations; there is a user-defined friction coefficient applied between the tire and the road. The entire finite element model is flexible except for the rigid rim and the rigid road. These rigid components are usually masked in the images of the model.

Material properties for the tire finite element model were obtained through dedicated physical tests performed as part of the STSS research project. Rubber is modeled as both a hyperelastic and a viscoelastic material in the model. Material damping is applied to the tire rubber through its viscoelastic material properties. Viscoelastic material properties were not used by the static finite element analyses. However, they were used in simulated frequency response measurements performed in order to calculate damping in the modes of the tire. In that case the ABAQUS procedure used was \*STEADY STATE DYNAMICS, DIRECT, which is a relatively expensive direct dynamics method that calculates the response of a structure directly in terms of its physical degrees of freedom. All finite element analysis results were obtained using static and steady-state transport procedures in ABAQUS/Standard, which uses implicit finite element analysis methods.

**A.2.1 Static Analysis**

Most of the tire finite element analyses performed during the STSS research project were simulations of dynamic events using the steady-state transport method. Before dynamic events can be analyzed, however, two non-linear static analysis steps are performed using ABAQUS procedure \*STATIC. Each analysis step calculates the base state for the subsequent analysis step, regardless of whether it is static or dynamic. A flowchart listing all the analysis steps is shown in Figure A.1. The air inflation pressure of Step 1 is varied depending on the analysis performed. The value of vertical load (i.e. vehicle corner weight) in Step 2 is also modified depending on the analysis. An overview of the two static steps is included in Table A.1.

### A.2.2 Steady-State Dynamic Analysis

The steady-state transport finite element analysis approach (ABAQUS procedure \*STEADY STATE TRANSPORT) used for tire dynamic analysis in the STSS research project is a mixed Lagrangian / Eulerian method [62]. Rigid body motion is analyzed using a spatial (Eulerian) approach. Deformation is analyzed using a material (Lagrangian) approach; it is calculated relative to the rigid body rotation of the tire.

Steady-state transport analysis is suitable for the analysis of rolling and sliding contact between a tire and a flat, convex or concave road. In this method the reference frame is attached to the axle. An observer in this reference frame would perceive the nodes of the tire finite element model as stationary; the material would move with respect to the nodes. Thus the tire finite element model does not undergo large rigid body rotation in steady-state transport analysis. The analysis procedure includes inertial (“d’Alembert”) forces, both centrifugal and Coriolis forces, which are associated with rotation.

**Table A.1 – Tire Finite Element Model Static Load Cases**

Anal- ysis Step No.	Step Name	Load Value	Load Location
1	Inflation	120 to 280 kPa (17.4 to 40.6 psi)	Distributed Surface Load Applied to Inside of Tire
2	Vertical Load	5050 to 7600 N (1135 to 1710 lb)	Concentrated Translational Load Applied Vertically at Wheel Center
Anal- ysis Step No.	Load Value Based On	Boundary Conditions On Rigid Rim	Boundary Conditions On Rigid Road
1	Typical Air Pressure Range	Fixed to Zero Displacement	Fixed to Zero Displacement
2	Expected Vehicle Corner Weight Range	Fixed to Zero Displacement in All Degrees of Freedom Except Vertical Translation	Fixed to Zero Displacement

The main advantage of the steady-state transport method, as opposed to the explicit approach to dynamic finite element analysis, is that the cost of the steady-state transport analysis is independent of tire rolling speed. In an explicit dynamic analysis the rolling

---

## APPENDIX A. TIRE FEM PROCEDURES AND GEOMETRY

---

motion of the tire is a time-dependent process; a very small analysis time increment may be necessary. Therefore, the cost of the explicit dynamic analysis increases with rolling speed. However, it must be noted that the explicit dynamic finite element method is required for analysis of the interaction between a tire and an arbitrary road.

Tire sweep tests simulated using the steady-state transport method in ABAQUS are listed in Table A.2. The braking test of Step 5A and the cornering test of Step 5B are described along with the nomenclature normally used for these sweep tests in the literature. In the simulated sweep tests the tire forces and moments are measured at the wheel center. Two analysis procedures precede the braking and cornering tests. Step 3 is performed to find a true free rolling velocity in which no brake or drive torques exist at the wheel center. Step 4 is a free rolling analysis. Step 5A and Step 5B are both performed after Step 4 is complete.

**Table A.2 – Tire Finite Element Model Steady-State Dynamic Load Cases**

Analysis Step No.	Step Name	Longitudinal Speed [KPH]	Slip Ratio
5A	Pure Braking	20 to 80 (Typically 60)	0 (Free Rolling) to 1 (Fully Locked and Skidding)
5B	Pure Cornering	20 to 80 (Typically 60)	0 (Free Rolling)
Analysis Step No.	Slip Angle [degree]	Vertical Load [kN]	Camber Angle [degree]
5A	0	5 to 7.6	0
5B	0 to 15	5 to 7.6	0

The 60 KPH longitudinal speed typically used in the simulations was selected since it is common city driving speed and it is in the range of speeds normally used during tire testing [18, 20, 21]. Tire forces and moments as determined during physical testing should not have a strong dependence on speed [8]. Normally, very high speeds are not used in physical tire testing since they result in premature tire wear and thus more examples of a particular tire are required during the test procedure. This is not an issue in the finite element analysis, but it explains why moderate speeds are usually used during tire physical tests.

### A.2.3 Assumptions

Assumptions regarding the static and steady-state transport finite element analysis procedures are enumerated below, along with the assumptions for the tire finite element model created specifically for use in the STSS research project.

## APPENDIX A. TIRE FEM PROCEDURES AND GEOMETRY

---

1. The steady-state transport procedure in ABAQUS is suitable for the analysis of steady operation of a tire in contact with a flat road, where frictional effects and material non-linearity are both important.
2. Analysis of transient dynamic events is not required for validation of a tire finite element model.
3. Both the wheel and the road can be modeled as rigid bodies; their flexibility does not significantly influence the behavior of the tire with respect to the tire forces developed and the deformation of the tire itself.
4. Temperature and aging effects on the behavior of rubber can be ignored.
5. Different rubber materials used in the construction of a tire can be represented with one general rubber material property; for example, the particular rubber material used in the tire inner liner that makes the tire impermeable to air can be modeled with the same rubber material that is used in the main body of the tire.
6. Deformation of the tire inner liner is strongly correlated with tire forces and air inflation pressure, and thus it is a good first guess for the location of strain sensors in the STSS.

Limitations of the static and steady-state transport finite element analysis procedures for tire applications are listed below.

- Time-dependent loads cannot be modeled; for example, the transient response of a tire in contact with a flat road when subjected to a rapid change in slip angle (i.e. cornering force) cannot be analyzed.
- Vehicle acceleration effects cannot be considered.
- Geometrically varying roads cannot be modeled, such as those containing potholes, speed bumps and a rough, inconsistent surface.
- Rapidly changing tire / road friction cannot be analyzed.

None of these limitations were important during the STSS research project, since it was a feasibility study during which basic tire events were modeled and analyzed. However, future smart tire development work may require the simulation of transient events such as traveling through an abrupt transition from smooth asphalt to loose gravel. Tire transient dynamic scenarios such as this example event can be analyzed using explicit finite element methods available in ABAQUS/Explicit, which were not investigated during the STSS research project.





Figure A.2 – Michelin Used Tires

### A.3 Physical Geometry

Tire physical geometry for finite element model creation was obtained using a reverse engineering process, as design drawings of the tire under study were not available. Figure A.2 shows the Michelin used tires acquired for use during the model creation process; in this photograph a sector is cut from the tire at the top of the stack. The used tires were obtained for the purpose of physical testing and to aid in the tire finite element model creation process. Basic information acquired from the used tire sidewalls is listed in Table A.3. The set of four used tires was taken off of a single vehicle; its tires were around 75% used when they were taken off. The acquisition of well used tires was a deliberate choice, since they are considered representative of typical tires on actual vehicles in highway service.

#### A.3.1 Tread and Cross-Section

Figure A.3 shows a scan of the Michelin tire tread. Tread wear is clearly visible, as some sipes have practically no depth remaining. The passenger car tires employed during the STSS research project did not have pronounced “lugs” even when they were new; in the worn condition as received, the lug motion frequency associated with the passing of the

---

**APPENDIX A. TIRE FEM PROCEDURES AND GEOMETRY**

---

**Table A.3 – Information From Michelin Used Tire Sidewalls**

Make	Michelin
Model	Pilot HX MXM4
Type	All-Season Passenger Car
Size	P 235 / 50 R 18 97V
Maximum Load [kg]	730
Maximum Pressure [kPa]	300
Tread Plies	2 Polyester, 2 Steel, 1 Polyamide
Sidewall Plies	2 Polyester

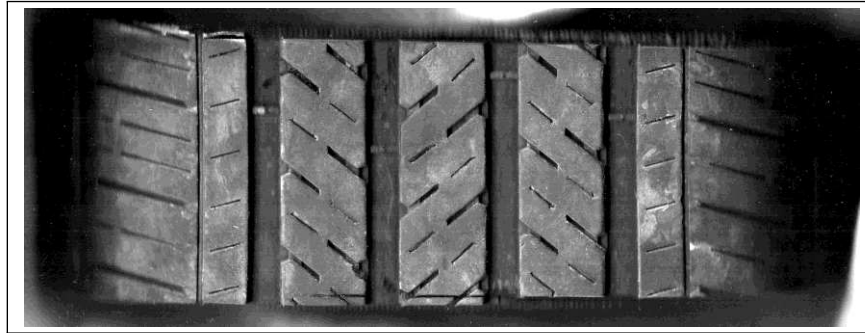


**Figure A.3 – Scan of Michelin Tire Tread**

lugs through the contact patch was unlikely to be measured in the physical tests. The tires had three continuous rubber tread bands around the circumference of the tire. Each of these bands was interrupted with sipes, not lugs. Two continuous bands at the lateral periphery of the tires consisted of minor lugs with a quantity of approximately 80 per complete revolution of the tire. Therefore, at a wheel fundamental frequency of 5 Hz, the lug passing frequency would be around 400 Hz.

Figure A.4 shows an annotated scan of the Michelin tire cross-section. Components identified with white labels are made from rubber; components labelled in color are made from other materials. The scans in Figures A.3 and A.4 are images of the sector cut from one of the used tires. These scans were used to determine the basic geometry of the tire for finite element model creation.

Figure A.5 shows the tire cross-section right hand side feature lines obtained from the scan using the MATLAB Version R2013a Image Processing Toolbox. Figure A.6 shows the full tire cross-section feature lines in their proper spatial orientation and position. The uninflated outer diameter of the tire is 0.7-m  $\approx$  27-in. Axi-symmetric finite element models of the tire cross-section were created based on the feature lines. The axi-symmetric tire finite element models were extruded and revolved in order to create the full three-dimensional tire finite element models.

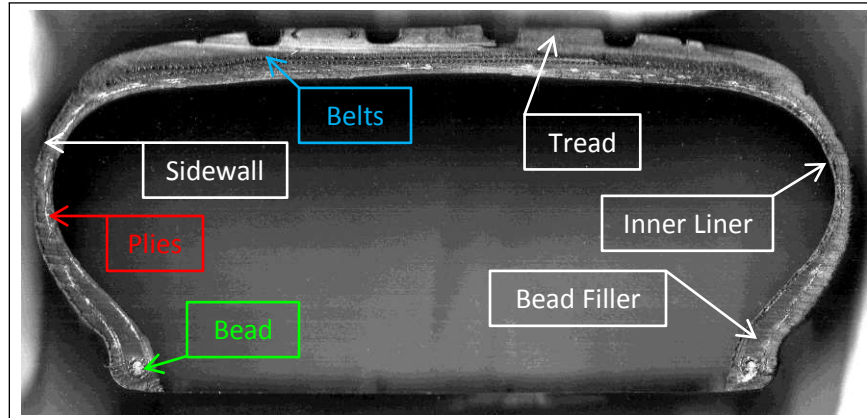


Figure A.4 – Annotated Scan of Michelin Tire Cross-Section

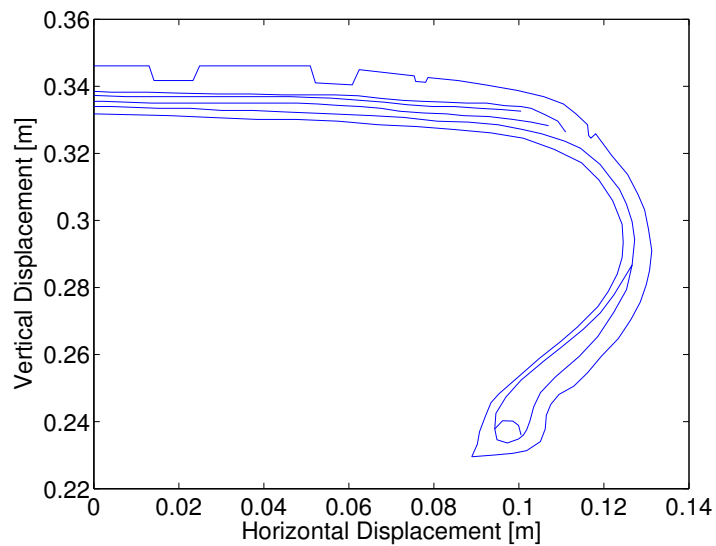


Figure A.5 – Half of Tire Cross-Section Feature Lines

### A.3.2 Fiber Reinforcement

Fiber reinforcement properties were obtained simply by making measurements of exposed fibers in cut tire samples using a ruler and a protractor. Tables A.4 and A.5 list the location and orientation of the fiber reinforcement layers, as well as the diameter and spacing of the fibers themselves. It is important to note that these are estimates used in the finite element model creation process; in some cases the values were modified later for better correlation with experimental results. For example, in Table A.4 the bottom

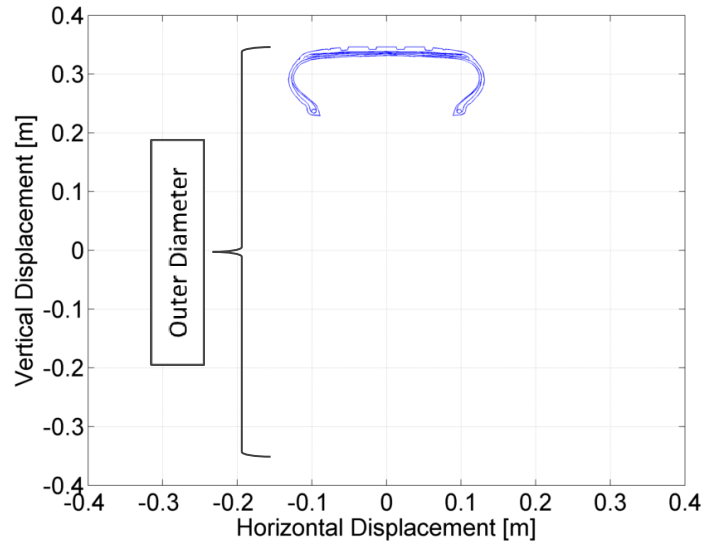


Figure A.6 – Full Tire Cross-Section Feature Lines

polyester layer is listed as 1 mm from the inside surface of the tire. This value is an approximation that is appropriate given the precision of the instruments used to make the measurements.

Table A.4 – Location and Orientation of Fiber Reinforcements

Name of Rebar Layer	Distance from Inside Surface of Tire [mm]	Angular Orientation of Rebar w.r.t. Longitudinal Direction (Degree)
Polyamide_Layer	7	0
Steel_Top_Layer	5	-30
Steel_Bottom_Layer	4	30
Polyester_Top_Layer	2	90
Polyester_Bottom_Layer	1	90

**Table A.5 – Diameter and Spacing of Fiber Reinforcements**

Name of Rebar Layer	Diameter of Rebar [mm]	Spacing of Rebar [mm]
Polyamide_Layer	0.33	0.83
Steel_Top_Layer	0.33	1.25
Steel_Bottom_Layer	0.33	1.25
Polyester_Top_Layer	0.25	1
Polyester_Bottom_Layer	0.25	1

## A.4 Mesh Geometry

### A.4.1 Finite Element Size

A mesh convergence study was used to find the optimum finite element size for the tire finite element model, given the tire physical geometry and the computer hardware constraints on the STSS research project. The intent of a mesh convergence study is to identify a compromise between accuracy of results and computational expense. The steps in a tire mesh convergence study are as follows. First, the tire is modeled using the largest finite elements reasonably possible (given the geometry) and solved. Second, the tire is modeled with smaller finite elements and solved. The second finite element analysis results are compared with the results from the first rougher mesh. This process of decreasing the finite element size is continued until the results converge.

Any relevant results from the finite element models can be compared. In the case of the tire model, the focus was on 1) displacement due to air inflation pressure and 2) strain at the tire inner liner during rolling events. Converged strain predictions from the tire finite element model were important since strain sensors were investigated for in-tire use in the STSS. Thus, the tire finite element model being used as a design tool was required to calculate displacements and strains with reasonable accuracy.

Simplified tire finite element models were created for use in the mesh convergence study. The basic tire geometry was obtained from the reverse engineering process, but not all of the reinforcement plies were included (the reinforcements were modeled in detail in later models). In the simplified model, a polyester fiber carcass was modeled along with two steel belts; one rubber material was used to represent the tire body. Preliminary material properties and ply geometries were obtained from a SAE paper on the subject of tire finite element analysis [53]; these properties were further modified and improved subsequent to the mesh convergence study.

Three axi-symmetric tire finite element models were built for the mesh convergence study, with finite elements of approximately 5-mm (coarse density), 2.5-mm (medium density) and 1-mm (fine density) in size. Each model consisted of rectangular elements very close to square in shape. Each model also had two versions; one with linear in-

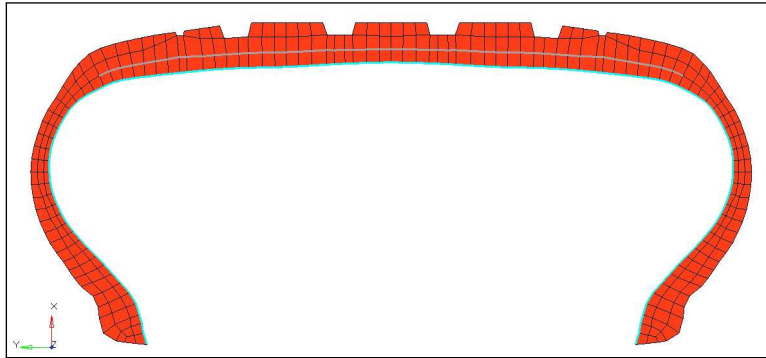


Figure A.7 – Simplified Tire FEM with Element Size = 5-mm

terpolation elements and another with quadratic interpolation elements having mid-side nodes. Figure A.7 shows the 5-mm model.

Von Mises stress contours for the 5-mm finite element model in the 2D axi-symmetric inflation analysis are shown in Figure A.8. The analysis ended prematurely at the one-third point; results from this analysis time are shown. The checker-board stress pattern and sawtooth deformation shape are evidence of a mesh instability called “shear / volumetric locking” [62]. This problem occurs when the element length is too close to the thickness dimension. Per the ABAQUS documentation, four elements should be required through the thickness. Previous personal experience with finite element modeling of rubbery materials (for use in surface layer damping treatments) suggests that there should be at least three elements through the thickness. Clearly the two elements through the thickness of the tire in the tread area immediately underneath the grooves of the 5-mm model was insufficient.

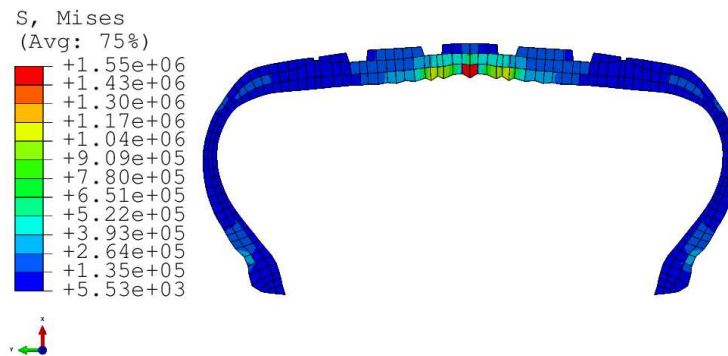
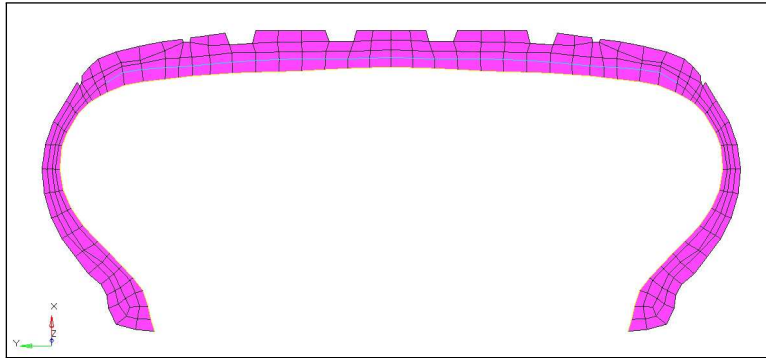


Figure A.8 – Incorrect Inflation Stress Contours in 5-mm FEM



**Figure A.9 – Simplified Tire FEM with Element Size = 8-mm**

Due to the failure of the coarse 5-mm finite element model, a different coarse finite element model was created with elements of approximately 8-mm size. The purpose in creating the 8-mm (coarse density) model was to create finite element analysis results from a rough approximation of the tire cross-section for comparison with the medium and fine density models that was capable of solving successfully. Since the coarse model had to solve in relatively short wall-clock times, in addition to solving successfully (implying three or four elements through the thickness), the 8-mm model was created with rectangular shape elements rather than the ideal square shape elements. Figure A.9 shows the 8-mm finite element model with coarse element density.

Figure A.10 shows 3D tire finite element models used in the air inflation analysis; half of the model is masked such that the cross-section is visible. All of the 3D models depicted are based on a 2.5-mm (medium density) 2D axi-symmetric model. The 3D models differ with respect to sector size; that is, extruded thickness. The largest sector size of  $3^\circ$  was chosen for use in the mesh convergence study, since that was the only sector size with reasonable computational requirements, given the desktop computer in use. See Table B.3 in Appendix B for an overview of the configuration of the computer used in the STSS research project to solve ABAQUS jobs.

The air inflation analysis for the model of Figure A.10a ( $3^\circ$ ) required 4065 MB physical memory and 23 minutes wall-clock time, which was acceptable. The models of Figure A.10b ( $1.5^\circ$ ) and Figure A.10c ( $1^\circ$ ) required 7546 and 13010 MB of physical memory, respectively. The air inflation analysis process for the  $1.5^\circ$  model (midsize extruded thickness) was terminated after several hours of wall-clock time, with the analysis still incomplete, due to unreasonable solve time requirements. The desktop computer used was not capable of solving the  $1^\circ$  model due to insufficient physical memory. Therefore, due to computational limitations the various 2D axi-symmetric models were always extruded with a sector size of  $3^\circ$ , as smaller sector sizes could not be solved.

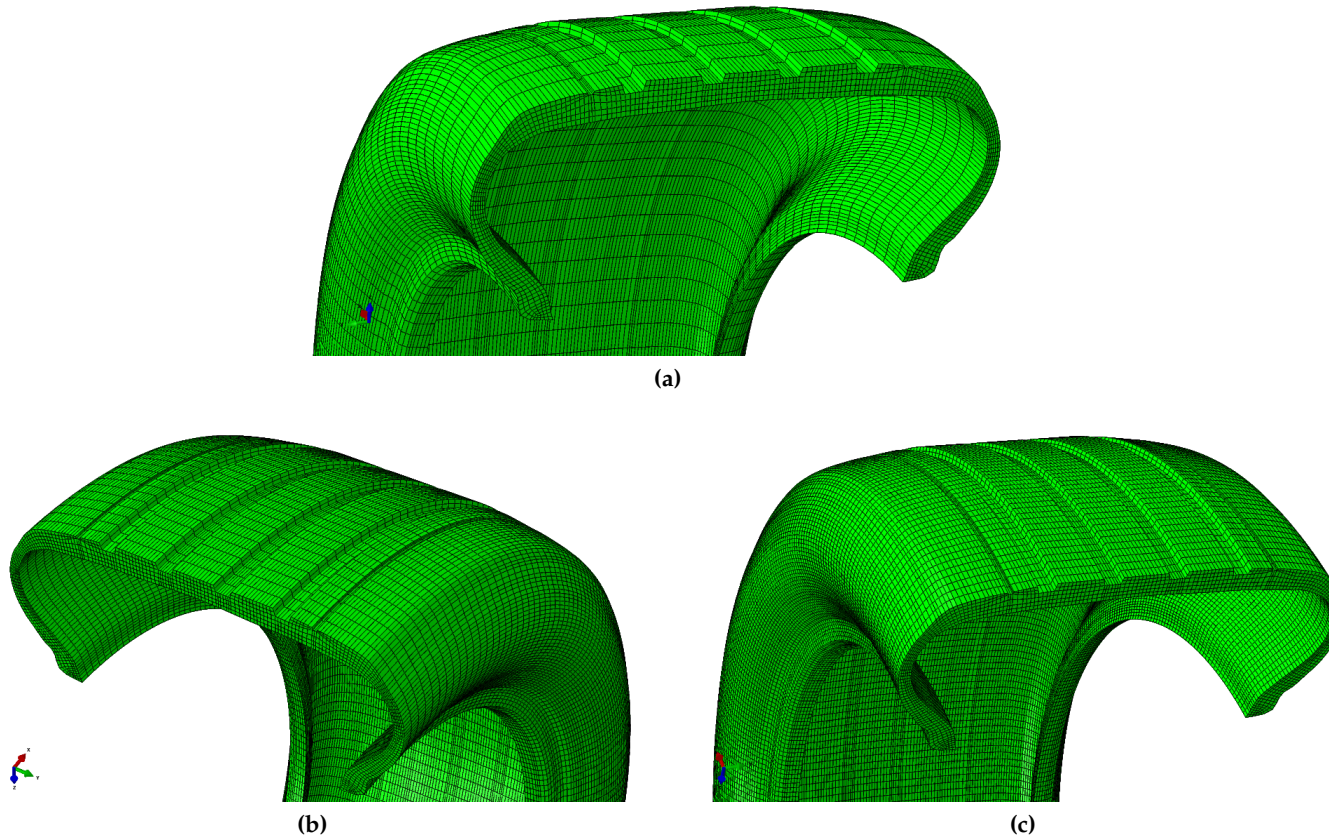


Figure A.10 – 3D Tire FEM Sector Size with 2.5-mm Cross-Section: (a)  $3^\circ$  (b)  $1.5^\circ$  (c)  $1^\circ$



---

**APPENDIX A. TIRE FEM PROCEDURES AND GEOMETRY**

---

All of the two-dimensional axi-symmetric finite element models could solve successfully on the desktop computer in an air inflation analysis within a few minutes. This is the only analysis type in which the 1-mm models were able to finish solving; the three-dimensional models based on the 1-mm axi-symmetric models could not be solved due to excessive memory requirements in the tens of thousands of megabytes. In general, the 2.5-mm quadratic model also had memory requirements that were too high for the desktop. Only the coarse 8-mm linear model could be solved in all of the desired analyses that are summarized in Table A.6. Table A.6 also lists the computer resources required for each finite element analysis using the coarse model. Analysis jobs for this model required around 1200 megabytes of memory. The jobs required (at most) several hours of wall-clock time to finish.

**Table A.6 – Computer Resources Required for 8-mm Linear FEM**

Analysis Step No.	Analysis Type	Time / Memory
Preliminary	2D Axi-symmetric Inflation 220 kPa	1 sec / 24 MB
1	3D Inflation 220 kPa	2 min / 631 MB
2	Vertical Load 4 kN	6 min / 684 MB
4	Free Rolling 60 KPH	11 min / 1164 MB
5A	Pure Braking Sweep to Lockup Slip Ratio of 100 Percent (Time Step = 0.0025 s)	2.1 hr / 1124 MB
5B	Pure Cornering Sweep to Slip Angle of 15 Degrees (Time Step = 0.025 s)	32 min / 1124 MB

Table A.7 shows the peak displacement values in an inflation analysis, using the 2D axi-symmetric finite element model. The displacement change from the 8-mm linear model to the 1-mm quadratic model is 16 percent, and therefore the results from 8-mm linear model are not converged. The displacement results are noteworthy, since the most important quantity to be predicted by the tire finite element model is strain, which is determined from displacement. Based on the mesh convergence study results, therefore, the coarse 8-mm finite element model is not converged and its displacement and strain results are expected to be inaccurate. Furthermore, the optimum tire finite element mesh size is small, around a few millimeters in size at most. The computational expense associated with the optimum element size is too high for the STSS research project, given its computer hardware limitations. Wall-clock times and memory requirements are excessive with medium and fine density models, especially if the model is solved many times.

---

## APPENDIX A. TIRE FEM PROCEDURES AND GEOMETRY

---

**Table A.7 – Displacement in 2D Inflation Analysis, P = 220 kPa**

Model	Maximum Displacement Magnitude [mm]
8-mm Linear	1.89
8-mm Quadratic	2.06
2.5-mm Linear	2.06
2.5-mm Quadratic	2.10
1-mm Linear	2.23
1-mm Quadratic	2.20

Figures A.11 through A.13 show magnitude of displacement contours in the 2D axisymmetric inflation analysis. The scale is the same in every plot. Trends are similar, in the sense that the maximum displacement location always occurs in the same place, at the sidewall near the rim. Peak displacement values differ, however. Larger elements result in lower displacements.

Only two of the 3D tire finite element models built could be solved in all of the analysis steps (due to computer hardware limitations); the models based on the 2.5- and 8-mm 2D cross-sections could be solved successfully, but only in the special case of extruding the cross-sections into 3° sector size elements. These two 3D models were solved in the pure braking simulation and all of the previous analysis steps, to better understand the accumulated error from the incremental finite element scheme as designed, especially as it relates to the errors produced by the coarse density 3D finite element model. Table A.8 lists the maximum lateral sidewall displacement for the 3D models. Figure A.14 shows the lateral displacement contours in these models in the inflation analysis. Half the model is masked in the contour plots so the cross-section can be seen clearly. Note that local modifications to cross-section element size were not pursued, such as the use of smaller elements at the sidewalls and larger elements at the tread. A mixed element size modeling approach may have resulted in reasonable solve times for the 3D tire model, but the high importance of sidewall deformation measurement in the STSS was not recognized at the time of finite element model creation, which occurred early in the research project.

From Table A.8 it can be seen that the coarse density 3D model predicts lower sidewall displacement in all of the simulations, meaning that its sidewalls are relatively stiff in comparison to the medium density 3D model. This result is consistent with the inflation simulation results from the 2D axisymmetric models, which show that larger elements result in lower sidewall displacement levels. Therefore, the coarse density 3D tire model, which was adopted for general use in the STSS research project, is expected to under predict sidewall displacement and strain levels. Table A.8 also shows that errors accumulate over the analysis steps in the coarse model; at the end of the free rolling analysis the total accumulated error is 11%, and this is in comparison with a medium density model that is itself not converged. Therefore, the coarse density tire finite element model used in the STSS research project, along with its incremental analysis procedure, is known to be

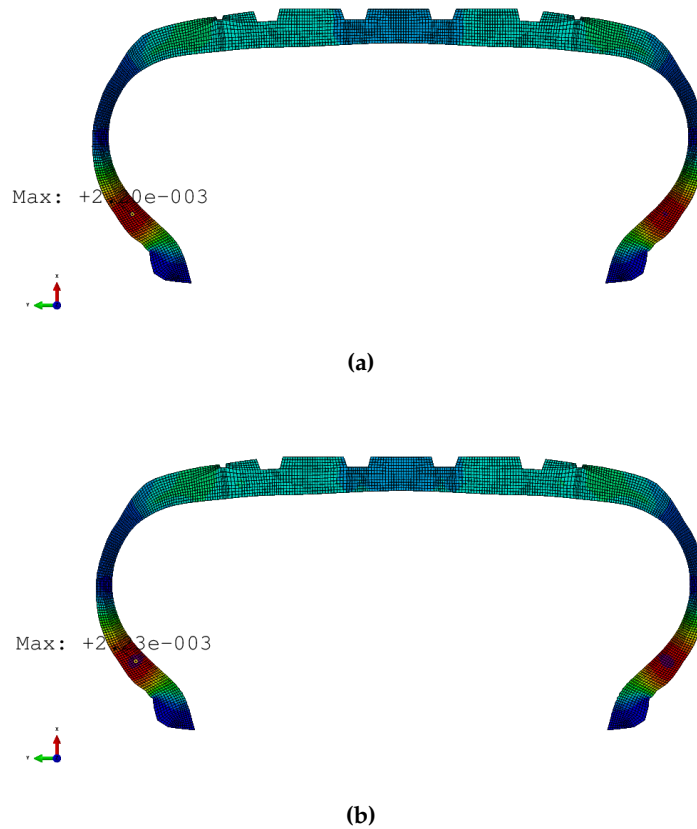
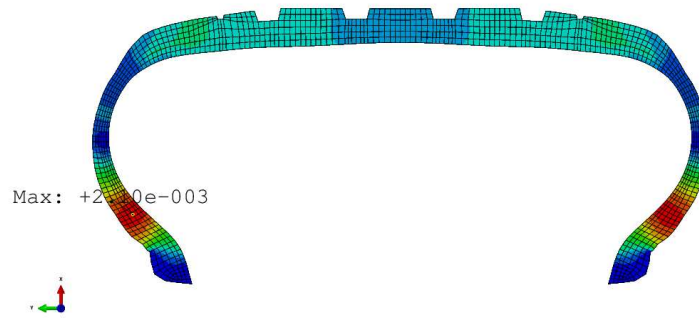


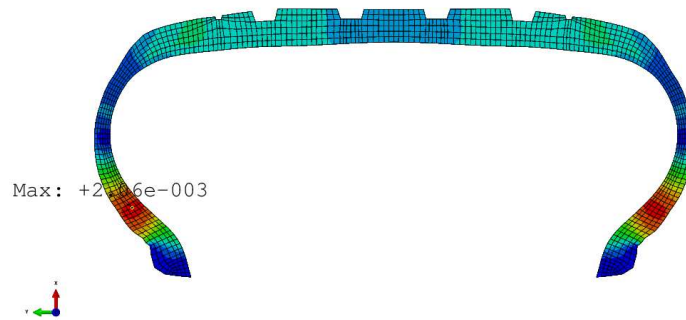
**Figure A.11 – 2D Tire Axi-symmetric Inflation Analysis for 1-mm FEM: (a) Quadratic (b) Linear**

inaccurate in an absolute sense, but is assumed to be suitable for the analysis of the tire dynamics phenomena that are relevant to the project.

Figures A.15 through A.17 show strain contours in several simulations for the 8-mm linear 3D finite element model with 3° sector size. All of these finite element analysis jobs had reasonable computational requirements. Although the coarse 8-mm model was not converged, the trends in the strain patterns are as expected. In the free rolling strain pattern that appears in Figure A.15, the distribution is nearly symmetrical, meaning the tire as modeled has very little rolling resistance. Slip is present in a free rolling tire, even in the absence of drive and brake torques, and this leads to an asymmetrical longitudinal shear stress distribution in the tire / road contact region that results in a small “brake” force usually called the rolling resistance [12]. If the tire had greater rolling resistance, the strain distribution would have an asymmetrical appearance, similar to a braking strain pattern.



(a)



(b)

**Figure A.12 – 2D Tire Axi-symmetric Inflation Analysis for 2.5-mm FEM: (a) Quadratic (b) Linear**

Figure A.16 presents three views of the pure braking simulation results, with circumferential (longitudinal) strain contours shown. In these plots, and the entire STSS research project, tensile strain is positive and compressive strain is negative. In Figure A.16 the direction of forward motion is to the right; therefore, the front of the tire is on the right side of the image and the rear of the tire is on the left side. In braking, the tread material just in front of the contact patch is expected to be in tension; the tread material immediately behind should be in compression. The tire finite element model predicts these trends exactly, as can be seen in Figure A.16a. Figure A.16b shows that the contact patch is in longitudinal compression at the tire / road interface, but the tire inner liner immediately above this area is in longitudinal tension, as shown in Figure A.16c. Therefore, the longitudinal strain through the composite tire material thickness in the contact patch area changes significantly with vertical travel.

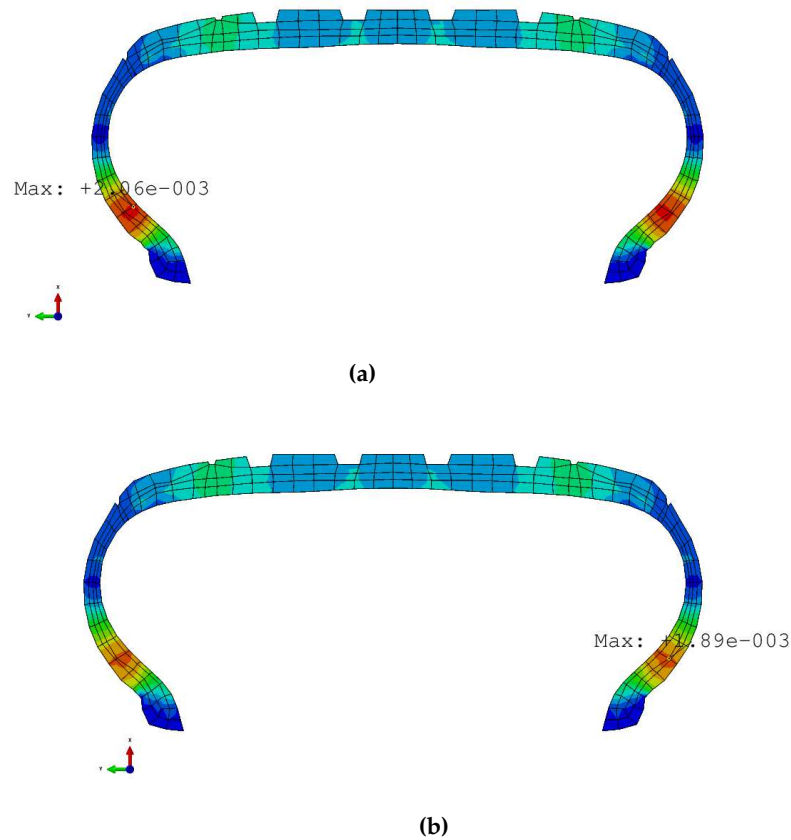


**Figure A.13 – 2D Tire Axi-symmetric Inflation Analysis for 8-mm FEM: (a) Quadratic (b) Linear**

Figure A.17 shows the strain contours in the pure cornering simulation. In this plot the direction of forward motion is to the left; therefore, the front of the tire is on the left side of the image and the rear of the tire is on the right side. The tire finite element model is simulated in a left turn, as is always true of the pure cornering analyses performed during the STSS research project. The triangular shape of the footprint is the expected result. Due to the qualitatively correct results from the coarse tire finite element model in the pure cornering simulation and others, its element size of approximately  $18 \times 8 \times 4$ -mm produced by the 8-mm cross-section and the  $3^\circ$  extrusion angular distance was selected for use in the STSS research project, although the material properties and reinforcement geometries were improved later.

**Table A.8 – Maximum Lateral Displacement in Sidewall for 3D Models**

Model	Number of Elements	Inflation 220 kPa	Vertical Load 4 kN	Free Rolling 60 KPH	Pure Braking Sweep to Slip Ratio of 20%
Medium Density: 2.5-mm Linear w/ 3° Sector	209162	1.88 mm	4.80 mm	4.64 mm	4.67 mm
Coarse Density: 8-mm Linear w/ 3° Sector	48122	1.72 mm	4.73 mm	4.57 mm	4.41 mm
Magnitude of Change		9%	1%	1%	6%

### A.4.2 Parallel Processing

In order to determine if ABAQUS solve times could be reduced, a parallel processing speedup time study was conducted. The purpose was to see if the analysis jobs using the tire finite element model could benefit from parallel processing, especially since long solve times were the reason for using an unconverged model with large elements. Previously the ABAQUS jobs had been performed using only one of the logical CPUs of the four core processor in the desktop computer.

ABAQUS compute processes can take advantage of two types of parallelization [62]. The first type, Shared Memory Parallel (SMP) processing, is available on shared memory platforms such as the desktop computer used during the smart tire project. These thread-based parallel processes share the same memory. The second type, Distributed Memory Parallel (DMP) processing, is most commonly used for parallel execution on compute clusters or networks of workstations. These Message Passing Interface (MPI) parallel processes have their own memory. The MPI standard includes software libraries used to parallelize software, and therefore installation of MPI components is required in the computer system to be used. In general, when MPI parallel processing is available, it is preferable to SMP processing. In ABAQUS parallelization, thread-based processing is activated only when an MPI-based implementation does not exist for a particular solver or computer system. Some processes are more suited to parallelization than others, depending on the analysis type.

Figure A.18 is a graph containing the results of the SMP parallelization study for the tire finite element model using the desktop computer. The plot shows speedup factor versus number of logical CPUs in the ABAQUS jobs that were run specifically for this study. In this context speedup is defined as the ratio of the total wall-clock time of the process using one CPU to the total wall-clock time of the process using two or more CPUs. Perfect parallelization is shown as a dashed black line; this line represents the ideal case, where the number of CPUs results in a speedup factor of the same value. For example,

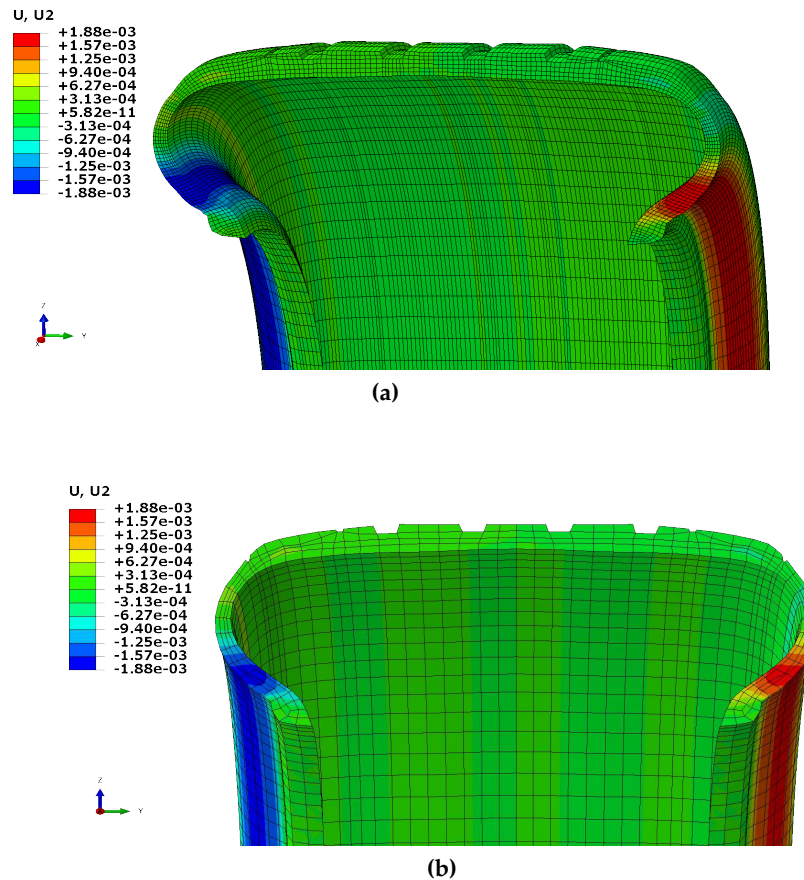


Figure A.14 – Lateral Displacement Contours in Inflation Analysis Using 3D Models: (a) Medium Density: 2.5-mm Linear w/ 3° Sector (b) Coarse Density: 8-mm Linear w/ 3° Sector

the use of two CPUs would ideally speedup the process by a factor of two, cutting the total wall-clock time in half.

Three different analysis types in ABAQUS were tested using the tire finite element model; static stress, direct-solution steady state dynamics and steady-state transport. The most important of these for the tire is steady-state transport, since this procedure was used to simulate free rolling, braking and cornering. These were the most important events to simulate considering the overall program goals; in addition, they required the longest wall-clock times, especially the braking analysis. From Figure A.18 it can be seen that the static stress analysis type benefited most from thread-based parallelization. With four logical CPUs the speedup factor was 2.8 times. Direct-solution steady state dynamics analysis also benefited from parallelization, but not as much as static analysis.

---

## APPENDIX A. TIRE FEM PROCEDURES AND GEOMETRY

---

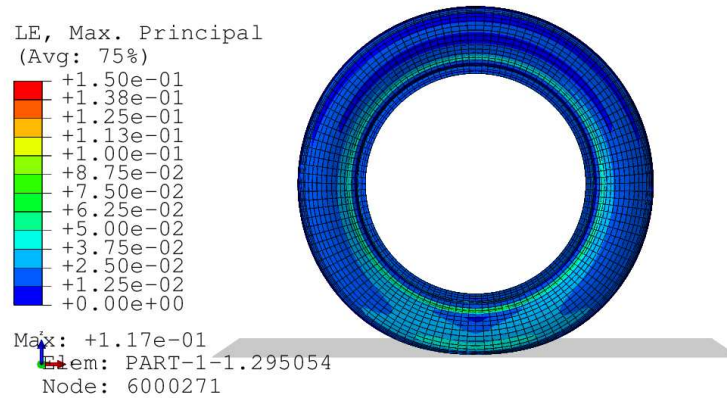


**Figure A.15 – Coarse FEM Strain Free Rolling**

Speedup for the steady-state transport analysis procedure was not impressive with more logical CPUs. Four logical CPUs resulted in a speedup factor of only 1.4 times; furthermore, it can be seen that performance with additional CPUs was already levelling off at three CPUs. This poor result discouraged further investigation into MPI parallel computing; thus the desktop computer continued to be used, taking advantage of its four logical CPUs depending on the particular analysis being performed and the demand for ABAQUS research licenses (which were checked out from the license server based on the number of CPUs allocated to each process).



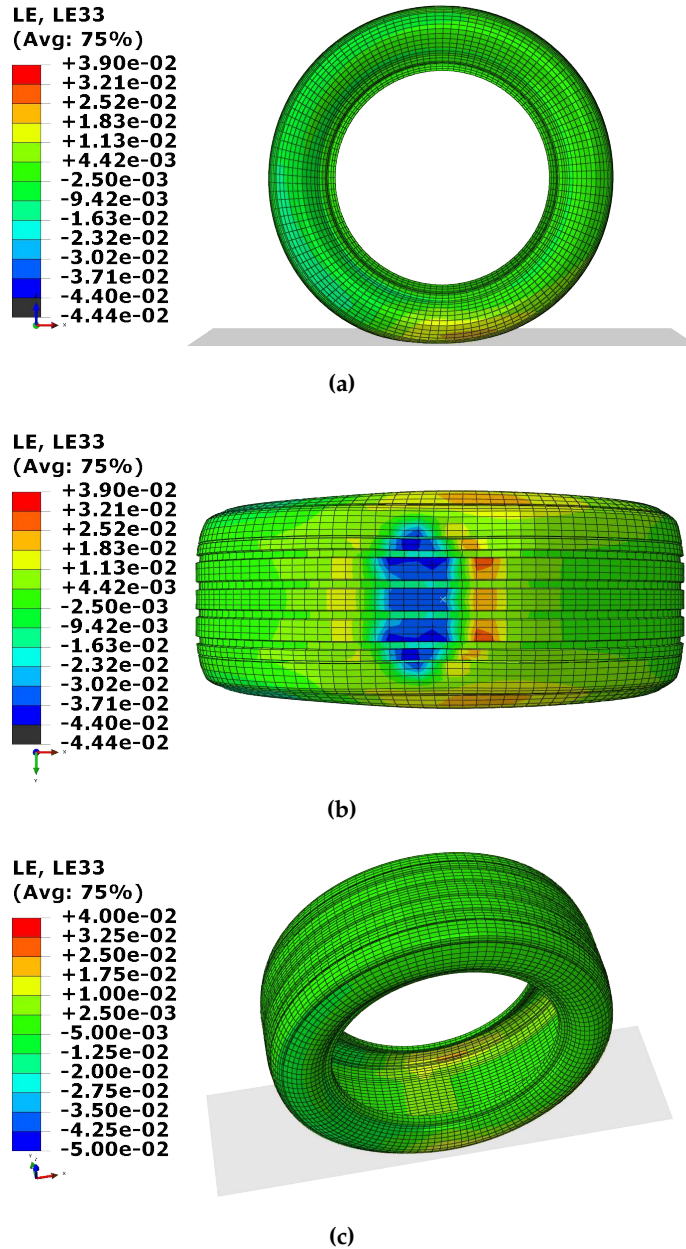


Figure A.16 – Coarse FEM Strain Pure Braking: (a) Side View (b) Bottom View (c) Inside Detail View

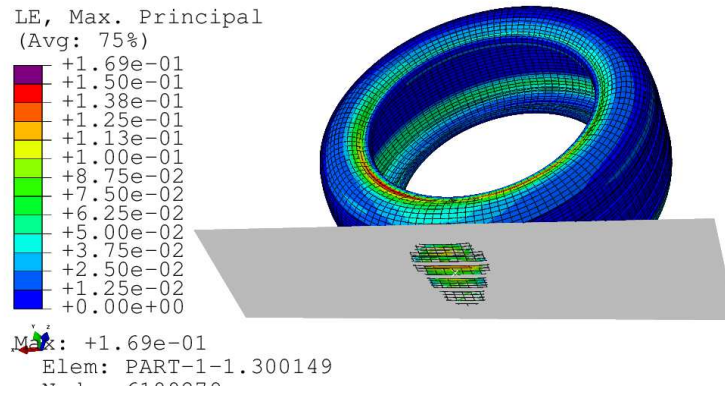


Figure A.17 – Coarse FEM Strain Pure Cornering Oblique View

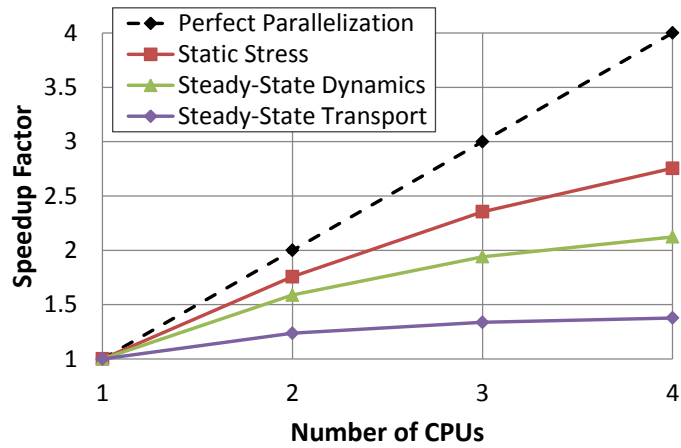


Figure A.18 – Speedup Factor versus Number of CPUs in ABAQUS Jobs

## Appendix B

# Computer Specifications

Hardware and software in the three computers used to solve the neural networks in MATLAB and the finite element models in ABAQUS appears in Tables B.1 through B.3.

**Table B.1 – Specifications of Computer A: Lenovo Laptop**

Manufacturer	Lenovo
Type	Laptop
Processor	Intel Core i5-2410M CPU @ 2.30 GHz (2 Cores)
Installed Memory [RAM]	4 GB
Operating System	openSUSE 12.3 Dartmouth
MATLAB Version	R2013a 64-bit

**Table B.2 – Specifications of Computer B: Hewlett-Packard Laptop**

Manufacturer	Hewlett-Packard
Type	Laptop
Processor	Intel Core i7-2630QM CPU @ 2.00 GHz (4 Cores)
Installed Memory [RAM]	8 GB
Operating System	Windows 7 Professional
MATLAB Version	R2013a 32-bit

---

**APPENDIX B. COMPUTER SPECIFICATIONS**

---

**Table B.3 – Specifications of Computer C: Lenovo Desktop**

Manufacturer	Lenovo
Type	Desktop
Processor	Intel Core i7-2600 CPU @ 3.40 GHz (4 Cores)
Installed Memory [RAM]	12 GB
Operating System	Windows 7 Professional
MATLAB Version	R2010b Service Pack 1 64-bit
ABAQUS Version	6.12-3 with Research License

# Appendix C

## Tire FEA Studies

### C.1 Supplemental Analysis Studies

#### C.1.1 Tire Size Effect

The tire size effect study was conducted to determine if changes in tire size would result in significantly different displacement and strain patterns, especially at the tire inner liner, which is the most likely location for strain sensors. Ideally, the STSS will be applied to different tire sizes, and ultimately different tire makes and models, without significant changes to the system. This may be possible if the displacement and strain patterns are similar when comparing different tires, even if the levels measured by the sensors are different.

In order to represent different tire sizes, the finite element model of the P 235 / 50 R 18 tire was modified by expanding and contracting the node positions in the radial direction; therefore, the models were identical except for the tire size being represented and the aspect ratios of the finite elements. Six tire sizes were modeled to investigate changes in the finite element analysis results. The fixed features in this study were the tire outside radius and the tire width. The variable features were the aspect ratio and the rim diameter.

Table C.1 lists dimensions and characteristics of the six different tire sizes modeled in finite elements. All of the tire sizes modeled are available for sale, with the possible exception of the highest profile size, P 235 / 70 R 14, which was used on some American cars in the 1970s and is now defunct. Sketches showing the axi-symmetric cross-sections of the six tire finite element models appear in Figure C.1.

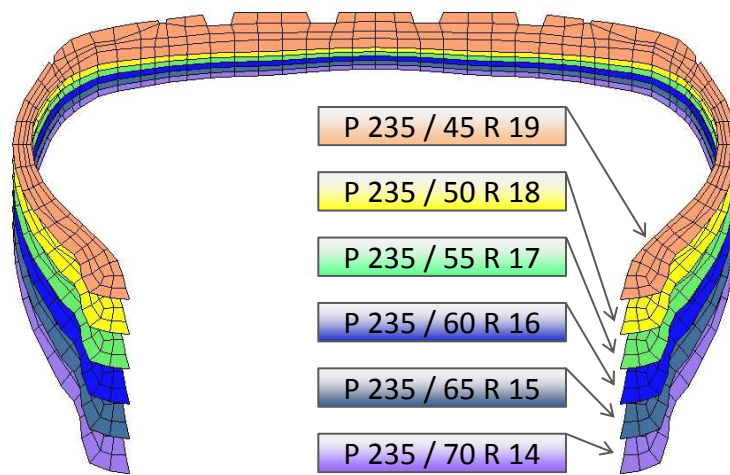


Figure C.1 – Tire Size Study FEM Cross-Sections

**Table C.1 – Tire Size Study Overview**

<b>Tire Size</b>	<b>P 235 / 70 R 14</b>	<b>P 235 / 65 R 15</b>	<b>P 235 / 60 R 16</b>	<b>P 235 / 55 R 17</b>	<b>P 235 / 50 R 18</b>	<b>P 235 / 45 R 19</b>
<b>Available for Purchase?</b>	No	Yes	Yes	Yes	Yes	Yes
<b>Tire Width [mm]</b>	235	235	235	235	235	235
<b>Tire Outside Radius [mm]</b>	346.1	346.1	346.1	346.1	346.1	346.1
<b>Tire Aspect Ratio [%]</b>	72	66	61	55	50	45
<b>Rim Diameter [in]</b>	14	15	16	17	18	19
<b>Sidewall Height [mm]</b>	168.3	155.6	142.9	130.2	117.5	104.8
<b>Sidewall Height Factor w.r.t. 235 / 50 R 18</b>	1.4	1.3	1.2	1.1	1.0	0.9

---

## APPENDIX C. TIRE FEA STUDIES

---

Figure C.2 shows the magnitude of displacement contours for the 15, 17 and 19 inch tire sizes in the 2D axi-symmetric inflation analysis with an applied air pressure of 220 kPa. The maximum displacement location is in the sidewall is near the bead, which is true for these three tires as well as all the finite element models, regardless of tire size. The peak displacement values differ, but the displacement patterns are similar in the inflation analyses.

Figure C.3 shows the magnitude of displacement contours for the 15, 17 and 19 inch tire sizes in the 3D vertical load analysis (performed subsequent to the inflation analysis) with an applied vertical load of 4000 N. The tire inner liner is depicted; all other components are masked. As in the inflation analysis, trends in the displacement contours in the vertical load analysis are similar although maximum displacement values are different.

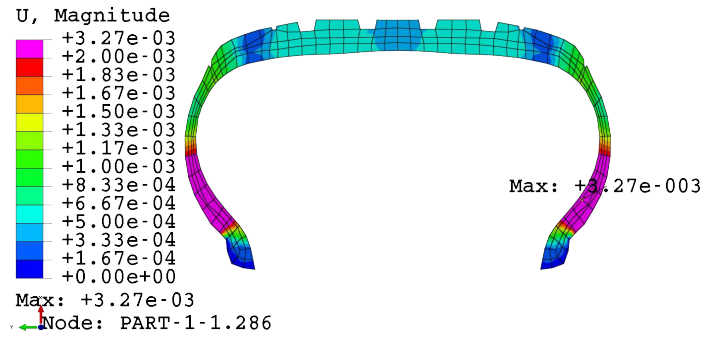
Figure C.4 is a graph showing maximum magnitude of displacement values for the tire finite element models in the inflation and vertical load analyses. The maximum value calculated by the finite element model is reported. In the case of the inflation analyses the maximum value location is near the bead. In the case of the vertical load analyses the maximum value is located in the sidewall that is diametrically opposed to the contact patch.

Sidewall displacement decreases with increasing increasing rim size when the tire is subjected to inflation pressure. This is an expected result since the sidewall height decreases with a larger rim; a lower profile tire should have a sidewall that is stiffer than the a higher profile tire and therefore the analysis results are reasonable. There are insignificant changes in maximum tire displacement due to vertical load when considering the various tire sizes analyzed. The 17 inch tire has a maximum displacement value that is 3% higher than the 14 inch tire. Thus, the general trend is to similar total deflection of the tire due to a vertical load considering various tire profiles along with a fixed outer radius and width.

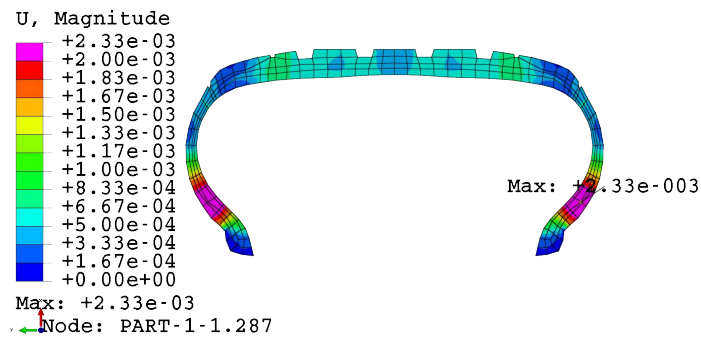
The results of the tire size effect study show that tire displacement patterns due to inflation pressure and vertical load do not differ significantly with tire size. Results of the inflation analyses demonstrate that increasing the rim diameter / decreasing the tire aspect ratio results in decreased sidewall maximum displacement and increased sidewall stiffness, as expected. The vertical load analysis results show that the maximum overall displacement of the tire is not significantly altered by the rim diameter. Therefore, the STSS can likely be used with different tire sizes without major modifications.



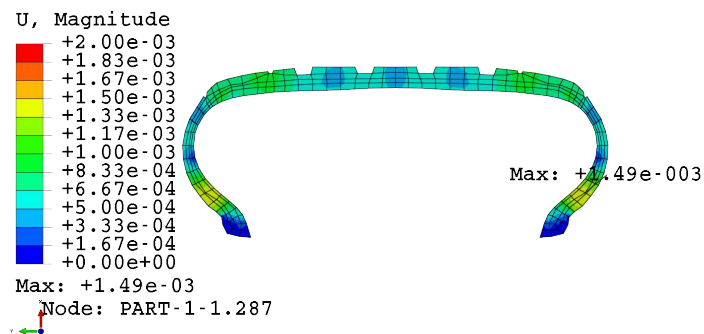
## APPENDIX C. TIRE FEA STUDIES



(a)



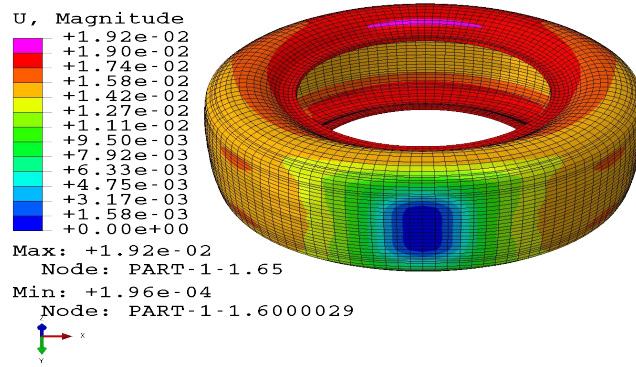
(b)



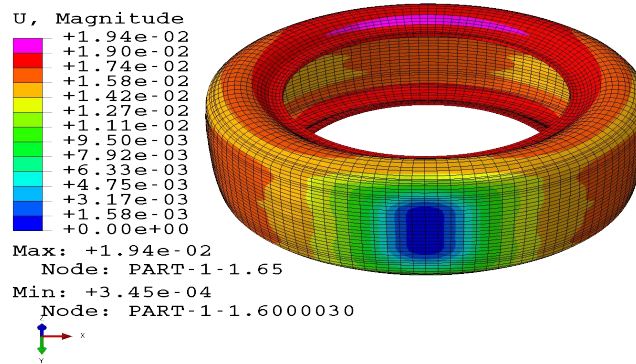
(c)

Figure C.2 – Magnitude of Displacement in Tire Size Study Inflation Analysis: (a) P 235 / 65 R 15 (b) P 235 / 55 R 17 (c) P 235 / 45 R 19

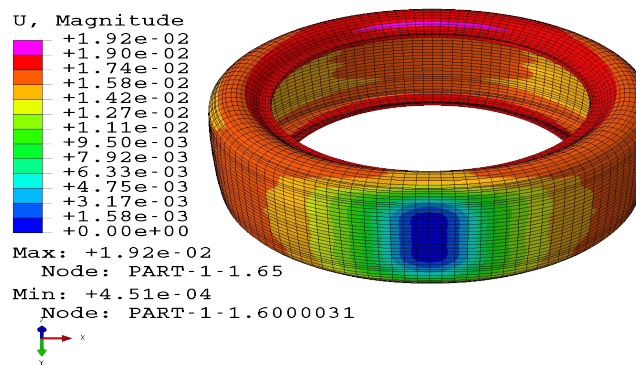
## APPENDIX C. TIRE FEA STUDIES



(a)



(b)

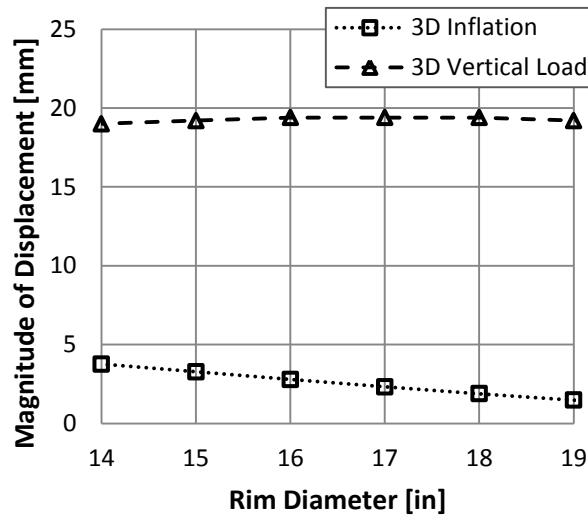


(c)

Figure C.3 – Magnitude of Displacement in Tire Size Study Vertical Load Analysis, Tire Inner Liner Shown: (a) P 235 / 65 R 15 (b) P 235 / 55 R 17 (c) P 235 / 45 R 19

**C.1.2 Tread Geometry Effect**

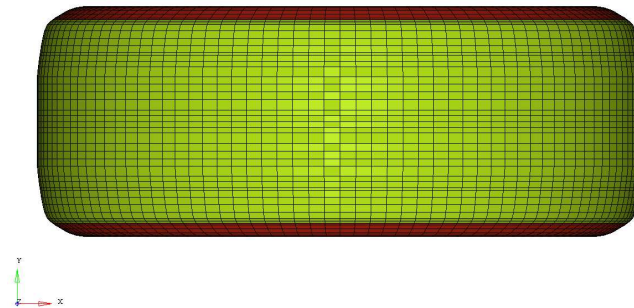
Three tire finite element models with three different tread geometry representations were built and analyzed in order to select and finalize the tread pattern in the model. The basic groove geometry of the original model was selected, with the reasons summarized here. The tread geometry effect study is also used to illustrate typical results from the simulated sweep tests performed using the tire finite element model, including displacement, strain and stress patterns in the overall tire, as well as in-tire strain measurements and wheel center tire force measurements.



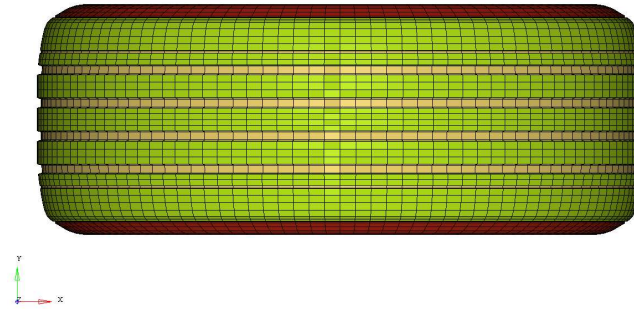
**Figure C.4 – Maximum Magnitude of Displacement versus Rim Diameter in the Tire Size Study**

Figure C.5 shows the tire finite element models that were built as part of the tread geometry study. The “baseline” grooved tire model appears in Figure C.5b; this model with the main tire grooves included was built first, since it incorporated some of the tread geometry and had the smallest number of finite elements. Figure C.5a shows the slick tire model. This model was created simply by filling in the grooves of the grooved model with finite elements.

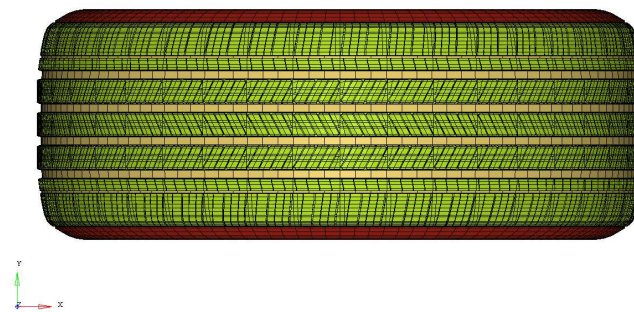
The treaded model of Figure C.5c was the most expensive to build. A 9° solid sector was created and revolved / copied 40 times to create the full 3D treaded tire finite element model. Details of the solid sector can be seen in Figure C.6, where the mesh is shown along with the displacement contours from a sector inflation analysis, which is analogous to the axi-symmetric inflation analyses performed using the 2D cross-section models. In the treaded tire model, “tied contact” is used to attach dissimilar tire tread and tire body meshes.



(a)



(b)



(c)

Figure C.5 – Tread Geometry Effect Study Tire Finite Element Models: (a) Slick (b) Grooved (c) Treaded

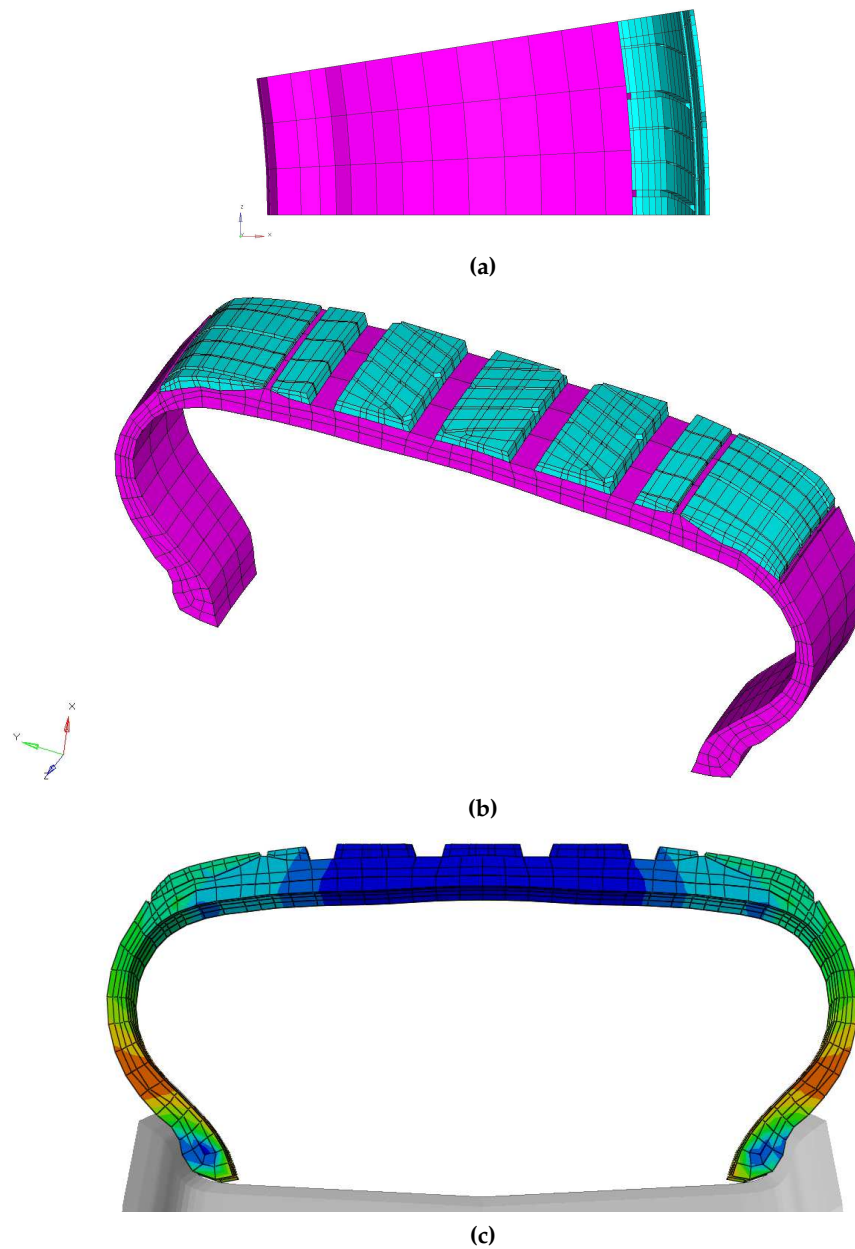


Figure C.6 – Treaded Tire Finite Element Sector: (a) Mesh Side View (b) Mesh Oblique View (c) Inflation Magnitude of Displacement Contours

### C.1.2.1 Inflation Analysis

Table C.2 lists the inflation analysis results for an air pressure of 220 kPa. Radial expansion of the tire is about 0.5-mm, regardless of the tread geometry. This is a reasonable

---

## APPENDIX C. TIRE FEA STUDIES

---

result, considering that radial expansion due to air inflation is practically restricted by the steel reinforcements; these reinforcements are always the same in the three tread finite element models. Figure C.7 shows magnitude of displacement contours in the models, which are very similar (same trends and peak values) in the inflation analysis regardless of the tread representation.

**Table C.2 – Radial Expansion of Tire FEM With P = 220 kPa**

Tire FEM	Uninflated Radius [mm]	Inflated Radius [mm]	Radial Expansion [mm]
Slick	346.100	346.652	0.552
Grooved	346.100	346.633	0.533
Treaded	346.100	346.634	0.534

### C.1.2.2 Vertical Load Analysis

Table C.3 lists the vertical load analysis results for a downward force of 4000 N. Maximum contact stress levels in the contact patch vary significantly with tread geometry, due to small local geometry differences. The grooves and sipes both increase stress levels in the tread compared to a slick tire. However, the footprint size and shape is similar in all tread representations, as can be seen in Figure C.8, which shows contact pressure contours at the tire / road interface. While local tread stresses are altered by modifying the tread geometry, displacement and strain levels on the inside of the tire are not significantly modified.

Since results from both static simulations, including the inflation analysis and the vertical load analysis, are similar for all three tread geometry models, this suggests that the tread representation in the tire finite element model should not be a significant factor in the results produced by the model. Further study of the slick and grooved tread models was conducted to investigate possible differences in the in-tire strain and the tire forces developed. However, further study of the treaded model could not be conducted due to contact problems with the model. The vertical load analysis was the only simulation that finished completely using the treaded model. The sweep simulations with the treaded model ended prematurely due to contact failures. Many attempts to improve the model by modifying contact parameters were unsuccessful.

**Table C.3 – Maximum Contact Stress in Tire FEM With  $F_z = 4000$  N**

Tire FEM	Contact Stress [Pa]	Change from Slick Tire
Slick	$4.34 \times 10^5$	N/A
Grooved	$5.70 \times 10^5$	31%
Treaded	$9.67 \times 10^5$	123%

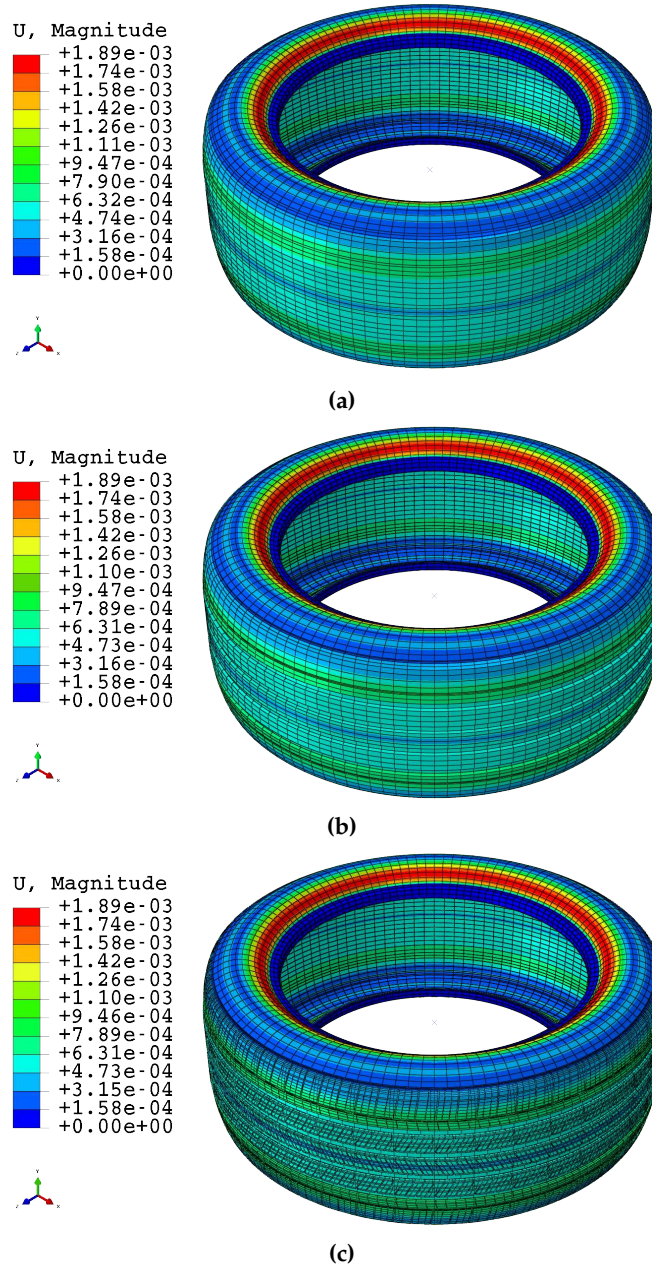
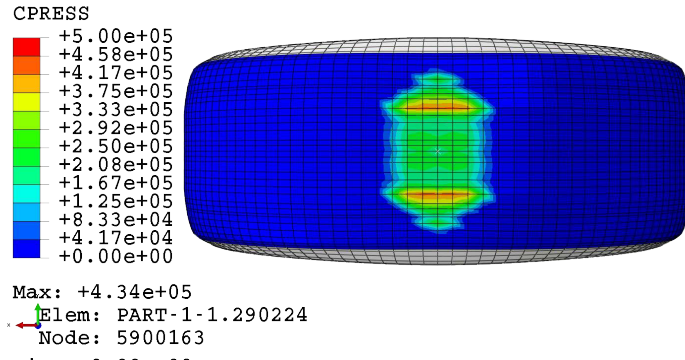
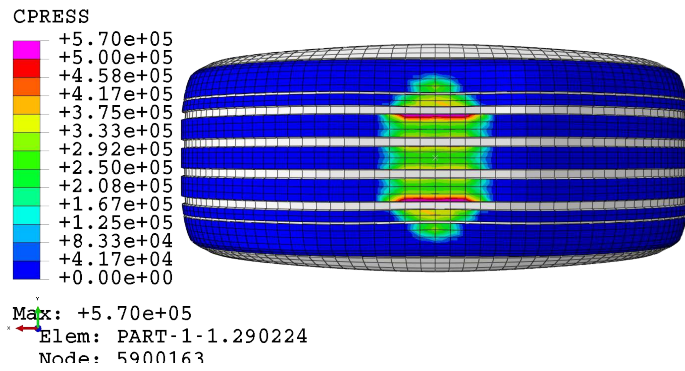


Figure C.7 – Magnitude of Displacement Contours in Inflation Analysis With P = 220 kPa: (a) Slick (b) Grooved (c) Treaded

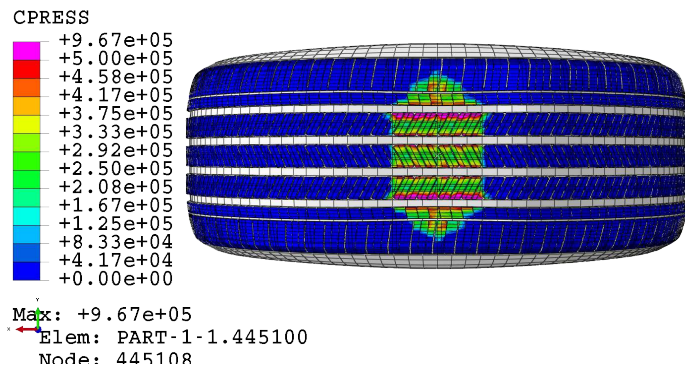
APPENDIX C. TIRE FEA STUDIES



(a)



(b)



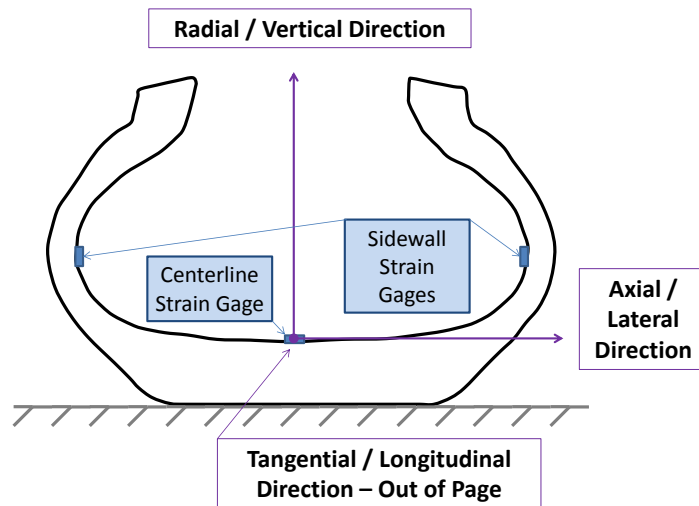
(c)

Figure C.8 – Contact Pressure Contours in Vertical Load Analysis With  $F_z = 4000$  N:  
 (a) Slick (b) Grooved (c) Treaded



**C.1.2.3 Strain Measurement Locations**

A preliminary tire finite element analysis study for a tire of smaller size with similar construction [74] revealed that the peak lateral compressive strain (measured at the tire inner liner, tread centerline) can be used to determine cornering force. This peak is strongly influenced by cornering force and relatively insensitive to braking force. Therefore, tread centerline in-tire strain measurements were carried over into the finite element model of the 235 / 50 R 18 tire, in the longitudinal and lateral directions. Four sidewall strain measurements were added in the new model; one pair on each sidewall, with each pair having a longitudinal and lateral measurement. Figure C.9 is a sketch showing the virtual strain measurement locations. The strain locations and directions are summarized in Table C.4.



**Figure C.9 – Tire Inner Liner Strain Gage Locations**

**Table C.4 – Strain Measurement Locations and Directions**

Location	Direction	Abbreviation
Tread Centerline	Longitudinal	CL-LON
Tread Centerline	Lateral	CL-LAT
Sidewall Left	Longitudinal	SWL-LON
Sidewall Left	Radial	SWL-RAD
Sidewall Right	Longitudinal	SWR-LON
Sidewall Right	Radial	SWR-RAD

**C.1.2.4 Free Rolling Analysis**

Figures C.10 and C.11 show in-tire strain measured at the tire inner liner centerline in the tire finite element model, for the longitudinal and lateral directions. These plots show that the measured strain is almost the same in the free rolling case, regardless of tread geometry. Therefore, tread representation in the finite element model is not expected to modify in-tire strain in free rolling.

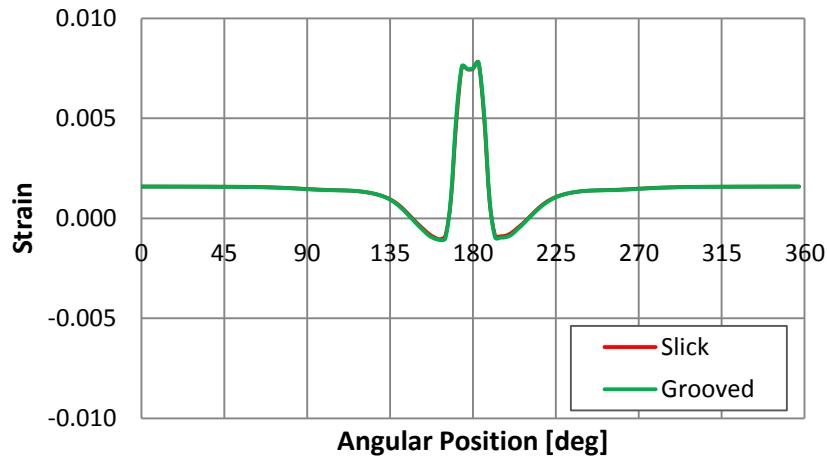


**Figure C.10 – Longitudinal Strain at Tire Inner Liner Centerline versus Angular Position for Free Rolling in the Tread Geometry Study**

**C.1.2.5 Pure Braking Analysis**

Figure C.12 shows longitudinal force versus slip ratio in the pure braking analysis, for the slick and grooved tire finite element models. Brake force curves are similar, although the slick tire has 5% higher braking force at a slip ratio of 4% compared to the grooved tire, which is consistent with performance expectations for a slick (“race”) tire versus a grooved (“rain”) tire. Maximum braking force is also developed earlier in the slick tire, at a slip ratio of 8% for the slick tire compared to 10% for the grooved tire. Both are reasonable peaks, as they are expected to occur for passenger car tires at a slip ratio of around 15% [12]. In general, the brake force curves have the expected shape, with a roughly bi-linear appearance. The first region is linear and increasing; the second region is linear and flat or decreasing, which represents the longitudinal force capacity of the tire.

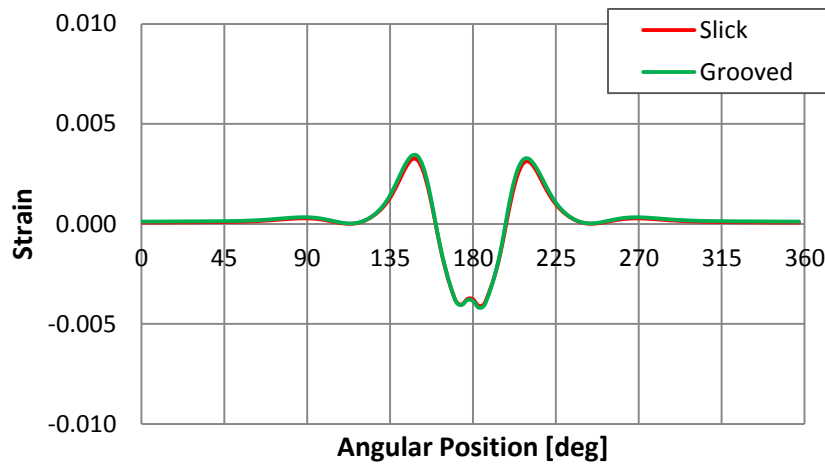


**Figure C.11 – Lateral Strain at Tire Inner Liner Centerline versus Angular Position for Free Rolling in the Tread Geometry Study**

For both tires, the maximum braking force is reached in the 8 to 10% slip ratio range and then maintained without reduction up to a 100% slip ratio. This behavior is unrealistic for most real tires. In physical brake sweep tire tests, the maximum brake force peaks, then falls off in an approximately linear fashion. The reason is related to differing friction coefficients. There is a different friction coefficient associated with peak braking force compared to the friction coefficient associated with fully locked and skidding at 100% slip ratio. The tire finite element model does not recognize this difference, as one single friction coefficient is applied throughout the entire analysis. Future work to improve the tire finite element model could include research to find out if the frictional characteristics of the tire / road interface can be modified mid-simulation in order to make the braking analysis more realistic.

Figure C.13 shows in-tire strain measured at the tire inner liner centerline for the longitudinal direction. Waveforms from the slick and grooved tire finite element models are very similar, except for the peak, which is 5% higher in the slick tire compared to the grooved tire. Braking force in the slick tire is also about 5% higher; thus, the difference in brake force developed at the wheel center manifests itself in a peak difference in the in-tire strain measurement.

#### **C.1.2.6 Pure Cornering Analysis**

Figure C.14 shows lateral force versus slip angle in the pure cornering analysis, for the slick and grooved tire finite element models. Lateral force curves are similar, although

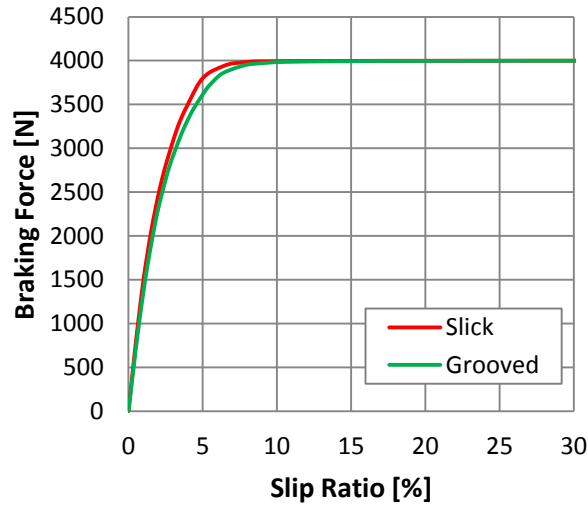


Figure C.12 – Braking Force versus Slip Ratio in the Tread Geometry Study

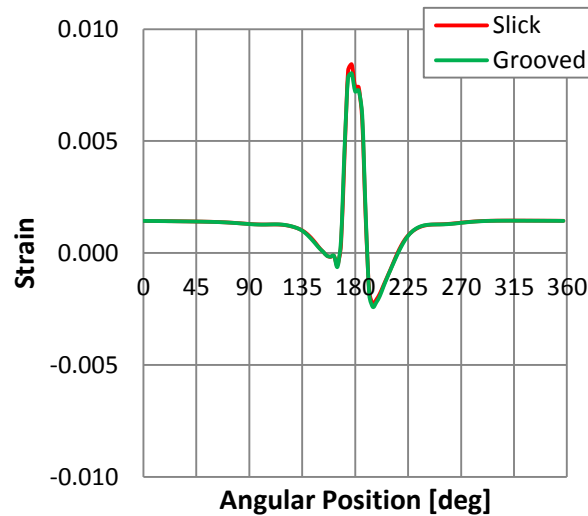


Figure C.13 – Longitudinal Strain at Tire Inner Liner Centerline versus Angular Position for Braking in the Tread Geometry Study

the slick tire has 5% higher lateral force at a slip angle of 2° compared to the grooved tire, which is again consistent with performance expectations for a slick tire. The lateral force curves have the expected shape, which is similar to the longitudinal force curves, although in practice the lateral force does not drop off at high slip angles to the same

extent it does at high slip ratios in the case of longitudinal force. Neither longitudinal nor lateral reduction in force at high slip is observed in the tire finite element model due to its simplified friction setup. In the case of the lateral force curves, the general behavior represented is realistic, as the linear region is expected to extent to 1 or 2° slip angle [12]; the tire finite element model calculates the linear region as ending at 2° for both the slick and the grooved tires.

The aligning moment versus slip angle in the pure cornering analysis appears in Figure C.15; the slick tire has a peak aligning moment of 2% higher than the grooved tire, which is reasonable considering that the slick tire also generates more lateral force. The aligning moment curves have the expected shape, which is more complex than the longitudinal and lateral force curves. The first region is linear and increasing, the second region contains the peak and the third region is decreasing, although usually not in a linear fashion. The maximum aligning moment should occur between 4 and 6° for most tires [12]. The tire finite element model predicts the maximum at around 1.5° for both the slick and grooved tires; this value is low but still reasonable.

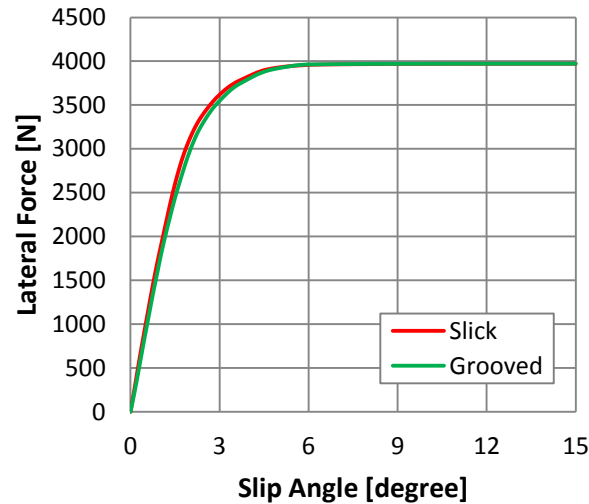


Figure C.14 – Lateral Force versus Slip Angle in the Tread Geometry Study

Figure C.16 shows in-tire strain measured at the tire inner liner centerline for the lateral direction. Waveforms from the slick and grooved tire finite element models are very similar, except for the peak, which is 8% higher in the slick tire compared to the grooved tire, in terms of absolute values. Lateral force in the slick tire is about 5% higher; thus, the difference in lateral force developed at the wheel center manifests itself in a peak difference in the in-tire strain measurement.

The overall results of the tread geometry effect study show that for a slick tire versus a grooved tire, braking force is about 5% higher at low slip ratios and cornering force

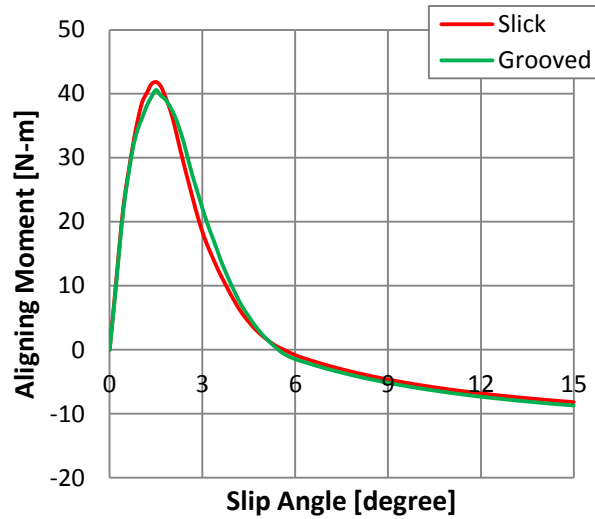


Figure C.15 – Aligning Moment versus Slip Angle in the Tread Geometry Study

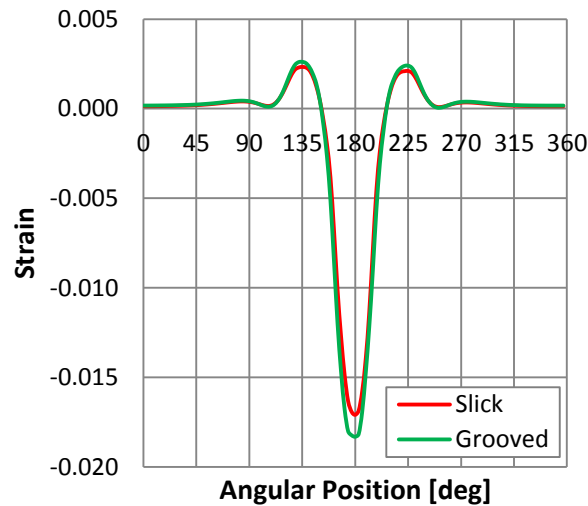


Figure C.16 – Lateral Strain at Tire Inner Liner Centerline versus Angular Position for Cornering in the Tread Geometry Study

is about 5% higher at low slip angles. In-tire strain measurements are similar when comparing waveform shapes, although peak strain levels are 5 to 8% higher in the slick tire, which suggests a relationship between tire forces generated and peak strain. These results are reasonable with respect to the expected trends; however, the tire forces and

strains did not exhibit large modifications when the tread representation in the tire finite element model was altered. Therefore, the grooved tire finite element model was selected as the final version, since the tire under study has the grooves that were modeled, and this model did not suffer from the contact problems of the fully treaded model.

### C.1.3 Modal Analysis

The simulated modal analysis results are summarized in Table C.5. In the modal analysis, the tire finite element model is fixed to zero displacement in all degrees of freedom at the center of the rigid rim. The first six modes of the tire are reported; these modes have significant modal mass, whereas higher frequency modes have almost no modal mass. In the first six modes there are two pairs of repeated roots, which are modes that share the same frequency due to the axi-symmetric geometry of the tire. The analysis procedure used calculates undamped natural frequencies.

The modal analysis results are listed for four different air inflation pressures. The natural frequencies of the tire increase with increasing inflation pressure, as expected, since the addition of air effectively stiffens the tire. Figures C.17 and C.18 illustrate the first six mode shapes of the tire finite element model with an air inflation pressure of 220 kPa (32 psi). Relative displacement contours are plotted for each mode, all of which are subject to a displacement normalization procedure.

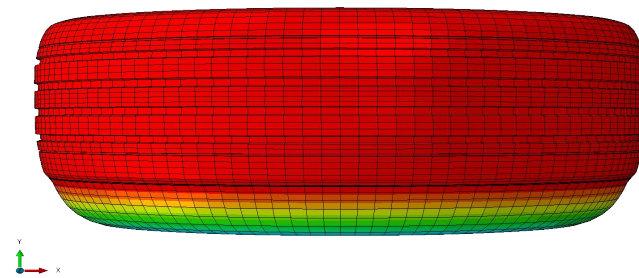
The first mode shape of the tire, as calculated using FEA, was lateral translation with a frequency of 44 Hz. This result was for an air inflation pressure of 220 kPa. In physical component modal analysis of the tire, the frequency of this first lateral mode at the same inflation pressure was determined to be 37 Hz, which is 16% lower than the analysis. This suggests that the sidewall static stiffness (which is related to the frequency of the global lateral mode) is higher in the tire model than in the actual tire, a result consistent with the mesh convergence studies which found that the coarse element size used is acceptable, but likely to over-predict the stiffness of the sidewalls.

In the on-road physical testing of the STSS, a low-pass filter was applied to the piezo-electric deformation measurements with a cutoff frequency of 35 Hz. This filter was applied in order to remove all of the tire vibration modes from the test data, since the first mode was known to occur at a frequency of 37 Hz based on the physical modal analysis results.

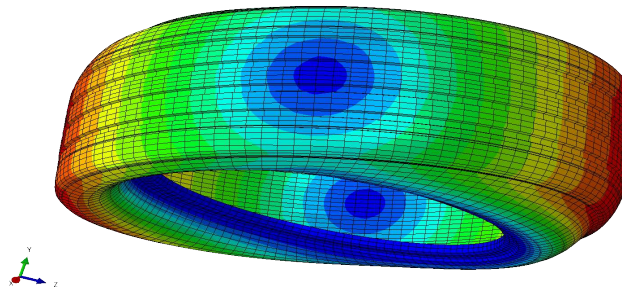
**Table C.5 – Tire Natural Frequencies and Mode Shapes in Simulated Modal Analysis**

Air Inflation Pressure						
Mode No.	140 kPa	180 kPa	220 kPa	252 kPa	Mode Shape	Notes
1	39 Hz	42 Hz	44 Hz	46 Hz	Translation Along Lateral Axis	
2	53 Hz	55 Hz	58 Hz	60 Hz	Torsion About Longitudinal Axis	Repeated Roots
3	53 Hz	55 Hz	58 Hz	60 Hz	Torsion About Vertical Axis	
4	62 Hz	63 Hz	64 Hz	65 Hz	Torsion About Lateral Axis	
5	67 Hz	70 Hz	72 Hz	74 Hz	Translation Along Longitudinal Axis	Repeated Roots
6	67 Hz	70 Hz	72 Hz	74 Hz	Translation Along Vertical Axis	

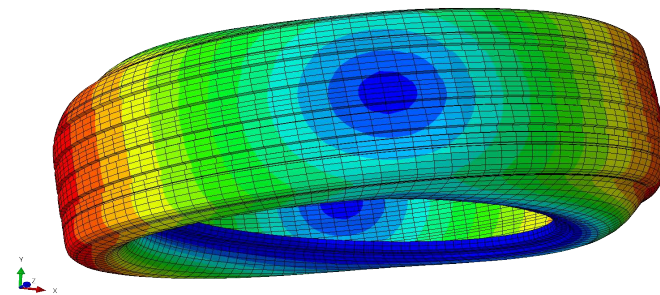




(a)



(b)



(c)

Figure C.17 – First, Second and Third Mode of Tire Finite Element Model, Air Inflation Pressure = 220 kPa:

(a) Shape = Translation Along Lateral Axis, Frequency = 44 Hz

(b) Shape = Torsion About Longitudinal Axis, Frequency = 58 Hz

(c) Shape = Torsion About Vertical Axis, Frequency = 58 Hz

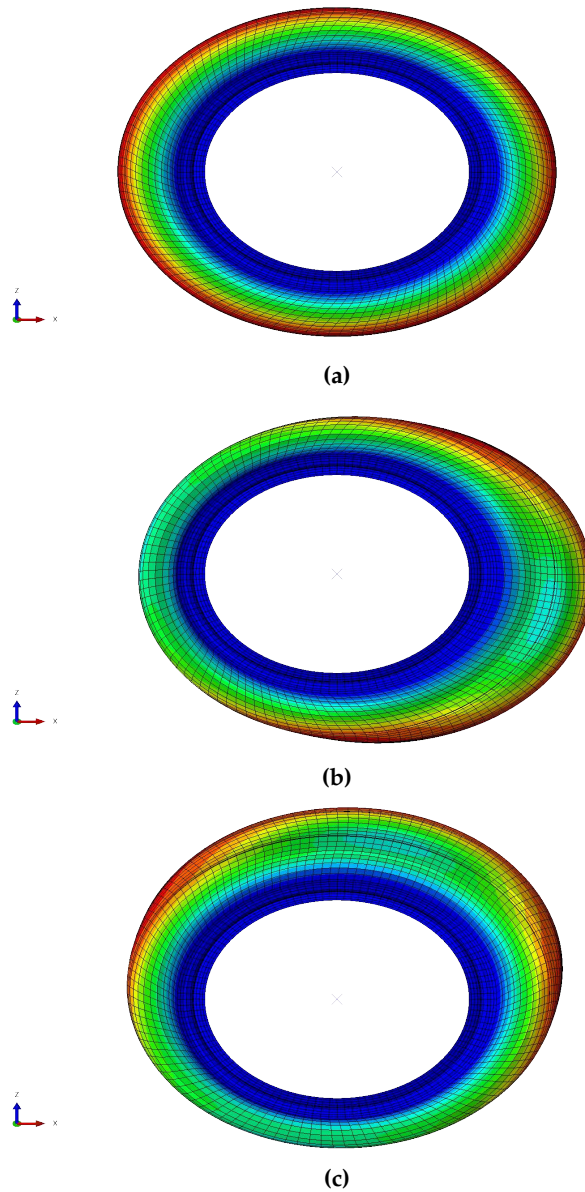


Figure C.18 – Fourth, Fifth and Sixth Mode of Tire Finite Element Model, Air Inflation Pressure = 220 kPa:

(a) Shape = Torsion About Lateral Axis, Frequency = 64 Hz

(b) Shape = Translation Along Longitudinal Axis, Frequency = 72 Hz

(c) Shape = Translation Along Vertical Axis, Frequency = 72 Hz

## **Appendix D**

# **Virtual Strain in Pure Slip**

Strain versus angular position plots as calculated in the tire FEA for pure slip scenarios are included here.

## D.1 Pure Braking Strain

Strain versus angular position in pure braking appears in Figures D.1 through D.12.

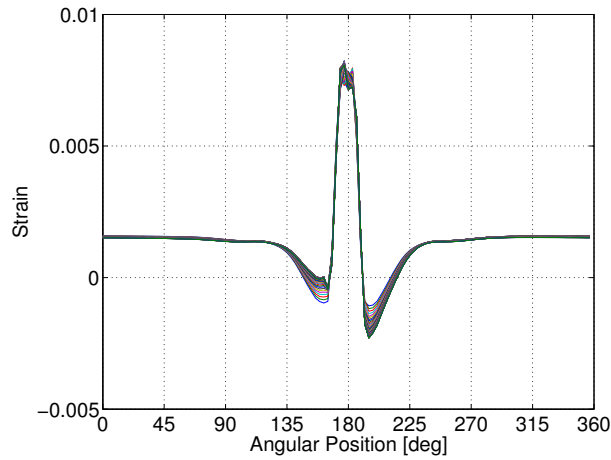


Figure D.1 – Training Data: Tread Centerline Longitudinal Strain versus Angular Position in Pure Braking

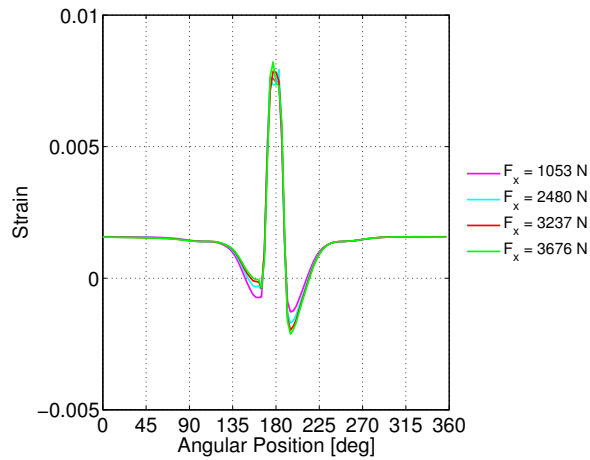


Figure D.2 – Training Data: Tread Centerline Longitudinal Strain versus Angular Position in Pure Braking – Detail

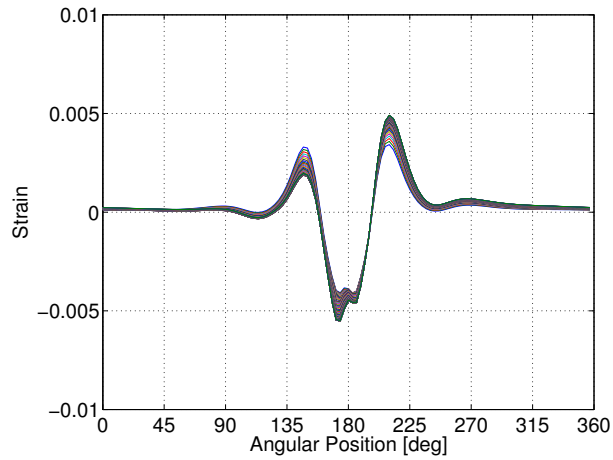


Figure D.3 – Training Data: Tread Centerline Lateral Strain versus Angular Position in Pure Braking

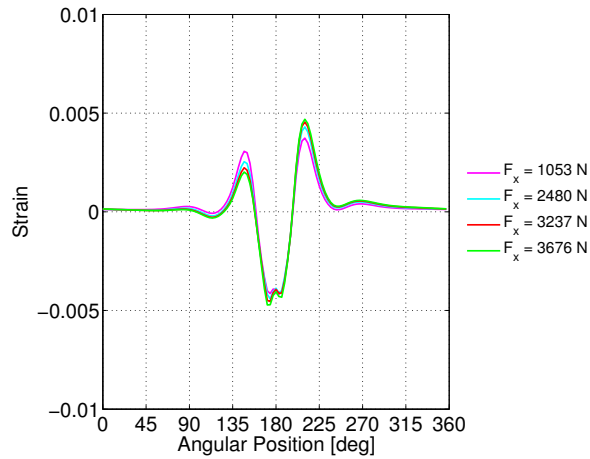


Figure D.4 – Training Data: Tread Centerline Lateral Strain versus Angular Position in Pure Braking – Detail

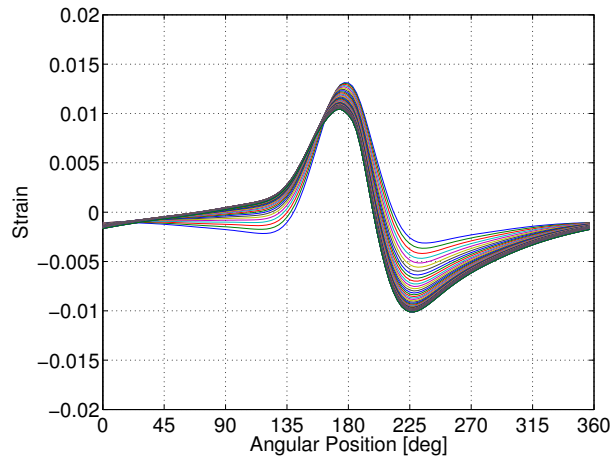


Figure D.5 – Training Data: Sidewall Left Longitudinal Strain versus Angular Position in Pure Braking

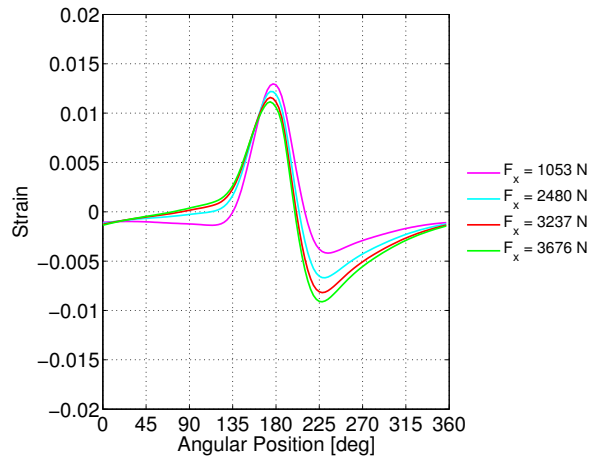


Figure D.6 – Training Data: Sidewall Left Longitudinal Strain versus Angular Position in Pure Braking – Detail

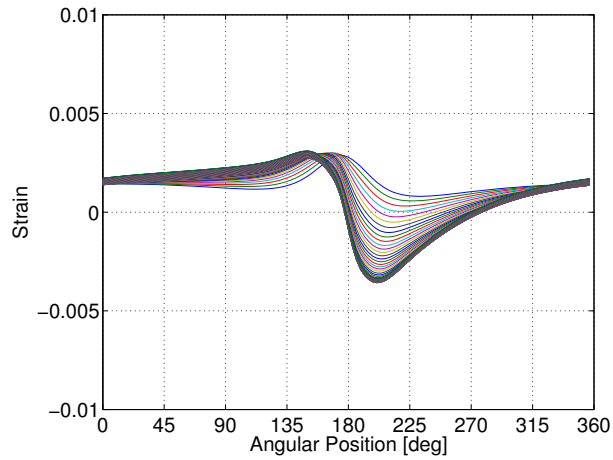


Figure D.7 – Training Data: Sidewall Left Radial Strain versus Angular Position in Pure Braking

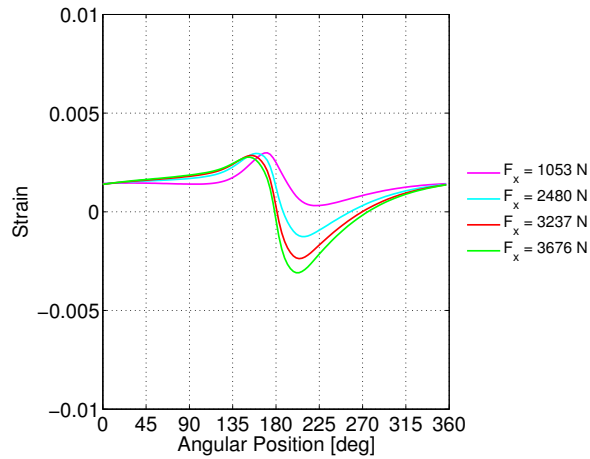


Figure D.8 – Training Data: Sidewall Left Radial Strain versus Angular Position in Pure Braking – Detail

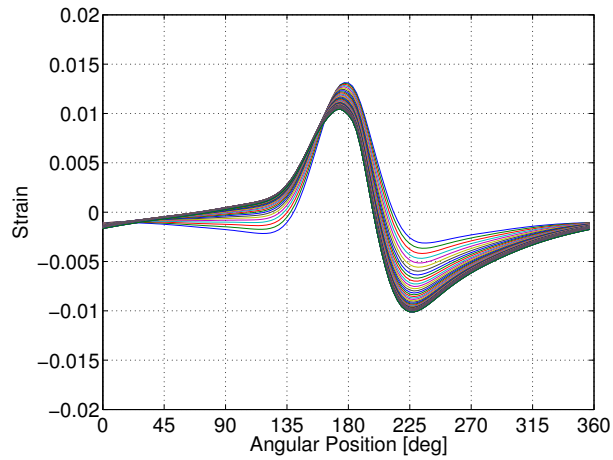


Figure D.9 – Training Data: Sidewall Right Longitudinal Strain versus Angular Position in Pure Braking

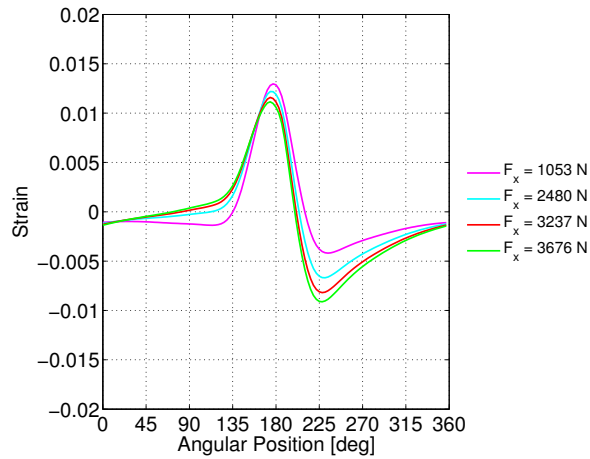


Figure D.10 – Training Data: Sidewall Right Longitudinal Strain versus Angular Position in Pure Braking – Detail



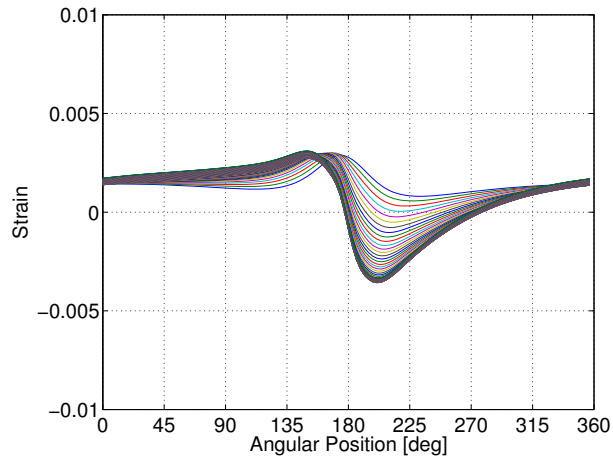


Figure D.11 – Training Data: Sidewall Right Radial Strain versus Angular Position in Pure Braking

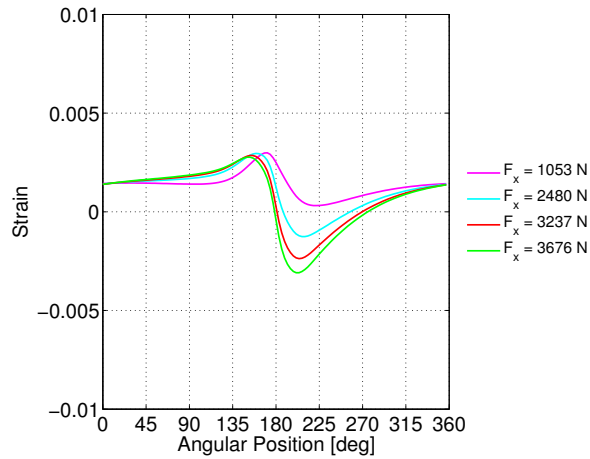


Figure D.12 – Training Data: Sidewall Right Radial Strain versus Angular Position in Pure Braking – Detail

## D.2 Pure Cornering Strain

Strain versus angular position in pure cornering appears in Figures D.13 through D.24.

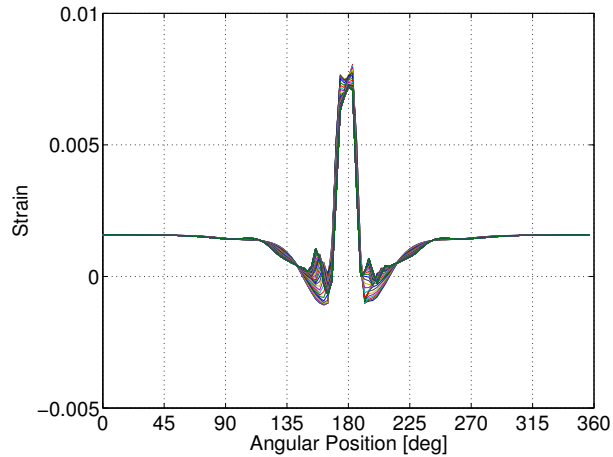


Figure D.13 – Training Data: Tread Centerline Longitudinal Strain versus Angular Position in Pure Cornering

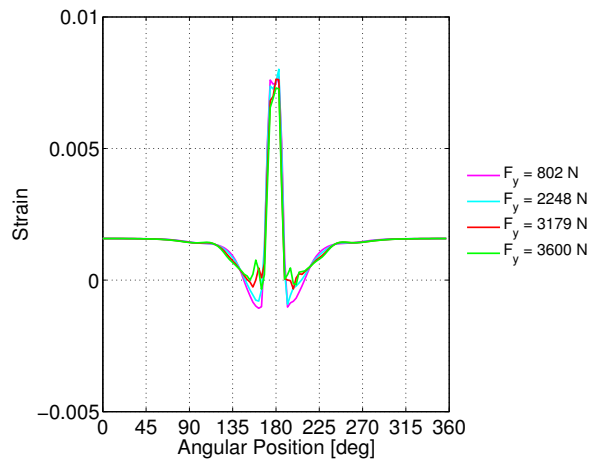


Figure D.14 – Training Data: Tread Centerline Longitudinal Strain versus Angular Position in Pure Cornering – Detail

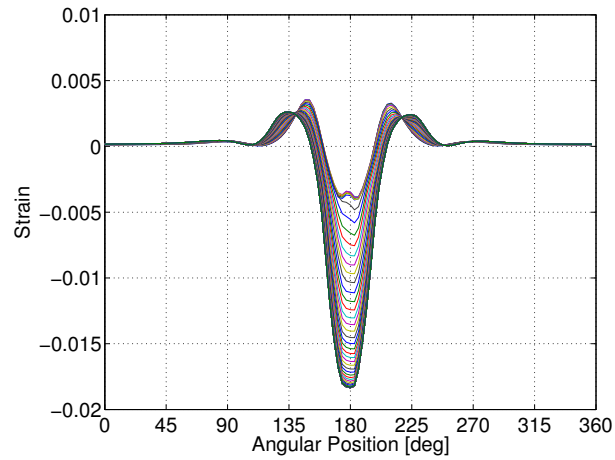


Figure D.15 – Training Data: Tread Centerline Lateral Strain versus Angular Position in Pure Cornering

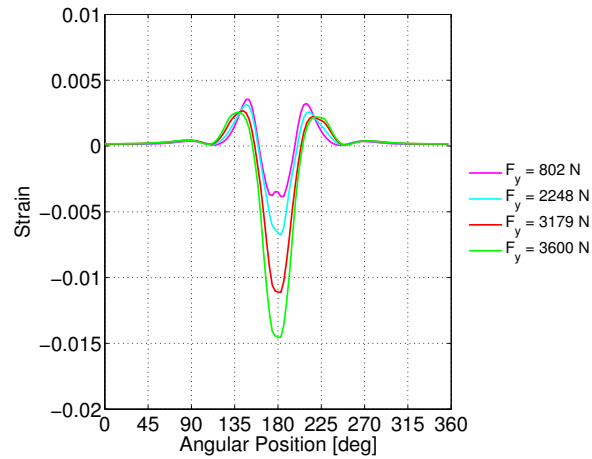


Figure D.16 – Training Data: Tread Centerline Lateral Strain versus Angular Position in Pure Cornering – Detail

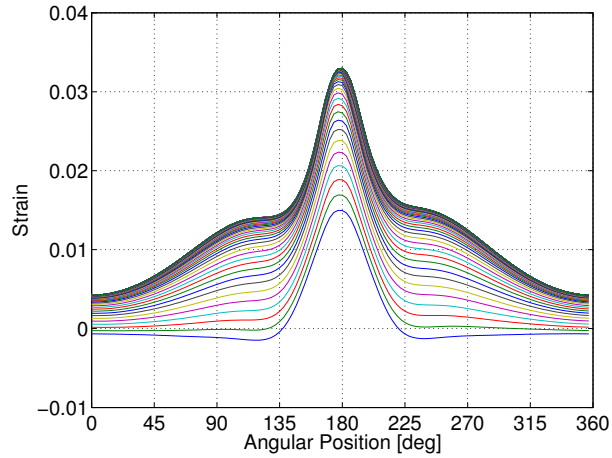


Figure D.17 – Training Data: Sidewall Left Longitudinal Strain versus Angular Position in Pure Cornering

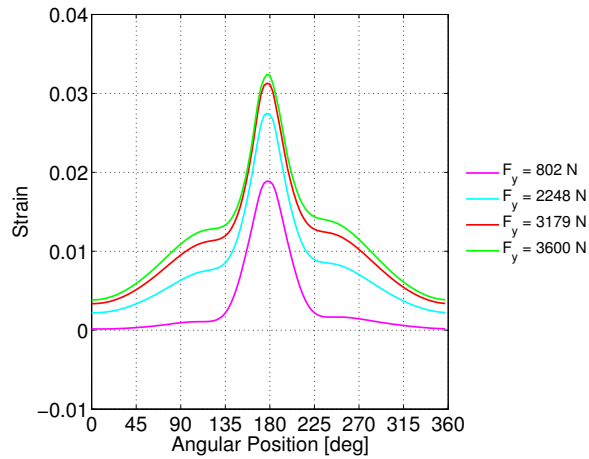


Figure D.18 – Training Data: Sidewall Left Longitudinal Strain versus Angular Position in Pure Cornering – Detail

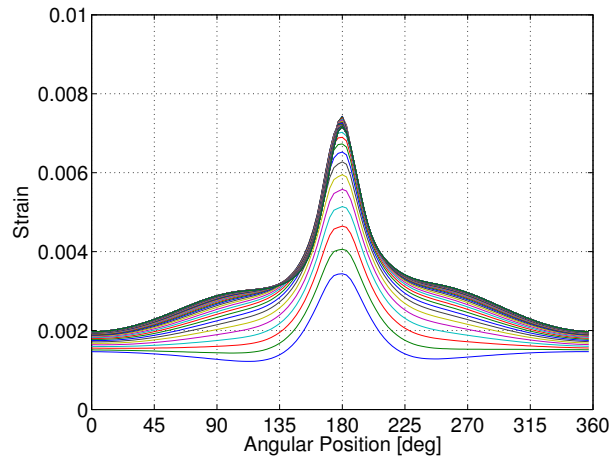


Figure D.19 – Training Data: Sidewall Left Radial Strain versus Angular Position in Pure Cornering

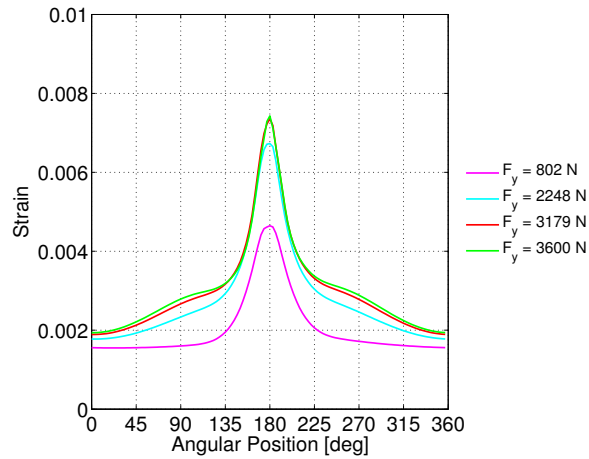


Figure D.20 – Training Data: Sidewall Left Radial Strain versus Angular Position in Pure Cornering – Detail

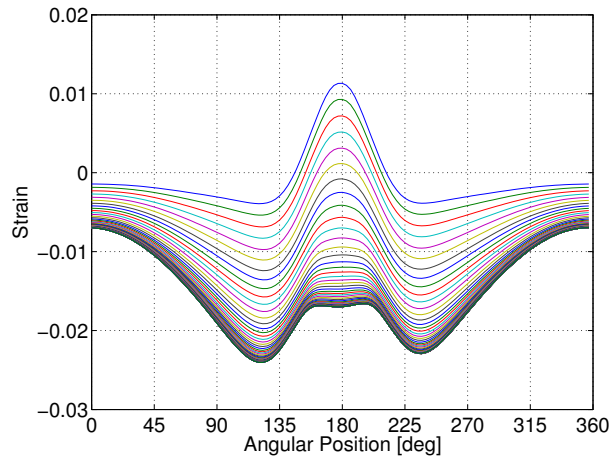


Figure D.21 – Training Data: Sidewall Right Longitudinal Strain versus Angular Position in Pure Cornering

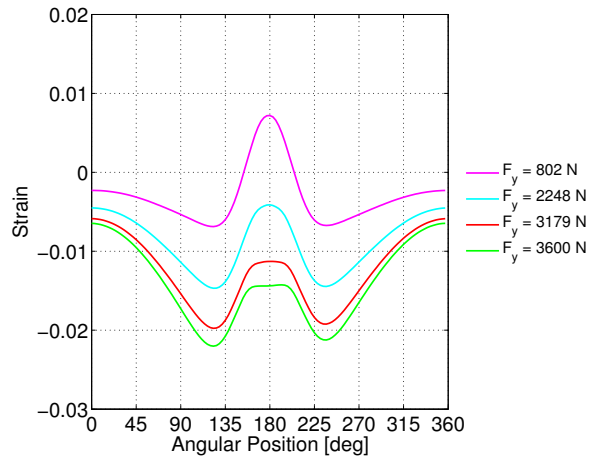


Figure D.22 – Training Data: Sidewall Right Longitudinal Strain versus Angular Position in Pure Cornering – Detail

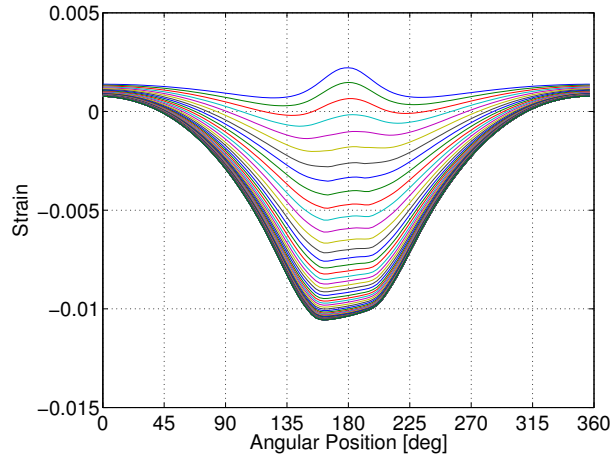


Figure D.23 – Training Data: Sidewall Right Radial Strain versus Angular Position in Pure Cornering

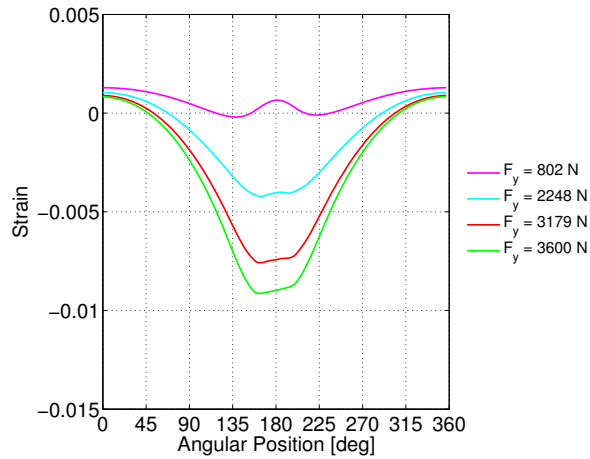


Figure D.24 – Training Data: Sidewall Right Radial Strain versus Angular Position in Pure Cornering – Detail

# Appendix E

## Virtual Strain Studies

### E.1 Supplemental Neural Network Studies

#### E.1.1 Footprint Section

The purpose of the footprint section study is to ascertain if a segment of the strain data, taken from each wheel revolution, can be used to train the networks instead of data taken from the entire 360 degrees. This approach, if successful, would reduce the large size of the function fitting problem submitted to the networks. Footprint refers to the tire contact patch, where the strain waveforms vary the most; presumably this section contains the most information.

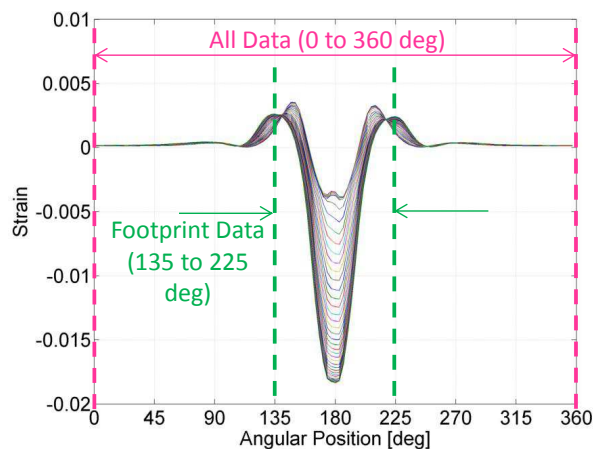


Figure E.1 – Tread Centerline Lateral Strain versus Angular Position in Pure Cornering with Footprint Data Section Highlighted



---

## APPENDIX E. VIRTUAL STRAIN STUDIES

---

In the footprint section study all six sensors are used, and the footprint strain data from 135 to 225 degrees (for a total of 90 degrees) are retained, while the data outside the footprint are discarded as illustrated in Figure E.1. Since the original sample rate is retained, the problem is reduced in size, as summarized in Table E.1. Worst case testing error from the all data and footprint data cases is summarized in Table E.2.

**Table E.1 – Reduced Size of Training Vectors in Footprint Study**

Training Data Type	Training Target Vector Size (Contains Tire Force Data)	Training Input Vector Size (Contains Strain Data)	Training Input Vector Description
All Data (0 to 360 deg)	3 x 1	720 x 1	6x120 Matrix Unfolded Into Column Vector
Footprint Data (135 to 225 deg)	3 x 1	186 x 1	6x31 Matrix Unfolded Into Column Vector

The results of Table E.2 show that the calculated forces from the footprint data are within 4%, so they are still fine even though they are not as good as the results using all data. The moments calculated from the footprint data, however, are within 55%, indicating that the moment information is somehow stored outside of the footprint portion of the strain signals. Since the moments results for the footprint training data are unacceptable, the footprint problem size reduction approach cannot be used in the STSS.

**Table E.2 – Worst Case Test Error for Network Trained on Footprint Data (All Six Strain Sensors Used in Training)**

Data Subset	All Data	Footprint Data
Change in $F_x$ [%]	1	4
Change in $F_y$ [%]	1	2
Change in $M_z$ [%]	14	55

### E.1.2 Peaks and Valleys

This goal of the peaks and valleys study is to establish if a dramatically reduced data subset can be used, in particular the peaks and valleys identified in the strain measurements. In the peaks and valleys study the two sidewall left sensors are used to train the neural networks. This is true of all the neural network studies from this point forward. Figures E.2 and E.3 show peaks and valleys in two sidewall left strain measurements in the pure slip simulations.

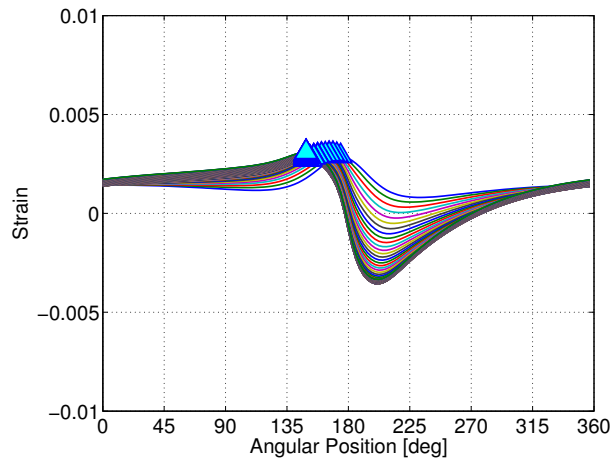


**Figure E.2 – Sidewall Left Radial Strain in Pure Braking – Peaks Indicated With Triangle Marker**

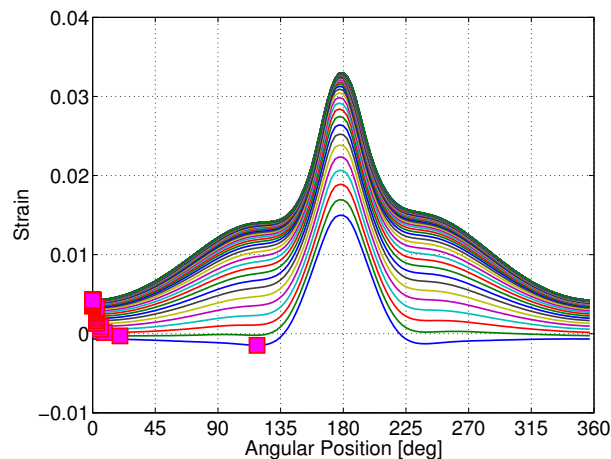


**Figure E.3 – Sidewall Left Longitudinal Strain in Pure Cornering – Valleys Indicated With Square Marker**

In the strain data the peaks occur at (or near) the center of the contact patch (at 180 degrees), in both braking and cornering. The valleys occur at the rear of the contact patch in braking and opposite from the contact patch in cornering. Tables E.3 and E.4 summarize the worst case testing error from the peaks and valleys study. The networks were trained on the peaks or the valleys of the strain waveforms or both, except in one peaks trial when the associated angular position was added to the peaks data. In that case the angular position was scaled from 0 to 0.01 to produce levels similar to the strain amplitudes for the purpose of minimizing numerical problems with the networks.

---

**APPENDIX E. VIRTUAL STRAIN STUDIES**

---

**Table E.3 – Worst Case Test Error for Network Trained on Peaks Data (Two Sidewall Left Strain Sensors Used in Training)**

Trial	All Data	Peaks	Peaks With Angular Position
Change in $F_x$ [%]	1	141	52
Change in $F_y$ [%]	1	27	6
Change in $M_z$ [%]	1	56	59

**Table E.4 – Worst Case Test Error for Network Trained on Valleys Data (Two Sidewall Left Strain Sensors Used in Training)**

Trial	All Data	Valleys	Peaks and Valleys
Change in $F_x$ [%]	1	142	143
Change in $F_y$ [%]	1	115	75
Change in $M_z$ [%]	1	92	66

From Tables E.3 and E.4 it can be seen that the neural networks are not capable of estimating the forces when trained on peaks and valley data alone. Tire force values are around 150% incorrect in the longitudinal force case, with the other force outputs not much better. Adding the angular position to the peaks improved the force estimates, but not enough to produce acceptable results. The networks produced worse results from training on valleys compared to training on peaks, and combining the two data sets did not improve the output from the networks. The results of the peaks and valleys study shows that peak-picking produces an insufficient training data set for the neural networks. Peaks and valleys cannot be used as a problem size reduction approach in the STSS.

### **E.1.3 Sample Rate**

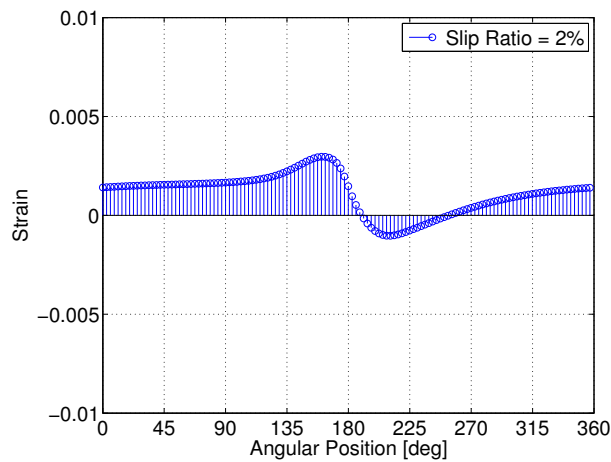
This purpose of the sample rate study is to determine if a reduced training data set can be used, particularly by reducing the sample rate. In this case, strain data collected over 360 degrees are used to train the neural networks, but the data are thinned out consistently using a lower sample rate. The tire finite element model as designed has an effective sampling frequency of 1000 Hz at 60 KPH. Figure E.4 shows one of the 1000 Hz strain measurements using a stem plot. Figure E.5 shows how this same signal appears when downsampled to 200 Hz.

Table E.5 shows the results of training the neural networks on five different sampling frequencies. Tire force outputs are calculated to within 5% of their actual values with a sampling frequency of 200 Hz. Lower sampling frequencies result in unacceptable output accuracy. Results of the sample rate study show that it may be possible to use a relatively low sampling frequency, such as 200 Hz, in the STSS. This is important since other attempts at reducing the size of the problem, namely, the footprint section approach

---

APPENDIX E. VIRTUAL STRAIN STUDIES

---



**Figure E.4 – Sidewall Left Radial Strain in Pure Braking – Sampling Frequency = 1000 Hz**

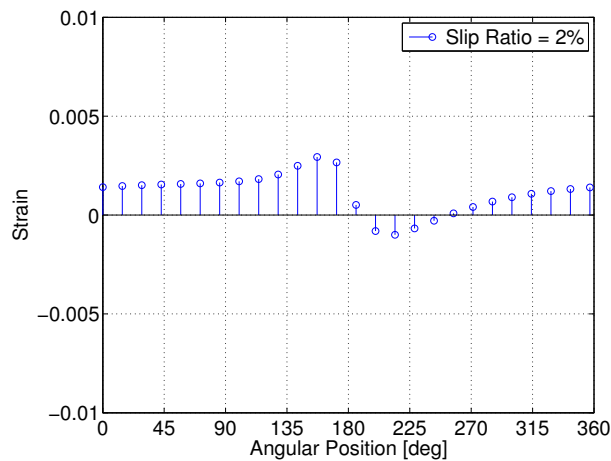


**Figure E.5 – Sidewall Left Radial Strain in Pure Braking – Sampling Frequency = 200 Hz**

and the peaks and valleys method, have not been successful. The use of a low sample rate should be investigated at higher translational velocities, in both the tire finite element model and the real STSS, since very high wheel angular speeds in combination with a low sampling frequency may result in too little training data for the networks.

**Table E.5 – Worst Case Test Error for Network Trained on Different Sampling Frequencies (Two Sidewall Left Strain Sensors Used in Training)**

Trial No.	1	2	3	4	5
Translational Velocity [KPH]	60	60	60	60	60
Sampling Frequency [Hz]	50	100	200	500	1000
No. of Points per Waveform	6	13	26	64	128
Change in $F_x$ [%]	19	1	1	1	1
Change in $F_y$ [%]	6	6	5	2	1
Change in $M_z$ [%]	91	15	3	3	1

#### E.1.4 Translational Velocity

The purpose of this study is to determine the effect that translational velocity has on in-tire strain, and ultimately on the tire force outputs calculated by the neural networks. For example, suppose that the networks are trained at one translational speed, but tested at a different translational speed. To what extent are the tire force estimates deteriorated? In order to study this question, the tire finite element model was solved at four different translational speeds: 20, 40, 60 and 80 KPH. The two sidewall left strain measurements were recorded in these velocity FEA jobs for use in the neural networks.

A qualitative review of the virtual strain data calculated for the different translational velocities shows that strain varies somewhat with velocity, although it is not a large effect. For the sidewall longitudinal strain, the “Direct Current (DC) offset” increases insignificantly with increasing velocity, as shown in Figure E.6. Sidewall radial strain shows more velocity dependence; the DC offset decreases with increasing velocity, as shown in Figure E.7. Overall strain waveforms retain their shape with differing translational velocities, despite vertical motion.

Table E.6 shows the results of training the neural networks on four different translational velocities and testing them on one velocity (60 KPH). Trial 1 has the worst performance; in this case the networks were trained on 20 KPH data and tested on 60 KPH data. Despite this significant discrepancy in translational velocity, the forces calculated were still within about 15%. Therefore, the training velocity, if different from the testing velocity, decreases the accuracy of the outputs from the networks, but it is not a strong effect.

An additional study was performed to investigate the effect of both differing translational velocity and brake torques on network outputs. Figures E.8 and E.9 illustrate the problem. Sidewall left longitudinal and radial strain curves are shown in the plots. The dotted magenta line is the “baseline” case. The solid red line represents the case where the translational velocity is doubled *and* the brake torque is 50% higher. These curves exhibit the same general trends as the speed increase only, in the sense of being offset

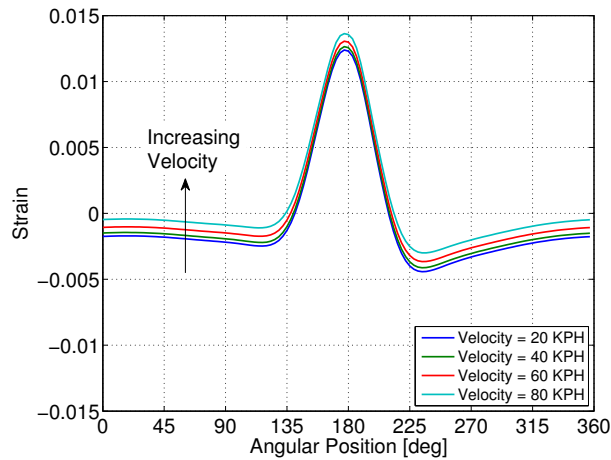


Figure E.6 – Sidewall Left Longitudinal Strain in Pure Braking – Brake Torque = 240 N-m

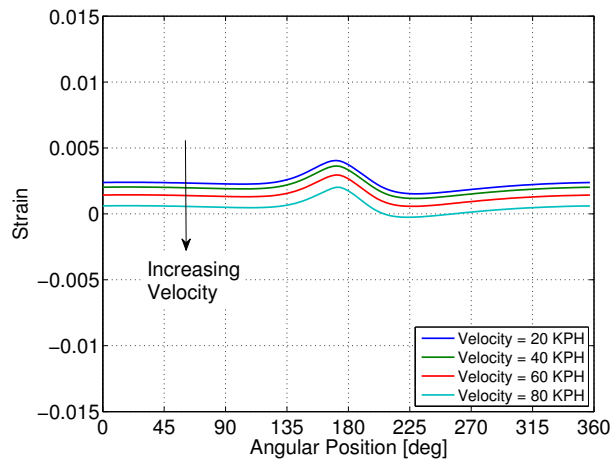


Figure E.7 – Sidewall Left Radial Strain in Pure Braking – Brake Torque = 240 N-m

from one another. The increased torque is apparent in a small modification to the wave-forms at the rear of the contact patch. There the strain curves are either relatively closer together or further apart depending on whether the sensor is in the longitudinal or radial orientation, respectively.

Table E.7 shows the results of training the neural networks on one translational velocity (40 KPH) and testing them on another translational velocity (80 KPH) using two different pure longitudinal slip test cases, each representing a different brake torque. In this scenario the network calculated longitudinal forces are within 11%. This result is similar to the previous velocity study in which the longitudinal forces were calculated

Table E.6 – Worst Case Test Error for Network Trained on Differing Velocities (Two Sidewall Left Strain Sensors Used in Training)

Trial No.	1	2	3	4
Training Velocity [KPH]	20	40	60	80
Testing Velocity [KPH]	60	60	60	60
Change in $F_x$ [%]	14	3	1	3
Change in $F_y$ [%]	3	4	1	6
Change in $M_z$ [%]	16	9	1	6
Rank	4	2	1	3

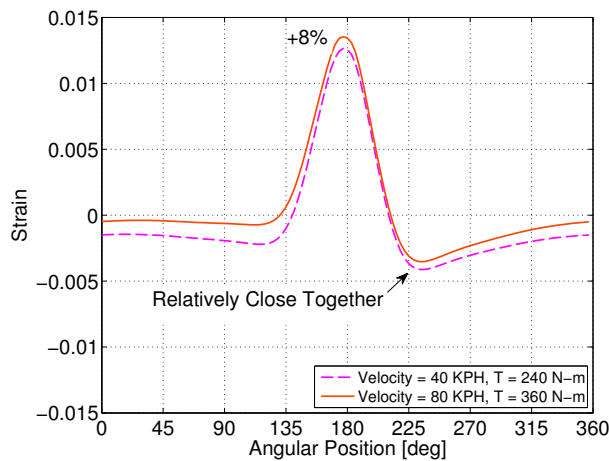


Figure E.8 – Sidewall Left Longitudinal Strain in Pure Braking – Two Velocities and Brake Torques

within 14%, in the case of a different 40 KPH velocity discrepancy. Therefore, the results of the translational velocity study show that if the testing data are 40 KPH different from the training data, the tire forces will be incorrect by approximately 15%. The velocity effect is not big, but it is still significant. It may require some form of compensation in the real STSS.

### E.1.5 Angular Position Shift

The purpose of the angular position shift study is to investigate the sensitivity of the neural networks to incorrect angular position data. In practice, the STSS will require a very good angular position sensor such as a rotary encoder that can trigger data acquisition with each of its pulses, resulting in strain data recorded at regular angular increments. To study the effect of inconsistent angular position data, the seven combined slip test cases were modified with deliberately induced angular position errors. The training data were

APPENDIX E. VIRTUAL STRAIN STUDIES

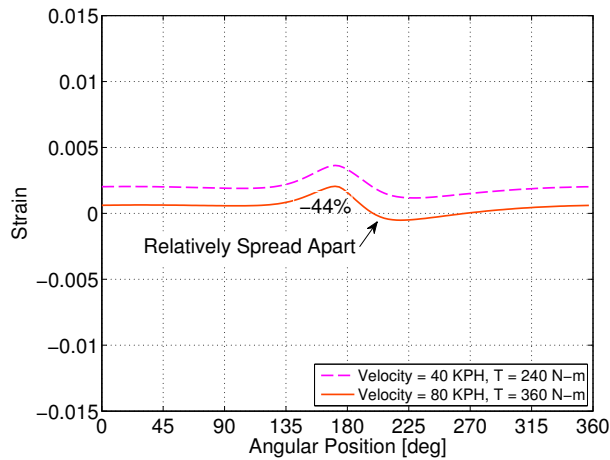


Figure E.9 – Sidewall Left Radial Strain in Pure Braking – Two Velocities and Brake Torques

Table E.7 – Worst Case Test Error for Network Trained on Differing Velocities and Torques (Two Sidewall Left Strain Sensors Used in Training)

Trial No.	1	2
Training Velocity	40 KPH	40 KPH
Testing Velocity / Torque Case	80 KPH / 240 N-m	80 KPH / 360 N-m
$F_x$ , Target	716.2	1050.2
$F_x$ , Calculated	797.9	1123.3
Change	11%	7%

unmodified. The same angular position errors were applied to both sidewall sensors in the test cases. Figure E.10 shows the sidewall left longitudinal test case strain measurements with a random angular shift of + / - 10% applied. Figure E.11 shows this same data with a retarded fixed angular shift of 10% applied. The original unmodified test data are shown in Figure 4.18.

Table E.8 lists the results of testing the neural networks on the random shifted data, and Table E.9 records the testing results for the fixed shifted data. A review of these results shows that the networks performed very poorly when the testing data were angularly shifted compared to the training data. The best results were for Trial 1, which had test data with a random angular shift of + / - 2%. In that case the tire forces were incorrect by 21 to 136%. The remaining trials had worse performance. The results of the angular position study show that a very good angular position sensor is required in the STSS, which can consistently acquire data at regular angular intervals. Inconsistencies in the angular position measurement resulting in lateral shifting of the strain data will lead to highly inaccurate forces estimated by the STSS. In order to duplicate the performance



---

APPENDIX E. VIRTUAL STRAIN STUDIES

---

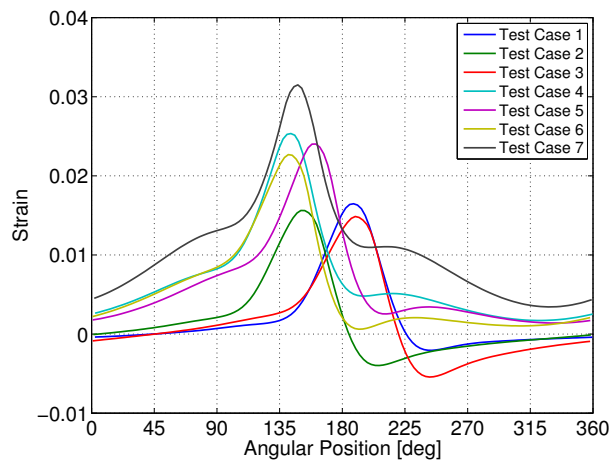


**Figure E.10 – Sidewall Left Longitudinal Strain in Combined Slip – Random Angular Shift Within + / - 10%**

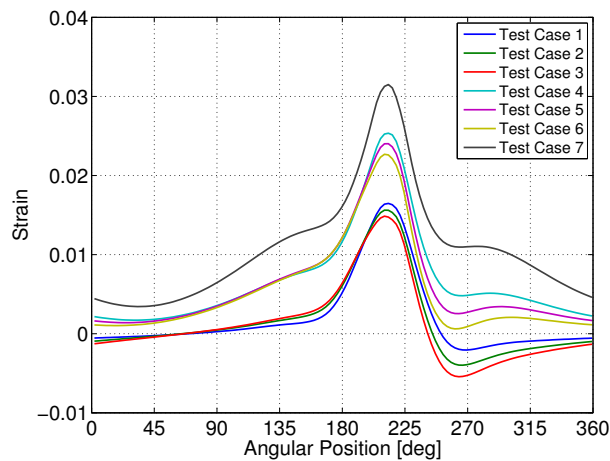


**Figure E.11 – Sidewall Left Longitudinal Strain in Combined Slip – Fixed Retarded Angular Shift of 10%**

of the reduced system as tested on the virtual strain data, the real STSS requires a 128 pulse per revolution encoder, at minimum.

APPENDIX E. VIRTUAL STRAIN STUDIES

---

**Table E.8 – Worst Case Test Error for Network Tested on Random Angular Shift Data (Two Sidewall Left Strain Sensors Used in Training)**

Trial No.	All Data	1	2	3
Description	No Shift	Random Shift + / - 2%	Random Shift + / - 5%	Random Shift + / - 10%
Change in $F_x$ [%]	1	54	130	267
Change in $F_y$ [%]	1	21	26	57
Change in $M_z$ [%]	1	136	477	803

**Table E.9 – Worst Case Test Error for Network Tested on Fixed Angular Shift Data (Two Sidewall Left Strain Sensors Used in Training)**

Trial No.	All Data	4	5
Description	No Shift	Fixed Shift Retarded 10%	Fixed Shift Advanced 10%
Change in $F_x$ [%]	1	322	342
Change in $F_y$ [%]	1	131	164
Change in $M_z$ [%]	1	1955	1248

## Appendix F

# Sensor Durability Bench Test

### F.1 In-Tire Piezoelectric Sensor

The piezoelectric effect is the coupling of the strain in a material with an electric field [76]. An electric field causes the piezoelectric material to strain; the converse is also true, where mechanical deformation results in electrical generation. Piezoelectric strain and deformation sensors have several desirable features considering an in-tire application, including low cost, mechanical flexibility and independence from external power supplies and amplifiers.

Despite these advantages, commercially available piezoelectric strain sensors have a significant disadvantage, which is that very little information is available to the consumer concerning the strain range of the sensors and the durability of the sensors when subjected to multiple strain cycles. This is in contrast with conventional foil-type strain gauges, where the strain range of the sensor is usually provided by the manufacturer. In some cases, extensive durability test results are provided showing the relationship between the fatigue life of the sensor and the number of strain cycles it is subjected to.

In the case of piezoelectric sensors, published studies tend to focus on the measurement of small strains, since the interest of the authors is usually to investigate whether conventional strain gages (for small strain applications) can be replaced with piezoelectric strain gages. In one study, the authors advise that piezoelectric sensors be limited to measuring 150 microstrain or less [77], which is around 300 times smaller than the expected worst case tire sidewall strain level during each wheel revolution. However, their advice is not based on test results at higher strains, as results are shown for measurement of a few hundred microstrain at most. Instead, general comments are made regarding expected problems with sensor calibration values at high strains, due to the non-linear behavior of piezoelectric materials.

### F.1.1 Sensor Durability Test Overview

Due to the missing strain range and fatigue life information, a physical durability bench test of a commercially available piezoelectric sensor was conducted. The purpose of the test was to determine if the sensor could withstand the many high strain cycles imposed on it when installed on the inside surface of a tire. Results from a preliminary tire finite element analysis study showed that longitudinal tire sidewall strain may peak in the 5 to 6% range for a high profile passenger car tire [74]. The question was whether the piezoelectric sensors are capable of surviving many cycles at this strain level, and if so, are the measurements repeatable?

A dedicated durability bench test rig was fabricated for the purpose of testing the piezoelectric sensor. The durability testing machine was designed to deform a tire sample with a sensor attached to its inside surface. The tire sample was cut from the sidewall of a radial passenger car tire, since the results of the tire FEA study showed that the sidewall should experience the worst case deformation. The piezoelectric sensor was attached to the sidewall sample in the radial direction of the tire, and the test rig applied a cyclic loading to the sample in the radial direction. Each strain cycle induced by the testing machine was designed to simulate one full revolution of the tire; it was especially important to replicate the deformation experienced by the sidewall when traveling through the tire / road contact patch.

The test rig operated at a constant frequency of 4 Hz, which was equivalent to a vehicle translational speed of 30 KPH for the tire under study. The multi-day durability test was conducted for approximately 6 hour time segments per day, for a period of up to several weeks, with sensor output recorded every hour. This was a realistic, and rather low, amount of durability test time in a tire application, since the expected tire service life is far longer than the total time of the test, which was equivalent to approximately 600,000 cycles, or around 1,300 kilometers of vehicle travel, assuming a 7 day test.

Output from the piezoelectric sensor at the beginning of the test was impressive, with unamplified voltage levels in the +/- 3V range and a low noise, approximately sinusoidal shape waveform. In time, however, sensor peak-to-peak voltage levels decreased and sensor signal quality deteriorated, with noisy sensor output. Results show that sensor output levels and signal quality were relatively consistent for the first hour only. Assuming that a 5% decrease in voltage is the not-to-exceed target, the piezoelectric sensor should not be used for more than one hour at 30 KPH travel, limiting the sensor to less than 13,500 cycles. While these results indicate that the piezoelectric sensor is not suited to the STSS, it may be appropriate for other dynamic high strain measurement applications with lower durability requirements, where the peak strain is around 5% and the total number of strain cycles is in the thousands.

### F.1.2 Sensor Description

Details of the piezoelectric sensor type tested are listed in Table F.1, which were obtained from the shipping materials delivered with a package of twenty piezoelectric sensors. The LDT series sensor tested was much larger than a typical foil-type strain gauge. The shape was rectangular, with an overall width of 16-mm (0.63-in) and an overall length of 72-mm (2.83-in). They were very thin, with a thickness of 0.2-mm (< 0.01-in). Subjectively, they were much stiffer than rubber, with very little longitudinal deformation when extended by hand, similar to typical plastic films.

**Table F.1 – Piezoelectric Strain Sensor Information**

Supplier	Measurement Specialties, Inc.
Model	LDT2-28K with Lead / Rivet
Part Number	1-1003745-0
Quantity	20 Pieces
Manufacture Date	April 8, 2014

The piezoelectric sensor as tested consisted of a piezo film sandwiched between two electrodes [78]. The piezo film was a compound layer consisting of a thin layer of polyvinylidene fluoride (PVDF) fluoropolymer laminated to a thin layer of polyester. PVDF was the piezoelectric material; polyester was bonded to it to create a two-layer composite “beam”. When the beam was subjected to bending, the neutral axis of zero bending stress was located in the polyester layer, resulting in relatively higher strain in the PVDF layer (compared to the unlaminated scenario with only a PVDF layer), and ultimately higher voltage output from the sensor.

The electrode layers were made from silver ink using a screen printing process. The complete sensor lay-up was coated on both sides with protective urethane layers. Each sensor was delivered with 26 American Wire Gage (AWG) lead wires already attached using rivets. The recommended adhesive for sensor attachment was epoxy. A photograph of one of the sensors appears in Figure F.1.

The electrical capacitance of the sensor was directly proportional to its area and inversely proportional to its thickness. The laminated sensor should have been very sensitive to both strain and bending deformation modes, although a particular sensitivity was not provided. According to the manufacturer, a similar piezoelectric sensor with a simple PVDF layer (no polyester layer bonded to it) should have a sensitivity of up to 100 V per 1% of strain, depending on the frequency of excitation. Such a high sensitivity was expected at high frequencies, since the piezoelectric sensor, when connected to a data acquisition system, acted as a high-pass filter that attenuated higher frequencies less than lower frequencies, as shown in Figure F.2. As shown in the sketch, both the voltage source,  $V_{in}$ , and the capacitance in series with it,  $C$ , are produced by the piezoelectric

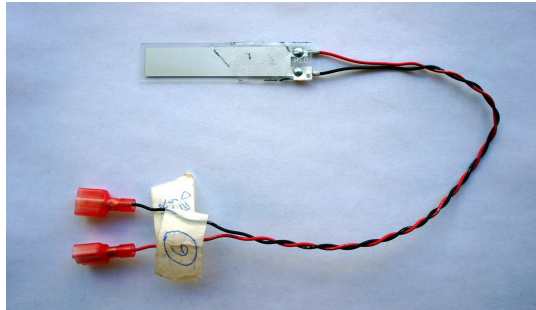


Figure F.1 – Piezoelectric Deformation Sensor

sensor. The resistance,  $R$ , is provided by the measuring device. The output voltage,  $V_{out}$ , is measured across  $R$ . The high-pass cutoff frequency with 3 dB attenuation is  $f_c = \frac{1}{2\pi RC}$ .

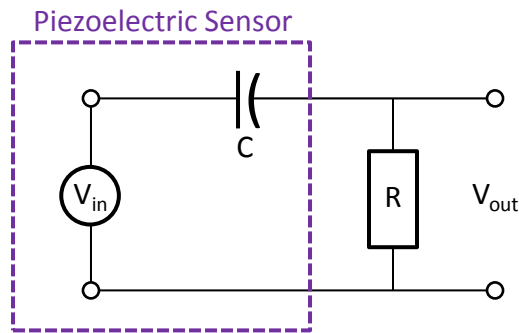


Figure F.2 – Piezoelectric Sensor Electric Circuit

The piezoelectric sensor as tested had several desirable features considering the STSS application, including the following.

- Inexpensive retail cost  $\simeq$  US \$7 per piece.
- Mechanically flexible enough to conform to curved surfaces.
- Independent from external power supplies or amplifiers.

One limitation of the piezoelectric sensor was that it had no static strain measurement capabilities; it was a dynamic strain sensor only. Therefore, the piezoelectric sensors could not be installed inside a set of tires and used to estimate the static curb weight of a vehicle when the vehicle was parked, for example. The most important disadvantage of the piezoelectric sensor was that very little information was available concerning its strain range and its fatigue life when subjected to multiple strain cycles. When specifying conventional foil-type strain gauges, the strain range of the sensor is provided, and

---

## APPENDIX F. SENSOR DURABILITY BENCH TEST

---

durability test results are often available showing the relationship between fatigue and number of strain cycles; see [79] for one example. In the case of the piezoelectric sensor, no such information was forthcoming.

Two different distributors of the same piezoelectric sensor model were contacted in an attempt to obtain information about the strain range and fatigue life of the sensor. The first distributor said that the sensors were “suitable for strain measurement of rubber or similar materials”, although they would not commit to a strain range. In conversation with a second (unrelated) distributor, their representative would not give a strain range for the sensor, saying that this information is “not published”.

Since the piezoelectric sensor had some advantageous characteristics, but information about its strain range and fatigue life could not be obtained from the distributors, a physical durability bench test of the sensor was conducted. The purpose of the test was to determine if the piezoelectric sensor could withstand the many high strain cycles imposed on it when installed inside of a tire, and if so, whether or not the measurements were repeatable. The physical durability testing of the piezoelectric sensor was also used to investigate adhesives and attachment schemes.

### F.1.3 Sensor Durability Bench Test

#### F.1.3.1 Bench Test Parameters

When the durability bench testing machine was first designed, its original purpose was to determine if the piezoelectric sensor could survive several trips around the University of Waterloo (UW) ring road, since such a trip would be the minimum on-road vehicle test that could be performed to study the performance of the prototype STSS, given the financial constraints on the research project and other limitations, including the use of a research vehicle not registered for use on public roads.

Figure F.3 shows sketches of the ring road and the tire / wheel, with quantities used in the wheel frequency calculation.  $R$  refers to the tire radius (the unloaded radius is used as an approximation to the effective radius) and  $v$  is the translational velocity of the wheel. The grey ring road of 2.8 km length circumscribes most of the campus buildings, shown in yellow. The ring road is private, and therefore the responsibility of UW campus police, along with the parking lots that were used for additional on-road vehicle testing.

**Wheel Frequency.** The durability bench testing rig was operated at the approximate average vehicle speed on the ring road, which was assumed to be around 30 KPH. Equations (F.1) through (F.5) show the calculations used to determine the fundamental wheel frequency on the ring road, which is 4 Hz:

$$R = 0.35 \text{ m} , \tag{F.1}$$

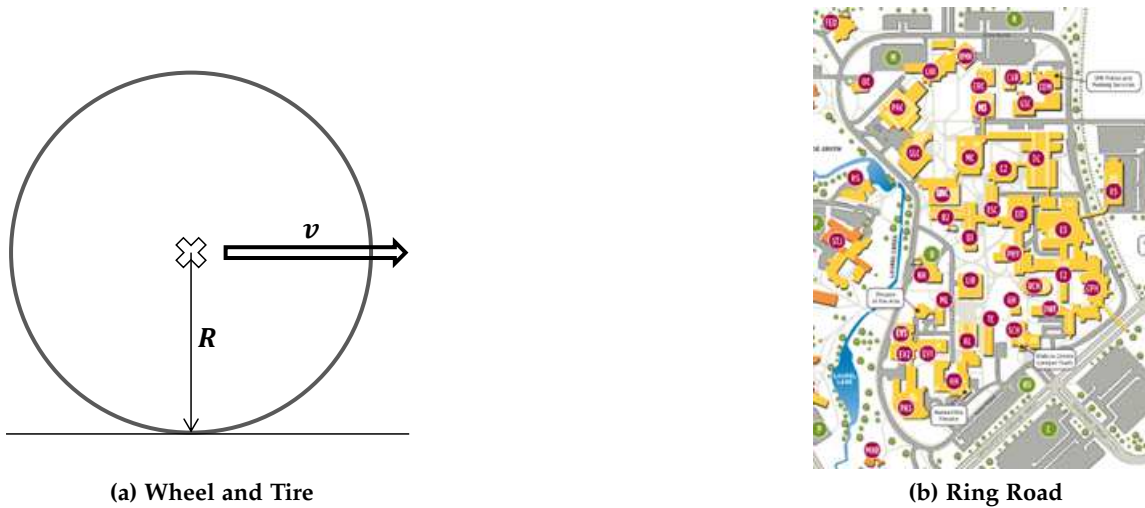


Figure F.3 – Sketches for Bench Test Parameters Calculations

$$v = 31.7 \text{ KPH} = 8.8 \frac{\text{m}}{\text{s}} , \quad (\text{F.2})$$

$$C = 2\pi R = 2\pi (0.35 \text{ m}) = 2.2 \text{ m} , \quad (\text{F.3})$$

$$T = \frac{2.2 \text{ m}}{8.8 \frac{\text{m}}{\text{s}}} = 0.25 \text{ s} \quad \text{and} \quad (\text{F.4})$$

$$F = \frac{1}{T} = 4 \text{ Hz} \quad (\text{F.5})$$

where  $C$  refers to the circumference of the tire,  $T$  is the time per wheel revolution and  $F$  is the wheel frequency.

**Number of Cycles.** Calculations to determine the total number of wheel revolutions (cycles) in the proposed ring road test appear in Table F.2. It can be seen that the sensors would be subjected to more than 10,000 strain cycles in the proposed ring road test, which consisted of only eight trips around the ring road requiring less than 45 minutes total travel time. This calculation illustrates the very high durability requirement for the in-tire sensors, and tires in general. According to the United States Department of Transportation, a customary on-highway tire endurance test is conducted for a distance of 40,000 mi (around 64,000 km) [80], meaning that the tire under study would experience more than 29 million cycles over the span of this endurance test that is intended to represent its service life.



**APPENDIX F. SENSOR DURABILITY BENCH TEST**

---

**Table F.2 – Number of Cycles in Proposed Ring Road Test**

Length of Ring Road [m], L	2759.4
Circumference of Tire [m], C	2.2
Number of Wheel Revolutions per Ring Road Circuit, $N_{rev} = \frac{L}{C}$	1254.8
Number of Ring Road Circuits, $N_{circ}$	8
Total Number of Wheel Revolutions, $N_{total} = N_{rev} \times N_{circ}$	10,038

**Deformation Level.** Sidewall deformation was investigated using the durability bench testing machine. Figure F.4 shows tire strain contours in a braking finite element analysis, in the fully locked and skidding condition, along with a yellow rectangle indicating the approximate location and orientation of the sidewall radial piezoelectric sensor in the worst case contact patch deformation area.

Deformation in the elements underneath the sensor was calculated using the tire finite element model, as shown in Figure F.5, where the undeformed model is gray in color. The deformed model is rainbow color with magnitude of displacement contours shown. The model predicts a maximum displacement magnitude of 17 mm; the goal in the durability bench test was to replicate this level of sidewall deformation.

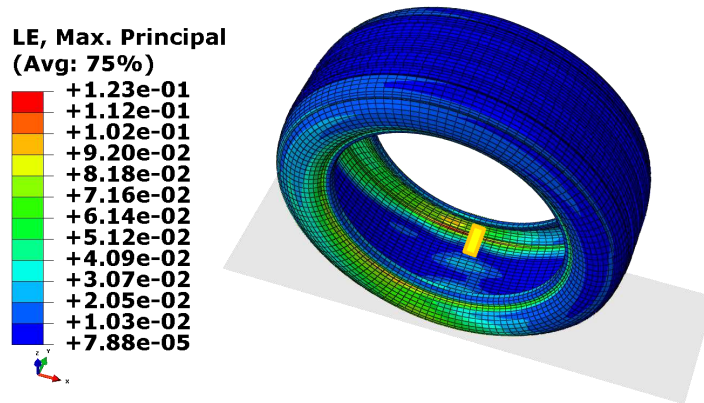


**Figure F.4 – Tire Braking Strain with Sidewall Radial Sensor**

**F.1.3.2 Bench Test Apparatus**

A photograph of the durability bench testing machine appears in Figure F.6. The machine was fabricated entirely from scrap and reused components. In function it was a crank-slider mechanism, with a rotating crank, a connecting rod and a reciprocating slider. The slider contacted the tire sample and compressed it, producing the desired deformation. The crank was part of the 15:1 ratio worm gearbox assembly on the electric motor, shown

---

## APPENDIX F. SENSOR DURABILITY BENCH TEST

---

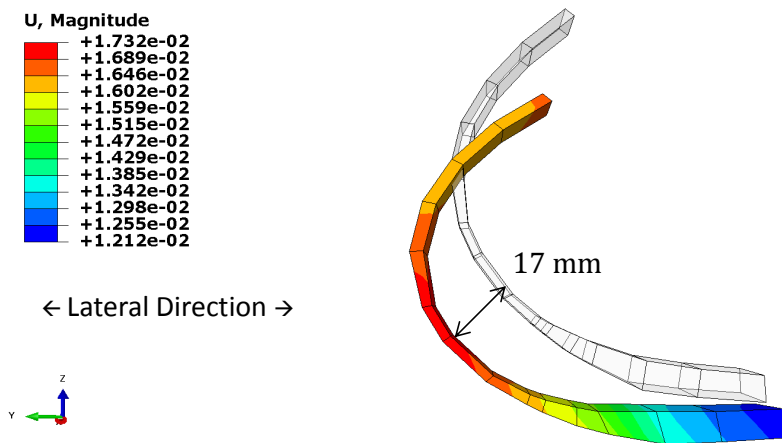


Figure F.5 – Tire Braking Displacement of Sidewall Radial Sensor

in Figure F.7. Application of 24 Volts Direct Current (VDC) input voltage to the electric motor resulted in an output angular speed of just below 4 Hz, which was the target frequency representing a 30 KPH vehicle speed on the ring road. A 45 minute bench test subjected the tire sample to 10,000 strain cycles.

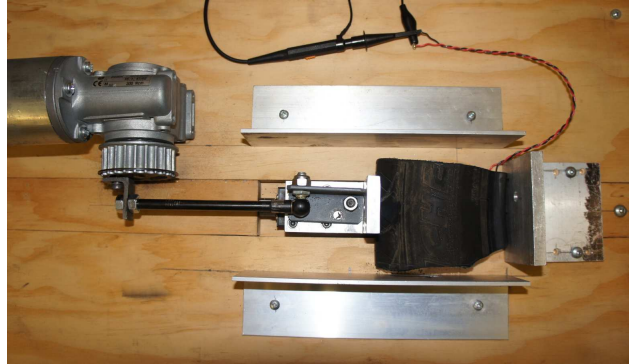


Figure F.6 – Durability Bench Testing Machine with Tire Sample

Tire sidewall samples were cut such that the radial direction was parallel to the reciprocating slider axis in the durability bench testing machine; piezoelectric sensors were bonded to these samples in the radial direction using adhesives (the sensor was on the underside of the sample during the test documented in Figure F.6). In order to obtain the 17 mm of displacement required per the tire FEA, a stroke of 35 mm was required from the machine, as shown in Figure F.8. This stroke value was determined by physical measurement and manipulation of a typical tire sample. The connecting rod joint location on the crank component was adjusted to create the 35 mm stroke required.

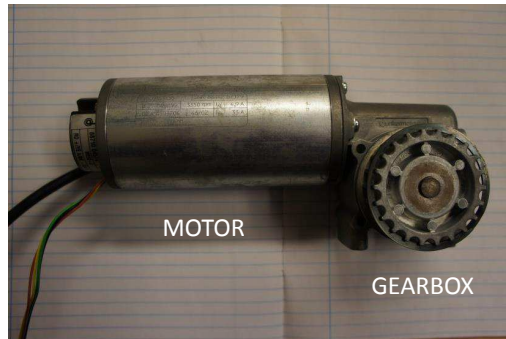


Figure F.7 – Electric Motor in Durability Bench Testing Machine

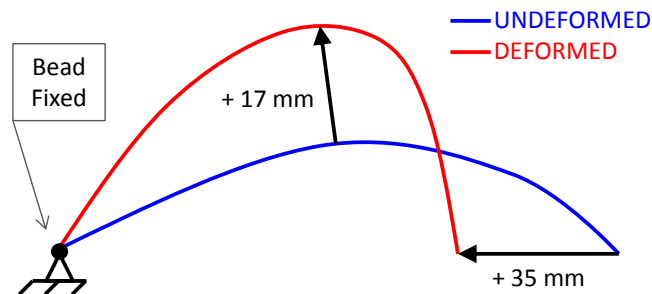


Figure F.8 – Deformation of Tire Sample in Bench Test – Side View, Centerline Shown, Not to Scale

### F.1.3.3 Bench Test Samples

Table F.3 provides an overview of the tire samples that were fabricated and tested using the durability bench testing machine. All of the adhesives used for sensor attachment were mass produced, locally available and low in toxicity. Five tire samples were tested; four had sensors bonded to the inside of the tire sample over the entire sensor area. The fifth sample was bonded only at the top third area of the sensor, where top refers to the end with the leads. At the bottom third the sensor was retained with a paper clip, which was itself bonded to the tire rubber at either side of the sensor. The paper clip was used to inhibit large motions of the sensor free end and thus minimize the likelihood of the free end pulling the bonded end away from the tire.

A modified (M) version of sample no. five was the “winner” in the durability bench tests. The modified version had plastic underneath the free end of the sensor, which prevented the sensor from abrading and removing the tire rubber at the free end. A photograph of the modified fifth sample is shown in Figure F.9. Modified sample no. 5 was the most durable sample tested using the durability bench testing machine, but its durability was determined to be unacceptable for use in the STSS. Unacceptable performance

## APPENDIX F. SENSOR DURABILITY BENCH TEST

---

was observed in all of the samples tested, as in most cases sensor voltage levels decreased over the tests, and in all cases the sensor signal quality deteriorated significantly with increasing durability test time.

**Table F.3 – Tire Sidewall Sample / Piezoelectric Sensor Attachment Durability Trials**






Sample No.	Image	Entire Sensor Bonded?	Description	Results	Stable Sensor System?
1		Yes	Entire sensor attached with “Amazing Goop Household” adhesive; sensor may be skewed w.r.t. sidewall radial direction. Sensor covered with bicycle tire repair kit rubber patch.	Sensor voltage level <i>decreases</i> and signal quality deteriorates with increased durability test time.	No
2		Yes	Entire sensor attached and covered with “Liquid Patch” adhesive; also a 3M foam base layer bonded using “Pres-Tite Contact Cement”.		
3		Yes	Entire sensor attached with “Chemical Vulcanizing Fluid” adhesive. Sensor covered with tube tire repair kit rubber patch.		
4	Appearance very similar to no. 1.	Yes	Same as no. 1 except sensor confirmed parallel to sidewall radial direction.		
5		No	Top third of sensor attached with cyano-acrylate superglue; bottom third of sensor retained with paper clip (bonded to rubber with “Amazing Goop Household” adhesive).	Sensor voltage level <i>increases</i> and signal quality deteriorates with increased durability test time.	No
5M		No	Plastic added under free end of no. 5.	Sensor voltage level <i>decreases</i> and signal quality deteriorates with increased durability test time.	No



Figure F.9 – Modified Tire Sidewall Sample No. 5

#### F.1.3.4 Bench Test Results

The durability performance of each tire sample in the durability bench tests is reviewed. Plots show time domain output and also maximum voltage levels. Graphs showing voltage versus time are time captures made using a HP 35670A dynamic signal analyzer; these plots clearly show the sinusoidal nature of the voltage output from the piezoelectric sensors in the bench test deformation cycles. The time histories are always plotted using the same scales such that the waveforms can be compared. The horizontal time scale is 2 seconds in length and the vertical voltage scale ranges from -3 to +3 volts. The starting point in the time captures are random, since the data acquisition was not triggered in any way.

The maximum voltage levels were determined using a Fourier analysis of measured sensor time data. An amplitude frequency spectrum was calculated that was used to determine the voltage level at 4 Hz, which was the fundamental frequency of the durability bench testing machine. The 4 Hz voltage level is reported as the maximum voltage level.

**Sample No. 1.** Figure F.10 shows time domain signals from the sample no. 1 piezoelectric sensor on the first day of testing. The signal at the start of the test appears in Figure F.10a. The signal after 60 minutes of durability test time appears in Figure F.10b. These plots show the innately high output voltage from the piezoelectric sensors, which do not require amplification. It can be seen that there was a reduction in peak-to-peak voltage levels over the one hour durability test, with the maximum voltage level being 30% lower after 60 minutes. Based on this result, further durability testing of sample no. 1 was performed to find out if voltage levels would continue to decrease.

Time domain signals from the sample no. 1 piezoelectric sensor on the second day of testing are shown in Figure F.11. Times in minutes shown in the plots indicates total durability test time accumulated on the sample. For example, Figure F.11a shows the

## APPENDIX F. SENSOR DURABILITY BENCH TEST

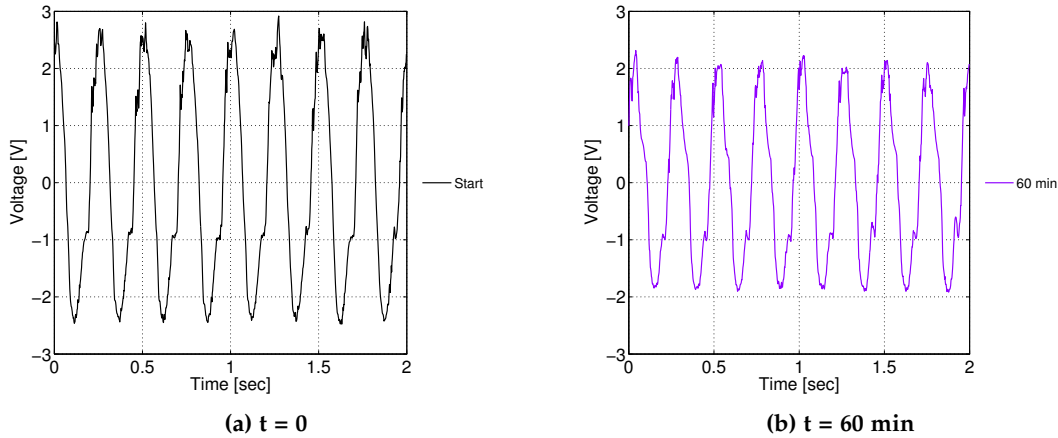


Figure F.10 – Sample No. 1 Time Domain Signals in Durability Test – Day 1

sensor output after 90 minutes of total test time; 60 of these minutes were accumulated on the first test day. Therefore, at the 90 minute time point, the sample had experienced 30 minutes of durability test time on the second test day.

From Figure F.11 it can be seen that the output from the sample no. 1 piezoelectric sensor had deteriorated dramatically at the beginning of the second test day, with far lower maximum voltage levels and a much noisier signal. At the end of the second testing day, sample no. 1 had logged eight hours of total durability test time. Comparing Figure F.11a with Figure F.11b reveals a decrease in peak-to-peak voltage levels over the second test day. Maximum voltage level versus time for sample no. 1 is plotted in Figure F.12. A review of this plot shows that there was a large drop in sensor voltage levels after the overnight pause in the test, then a slow decrease in sensor output over the second test day. The maximum voltage level decreased by 22% from three hours to eight hours on the second day.

**Sample No. 2.** Figure F.13 shows time domain signals from the sample no. 2 piezoelectric sensor on the first day of testing. Starting peak-to-peak voltage for sample no. 2 was lower than sample no. 1 due to a difference in mounting the piezoelectric sensors in the samples. In sample no. 2, the sensor was attached to a foam base, which was itself bonded to the tire rubber. The top surface of the foam apparently experienced less deformation compared to the bottom surface that was constrained to deflect with the tire rubber, since maximum voltage levels were lower in sample no. 2 compared to sample no. 1. A review of Figures F.13a and F.13b shows that there was a reduction in peak-to-peak voltage levels over the one hour durability test, with the maximum voltage level being 24% lower after 60 minutes, which was a similar trend compared to sample no. 1. Furthermore, there was an anomaly in the waveform that developed by 60 minutes of total

## APPENDIX F. SENSOR DURABILITY BENCH TEST

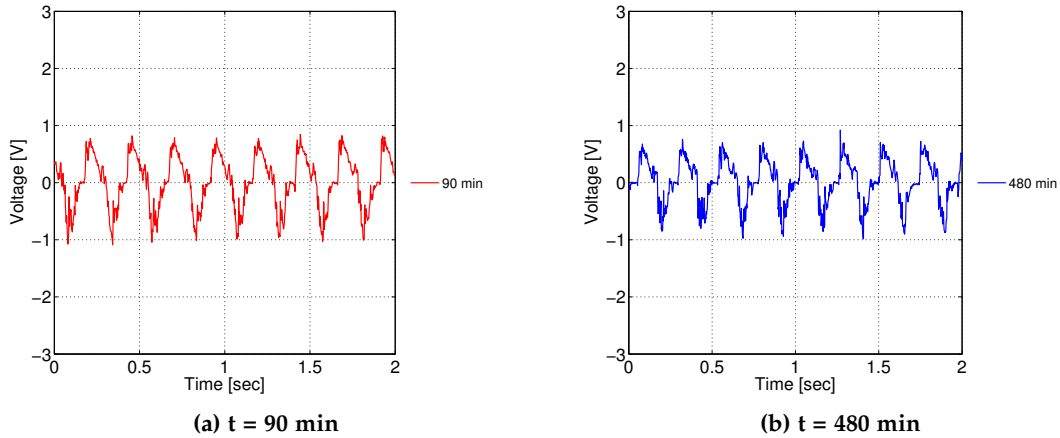


Figure F.11 – Sample No. 1 Time Domain Signals in Durability Test – Day 2

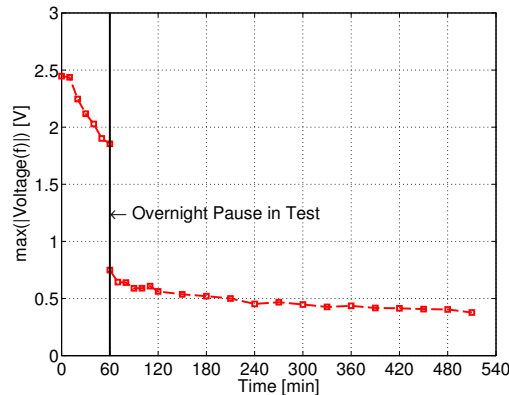


Figure F.12 – Maximum Voltage versus Durability Test Time for Sample No. 1

test time, where the waveform developed a pronounced shoulder on the negative slope of the signal.

Figure F.14 and Table F.4 compare the maximum voltage level results for the first two samples on the first day of durability testing. Results for both samples are similar; the maximum sensor voltage decreased significantly after one hour, by up to 30%. Sample no. 1 was selected over sample no. 2 for further testing, due to its higher starting voltage levels and its physical simplicity.

**Sample No. 3.** Figure F.15 shows time domain signals from the sample no. 3 piezoelectric sensor on the first day of testing. The signal at the start of the test appears in Figure F.15a. The signal after 60 minutes of durability test time appears in Figure F.15b. Peak-to-peak voltage levels are similar over the one hour durability test, although the



APPENDIX F. SENSOR DURABILITY BENCH TEST

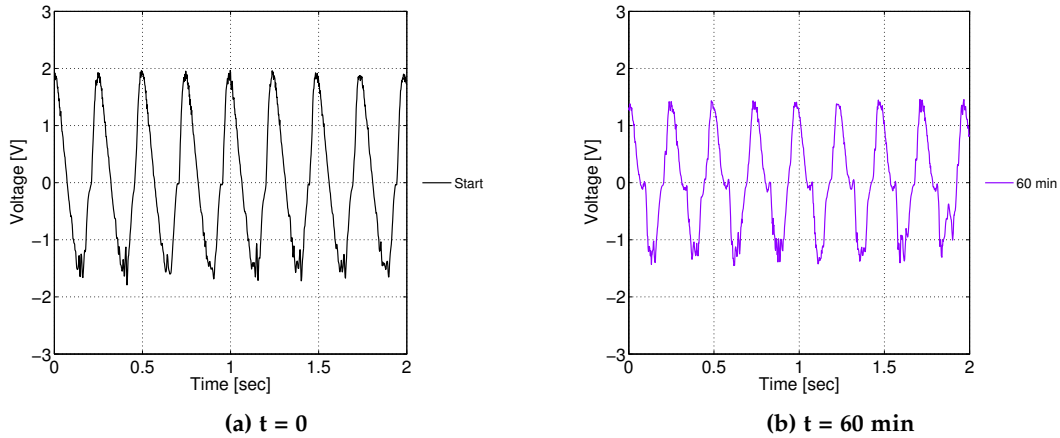


Figure F.13 – Sample No. 2 Time Domain Signals in Durability Test – Day 1

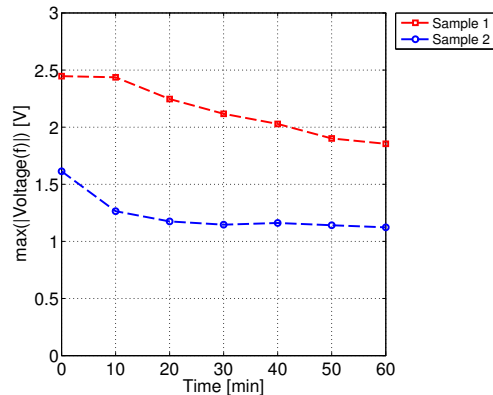


Figure F.14 – Maximum Voltage versus Durability Test Time for Sample No. 1 and Sample No. 2

starting voltage was much lower than the first two samples. This may be related to the “Chemical Vulcanizing Fluid” used in sample no. 3, which was intended to bond a rubber patch to an injured tire permanently and irreversibly. In sample no. 3 the sensor was sandwiched between the tire sample and a patch bonded to it using the vulcanizing fluid. The sensor was most likely “sliding” in sample no. 3, and therefore indirectly connected to the tire deformation, similar to the foam mounted sensor of sample no. 2.

The relatively lower voltage levels of sample no. 3 are also observed on the second day of testing as shown in Figure F.16. Output from sample no. 3 was similar on the first and second test days considering maximum voltage level, but the signal was much noisier on the second day, similar to the results from the first two samples. Maximum voltage level

APPENDIX F. SENSOR DURABILITY BENCH TEST

Table F.4 – Maximum Voltage Change After One Hour

Sample No.	Maximum Voltage at Start	Maximum Voltage at 60 min	Change
1	2.45	1.85	-24%
2	1.61	1.12	-30%

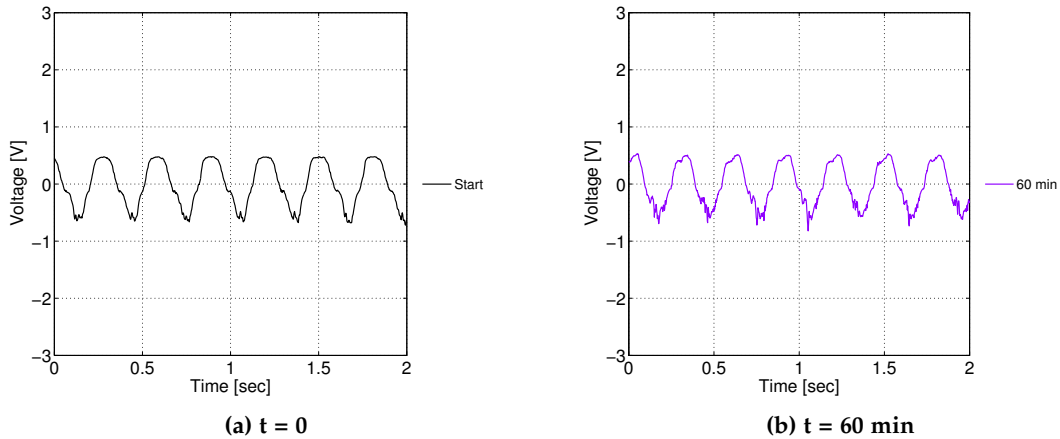


Figure F.15 – Sample No. 3 Time Domain Signals in Durability Test – Day 1

versus time for sample no. 3 is plotted in Figure F.17. A review of this plot shows that sensor voltage levels were more consistent over the two test days than the previous two samples. However, the maximum voltage level still decreased by 14% from three hours to eight hours on the second day. While sample no. 3 exhibited relative consistency in its voltage output compared with the other samples, it was rejected due to its low starting voltage levels, especially in comparison with sample no. 1.

**Sample No. 4.** Sample no. 1 was selected as the best of the first three samples, primarily due to the higher voltage output levels from its piezoelectric sensor at the start of testing. Sample no. 4 was a copy of sample no. 1, except that the sensor was confirmed parallel to the tire sidewall radial direction. In sample no. 1 the sensor was slightly skewed from the radial direction, due to inadequate restraint and subsequent rotation of the sensor during adhesive setup during the fabrication process. This problem was fixed in sample no. 4, and it was tested extensively over several calendar weeks using the durability bench testing machine. Each testing session lasted for 4 to 9 hours, with pauses ranging from overnight to one week. The main purpose of the extended durability testing of sample no. 4 was to understand the reason for the deterioration observed in sample no. 1, whether it was associated with fatigue of the sensor, fatigue of the adhesive, or both.

APPENDIX F. SENSOR DURABILITY BENCH TEST

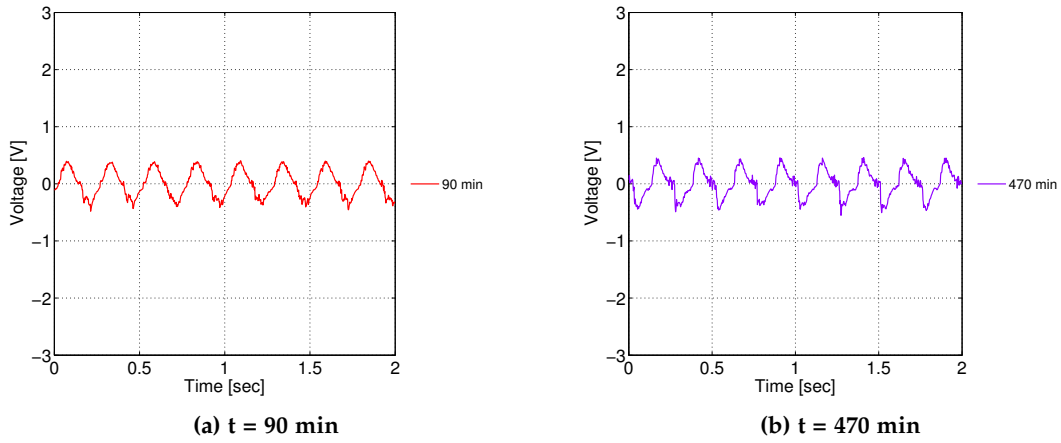


Figure F.16 – Sample No. 3 Time Domain Signals in Durability Test – Day 2

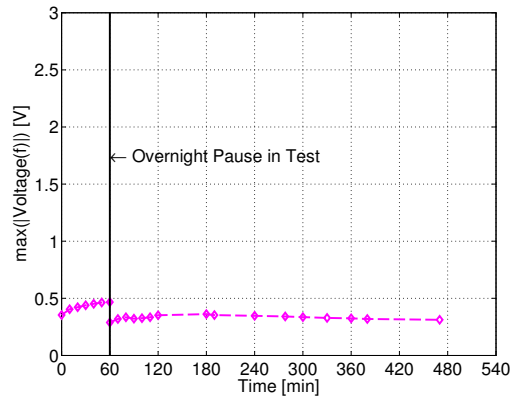
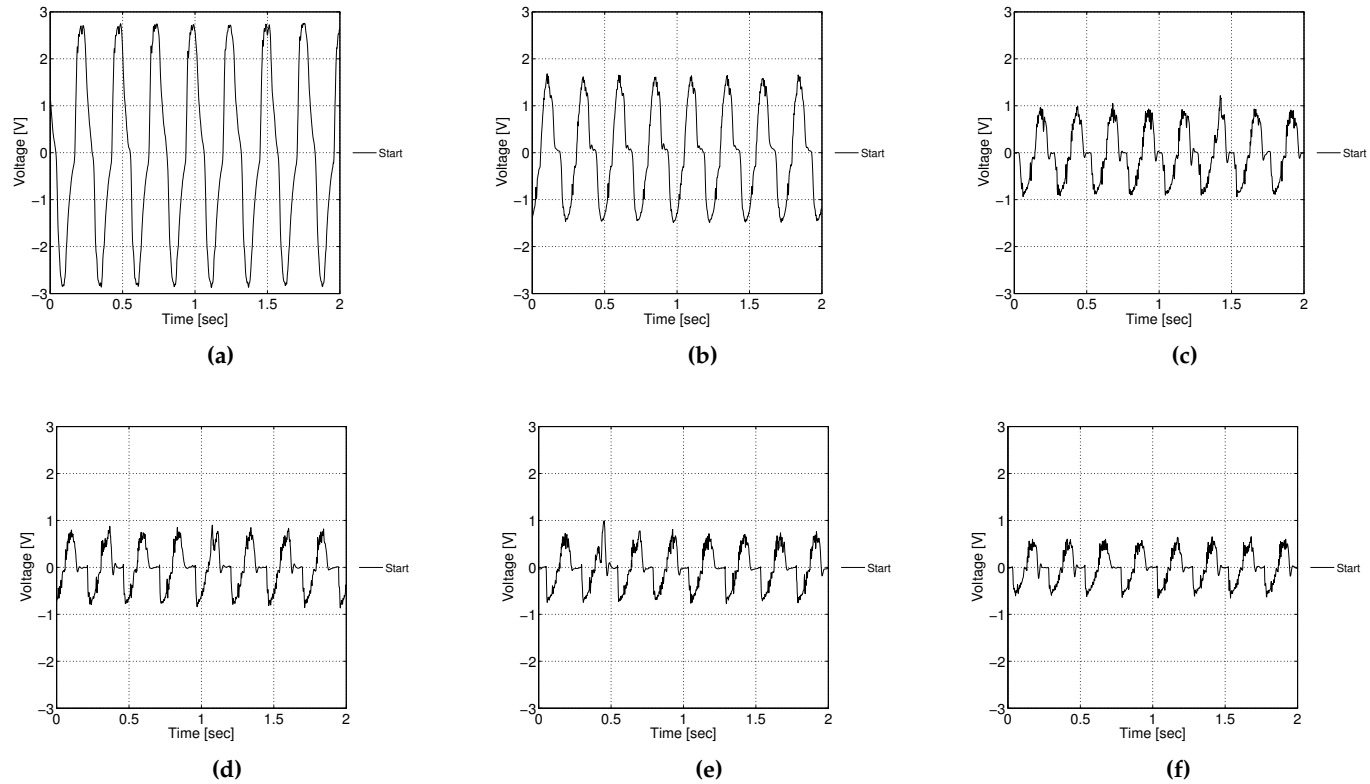


Figure F.17 – Maximum Voltage versus Durability Test Time for Sample No. 3



**Figure F.18 – Sample No. 4 Time Domain Signals in Multi-Day Durability Test: (a) Day 1 (b) Day 2 (c) Day 3 (d) Day 4 (e) Day 5 (f) Day 6**

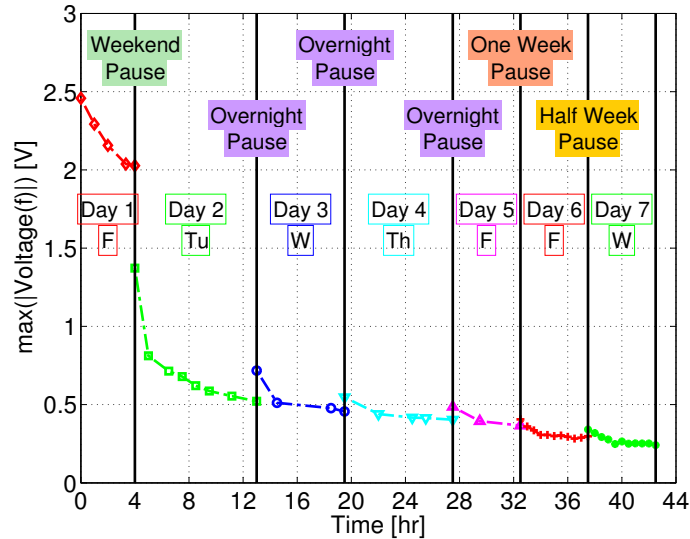


Figure F.19 – Maximum Voltage versus Durability Test Time for Sample No. 4

Figure F.18 shows time domain signals from the sample no. 4 piezoelectric sensor at the start of the test for the first six days of testing. These plots show that the output from the sensor deteriorated with each subsequent test day, with peak-to-peak voltage levels lower and a progressively noisier signal. The maximum voltage level versus time for sample no. 4 is plotted in Figure F.19. A review of this plot shows that there is a continual drop in sensor voltage levels over the time frame of the test. At the end of the durability test, sample no. 4 was disassembled and the piezoelectric sensor was cleaned and examined.

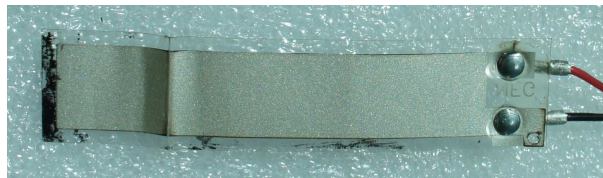


Figure F.20 – Piezoelectric Sensor From Sample No. 4 After Durability Testing

A photograph of the sample no. 4 sensor at the end of the durability test appears in Figure F.20, which shows that the sensor had buckled during the test. The sensor was permanently bent and deformed near its bottom due to the multiple strain cycles imposed on it. The likely cause of the deterioration in the sensor output, therefore, was fatigue of the sensor itself, and not a failure of the adhesive, or some other adhesive issue such as insufficient curing time before testing. Furthermore, the sensor was in good condition at the end of the test, other than the “kink”. There was no evidence that the coating of the sensor was attacked by the adhesive. Since the results showed that the piezoelectric

---

## APPENDIX F. SENSOR DURABILITY BENCH TEST

---

sensor was probably capable of surviving only a few deformation cycles (at this level) before fatigue failure, further samples were fabricated that attached only one-third of the sensor to the tire with adhesive. This was an attempt to avoid the buckling problem.

**Sample No. 5.** Figure F.21 shows time domain signals from the sample no. 5 piezoelectric sensor at the start of the test for the third and fourth days of testing. Output from the sensor in sample no. 5 deteriorated with each subsequent test day, with peak-to-peak voltage levels higher and a progressively noisier signal. The increase in voltage levels over a multi-day test was unique to sample no. 5, although voltage output at the start of the test was relatively low, which was expected since only one third of the sensor was attached to the tire. The increasing voltage phenomenon is illustrated in Figure F.22, which shows the maximum voltage level versus time for sample no. 5.

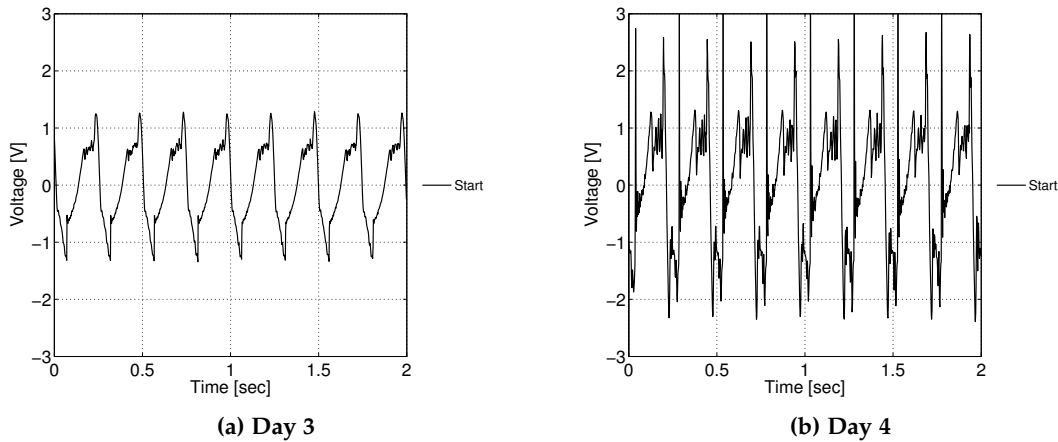


**Figure F.21 – Sample No. 5 Time Domain Signals in Multi-Day Durability Test**

At the end of the durability test, sample no. 5 was visually inspected, at which time a hole in the tire rubber was discovered at the free end of the sensor, where it had been gouged out by the sensor itself. At that point sensor no. 5 was modified by bonding a thin piece of plastic film to the tire rubber underneath the free end of the sensor, to create sensor no. 5M, or sensor no. 5 modified. The plastic film prevented abrasion removal of the tire rubber by the free end of the sensor.

**Sample No. 5M.** Figure F.23 shows time domain signals from the sample no. 5M piezoelectric sensor at the start of the test for the first four days of testing, which are also the sixth through ninth days of testing for sample no. 5. These plots show that the peak-to-peak voltage levels were reduced after the modification, since the addition of plastic film prevented the free end of the sensor from striking the hole it had dug for itself, and therefore there were no longer any voltage spikes associated with impacts between the sensor free end and the tire rubber. In general, peak-to-peak voltage levels were similar to those measured when sample no. 5 was fresh, but it can be seen that the signal was

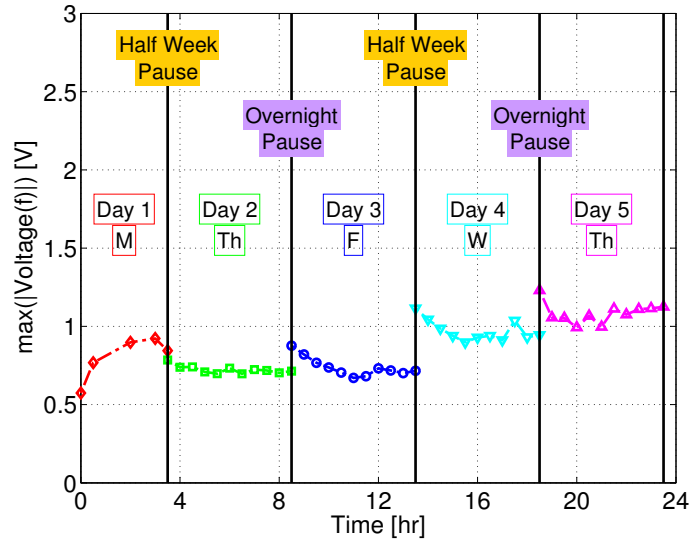


Figure F.22 – Maximum Voltage versus Durability Test Time for Sample No. 5

noisier with increased durability testing time, indicating that the configuration of sample no. 5M was still not sufficiently durable for the STSS, although it was the best option for the vehicle tests.

Maximum voltage level versus time for sample no. 5M for test day 6 is plotted in Figure F.24. A review of this plot shows that sensor voltage levels were reasonably consistent over a test day of five hours duration. Maximum voltage level at the start of the test was 0.75 volts. At a time of 30 minutes the peak level had increased from the starting voltage by 4%. At a time of 60 minutes the peak level had decreased from the starting voltage by 4%. Based on these results, important vehicle dynamics events were attempted within one hour of the start of an on-road vehicle test, since voltage levels from the piezoelectric sensors were expected to vary within 5%, which was considered acceptable. Beyond one hour, voltage levels from the sensors were expected to vary within 10%.

The results of the sensor durability bench test study show that the commercially available piezoelectric deformation sensors tested are not suitable for use in the STSS. The sensors suffered from fatigue failures, particularly permanent buckling, when subjected to a physical durability test that simulated several weeks of tire use, which was clearly an unacceptable performance given the long service life required of a typical tire. Furthermore, the signal quality from the sensors deteriorated within minutes of use, with the increase in signal noise being qualitatively apparent from inspection of the output voltage time histories.

The sensor configuration of sample no. 5M was selected for use in the smart tire prototypes due to its relatively stable voltage output levels, compared to the other samples

## APPENDIX F. SENSOR DURABILITY BENCH TEST

---

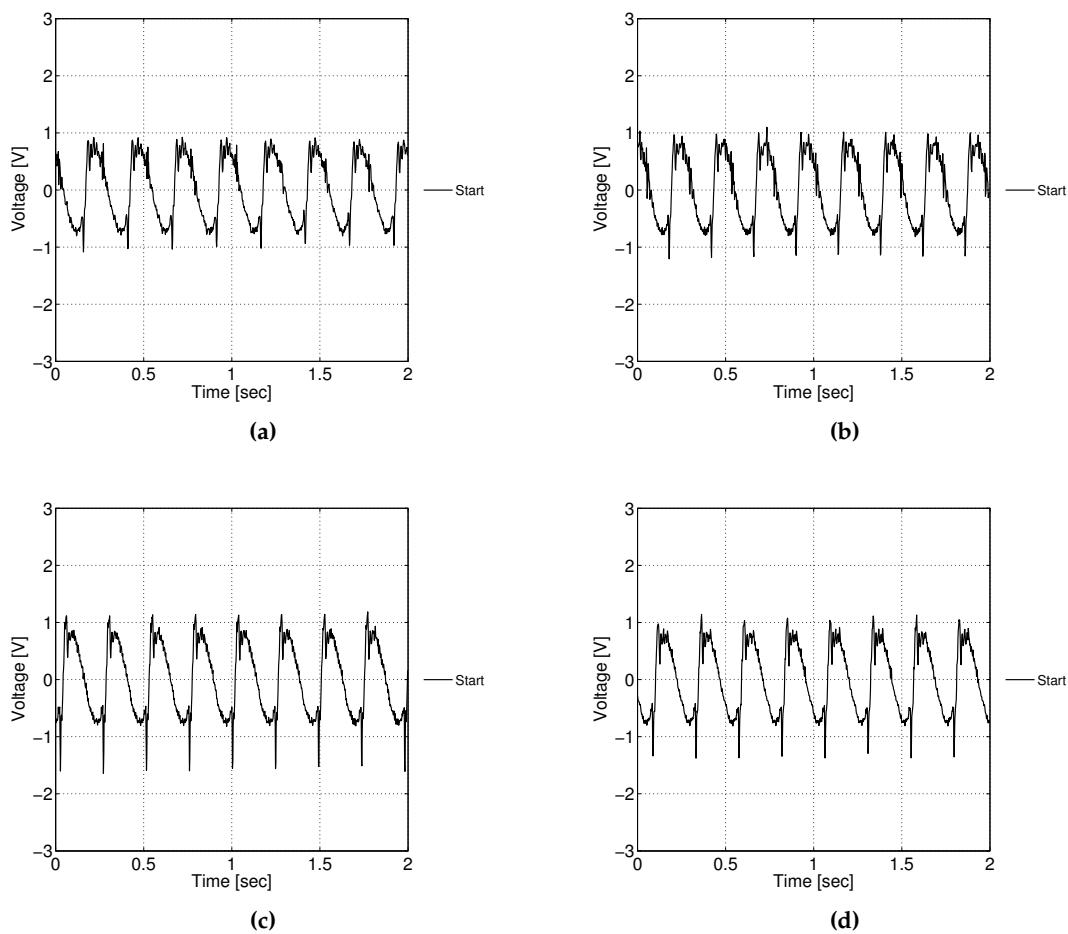
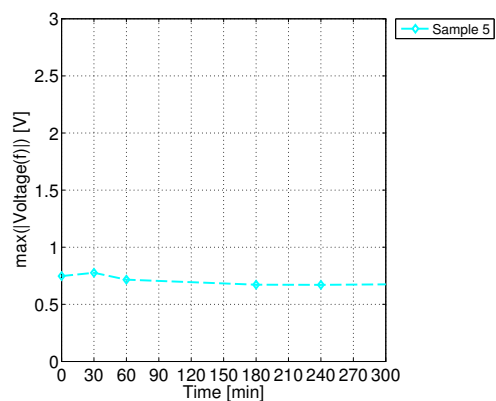


Figure F.23 – Sample No. 5M Time Domain Signals in Multi-Day Durability Test: (a) Day 6 (b) Day 7 (c) Day 8 (d) Day 9



## APPENDIX F. SENSOR DURABILITY BENCH TEST

---



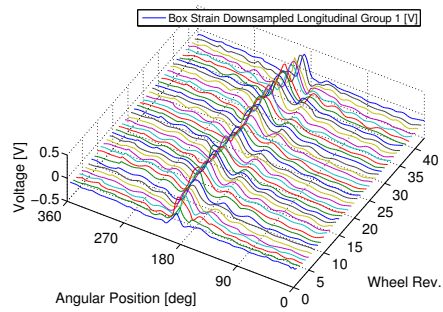
**Figure F.24 – Maximum Voltage versus Durability Test Time for Sample No. 5M – Day 6**

tested, but this configuration still was not acceptable, since serious signal quality issues appeared within an hour, which was true of the piezoelectric sensors regardless of sensor attachment method. In future work on the STSS, a deformation sensor for in-tire use must be identified that has similar – or greater – flexibility compared to tire rubber. Only a sensor with comparable stretch is likely to be sufficiently durable. Identification of this sensor is the biggest, and most important, problem that is part of STSS future work.

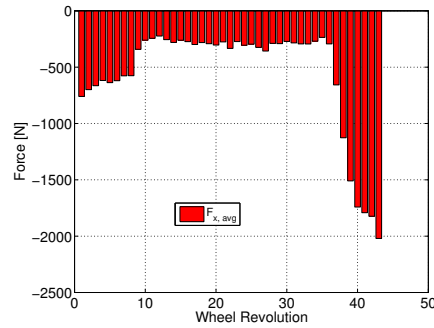
## **Appendix G**

# **Physical Sensor Measurements**

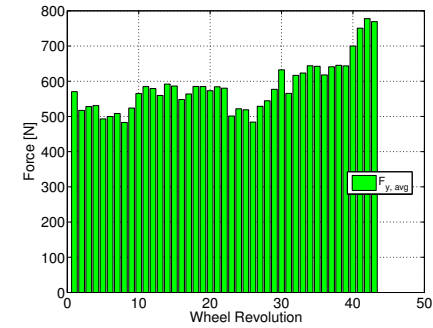
Physical sensor data from Round 1 testing of smart tire revision 2 are shown.



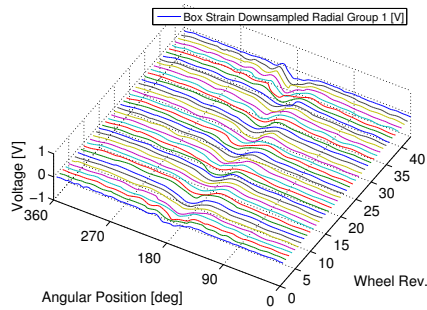
(a)



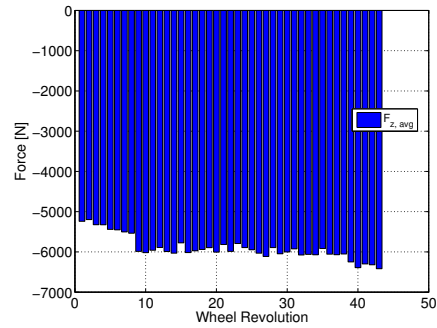
(b)



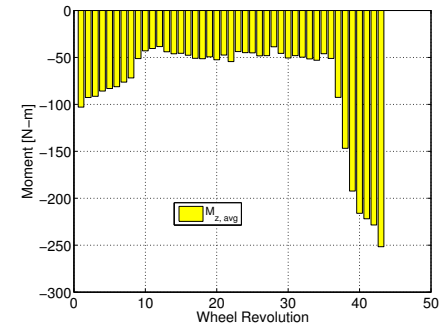
(c)



(d)

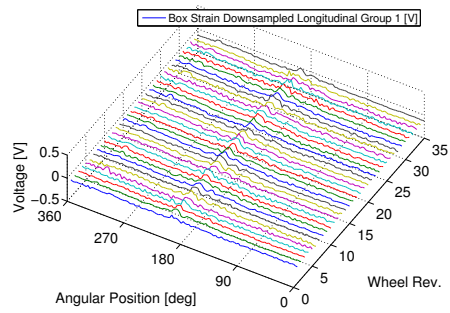


(e)

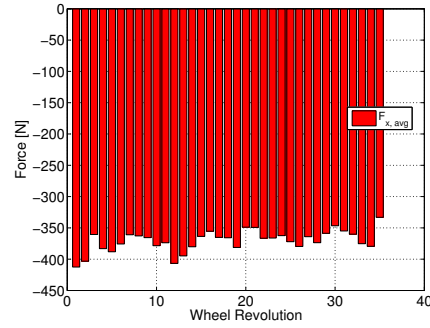


(f)

**Figure G.1 – Sensor Data in Straight Line Driving Test No. 4 From Smart Tire Revision 2: (a) Sidewall Left Longitudinal Deformation (b) Average Longitudinal Force (c) Average Lateral Force (d) Sidewall Left Radial Deformation (e) Average Vertical Force (f) Average Aligning Moment**



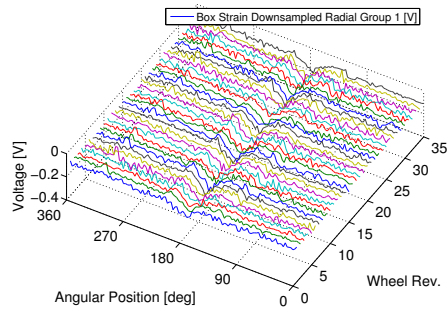
(a)



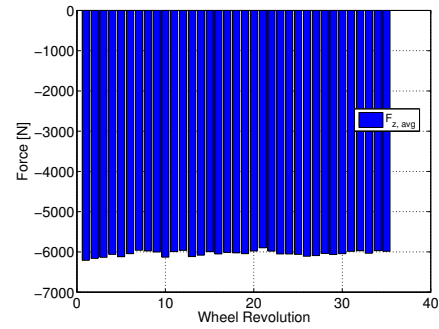
(b)



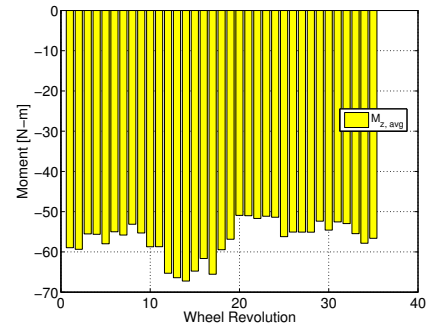
(c)



(d)

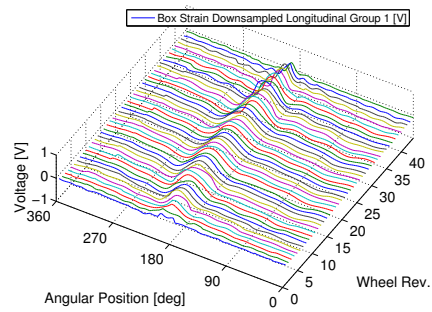


(e)

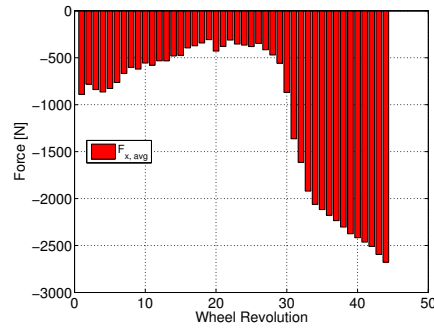


(f)

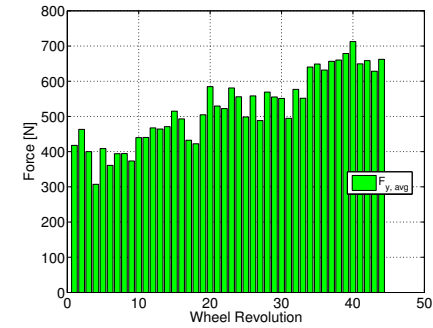
**Figure G.2 – Sensor Data in Straight Line Creeping Test No. 5 From Smart Tire Revision 2: (a) Sidewall Left Longitudinal Deformation (b) Average Longitudinal Force (c) Average Lateral Force (d) Sidewall Left Radial Deformation (e) Average Vertical Force (f) Average Aligning Moment**



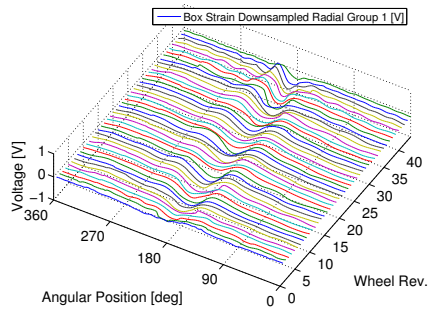
(a)



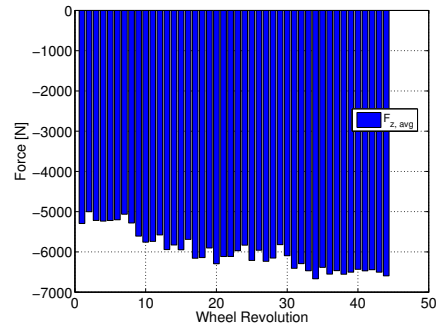
(b)



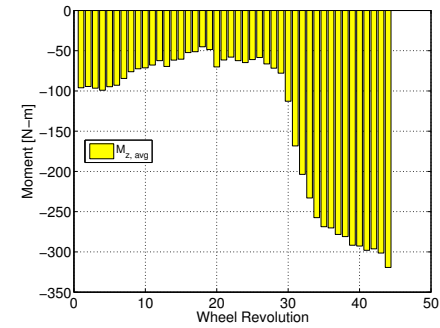
(c)



(d)

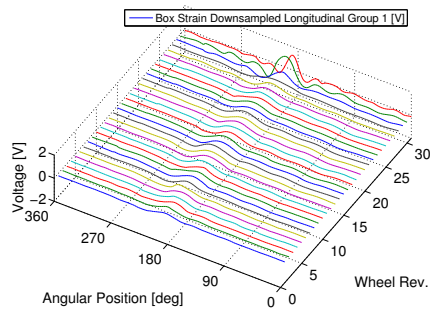


(e)



(f)

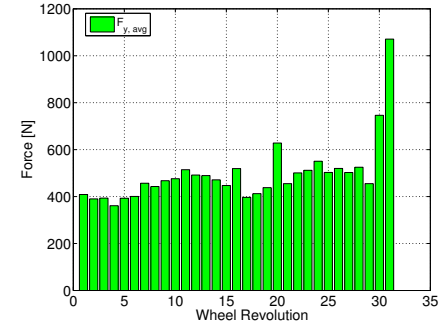
Figure G.3 – Sensor Data in Light Straight Line Acceleration Test No. 7 From Smart Tire Revision 2: (a) Sidewall Left Longitudinal Deformation (b) Average Longitudinal Force (c) Average Lateral Force (d) Sidewall Left Radial Deformation (e) Average Vertical Force (f) Average Aligning Moment



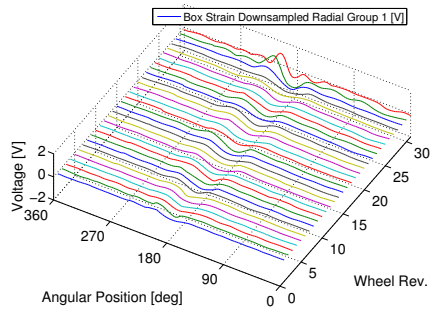
(a)



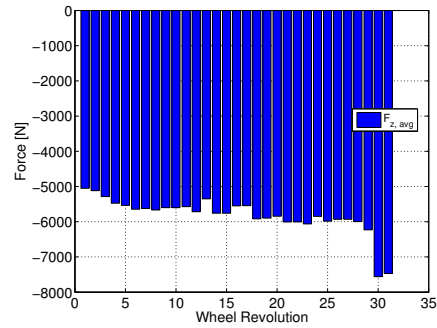
(b)



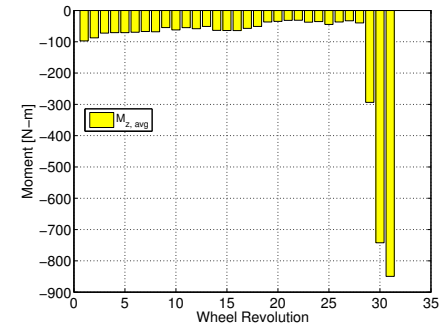
(c)



(d)

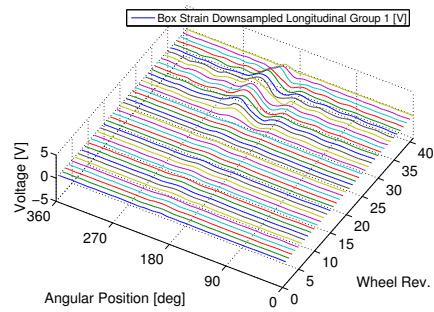


(e)

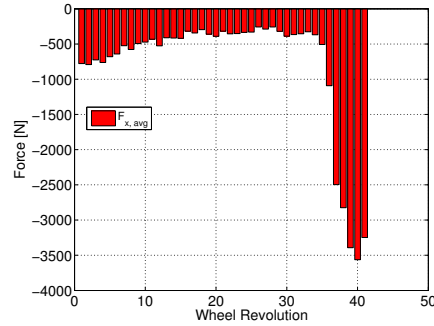


(f)

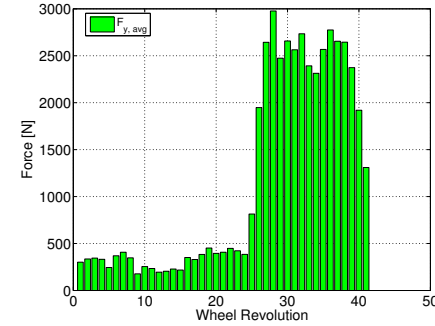
Figure G.4 – Sensor Data in Moderate Straight Line Braking Test No. 14 From Smart Tire Revision 2: (a) Sidwall Left Longitudinal Deformation (b) Average Longitudinal Force (c) Average Lateral Force (d) Sidwall Left Radial Deformation (e) Average Vertical Force (f) Average Aligning Moment



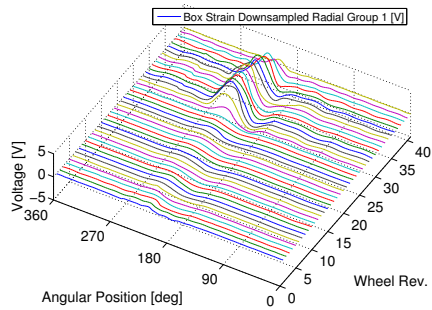
(a)



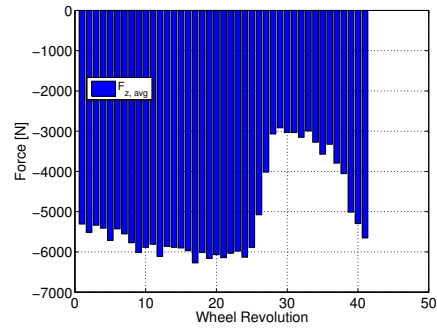
(b)



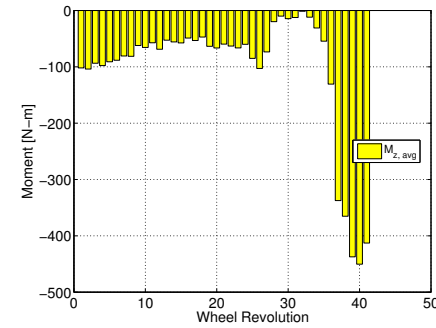
(c)



(d)

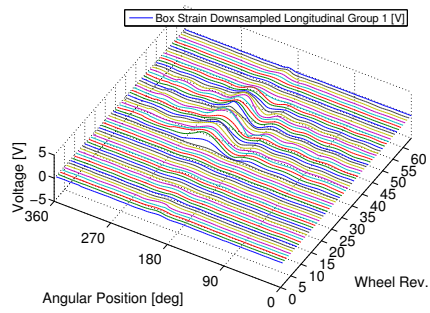


(e)

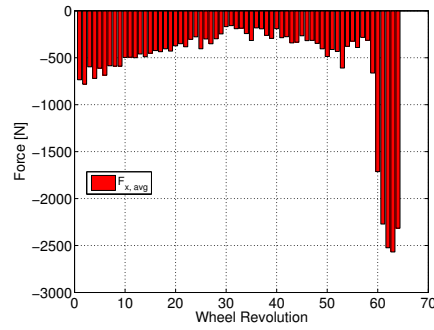


(f)

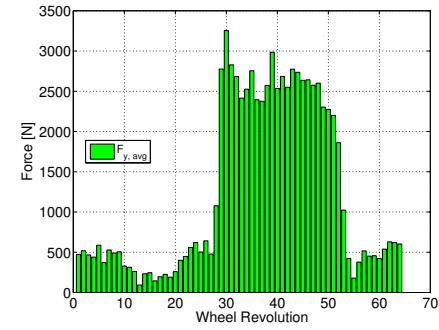
**Figure G.5 – Sensor Data in Braking in a Turn Right Test No. 26 From Smart Tire Revision 2: (a) Sidewall Left Longitudinal Deformation (b) Average Longitudinal Force (c) Average Lateral Force (d) Sidewall Left Radial Deformation (e) Average Vertical Force (f) Average Aligning Moment**



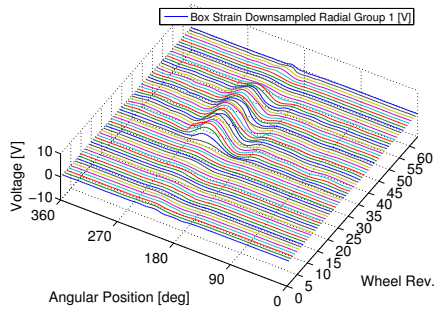
(a)



(b)



(c)



(d)



(e)



(f)

Figure G.6 – Sensor Data in Step Steer Right Test No. 28 From Smart Tire Revision 2: (a) Sidewall Left Longitudinal Deformation (b) Average Longitudinal Force (c) Average Lateral Force (d) Sidewall Left Radial Deformation (e) Average Vertical Force (f) Average Aligning Moment